A Study of Complex River Ice Processes in an Urban Reach of the North Saskatchewan
River
by

Rhodri Howley

A thesis submitted in partial fulfillment of the requirements for the degree of

Master of Science

in

WATER RESOURCE ENGINEERING

Department of Civil and Environmental Engineering
University of Alberta

Abstract

Northern rivers are affected by river ice processes for a significant portion of the year. This poses many challenges and opportunities to river ice engineers and geoscientists. Since 2009, several researchers have conducted a variety of river ice studies on the North Saskatchewan River through Edmonton, Alberta. This has resulted in a relatively comprehensive dataset which includes meteorological, hydrometric and river ice data. Analyses of these data have produced interesting results which are evidence of a highly complex ice regime. The conditions preceding and during freeze-up and break-up are highly variable.

The University of Alberta's River1D Ice Process model is used to investigate these phenomena by simulating the 2009-10 and 2010-11 winter seasons. The 29 km long study reach includes multiple bridging locations and the discharge from the Gold Bar Wastewater Treatment Plant (GBWTP). Simulation results are compared to the observed water surface elevation, ice front progression, surface pan concentration, border ice fraction, ice thickness, suspended frazil concentration, and water temperature data measured at several locations along the reach. Strong agreement between the observed and simulated data was achieved for an unprecedented number of river ice variables. The model can be sued as the foundation for future river ice studies in Edmonton and to help address specific problems or challenges that have been observed within the study reach.

Preface

This thesis is the original work of Rhodri Howley with the assistance of Dr Yuntong She and Dr Tadros Ghobrial. Parts of the thesis have been published as conference papers at the 20th Workshop on the Hydraulics of Ice Covered Rivers by the Committee on River Ice Processes and the Environment and the 25th International Symposium on Ice by the International Association of Hydro-Environment Engineering and Research. It is expected that sections of this thesis will be adapted for journal paper publication in 2021.

Acknowledgements

1   Table of Contents

List of Tables

Table of Figures

List of symbols and abbreviations

Abbreviations	
ADCP	Accoustic Doppler current profiler.
DDF	Degree-days of freezing (°C·Days).
DDT	Degree-days of thawing (°C·Days).
DMS	Degree-minutes of supercooling (°C·Minutes).
EAS	Earth and Atmospheric Sciences.
GBWTP	Gold Bar Wastewater Treatment Plant.
NSR	North Saskatchewan River.
SWIPS	Shallow water ice profiling sonar.

Symbols	
A	Cross-sectional area to the water surface (m^2).
A_{an}	Cross-sectional area of the anchor ice (m^2).
A_{fs}	Cross-sectional area of the stationary frazil slush layer (m^2).
A_i	Cross-sectional area of the surface ice including border ice and under-cover moving frazil (m^2).
A_{si}	Cross-sectional area of the solid ice layer (m^2).
A_{ui}	Cross-sectional area of the under-cover moving frazil layer (m^2).
A_w	Cross-Sectional area of water under and through the ice (m^2).
a	User defined coefficient used in the border ice equation.
B_b	Border ice width from a given bank (m).
B_o	The width of the water surface clear of border ice (m).
B_{ws}	Total width of the channel at the water surface, excluding any overbank flow (m).
b	User defined coefficient used in the border ice equation.
c	Wave celerity (m/s).
C_{an}	Fraction of bed covered by anchor ice.

C_f	Volumetric concentration of suspended frazil ice (%).
C_{fo}	Frazil seeding concentration (%).
C_i	Surface ice concentration (%).
C_p	Specific heat of water (J/g°C).
C_{pk}	Peak suspended frazil concentration (%).
D	Hydraulic depth (m).
D_{ui}	Undercover flow depth (m).
d_e	Typical frazil particle thickness (m).
d_s	Average diameter of the bed material (m).
e	User defined coefficient used in the border ice equation.
e_{wi}	Thermal energy per unit mass of ice-water mixture (J/kg).
F_r	Froude number.
f_l	Conditional constant used in the solid ice mass conservation equation.
f_b	Fraction of the channel covered by border ice.
g	Acceleration due to gravity (m/s^2).
H	Water surface elevation relative to a specified datum (m).
h_{ia}	Linear heat transfer coefficient (W/m^2/°C).
h_{wa}	Heat transfer coefficient (W/m^2/°C).
j_{wa}	Heat transfer coefficient (W/m^2/°C).
K_i	Thermal conductivity of ice (W/m/°C).
K_w	Thermal conductivity of water (W/m/°C).
k_{wa}	Heat transfer constant (W/m^2/°C).
L_i	Latent heat of ice (334 KJ/ kg).
L_m	Latent heat of fusion of ice (kJ/ kg).
N_u^f	Nusselt number of a suspended frazil particle.
n	Manning's roughness coefficient.
n_1	Roughness coefficient for the underside of an ice cover.
n_2	Roughness coefficient of the bed.
n_c	Composite roughness (bed and under ice cover).

P_b	Bed affected wetted perimeter (m).
P_i	Ice affected wetted perimeter (m).
p_a	Porosity of anchor ice
p_i	Expected porosity of the ice accumulation following formation of the ice cover.
p_f	Frazil slush porosity.
Q	Discharge (m$^{3/s}$).
Q_w	Discharge of water under and through the ice (m^3/s).
R	Hydraulic radius (m).
r_o	Typical frazil particle radius (m).
S	Channel slope.
S_f	Friction slope.
S_{ui}	Source term representing the exchange between the undercover moving and stationary frazil layers.
T_a	Air temperature (°C).
T_i	Ice temperature (°C).
T_w	Water temperature (°C).
t	Time (seconds, minutes, or hours).
t_{an}	Anchor ice thickness (m).
t_b	Border ice thickness (m).
t_f	Ice pan thickness (m).
t_{fs}	Thickness of the frazil slush layer (m).
t_i	Ice thickness (m).
t_{le}	Expected thickness of the ice accumulation following formation of the ice cover (m).
t_{si}	Thickness of the solid ice layer (m).
t_{ui}	Thickness of under-cover moving frazil layer (m).
t'_f	Thickness of new frazil pans (m).
t'_{si}	Initial thickness of ice which has newly formed between ice pans once they have stopped moving (m).

U_{cr}	Maximum water velocity for border ice accretion (m/s).
U_i	Ice velocity (m/s).
U_{i_re}	Ice velocity threshold for re-entrainment (m/s).
U_{ui}	Velocity of the under-cover moving frazil layer (m/s).
U_w	Average velocity of water flowing under and through the ice (m/s).
U_{wl}	Local water velocity in the open water adjacent to the edge of the border ice (m/s).
x	Streamwise path of the river (m).
α_1	Empirically derived and site-specific coefficient used in the Stefan Equation (m°C$^{-1/2}$Day$^{-1/2}$).
α	Albedo.
$\boldsymbol{\alpha_{wi}}$	The coefficient for turbulent heat exchange between water and ice (W·s$^{0.8}$/m$^{2.6}$/°C).
β_1	Empirically derived coefficient used in the degree-minutes of supercooling method (°C$^{-1/2}$·min$^{-1/2}$).
β	Momentum flux correction coefficient used in River1D hydrodynamic calculations (momentum equation).
β_{re}	Rate of surface ice re-entrainment (1/s).
γ	Rate of frazil ice accretion to the bed (m/s).
Δt	Time-step (seconds, minutes or hours).
Δt_j	Change in ice thickness (m).
η	Rate of frazil rise (m/s).
ρ_i	Density of ice (kg/m^3).
ρ_s	Density of bed material (kg/m^3).
ρ_w	Density of water (kg/m^3).
Φ	Ratio of the ice affected and bed affected wetted perimeters (P_i/P_b).
Φ_{DDF}	Rate of heat loss based on the degree-days of freezing (W/m^2).

ϕ_{ia}	Net rate of heat exchange per unit surface area between ice and air (W/m^2).
ϕ_s	Shortwave radiation (W/m^2).
ϕ_{wa}	Net rate of heat exchange per unit surface area between water and air (W/m^2).
ϕ_{wi}	Net rate of heat exchange, per unit surface area, between water and ice (W/m^2).
ϕ_{fw}	Net rate of heat exchange, per unit surface area, between suspended frazil particles and water (W/m^2).

1.0 Introduction

This thesis presents a modeling study of the river ice processes of the North Saskatchewan River (NSR) through an urban environment using River1D. For this, extensive data collected along the NSR through Edmonton between 2009 and 2011 were used to develop, calibrate and validate the model. Additional data from 2011 – 2019 is used to investigate and describe the thermal regime of this river. The data includes discharge, water surface elevation, water temperature, suspended frazil concentration, surface ice concentration, ice front progression and river ice thickness measurements.

1.1. Overview of river ice processes

Freeze-up is considered to be the period of time in which a stable ice cover forms and typically begins on Canadian rivers in the fall or early winter. The predominant heat loss in cooling of river water is heat transfer from rivers to overlying cooler air. Additional heat loss may occur due to precipitation (usually snowfall) and through loss to the riverbed and banks. Once river water is supercooled (Hicks, 2016), ice may begin to form in two different ways, depending upon the degree of mixing and turbulence. The turbulence in slow-moving and shallow sections of river, such as adjacent to the banks and in eddies or around islands, is often insufficient to mix supercooled water at the surface with the flow below (Ashton, 1979) or to entrain ice particles into the flow (Clark, 2013). In these locations, a thin layer of skim ice will form at the surface of the water. Skim ice which grows laterally from a riverbank towards the river channel is known as static border ice (Shen, 2010). In the initial stages of freeze-up, border ice grows laterally as heat is lost to the riverbank and thickens as heat is lost to the overlying cold air.

The second way in which ice forms in rivers is through the formation of frazil crystals by way of secondary nucleation on pre-existing ice crystals, known as seed crystals (Daly, 2013). This happens in areas of the river with greater turbulence, where the water is mixed, and the water temperature is roughly equal throughout the flow depth. In natural rivers, it usually forms with supercooling equal to or less than -0.06 °C (Hicks, 2016). However, greater levels of supercooling have been observed, including along the North Saskatchewan where supercooling of up to -0.106 °C has been observed (Kalke et al.,

2019). Collision of active frazil particles can cause fracturing and a multiplicative effect in the development of additional frazil. Owing to the adhesive behavior of frazil, flocculation and the formation of frazil flocs, or if frazil adheres to the riverbed, anchor ice may occur.

Frazil flocs, also known as frazil slush, remain in suspension until their buoyancy is sufficient to overcome the turbulence of the flow and rise to the surface. A portion of the slush is exposed above the water and interstitial freezing of water in this exposed section will lead to the formation of ice pans. Individual pans grow in surface area and thickness as additional flocs adhere laterally and to the underside of the pan. Collision of pans may cause crustal thickening, hydraulic thickening or edge-to-edge freezing of pans to occur.

Ice pans may contribute to border ice growth by adhering to pre-existing border ice (previously formed through thermal growth), in a process known as *buttering* (Clark, 2013; Hicks, 2016) or hydraulic accumulation (Shen, 2010). For border ice growth to occur in this mode, the streamwise forces acting upon an ice pan, such as drag and gravity, must be balanced by the frictional force between the ice pan and the border ice (Shen, 2010).

Ice pan concentration increases around bends and in constrictions such as between bridge piers, or in areas where border ice has narrowed the channel width. Under such circumstances, it becomes likely that the ice pans will become lodged and bridging is said to have occurred. For bridging to occur, the forces acting on the pans in the streamwise direction, such as the current, hydrodynamic forces, and streamwise weight, must be counterbalanced by the resisting forces associated with bank shear, ice strength, and downstream resistance provided by any obstructions (Judge et al., 1997; Matousek, 1988; Shen, 2010; Urroz & Ettema 1994). If resisting forces do not counterbalance the driving forces, the ice pans will either be forced through the constriction or may consolidate before either jamming or releasing from the bridging location. Surface and depth-averaged water velocities, water surface width or width of the gap in the surface obstruction, water depth, meteorological conditions, strength and thickness of ice pans, channel geometry (including bank roughness, slope, and curvature of channel bends), surface pan concentration, pan shape, Froude number, water discharge, and density and

porosity of ice pans all play a role in the bridging process (Johnson and Kostras, 1980; Matousek, 1988; Tatinclaux and Lee, 1978; Urroz & Etema, 1994; and Wang and Chen, 2011). Several bridging locations may exist within a single study reach, even where study reaches are relatively short (Howley et al., 2019; Jasek and Pryse-Phillips, 2015). This may cause a disjointed or fragmented ice front propagation.

The ice front progression rate, the rate at which an ice cover advances upstream, is a function of the channel geometry, gradient, water velocity, discharge, surface ice concentration and the upstream propagation mode. An ice pan advancing downstream towards an ice front may come to rest edge-to-edge with the ice front, extending the ice front upstream and creating a juxtaposed ice cover. The ice front will continue to propagate upstream in a juxtaposed manner unless the streamwise forces acting on an ice cover outbalance the internal strength of the ice cover. If this happens, the ice cover may collapse or shove, and mechanical thickening will occur resulting in a hummocky ice cover and/or freeze-up ice jams (Hicks, 2016). Alternatively, an incoming ice pan may submerge beneath the ice front and be deposited to the underside of the ice cover, thickening the ice cover in a process called hydraulic thickening (Hicks, 2016). Whether or not an incoming pan will submerge beneath an ice cover is largely controlled by the flow velocity, with the probability of submergence increasing with water velocity. Pan geometry, porosity and density also play a role in this process (Beltaos, 2013). It should be noted that it is also possible for this type of ice cover to collapse, inducing additional mechanical thickening.

The effect of stationary ice on river hydraulics is significant. The presence of a full or partial ice cover, including border ice, increases the wetted perimeter and reduces the hydraulic efficiency of the channel. Additionally, the Manning's n roughness of the underside of an ice cover can vary from approximately 0.01 to 0.1 (Hicks, 2016). These effects cause a reduction in the hydraulic efficiency of the channel and a sudden increase in stage, known as stage-up, as ice cover forms.

Once formed, an ice cover insulates the underlying water from cold overlying air and inhibits further supercooling and frazil production. However, wherever open leads exist, such as in locations where there is a warm water influx or where the flow velocity is

sufficient to prevent the formation of an ice cover, continuous frazil production may occur. The frazil produced will travel downstream and will either form ice pans or be swept beneath a downstream ice cover where it may be deposited, thickening the ice cover. If large enough quantities of frazil are deposited at the same location, a hanging dam will form (Ashton, 1979).

The thickness of an ice cover will generally continue to grow during winter. Thickening of the underside of the ice cover may occur due to heat loss through the ice cover itself to overlying cold air. This is called thermal growth. Accumulation of snow on an ice cover may cause the ice cover to depress or submerge, resulting in the upwelling of river water. The snow begins to saturate and forms slush, which then freezes forming snow ice.

Break-up begins with rising air temperatures and may take one of two forms: thermal break-up or dynamic break-up. Thermal break-up is directly driven by meteorological conditions, with ice covers melting in-situ. It is typically associated with gradually rising air temperatures. Thermal break-up is usually disjointed, with significant spatial variation in the timing of break up. This can be attributed to the spatial variability of shading effects and ice thickness. Owing to this, it is common for open leads to develop during the break-up process. Such open leads result in warming of river water which in turn may contribute to thermal melting of the underside of a downstream ice cover.

Dynamic break-up is largely driven by hydraulic processes which results in the mechanical breaking of the ice cover. A significant increase in discharge causes a rise in water level, lifting the ice cover and breaking it into floating ice sheets by separating it from the shorefast border ice. Dynamic break-up is also disjointed and break-up ice jams may form. The development of ice jams can cause an upstream cascade effect, with waves propagating upstream causing or contributing to the mechanical release of intact upstream ice covers. An ice jam release will allow ice rubble to proceed downstream, where it may jam again at the next constriction or obstruction (Jasek, 2019).

Dynamic break-up is much more likely when there is a rapid rise in air temperature, or when a rainfall event occurs, leading to rapid melt of the snowpack and a steep incline in

a river's hydrograph. Other factors, such as increased releases from hydropower facilities, dams or reservoirs, may also cause or contribute to dynamic break-up.

1.2. Motivation: challenges presented by river ice processes and the benefits of river ice modeling.

River ice processes present a number of challenges for engineers and geoscientists. River ice has a significant impact on water quality and ecology (Brown et al., 2000, Lindenschmidt et al., 2018; Prowse, 2001a; Prowse, 2001b; Whitfield and McNaughton, 1986), river scour (Hains and Zabilanksky, 2005), flooding (Kempema et al., 2019), power loss and operational challenges at hydro-power generating stations (Alfredsen, 2015; Girling and Groeneveld, 1999; Nguyen et al., 2017), and it may affect hydraulic structures and bridges (Beltaos et al., 2003; Gebre et al., 2014; Kempema and Ettema, 2015; Daly and Ettema, 2006). Although ice-jams are often considered to be a destructive process, they are also a beneficial and necessary process for inland deltas, providing essential nutrients to areas such as the Peace-Athabasca Delta, a UNESCO World Heritage Site (Rokaya et al., 2019).

Although there has been great advancement in the understanding of river ice processes over the last several decades, one of the greatest inhibitions to further advancement of knowledge and understanding is the difficulty of collecting data. An excellent summary of some of the challenges and problems associated with deploying and retrieving equipment for the collection of river ice data is provided in Turcotte et al. (2017). Among the most frequently encountered problems are harsh weather conditions, a short time period in which data can be collected, anchor and frazil ice build-up on equipment, equipment loss, damage or theft and battery failure.

Falling through the ice poses serious risk of hypothermia and extended exposure can lead to fatalities. River currents beneath the ice surface can sweep victims downstream, forcing them beneath the ice (Jasek and Lavalley, 2003). There have been several approaches to minimize or eliminate these risks including relying on experience, attending formal training and through work avoidance (Jasek and Lavalley, 2003). River ice models are viewed as a potential alternative to extensive and costly data collection field studies.

River ice modeling has been and continues to be an invaluable tool in investigating these challenges and phenomena. It can provide quantitative descriptions of the river ice conditions and insight into an ice regime and/or specific process (Blackburn and She, 2019; Shen, 2010). By running model simulations and comparing the results to observed data from the field it is also possible to identify and/or address weaknesses in the river ice community's understanding of specific processes.

To date, models have been used in a variety of projects including predicting the timing of break-up and freeze-up (Bijeljajin and Clark, 2011; Prowse et al., 2007; Rokaya et al., 2017), flood-forecasting (Rokaya et al., 2019), investigating flood-risk (Lindenschmidt, 2017), evaluating benefits and consequences of installing or constructing flood defences (Lindenschmidt, 2017) analyzing the possible effects of flow regime change (Liu et al., 2015), and assessing the effects of climate change (Andrishak and Hicks, 2008; Chen and She, 2019; Turcotte et al., 2019).

Numerical models used in the field of river ice engineering vary from component models, used to investigate a single specific variable or process, to comprehensive models designed to simulate the entire winter regime of a river. The most widely used models are 1D steady-state ice jam profile models such as HEC-RAS (Daly and Vuyovich, 2003; Beltaos and Tang, 2013), RIVJAM (Beltaos and Wong, 1986), ICEJAM (Flato and Gerard, 1986), and ICETHK (Tuthill et al. 1998). These models are typically used to generate an ice jam profile and the related water levels under steady state conditions. These models generally solve the equilibrium ice jam equation however some models are capable of providing ice jam profiles for non-equilibrium jams. Two-dimensional steady state-ice jam profile models are more computationally demanding but typically perform better where significant 2D flow effects exist, such as in deltas or braided channels or where the dynamics of structures and outfalls are key. When consideration of more processes or variables is required, steady ice process models, such as ICEPRO (TALAS, 1993 cited in Malenchak, 2011), ICESIM (Carson and Groeneveld, 1997) and SIMGLACE (Rousseau et al., 1983 cited in Melanchak 2011), may be used.

Several comprehensive one-dimensional and two-dimensional unsteady ice process models also exist. In practical applications, one-dimensional models are often preferred

to two-dimensional models as they are less computationally demanding and generally have much shorter simulation times. Among the most popular one-dimensional comprehensive river ice models are CRISSP, MIKE-ICE, River1D, and RIVICE. A brief litereature review of each of these models is provided in the following sections.

1.2.1. CRISSP

The Comprehensive River Ice Simulation System (CRISSP) is a proprietary model developed at Clarkson University under contract to CEA Technologies Inc. It includes both a 1D and a 2D model. CRISSP1D solves the 1D Saint-Venant equations using a four-point implicit finite difference method and the thermal-ice equations are solved using a Lagrangian parcel method (Chen et al., 2006).

CRISSP1D is capable of simulating water temperature, skim ice, border ice, suspended frazil ice, ice pan production, ice cover formation, under cover transport, ice front propagation, undercover accumulation and erosion, cover stability, secondary consolidation, ice jam evolution and break-up. Bridging criterion can be enabled allowing the simulation of bridging to take place given a maximum surface ice discharge or a maximum surface ice layer thickness relative to the depth of the channel. Alternatively, a user-specified time and location may be used for bridging. In addition to thermal break-up, CRISSP1D also gives consideration to mechanical break-up by way of a user-specified time and location, or by using stage or discharge criteria.

Chen et al. (2006) demonstrated the capability of CRISSP1D using data from the Peace River. CRISSP1D has also been used in investigating the release of anchor ice on the Peace River (Jasek et al., 2015), in exploring the use of SWIPS data (Jasek et al., 2011), and in investigating the effects of variables on a downstream propagating discharge wave following dynamic break-up (Jasek et al., 2005).

1.2.2. MIKE-ICE

MIKE-ICE is paired with the Danish Hydraulic Institute's (DHI) MIKE-11 hydrodynamics model and was developed by DHI in conjunction with La Groupe-Conseil Lasalle Inc (Theriault et al., 2010). It uses a six-point Abbott-Ionescu finite difference scheme in solving the 1D Saint-Venant equations. The model is capable of

simulating water temperature, border ice, supercooling, frazil generation, ice pan formation, ice cover formation, thermal decay and growth of ice, ice cover progression, and under ice sediment transport and deposition.

MIKE-ICE has most often been used in frazil ice studies rather than in studies of ice-jams (Carson et al., 2007). Timalsina et al. (2013) used the model to investigate the effects of potential future climates on the regulated Orkla river in Norway and Alfredsen (2015) used MIKE-ICE in modeling the ice effects on head loss at hydropower intakes.

1.2.3. RIVICE

RIVICE (Environment Canada, 2013) was developed by a consortium of organizations and engineering firms with the final work before its release in 2013 having been completed by KGS Group. It is a non-proprietary, open-source model that solves the 1D Saint-Venant equations using the Galerkan technique of weighted residuals. The ice modules are coupled to the hydrodynamic solution with water temperature and ice production mostly based on heat balance equations. In addition to water temperature and ice production, it is capable of simulating frazil generation, border ice, ice cover formation, ice front propagation, under-cover transport, and deposition, ice cover stability, mechanical thickening and also includes leading edge stability criteria. A sub-routine capable of simulating the following water quality indicators has been incorporated into the model: dissolved oxygen; biochemical oxygen demand; nitrogen and phosphorus levels; phytoplankton, zooplankton, fecal coliforms and conservative and decaying lignis (Environment Canada, 2013).

RIVICE has been tested with a number of studies including investigation of ice jam formation on the slave river delta (Zhang and Lindenschmidt, 2017), ice jam events on the Athabasca River in Fort McMurray (Lindenschmidt, 2017) and in near real-time flood hazard assessments on the Exploits River in Newfoundland (Warren et al., 2017).

1.2.4. River1D

River1D is the model selected for use in this study of the NSR. It is a public domain model which has been developed at the University of Alberta. The Characteristic Dissipative Galerkin method is used to solve the Sain Venant equations and the

Streamline Upwind Petrov-Galerkin finite element method is used to solve the ice transport equations (Blackburn and She, 2019). River1D is capable of simulating water temperatures and supercooling, frazil ice production, accretion and re-entrainment, dynamic and static border ice growth, border ice decay, ice pan production and ice cover formation, multiple user-defined bridging locations, ice front propagation using leading edge stability criteria, ice front retreat, anchor ice growth and release, and the thermal growth and decay of ice. A stand-alone ice-jam module is also included within River1D.

River1D has been used in a variety of studies including investigating the impacts of climate change on the thermal regime of the Peace River (Andrishak and Hicks, 2005), modeling ice cover consolidation on the Peace River (Hicks et al., 2009), and investigating the ice effects on flow distributions in the Mackenzie Delta (Blackburn et al., 2015). In addition to this, Ye and She (2019) tested mechanical break-up criteria using River1D and data from the Athabasca and Peace Rivers. The most recent version of River1D has been calibrated and validated using data from the Susitna River, Alaska (Blackburn and She, 2019).

1.3. Research objectives

The main goal of this study was to investigate the thermal regime of the North Saskatchewan River through Edmonton. Thus, the specific objectives are to:

- Collate and summarize the data available for the study reach.
- Investigate the variability in river ice conditions over the available years of observations, preceding and during freeze-up and break-up.
- Develop a validated hydraulic model that can simulate complex river ice processes over the entire winter season.
- Use the validated model to investigate the effects of urban outfalls on the river ice processes.

To achieve these objectives, first the available data from 2009 to 2019 was collated and analyzed to identify trends and patterns in freeze-up and break-up of the NSR. Several empirical relationships were developed between conditions and river ice phenomena. Subsequently, the University of Alberta's River1D Ice Process model was used to further

investigate these processes and phenomena. Model calibration was achieved using a range of realistic parameter values, published in the literature, and was assessed by comparing the simulation results with field data collected by Maxwell et al. (2011) during the 2010-11 ice season. Validation of the model was achieved using river ice data collected by Ghobrial et al. (2013) during the 2009-10 ice season.

1.4. Organization of the Thesis

Chapter 2.0 of this Thesis introduces the study site, reviews the studies which have previously been conducted along the North Saskatchewan River in Edmonton and provides an overview of the available data. Additionally, this data is analyzed and assessed, and the identified river ice phenomena are discussed. Chapter 3.0 includes details of the model configuration and the simulation results for the ice seasons of 2010-11 and 2009-10. Finally, a summary and conclusions of the research, along with recommendations for future studies, is provided in Chapter 4.0.

2.0 Analysis of the river ice regime of the North Saskatchewan River[1]

[1] A modified and shorter version of this chapter was published in the Committee on River Ice Processes and the Environment's 20th Workshop on River Ice (Howley et al., 2019).

2.1. Study site

The source of the North Saskatchewan River (NSR) is the Saskatchewan Glacier on the eastern slopes of the Canadian Rockies. As shown in Figure 2-1, from its source, the NSR flows approximately 100 km to the east before arriving at Abraham Lake and the Big Horn Dam. This dam was constructed in 1972 and is one of two hydro power operations which regulate the flow of the NSR through Edmonton. The second hydro power operation which regulates the flow of the NSR is the Brazeau Dam, which was constructed in 1963 on the Brazeau River, a major tributary of the NSR. The confluence of the Brazeau River and the NSR is approximately 165 km downstream of the Big Horn Dam.
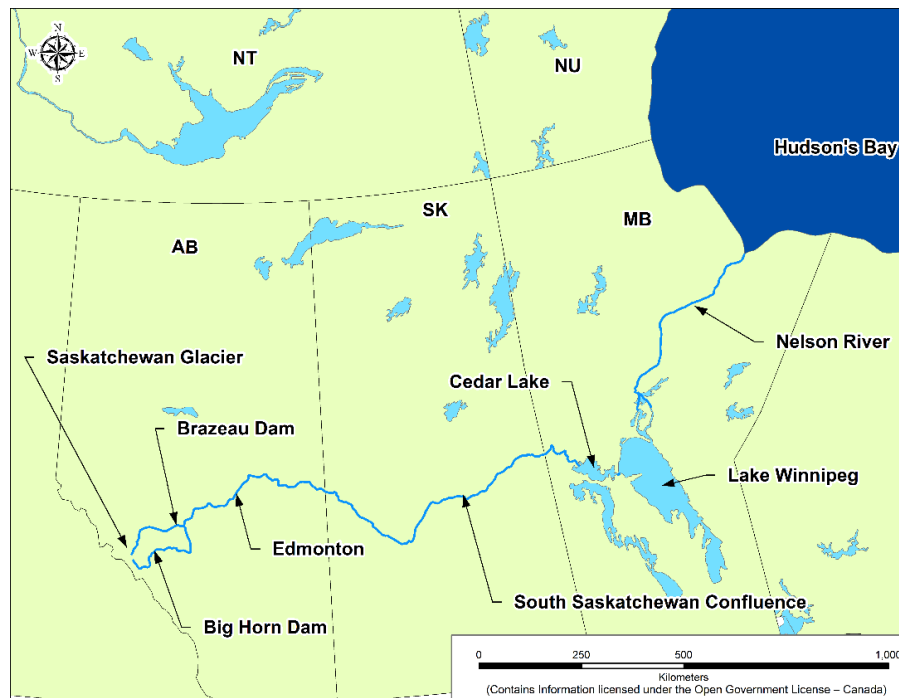
Figure 2-1. Large scale map of the North Saskatchewan River and other key locations.

From this confluence, the NSR flows to the north-east, towards the City of Edmonton, before continuing into the province of Saskatchewan. The NSR and the South

Saskatchewan River merge approximately 45 km east of Prince Albert and from this confluence, the Saskatchewan River flows to Hudson's Bay via Tobin Lake, Cedar Lake, Lake Winnipeg, and the Nelson River. Regulation of the river has changed the flow pattern in Edmonton with the average winter discharge (between November and March) having increased from approximately 44 m^3/s to 122 m^3/s (Total E&P Canada Ltd 2007).

The hydro-peaking pattern observed by the WSC gauge in Edmonton shows approximately one full wave cycle each day during open water conditions. Peak flows typically occur in the morning between 03:00 and 08:00 AM. The hydropeaking magnitude varies but is typically in the range of ± 15 m^3/s to 40 m^3/s.

As shown in Figure 2-2, the study reach is a 29 km section of the river through the City of Edmonton. From the upstream boundary at Riverbend, Station 0.00 km, the river flows in a north-easterly direction towards the downstream boundary at the Clover Bar Energy Centre, Station 28.84 km. Through Edmonton, the NSR is a large, irregularly meandering river which is partially entrenched. The average bed slope is 0.00034 and the channel is typically 90 to 250 m wide. River ice processes are prevalent for between 5 and 6 months each year. The Water Survey of Canada (WSC) Gauge (Gauge No. 05DF001), which is located at Station 14.48 km, has a record length of 109 years and at this location, the effective drainage area of the NSR is 27,100 km^2 (Environment Canada, 2018). There are several urban features within the study reach such as the Gold Bar Wastewater Treatment Plant (GBWTP), combined sewage outfalls, 15 bridges and water intakes for the University of Alberta, Rossdale Water Treatment Plant, several refineries, and a manufacturing plant.

Given the partially entrenched nature of Edmonton's River Valley, the risk of ice-jam flooding is deemed to be minor, with no evidence of ice jam flooding since 1825 (NHC, 2007). A break-up ice-jam was observed in 2020 but no flooding was reported. Other ice related challenges do exist within the study reach. It is known that water intakes within the study reach are sometimes blocked with frazil ice. Additionally, the turbidity of the NSR dramatically increases at break-up, causing some challenges for the operators of the city's two water treatment plants which extract water from the river.
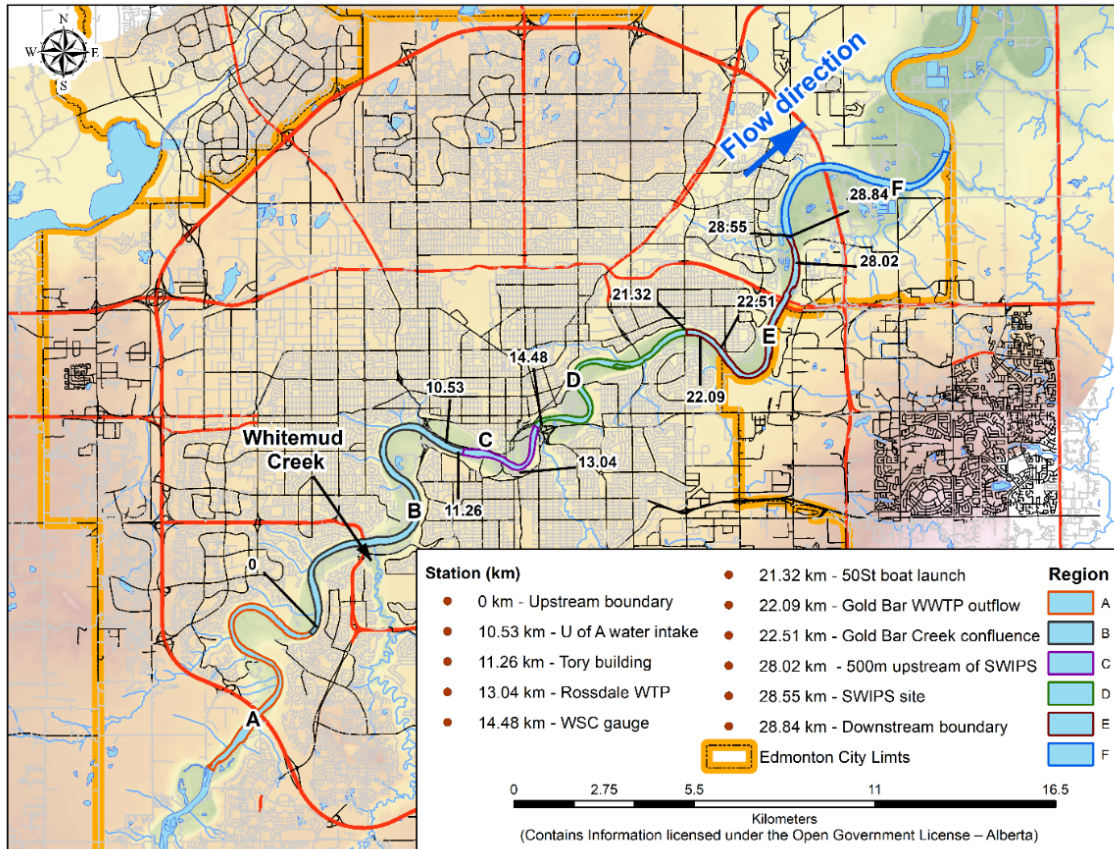
Figure 2-2. Map of the study reach; the North Saskatchewan River through Edmonton.

2.2. Previous studies on the NSR

Several river ice studies have been conducted on the NSR. In some instances, research has been conducted to investigate specific local problems. For example, both Hicks (1997) and Choles (1997) assessed freeze-up data for a section of the NSR between the Bighorn dam and the Brazeau confluence, approximately 200 km upstream of Edmonton, to address the optimization of the Bighorn dam. Maxwell et al. (2011) characterized the winter regime of the NSR in Edmonton during the winter of 2010-11 and investigated the formation and movement of an open lead downstream of Gold Bar Wastewater Treatment Plant.

On the other hand, the NSR has also been used, due to its accessibility, to assess or validate different theories and data collection methods. Gerard and Andres (1982) measured the roughness of the ice cover immediately following freeze-up in 1981 and documented the freeze-up process of that year. Ghobrial et al. (2013) investigated the use

of shallow water ice profiling sonar (SWIPS) as river ice data collection tools. While researching sediment transport in anchor ice, Kalke and Loewen (2017) used bridge-mounted game cameras on several rivers, including the NSR, to collect surface ice and rafted anchor ice concentrations. Kalke et al. (2019) measured supercooling in the NSR at four locations near Edmonton. Finally, McFarlane et al. (2017) collected water temperature data and suspended frazil ice concentration data on the NSR using an underwater camera system designed to investigate frazil particle characteristics. As a result of all of these studies, there is extensive valuable river ice data available for the NSR.

2.3. Synopsis of available data

2.3.1. Meteorological data

Meteorological data in Edmonton is available from two primary sources; the Edmonton City Centre Automated Weather Observing System (AWOS) situated at the old Blatchford Field Airport site (Environment Canada weather station ID: 3012209, from 1999 to 2019), and the University of Alberta Earth and Atmospheric Sciences (EAS) Weather Station (from 2000 to 2019), situated on top of the H.M. Tory Building (operated by the University of Alberta). Both weather stations record and provide air temperature, relative humidity, wind direction, wind speed, atmospheric pressure, and solar radiation data on an hourly timestep. Daily snowfall depth was also measured at the University of Alberta's Metabolic Centre (Environment Canada weather station ID: 301FFNJ, from 1986 to 2019). This data is supplemented by air temperature data recorded along the river at Station 28.55 km using Campbell weather station by Ghobrial et al. (2013) and Maxwell et al. (2011) during the winters of 2009-10 and 2010-11, respectively.

2.3.2. River ice data

Ghobrial et al. (2013) and Maxwell et al. (2011) deployed Shallow Water Ice Profiling Sonar (SWIPS) at Station 28.55 km between November 2009 and January 2010, and between November 2010 and March 2011, respectively. The following river ice data was estimated by Ghobrial et al. (2013) and Maxwell et al. (2011) from the SWIPS signal: pan thickness, pan concentration, pan length, suspended frazil concentration, and ice

cover thickness. Ice thickness data (from 2009 to 2015) was also collected by WSC as part of winter discharge measurements. These measurements were taken at Station 14.48 km during winter 2008-2009 and at Hawrelak Park footbridge (Station 6.87 km) thereafter. During the winter of 2010-11, Maxwell et al. (2011) also estimated pan concentrations from game cameras installed at nine locations along the NSR. Six of these were within the study reach (Stations 0.00 km, 13.04 km, 21.56 km, 28.02 km, 28.55 km, and 28.44 km) while the remaining three cameras were located 8.90 km and 19.00 km upstream, and 6.86 km downstream of the study reach. In winter 2016, a bridge mounted camera was installed at Fort Edmonton Footbridge (Station 1.76 km) which took images of the river for two weeks in November and December. The images captured were used to estimate anchor ice and surface ice concentrations (Kalke and Loewen 2017). McFarlane et al. (2017) collected suspended frazil concentrations using an underwater camera system at Emily Murphy Park (Station 10.10 km), Government House Park (Station 9.84 km) and Quesnell Bridge (Station 3.90 km) for short durations during freeze-up in 2014-2016.

A camera installed as part of the EAS Weather Station has recorded images of river conditions every 15 minutes at Station 11.26 km since 2009. These images were used in this study to determine the timing and date of freeze-up and break-up on the NSR. Aerial photographs collected on 22nd November 2009 and the images captured by Maxwell et al.'s (2011) game cameras have also been used to identify several bridging locations within the study reach.

2.3.3. Hydrometric and river temperature data

The WSC gauge (Station 14.48 km) provides water level data at 15-minute intervals throughout the year. During open water conditions (mid-April to mid-November), discharge is calculated using an open water rating curve. It is subsequently published, along with the water level data, on the Environment Canada website. The WSC typically collect under-ice discharge measurements three times a year. Prior to 2010, some of these measurements were conducted at the WSC gauge location (Station 14.48 km). However, from 2010 onwards, these measurements have been conducted upstream, at the Hawrelak Park footbridge (Station 6.87 km). Discharge from GBWWTP (Station 22.09) has a

significant influence on river ice processes of the NSR. Outflow discharge and temperature data for the winters of 2009-10 and 2010-11 has been provided by EPCOR Utilities Inc., who operate the plant.

During the 2009-10 and the 2010-11 seasons, the SWIPS collected water depth data through a pressure sensor at Station 28.55 km. Maxwell et al. (2011) also collected water depth data using Mini-Diver submersible dataloggers at four other locations: Stations 21.32 km, 22.51 km, 28.02 km, and 28.84 km. Along with the SWIPS instruments, an Acoustic Doppler Current Profiler (ADCP) was also deployed to collect water velocity profile data during these two seasons. Furthermore, both the SWIPS instruments and the Mini-Divers collected water temperature data. Additional water temperature data is available from the University of Alberta's District Energy System intake at Station 10.53 km. At this location, several Resistance Temperature Detectors (RTDs) are deployed in various chambers of the water extraction facility. Finally, water temperature data was collected at Quesnell Bridge (Station 3.90 km) and Emily Murphy Park (Station 10.10 km) using RBR temperature dataloggers during the winters of 2014 to 2018 (McFarlane et al., 2017). A summary of the data outlined in this section is available in Table 1.

Table 1. Summary of hydrometric, and river ice data available for the years 2009-2017.

Data Type	Parameter Name	Station (km)													
		0.00	3.90	6.87	9.84	10.10	10.53	13.04	14.48	21.56	22.09	22.51	28.02	28.55	28.84
Hydrometric	Water surface elevation			2009-15					2008-17	2010-11		2010-11	2010-11	2009-11	2010-11
	Open water discharge								2008-17						
	Winter discharge			2009-15					2008-09						
	GBWWTP discharge										2010-11				
	Depth-averaged velocity										2009-11				
	Surface velocity										2009-11				
	Water temperature		2015-17			2015-17	2009-17			2010-11	2010-11	2010-11	2010-11	2009-11	2010-11
Ice	Suspended frazil concentration		2014-15 2016-17		2014-15	2014-16								2009-11	
	Pan concentration	2010-11						2010-11		2010-11			2010-11	2009-11	2010-11
	Pan length													2009-11	
	Ice thickness			2009-15						2008-09				2009-11	
	Location of open lead											2010-11		2010-11	

2.4. Data Analyses

2.4.1. Degree days of freezing

Freeze-up on the NSR typically occurs in November or early-December. Using the images and the air temperatures measured from the EAS Weather Station, the cumulative degree-days of freezing (DDF) was calculated for: (i) appearance of the first ice pans at Station 11.26 km and, (ii) formation of a stable ice, also at Station 11.26 km. In this study, DDF calculation started with the first five consecutive days of sub-zero average daily air temperatures. Occasional above-zero air temperatures were subtracted in the calculations. As shown in Figure 2-3a the DDF required for the first pans to appear on the river is highly variable. First pans were observed with an average DDF value of 19 °C·Days and within a range of between zero and 43 °C·Days. Ice pans occurred with zero DDF on 5th November 2011. Although the air temperature was negative from the night of 3rd November through 5th November, it did not remain below zero for five consecutive days. DDF calculations did not start until 11th November. One possible explanation for this is that supercooling and frazil production likely does not require multiple consecutive days of sub-zero degree air temperatures. Also, snowfall may offer a large source of 'seed crystals' which could subsequently cause the formation of frazil slush and pans (Osterkamp 1978). Maxwell et al. (2011) noted that slushy frazil pans, such as those observed by the EAS camera in 2011 are always associated with snowfall events. Although no snowfall was observed by the cameras or meteorological instruments in Edmonton, it was quite possible that the frazil pans observed on 5th November had formed upstream of Edmonton, under colder conditions or during a localized snowfall event, and drifted downstream to pass through the reach.

A range of DDF values, between 52 °C·Days and 208 °C·Days, were calculated for a complete or stable ice cover to form. The highest DDF value by far, 208 °C·Days, was recorded during freeze-up in 2018. For comparison, the second highest value, 127 °C·Days was recorded during freeze-up in 2013. The DDF value of 2018 is an outlier and is likely caused by warmer air temperatures observed between mid-November and early December. The formation of the ice cover during this year was extraordinarily late, with a full ice cover forming on the 25th December 2018. A similar pattern is observed during freeze-up in 2019, albeit with a decline in DDF values through the second half of

November caused by positive air temperatures, followed by a second rise in DDF values and the formation of a stable ice cover. On average, there were 16 days between the observation of the first ice pans and the formation of a stable ice cover. However, in 2018 and 2019, this number far exceeded the average, with 48 and 33 days between the observation of the first ice pans and the formation of a stable ice cover, respectively.

Although DDF values at freeze-up are typically site specific, the range of DDF values identified for the NSR are largely in agreement with those included by Wazney et al. (2017) for the Dauphin River and Nafziger et al. (2011) for four small streams in New Brunswick and Newfoundland. If the exceptionally late freeze-up observed in 2018 is excluded, an interesting trend is observed with lower DDF values for the freeze-up events which occurred later in the season. For example, a late freeze-up was observed on 5th December 2009 and 27th November 2015. The DDF on these dates was only ~50 °C·Days. The scatter in this plot is likely caused by a number of factors including solar radiation, sensible heat exchange, urban factors such as outfall discharges and upstream influences such as dam releases.
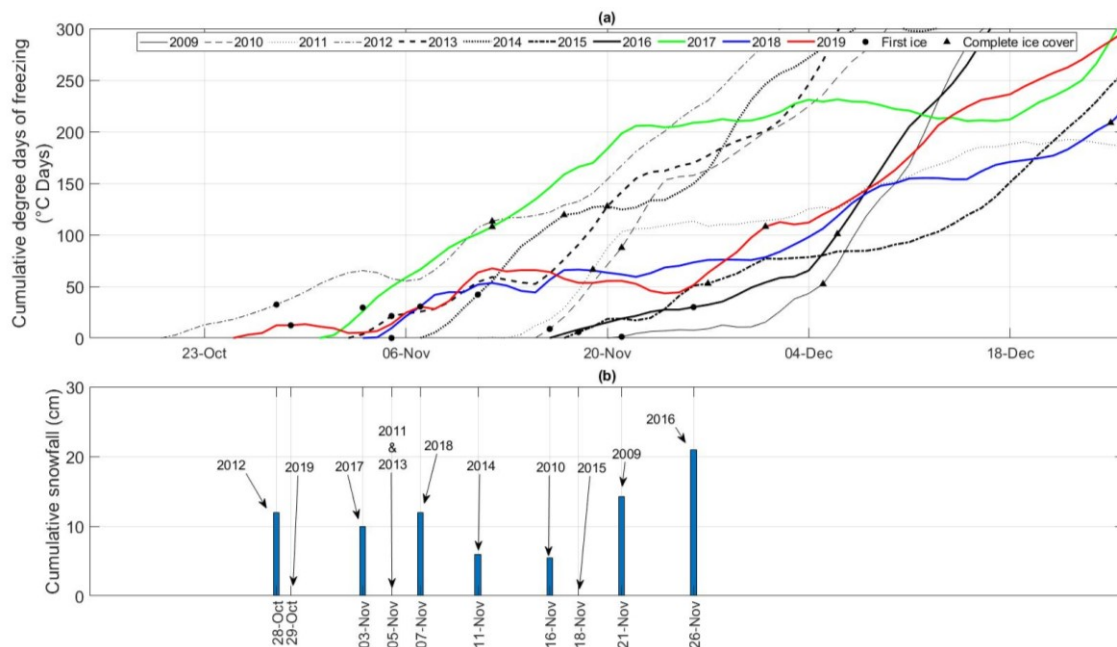
Figure 2-3. a) Cumulative degree-days of freezing for first observations of ice and a complete ice cover and; b) Accumulated snowfall prior to observation of the first ice pan.

2.4.2. Visual appearance of first ice pans

Maxwell (2012) used the volume backscatter strength values from the SWIPS at Station 28.55 km to differentiate between crusty and slushy pans formed in the GBWTP open lead during the 2010-11 season. In analyzing the pans, which had formed locally in the open lead and presumably only a short while prior to their observation by the SLR camera, Maxwell (2012) noted that it was not easily possible to visually differentiate between the two types of pans.

In this study, it was found that the first ice pans observed by the EAS camera could be divided into two similar categories, solid and slushy, based on their visual appearance (Table 2). It is important to note that the quality of the images captured by the EAS camera is relatively poor and the appearance of ice pans may be affected by other factors such as light conditions. Additionally, the angle of the EAS camera was changed and/or additional cameras were added to change or increase the field of view in 2011, 2012, 2015 and 2019. Despite this, it is still possible to visually separate the pans into two distinct categories. Images of the first ice pans for each year are included in Figure 2-4.

Pans which appeared to be translucent and slushy were most often observed, including in 2009, 2011, 2012, 2013, 2015, 2016 and 2019. Pans with a more solid, white and/or crusty appearance were observed in 2010, 2014, 2017 and 2018. These solid pans appeared to have a greater prominence, with more slush protruding above the water surface, which would indicate greater pan thickness. The average daily air temperature for pans which appear to be slushy was -5.3 °C with a standard deviation of 2.7 °C. The solid ice pans were observed with lower temperatures – the average daily air temperature for pans of this appearance was -11.0 °C with a standard deviation of 2.0 °C. This lends weight to the theory of the solid pans being thicker, as more frazil generation would be expected to occur with higher magnitudes and durations of supercooling (see Section 2.4.8), and larger slush accumulations could be expected to form, in turn leading to pans with greater prominence. There is also a correlation between the appearance of the pans and the DDF, with an average DDF of 14.7 °C·Days for slushy pans and an average DDF of 27.7 °C·Days for solid pans. One explanation for this is that the solid pans had formed

further upstream and solidified during the travel time to Edmonton while the slushy pans were formed more locally.

There is no clear association between the appearance of slushy or solid ice pans and the presence or absence of snowfall as measured at the University of Alberta Metabolic Center. According to the data from this station, during the 48 hours preceding the observation of the first ice pans, snowfall occurred three times; in 2009, 2012 and 2018. In both 2009 and 2012, the pans had a slushy appearance while in 2018 the pans had a solid appearance. However, hourly images captured by the EAS camera provided evidence of snowfall on five occasions, in 2009, 2012, 2014, 2017 and 2018. The first ice pans in three of these years, 2014, 2017 and 2018, appeared to be solid ice. As such, there were three occurrences of solid ice pans associated with snowfall and one occurrence of solid ice pans with no snowfall. The presence of snowfall may contribute to a greater concentration of seed crystals and greater generation of frazil ice. Snowfall could also accumulate on top of ice pans, thickening pans and also giving them a distinctive white appearance.

Table 2. Visual appearance of first ice pans.

Date of first ice pan	Appearance	Mean daily air temperature (°C)	Snowfall (cm) during preceding 48 hours	Evidence of snowfall EAS camera?
21/11/2009	Slushy	-1.2	6.8	Yes
16/11/2010	Solid	-8.8	0	No
05/11/2011	Slushy	-5.3	0	No
28/10/2012	Slushy	-5.4	12	Yes
05/11/2013	Slushy	-9.8	0	No
11/11/2014	Solid	-13.2	0	Yes
18/11/2015	Slushy	-5.7	0	No
26/11/2016	Slushy	-2.5	0	No
03/11/2017	Solid	-12.7	0	Yes
07/11/2018	Solid	-9.4	1	Yes
29/10/2019	Slushy	-7.5	0	No

21st November 2009 – slushy pans.

16th November 2010 – solid pans.

5th November 2011 – slushy pans.

28th October 2012 – slushy pans.

5th November 2013 – slushy pans.

11th November 2014 – solid pans.

18th November 2015 – slushy pans.

26th November 2016 – slushy pans.

3rd November 2017 – solid pans.

7th November 2018 – solid pans.

29th October 2019 – slushy pans.

Figure 2-4. Images of the first ice pans observed by the EAS camera.

2.4.3. Bridging locations

Ghobrial et al. (2013) collected several aerial images on 3rd December 2009, which show bridging locations and areas of surface ice congestion, as presented in Figure 2-5 and Figure 2-6, and summarized in Table 3. These images were georeferenced to establish the location and length of each ice congestion. Estimations of the border ice fractions and surface ice concentrations were obtained by visually inspecting the raw and georeferenced images.

At the time the photographs were taken, the only location at which bridging had occurred was the most downstream bridging location, Station 45.20 km, where the river bends sharply through approximately 180°. Very few ice pans or rafts are shown flowing out of the bend and a stable ice cover extended approximately 5.1 km upstream. In addition to bends in the river, border ice growth, such as at Station 28.65 km, and bridges, such as at Stations 18.27 km and 15.24 km were also causes of surface ice congestion. At Station 18.27 km, border ice was estimated to occupy at least 50% of the channel width and had completely obstructed the water surface between the two northern-most sets of the Dawson Bridge pillars. It is not possible to estimate the border ice extent at Hawrelak Park with a large degree of confidence given the angle and subject distance of the limited photographs.

At all sites, except the most downstream, ice rafts were observed flowing out of the constriction and as such, bridging cannot be said to have occurred at the time the images were captured. However, the surface ice concentration at each of these locations had approached or exceeded the value of 80-90% provided by Hicks (2016) as likely to lead

to bridging. Analysis of SWIPS data at Station 28.55 km (Figure 2-7) show that the surface ice concentration dropped on 4th and 5th December 2009, the day after the aerial photographs were taken. Either the production of ice pans came to a halt, both locally and upstream, or the conveyance of ice pans stopped somewhere upstream of this location. As such, it seems probable that bridging had occurred at one or more of the upstream locations. Throughout the remainder of this thesis, sites where bridging was not observed but where constrictions caused the surface ice concentration to exceed approximately 75% on 3rd December 2009 are referred to as suspected bridging locations.

Table 3. Bridging locations summary.

Station (km)[#]	Constriction type	Border ice fraction	Estimated surface ice concentration (%)	Length of ice front/ congestion (km)	Ice pans and rafts leaving constriction
45.20	Bend	0.5	100	5.1	No
38.77	Bend	0.4	90	1.1	Yes
35.53	Bend	0.5	90	0.4	Yes
28.65	Border ice	0.4	80	1.2	Yes
18.27	Dawson Bridge	0.5	90	1.3	Yes
16.43	Bend	0.4	75	0.6	Yes
15.24	Low-Level Bridge	0.4	85	1.2	Yes
13.48	Bend	0.5	80	1.3	Yes
9.35*	Bend	N/A	N/A	1.6	Yes
0.24	Bend	0.5	80	1.1	Yes

[#]Downstream extent of ice cover or congestion.

*Partial aerial photograph coverage.

(a) Bridging at Station 45.20 km.

(b) Congestion at Station 38.77 km.

(c) Congestion at Station 35.53 km

(d) Congestion upstream of SWIPS site, Station 27.53 km

(e) Congestion at Dawson Bridge, Station 18.27 km

(f) Congestion at Station 16.43 km.

(g) Congestion at the Low-level Bridge, Station 15.24 km

(h) Congestion at Rossdale, Station 13.48 km.

(i) Congestion at Hawrelak Park, Station 9.35 km.
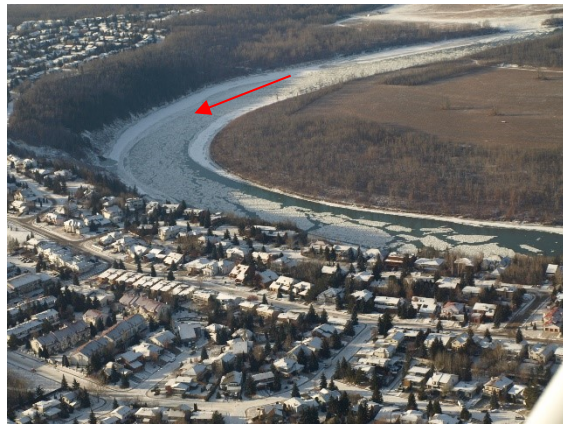
(j) Congestion at Riverbend, approx. 0.24 km upstream of study boundary.

Figure 2-5. Aerial photographs showing bridging and surface ice congestion on 3rd December 2009. Red arrows indicate the flow direction. Photo credit: Ghobrial (2013).
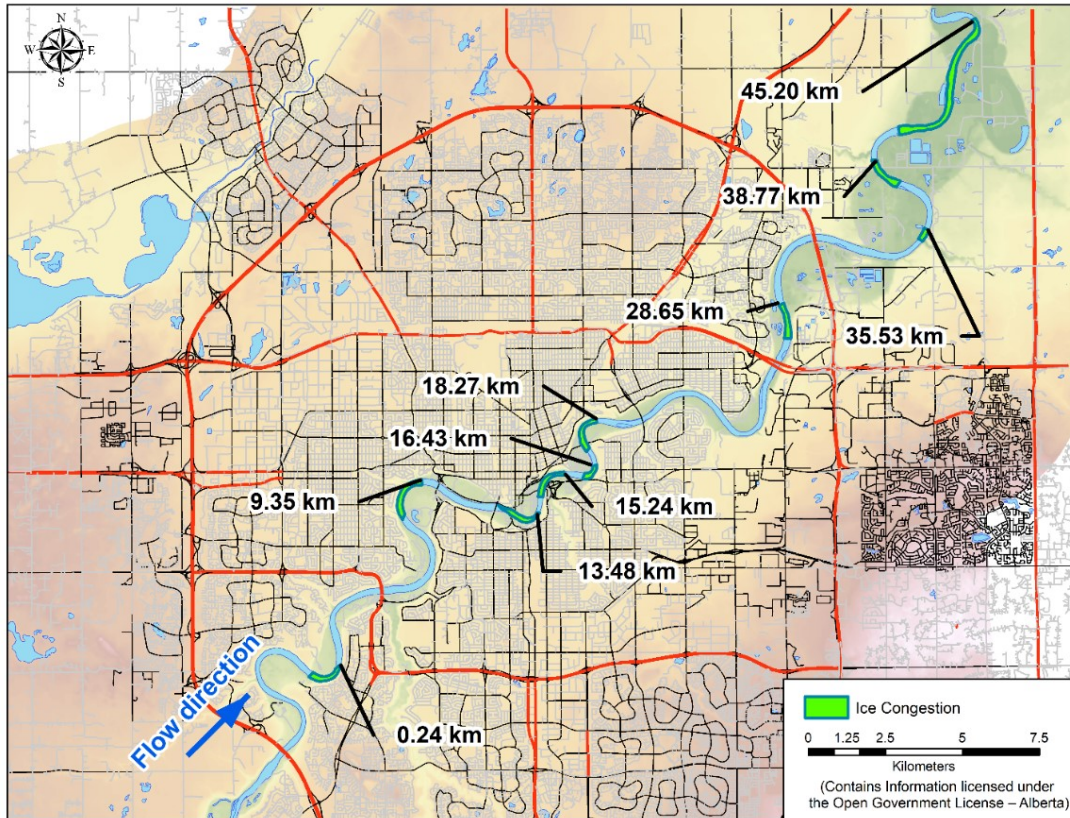
Figure 2-6. Suspected bridging locations.
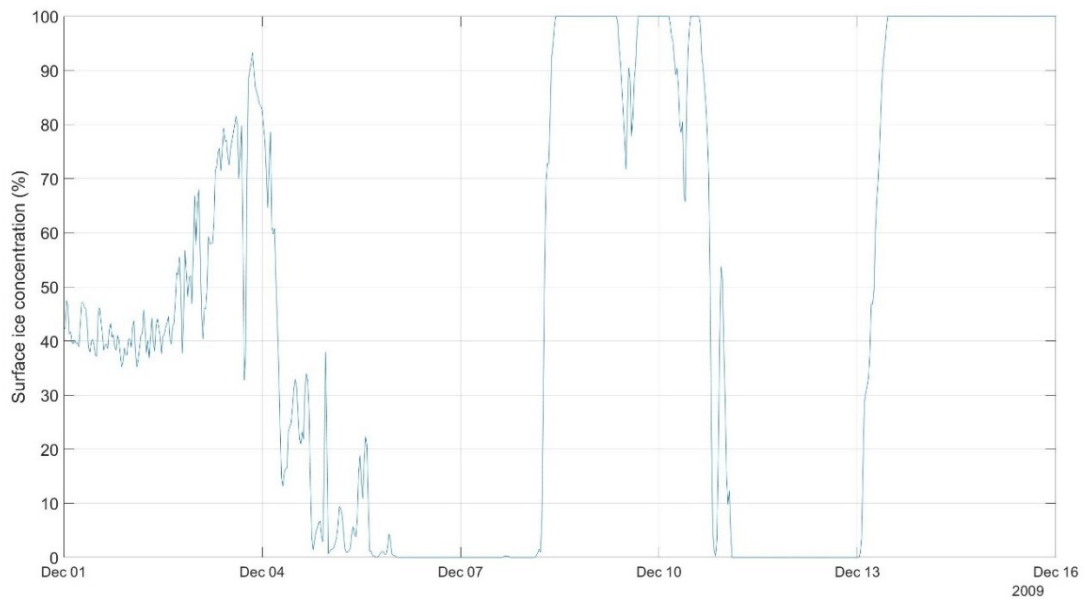
Figure 2-7. Surface ice concentration from 1st December to 16th December 2009, as measured by the SWIPS at Station 28.55 km (Ghobrial 2013).

2.4.4. Stage-up

The magnitude and duration of stage-up on the NSR caused by freeze-up is highly variable and appears unpredictable. Figure 2-8 shows stage-up for the freeze-up seasons of 2009-2019. Freeze-up typically causes a rise of between 0.8 m and 2.0 m. Although this rise in water surface elevation might seem significant, the NSR through Edmonton is not typically associated with the risk of river ice flooding due to the entrenched nature of the river valley. In 2012, 2015, 2018, and 2019 stage-up was very sudden. In the most extreme cases of 2012 and 2019, there was a very sudden stage-up event with water levels rising 1.9 m in 3 hours and 7 hours, respectively. There was also a large stage-up of in 2017 and 2018, albeit spread over longer durations of 53 and 14 hours, respectively. In the instances of sudden stage-up, the effect of the ice cover on the hydraulic efficiency of the channel is obvious. The water surface elevation remained elevated and relatively stable following stage-up in 2012, 2015 and 2017. Investigations conducted by Wazney et al. (2017) on the Dauphin River, have linked this type of stage-up to mechanical thickening and the immediate formation of a thick and stable-ice cover.

The freeze-up of 2017 (Figure 2-9) also shows evidence of jamming and mobilization events. Between 22:00 on 9th November and 03:30 on 12th November 2017 the water surface elevation rose by 2.0 m over three distinct events. The first event was caused by the effect of the ice front propagation and given the sudden increase in water surface elevations it is probable that some mechanical thickening occurred. On 10th November 2017, two spikes in water surface elevation were observed. Shoving or consolidation was the probable cause of the first spike. This theory is supported by images captured by the EAS camera at Station 11.26 km. The images show the ice front propagating upstream between 06:00 and 10:00 on the morning of 10th November. However, the ice cover had cleared by 11:00 on the same morning indicating movement in the ice cover at a downstream location. A steep decline in the water surface elevation followed the first spike in water surface elevation. This decline could be indicative of a temporary release event, followed by another jamming event and a second release event shortly thereafter. From 16:00 on 10th November 2017, the water surface elevation again began to rise, and a stable ice cover appears to have formed, remaining in place for the duration of 11th

November 2017. One final event was observed in the early hours of 12th November 2017 whereby the water surface elevation rose 0.6 m before stabilizing.

In 2018, the water surface elevation also varied significantly during stage-up (Figure 2-8j). Between 10:00 and 17:30 on 9th December 2018, the water surface elevation rose suddenly by approximately 0.6 m. This was followed by a sudden decline of 0.6 m in the water surface elevation by 11:00 on 10th December 2018. This behavior could be associated with temporary bridging or freeze-up jamming followed by a release event. Stage-up caused by the formation of a stable ice cover occurred 10 days later, on 20th December 2018, after which the water surface elevations remained elevated.

The most prominent peak in the water surface elevation data, a rise of 1.9 m in 7 hours, was observed at 17:00 on 4th December 2019 as shown in Figure 2-10. During the following 14 hours, water surface elevations dropped 2.9 m. The rapid rise in water surface elevations was likely caused by an ice jam event and the following decline in water surface elevations by release of the ice jam. Images captured by the EAS Camera at Station 11.26 km show an ice cover in place at 14:00 on 4th December. One hour later, the ice cover at Station 11.26 km had mobilized, confirming that a release event or a major consolidation event had occurred downstream. The location of the toe of the ice jam is unknown, but it is possible that jamming occurred approximately 700 m downstream of the WSC Gauge, at Station 15.50 km, where construction of a light rail transit bridge was constricting the channel. A second stage-up event began during the morning of 13th December after which the ice cover stabilized, and water surface elevations remained stable.

Figure 2-11 shows the correlation between the pre-stage-up depth and the magnitude of stage-up. There is a weak correlation with higher magnitude stage-up observed in years with higher pre-stage-up depths. The most prominent spike in water surface elevation, observed in 2019, coincided with the greatest pre-stage-up water depth. The pre-stage-up depth in 2019 was 0.5 m higher than during any of the other years under consideration. This may have been a contributing factor to the freeze-up ice jam in 2019. Analysis of the data from additional seasons is required to verify this relation.

In the remaining years, it seems likely that the ice cover at freeze-up was prone to smaller consolidation and shoving events. The effects of hydropeaking on the water level makes it more challenging to identify individual processes. Despite this, it is still possible to draw some conclusions from the data. In 2009, freeze-up occurred on 4th December at 20:00 and the water level rose 0.4 m in the span of 90 minutes. As shown in Figure 2-12, the water surface elevation data was relatively noisy in advance of freeze-up, suggesting several temporary bridging and mobilization events downstream of the gauge. Following the initial stage-up, there was a clear shove and consolidation event at 21:30 which caused the water surface elevation to drop before rising again as the ice cover re-stabilized. This process of minor consolidation and shoving events continued until approximately 05:00 on 5th December.

The pattern observed in 2009 is not common to all years of data. In 2010, several temporary bridging and mobilization events were identified prior to the formation of the first full ice cover. Although there was one minor shoving event identified at Station 14.48 km on 20th November, this event was not captured by the water level data measured by the SWIPS and Mini-Divers at Stations 21.56 km, 22.51 km and 28.55 km. The water level fluctuations caused by these shoving and consolidation events did not propagate downstream and are not shown in the SWIPS and Mini-Diver data.

Figure 2-13 shows a weak correlation between the average daily air temperature on the day of freeze-up and the stage-up depth. This is in agreement with research conducted by Anders (1999) whereby colder air temperatures were linked with juxtaposed ice covers and warmer air temperatures with hummocky ice covers. Freeze-up during 2009 is a clear exception to this trend; a stage-up depth of approximately 0.5 m was experienced despite the warmer average daily air temperature of -5 °C. Unfortunately, images from the EAS camera are not of sufficient resolution to differentiate between the two types of ice cover. A cold period followed by rapid warming could see a large mass of ice with weak bonds between ice floes. Under these conditions, consolidation events and a higher stage-up depth should be expected. This may have been the case in 2012, where the air temperature rose from -14.4 °C to -6.1 °C during the 24 hours preceding freeze-up. However, the only other year in which there was significant warming during the 24 hours

preceding stage-up was 2009, when a mild stage-up was observed. This suggests that other factors, such as the incoming ice flux, are also significant.

A simple investigation into the effect of variability in daily air temperature during the freeze-up process was also conducted. Figure 2-14 shows the relationship between the coefficient of variation of the air temperature during the 4 days preceding freeze-up and the percent increase in depth caused by the arrival of the ice front. There is a correlation between the two, with higher magnitude increases in depth observed in years with a lower coefficient of variation. This is the opposite of what would be expected and suggests that a higher variability in air temperatures during the freeze-up process generally results in a lower stage-up.

The channel geometry may also be an important factor during freeze-up in this section of the river. The WSC gauge is located in a section of the river which has a mild gradient of 0.0002. As such, a juxtaposed ice cover could be expected to form (Anders 1999; Jasek et al. 2013). However, 1.4 km upstream of the gauge there is a 3.3 km long section of river with a significantly steeper slope of 0.0009. As a result of the steeper gradient, ice pans carry greater momentum through this section and therefore consolidation events are more likely to occur.
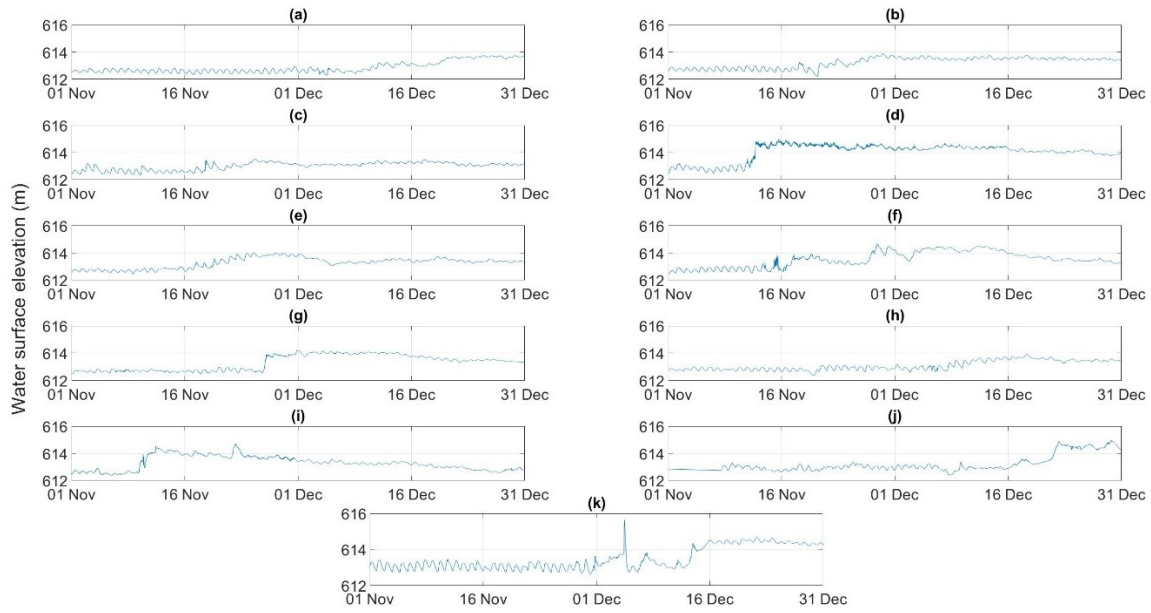
Figure 2-8. Stage-up at WSC Gauge, Station 14.48 km, in (a) 2009, (b) 2019, (c) 2011, (d) 2012, (e) 2013, (f) 2014, (g) 2015, (h) 2016, (i) 2017, (j) 2018, and (k) 2019.
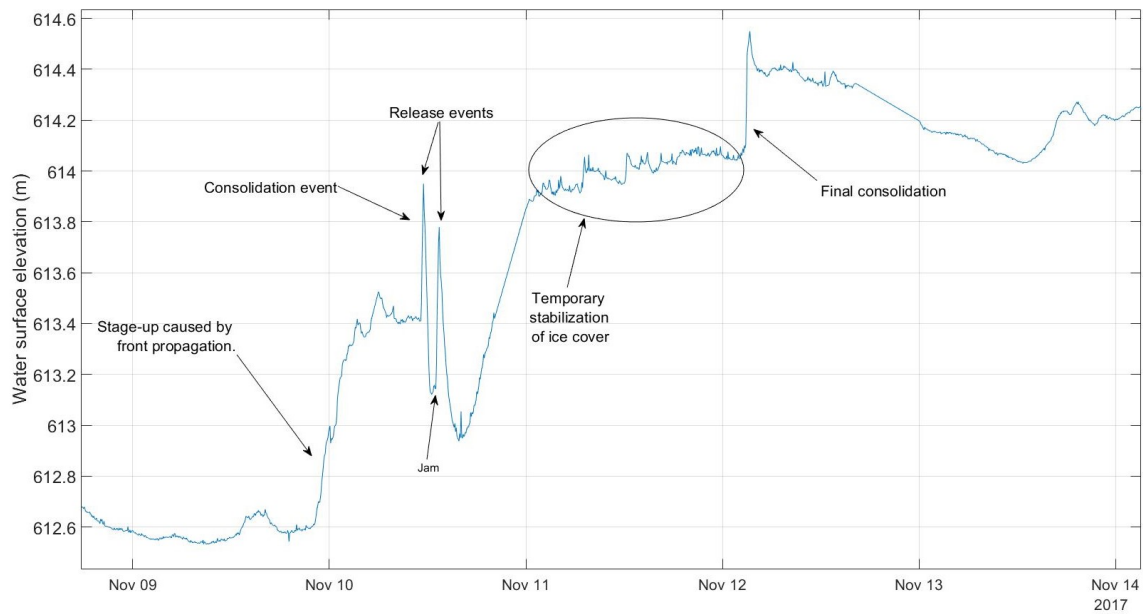
Figure 2-9. Stage-up, jamming and release events on the North Saskatchewan River at the WSC gauge (Station 14.48 km) in 2017.
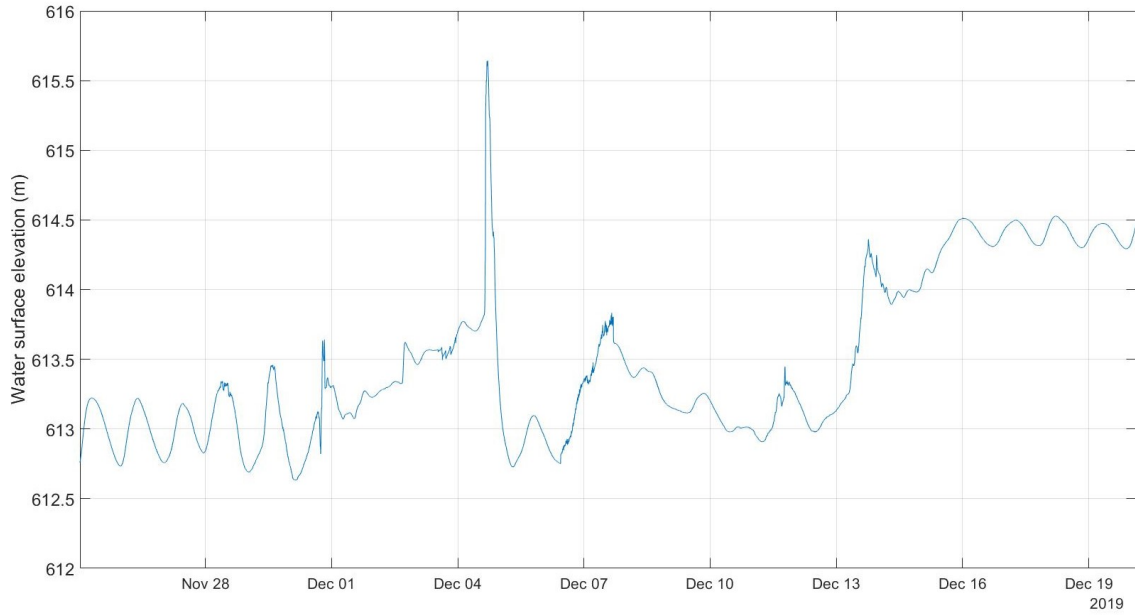
Figure 2-10. Stage-up on the North Saskatchewan River at the WSC gauge (Station 14.48 km) in 2019.
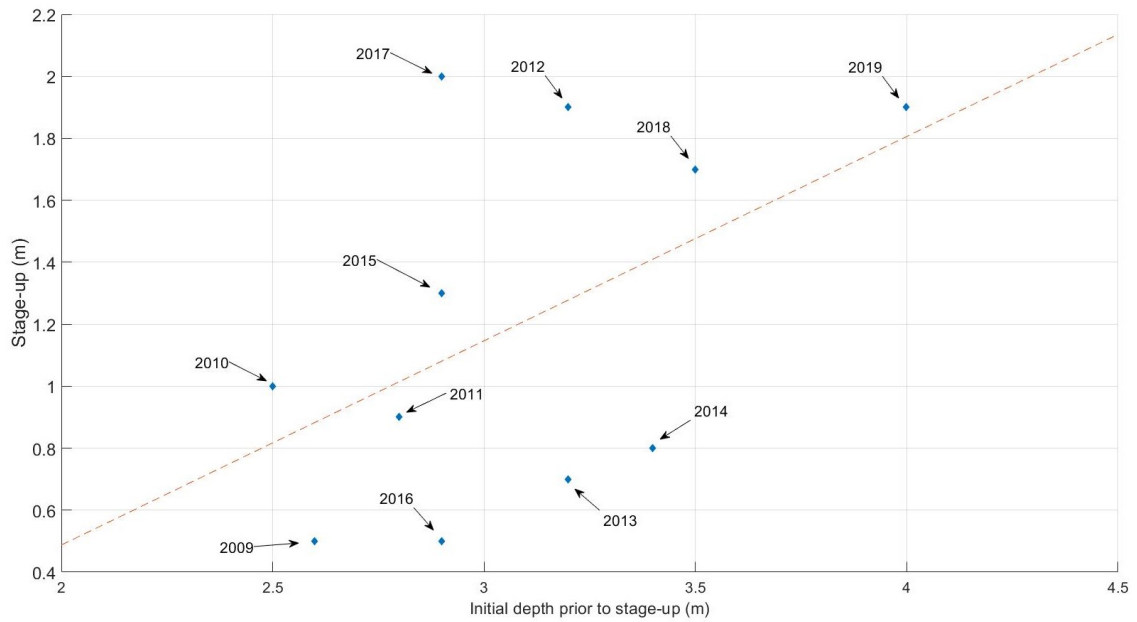
Figure 2-11. Relation between the depth prior to stage-up and the magnitude of stage-up.
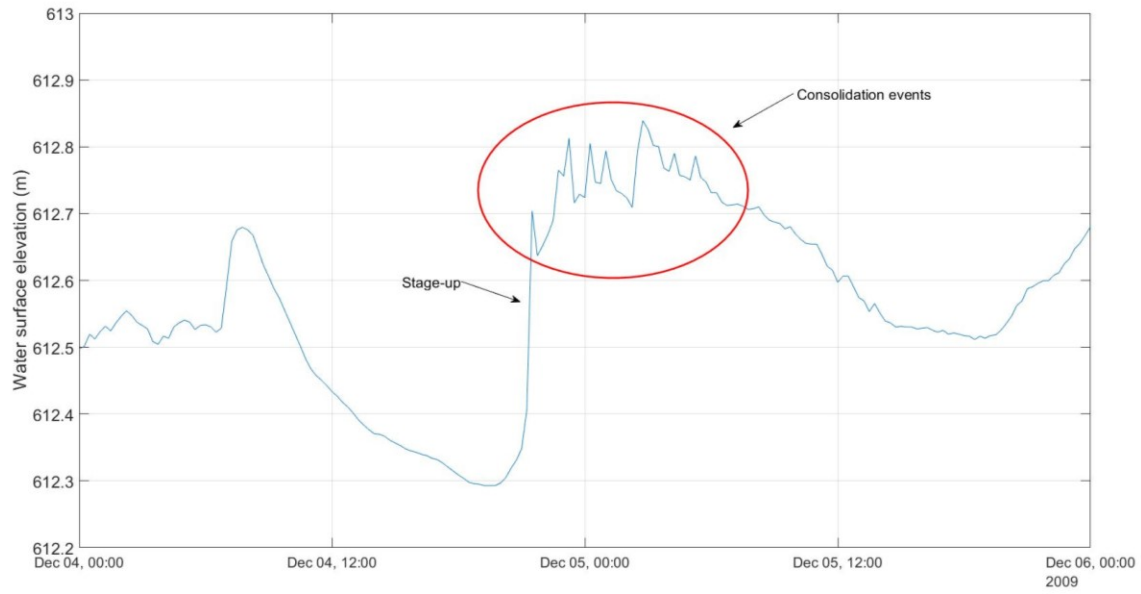
Figure 2-12. Stage-up and shoving and consolidation events on the North Saskatchewan River at the WSC gauge (Station 14.48 km) in 2009.
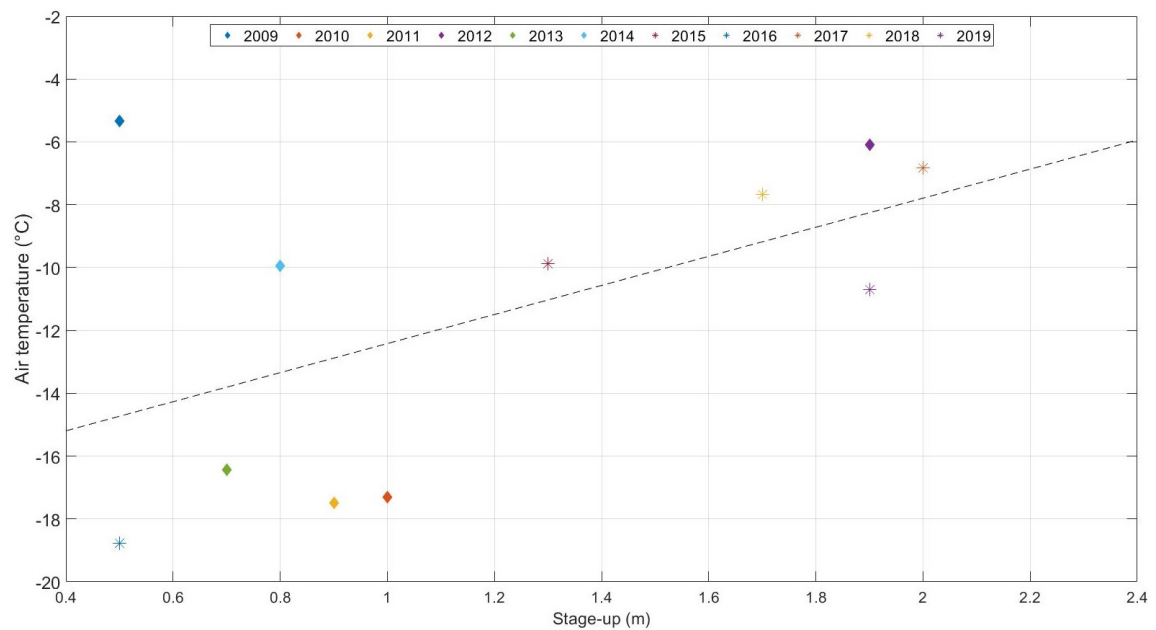
Figure 2-13. Correlation of stage-up depth and average daily air temperature on the day of freeze-up.
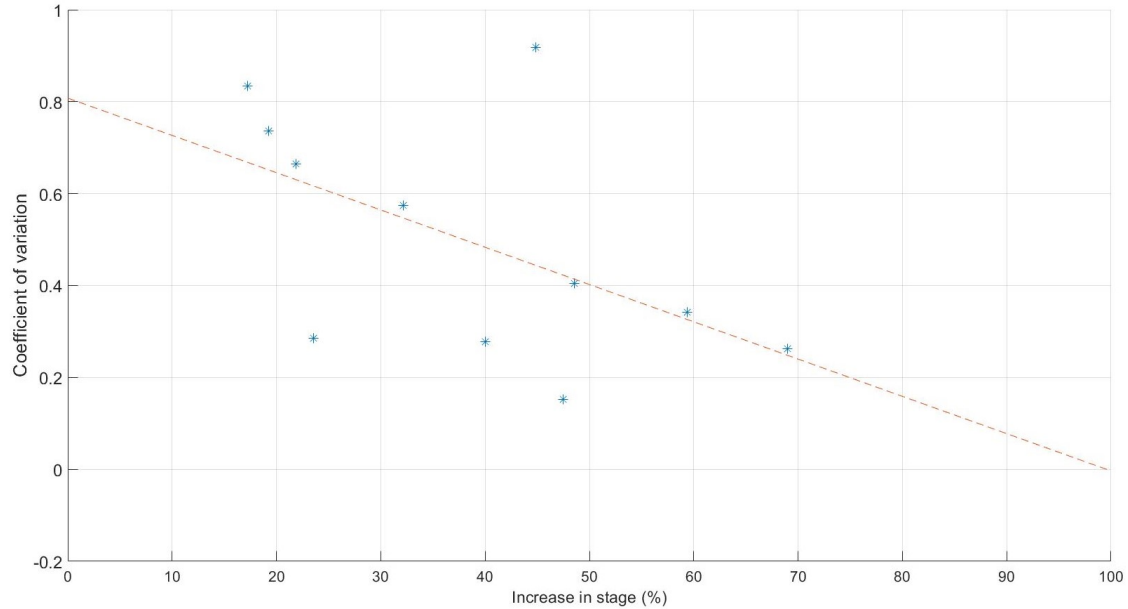
Figure 2-14. Relation between the coefficient of variation of the daily air temperature during the 4 days preceding freeze-up and the percent increase in stage caused by the arrival of the ice-front.

2.4.5. Ice front progression

Ice front progression rates were calculated using the times of freeze-up at the EAS camera site (Station 11.26 km) and the time of stage-up recorded by the WSC gauge (Station 14.48 km). The two stations are approximately 3.2 km apart. This yielded a range of progression rates from 0.96-8.6 km/day, as shown in Table 4(a). With the exception of the rates of 1.3 km/day and 0.96 km/day in 2017 and 2018, respectively, the values are similar to the 7 km/day progression rate recorded in 1981 by Gerard and Anders (1982), which were based on observed ice front progression at three locations: (i) Laurier Park (Station 4.9 km), (ii) the U of A's water intake (Station 11.26 km), and (iii) Dawson Bridge, (Station 17.14 km). Their analyses found a relatively constant progression rate between the three locations. Additional analysis would be required to investigate the reason for the slower progression rates in 2017 and 2018.

Investigation into the effect of the mean daily temperature on the day of freeze-up, the average mean daily temperature between stage-up at Station 14.48 km and freeze-up at Station 11.26 km, and the accumulated DDF on the day of freeze-up showed no

significant relation with the ice front propagation rate. As such, the front progression rate appears to be largely independent of the local air temperature, suggesting that the ice front progression is mostly controlled by ice production and pan formation upstream of the city.

Maxwell et al. (2011) deployed game cameras at nine locations along the NSR in Edmonton. This allowed the investigation of the progression rate along a longer reach. Figure 2-15 shows the ice front progression locations for each region of the study reach. The regions are separated based on changes in average bed slope as shown in Figure 2-2 and summarized in Table 4. In contrast to the consistent progression rates identified by Gerard and Anders (1982), the progression rates calculated for 2010 varied through the study reach (see Table 4b and Figure 2-15). The maximum progression rate of 30.0 km/day, which occurred in region D (Figure 2-2) may have been affected by bridging which is believed to have occurred a short distance downstream of the WSC gauge.

Figure 2-16 shows the correlation between the ice front progression rate and the channel slope. When excluding the front progression rate for Region D, which was likely affected by a bridging event, the R^2 value of 0.84 was estimated for the linear regression. Steeper sections are shown as having a slower progression rate. This trend suggests that there are different processes occurring in different sections of the study reach; juxtaposed ice cover in the flatter sections and mechanical thickening in the steeper sections. Channel width does not appear to have a significant influence on the ice progression through Edmonton. Further analysis is required to investigate the effects of air temperature on the ice progression rates.

Table 4. Ice front progression rates: a) 2009-2019 using the difference between the timing of freeze-up captured by the EAS camera and the stage-up time at the WSC gauge and, b) 2010 using multiple game cameras.

a)	Year	Ice front progression rate (km/day)
	1981*	7.0*
	2009	4.5
	2010	3.9
	2011	8.6
	2012	5.6
	2013	5.9
	2014	3.7
	2015	3.9
	2016	6.7
	2017	1.34
	2018	0.96
	2019	5.28

b)	Region [†]	2010 Ice front progression rate (km/day)	Channel slope
	A	8.2	0.0004
	B	14.2	0.0002
	C	3.9	0.0009
	D	30.7[‡]	0.0002
	E	11.6	0.0002
	F	11.8	0.0004

[†] Regions are shown in Figure 2-2.

[‡] Affected by bridging.
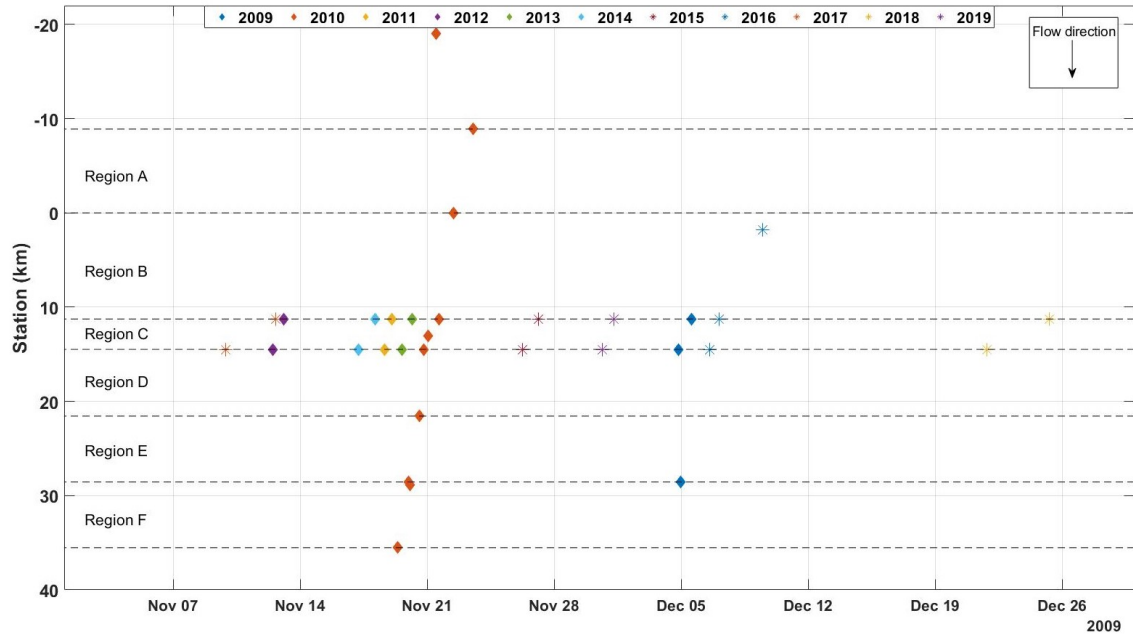
Figure 2-15. Ice front progression for 2009-2019.
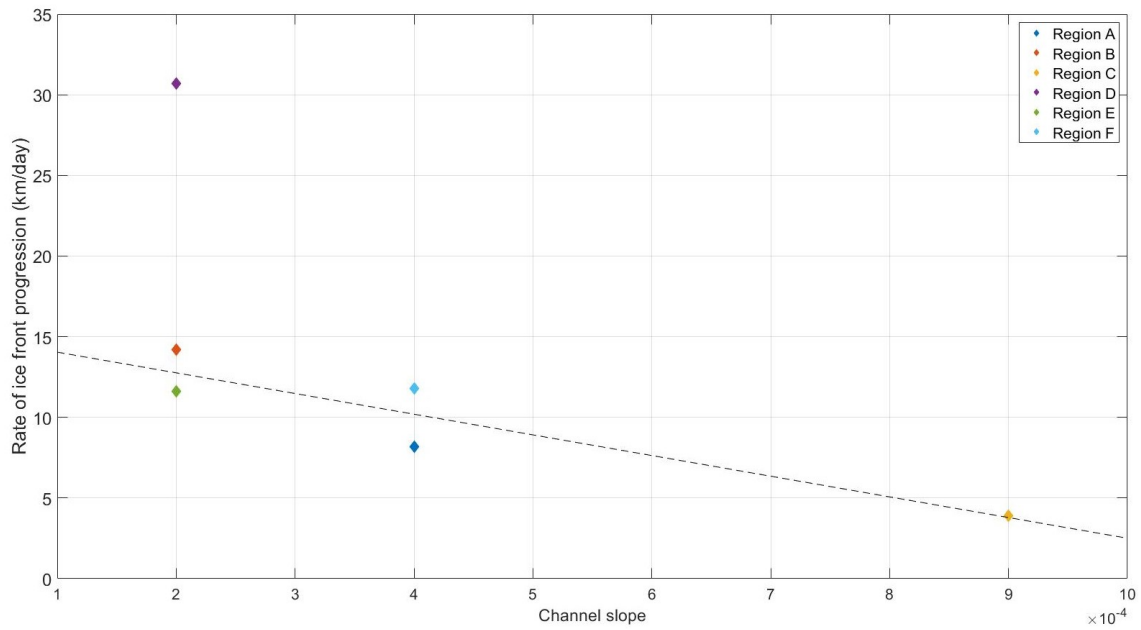
Figure 2-16. Correlation between the channel slope and the ice front progression rate as observed during freeze-up of 2010. The value for Region D has been excluded in plotting the trendline.

2.4.6. Ice thickness

During the winter of 2008-2009, the WSC ice thickness measurements were taken at Station 14.48 km. In each of the other years discussed in this section, 2009-10 to 2014-15, the WSC ice thickness measurements were taken at Station 6.87 km. Average ice thickness values were calculated for each profile and ranged between 0.27 m and 0.77 m. There was evidence of grounding at the banks in several of the ice cover profiles and as such, the average ice thicknesses were calculated excluding the first 30 m of ice thickness measurements adjacent to both banks. As an example, Figure 2-17 shows the ice cover profiles measured across the river for the 2008-2009 season, which were taken at Station 14.48 km. Not all of the ice profiles are as regular as that shown in Figure 2-17. Although not discussed in detail here, figures showing the ice profiles between 2009 and 2015 are included in Appendix B. In some years, there is greater variation in ice thickness over the width of the cover, with pronounced thicker measurements on either side of the thalweg. Figure 2-18 shows the development of the ice cover, in terms of the average thickness, over the winters of 2008-2015. In general, the ice gets thicker over the winter which can be attributed to thermal or "bottom growth" and snow ice growth or "surface growth" (Comfort and Abelnour 2013).

The 2010 ice front progression rate and channel slope indicate that ice cover in the area around Station 6.87 km is likely juxtaposed, with limited mechanical thickening. In both 2013 and 2014 the first ice thickness measurements were conducted on 9th December; freeze-up occurred on 20th November 2013 and 18th November 2014 and stage-up of 0.7 m and 0.8 m, respectively, were observed. On both occasions, the average thickness of the ice cover was reported to be approximately 0.30 m thick. For comparison, the average ice pan thickness observed by the SWIPS during the week preceding the arrival of the ice front in 2009 and 2010 was 0.33 m and 0.42 m, respectively. This lends further weight to the theory that the ice cover in this region develops as a juxtaposed ice cover.

The amount of initial consolidation/shoving during freeze-up, can affect the measured ice thicknesses at the gauge location. The thickest ice measurements belong to the winter of 2012-2013. Stage-up during this season, shown in Figure 2-8d, indicates that there was a large degree of mechanical thickening at Station 14.48 km. It is difficult to ascertain

whether a similar stage-up pattern would have occurred at the location of the ice measurements.

Figure 2-19 shows a strong correlation between ice thickness and DDF. The reduction in ice thickness between 11th February 2013 and 5th March 2013 is likely due to warmer than average air temperatures in late January and March; between these two dates, the increase in DDF was only 78 °C·Days. The ice thickness measurements taken on 30th January 2012 and 5th March 2012 show a very thick ice cover relative to the DDF (Figure 2-19). Air temperatures during winter 2011 to 2012 were the warmest during the observation period. However, there were two short-duration instances of very cold air temperatures during this season; -19.6 °C on 21st November and -28.3 °C on 17th January. Both instances were followed by immediate and sharp increases in the temperature to above 0 °C. These conditions match those described by Andres et al. (2003) as one of three possible criteria for mid-winter secondary consolidation events to occur.

DDF is frequently correlated with ice thickness using the Stefan equation (Michel 1971):

$$t_i = \alpha_1 \sqrt{DDF} \qquad\qquad [2\text{-}1]$$

where t_i represents the ice thickness (m) and α_1 represents an empirically derived and site-specific coefficient. Equation [2-1] with an α_1 value of 0.019 m°C$^{-1/2}$Day$^{-1/2}$, which appears to be representative of the data, is shown as a trend line in Figure 2-19. This α_1 value is close to the higher range of 0.014 m°C$^{-1/2}$Day$^{-1/2}$ - 0.017 m°C$^{-1/2}$Day$^{-1/2}$ associated with the snow-covered rivers (Hicks 2016). The measurements taken on 7th January 2010 and 3rd March 2010 were significantly smaller than would be expected according to the Stefan equation (Figure 2-19). Conversely, the measurements taken on 30th January and 5th March 2012 were much higher than would be predicted by the Stefan equation. This scatter is to be expected as factors other than cumulative air temperature also influence the development and thickness of river ice. One such factor is the presence and depth of snow, which can insulate and reduce thermal ice growth, on the ice cover (Andres and Van Der Vinne 2001).
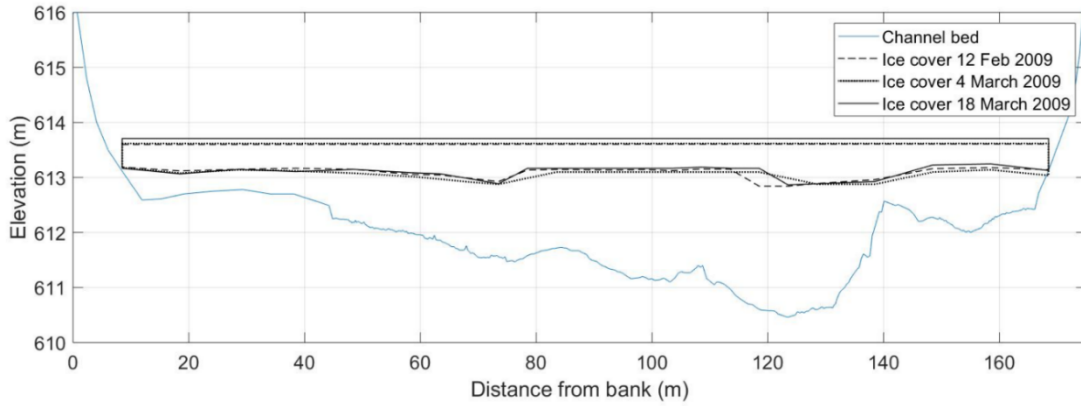
Figure 2-17. Ice thickness at WSC gauge, Station 14.48 km, 2009.
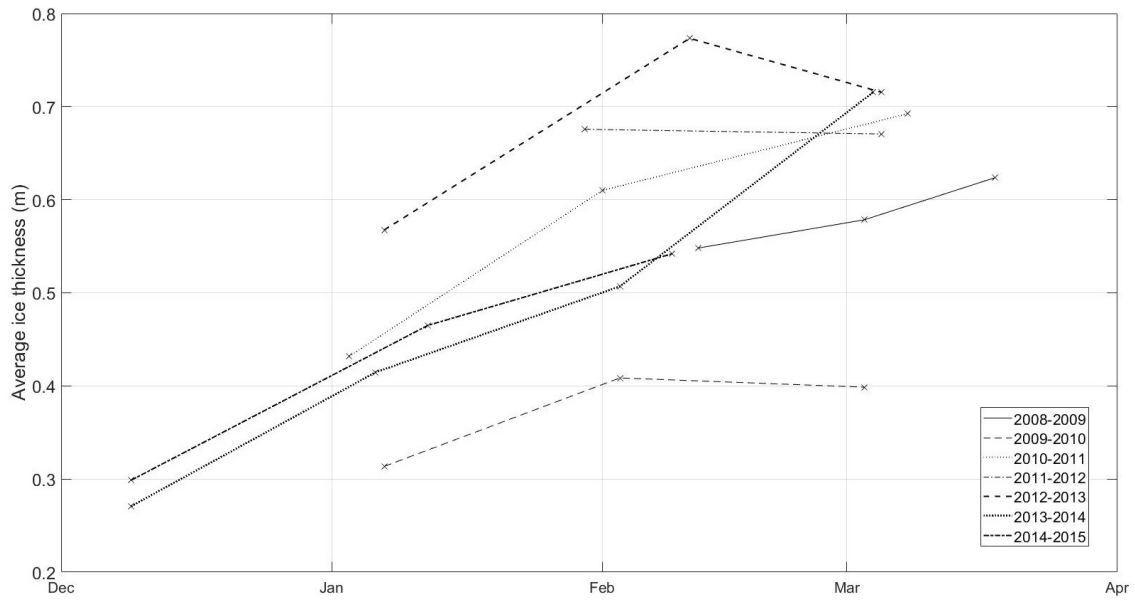
Figure 2-18. Ice thickness measurements for 2008-2015.
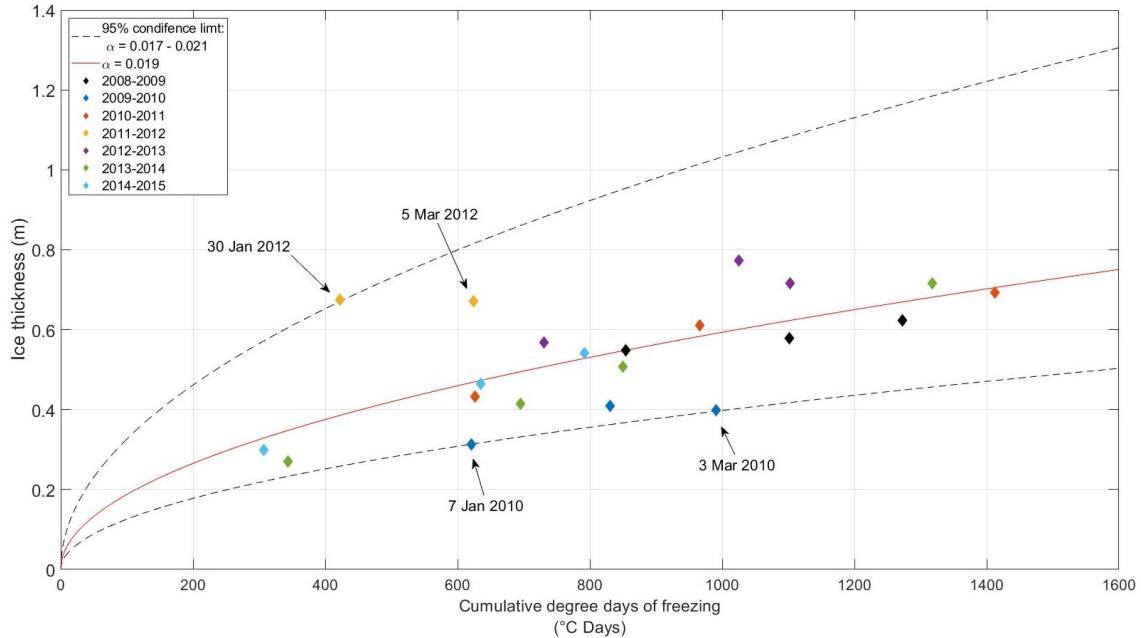
Figure 2-19. Cumulative degree-days of freezing model for estimation of ice thickness: calibration of the α coefficient.

2.4.7. GBWTP open lead: development, timing, and extent.

GBWTP was opened in 1956 and its treatment processes include grit chambers, settling processes (clarifiers), biological nutrient removal and UV disinfection. It is situated along the south bank of the NSR and the outfall discharges effluent into the river at Station 22.09 km. Although there is an additional outfall at Station 21.65 km, this outfall only discharges into the NSR during periods when the plant's tertiary treatment capacity is exceeded. There is typically no flow through this outfall during freeze-up or the winter months and so it is not considered to be a major influence on the thermal regime of the river. The design capacity for tertiary treatment is 310 million litres/day but on average the plant treats approximately 265 million litres/day (EPCOR, 2020). The warm water discharge from the GBWTP has a significant influence on the thermal regime of the NSR and is responsible for the development of a large open lead.

Images from game cameras and the SLR camera which were deployed along the banks of the NSR during the winter of 2010-11 have been used to estimate the channel coverage in terms of ice pans, solid ice and open water. These estimates were made by visually inspecting the captured images. These estimates were subsequently validated using a

MATLAB script to binarize a select number of images and calculate the fraction of the channel occupied by ice and the fraction of the channel deemed to be open water. Unfortunately, this process does not correct for the skew in images caused by low camera angles.

Figure 2-20, Figure 2-21 and Figure 2-22 show the surface ice concentration and river temperature at Stations 0.00 km, 11.26 km and 21.56 km, respectively. No river temperature data was collected at Station 0.00 km and so it is assumed that there is no temperature change between this location and the University of Alberta's water intake at Station 11.26 km. At all three stations, there is a short duration in which border ice (shown as solid ice) and ice pans are present. Once the surface ice concentration reaches 100%, the ice cover remains in place for the duration of the season. This is reflected in the river temperature measurements which do not fluctuate and remain close to 0 °C. An open lead often forms a short distance downstream of Station 11.26 km. However, this open lead, which is caused by warm water effluent from the University of Alberta, was not captured by the instrumentation. Additionally, a small open lead was observed late in the season along the right bank at Station 0.00 km. There is a large stormwater outfall within 100 m upstream of Station 0.00 km which, as the snowpack begins to melt early in the spring, may contribute warmer water to the NSR.

A larger open lead is known to form downstream of the GBWTP, Station 22.09 km, as a result of the warm water discharge from the plant. A sample image showing this open lead at each of Stations 22.51 km, 28.02 km, 28.55 km, 28.84 km and 35.70 km is included in Figure 2-23. The GBWTP open lead has been documented to form within days of the development of a stable ice cover (Maxwell et al. 2011). Although the downstream extent of the open lead has not been recorded, it is known to have passed further than Station 35.70 km. Maxwell et al. (2011) investigated the coverage of the open lead in relation to Stations 28.02 km, 28.55 km, 28.84 km, and 35.70 km using images from cameras. This information, along with GBWTP discharge and temperature, air temperature, and river temperature data has been used to produce Figure 2-24 to Figure 2-27, which show the evolution of the open lead during the 2010-11 season.

The temperature of the discharge from the GBWTP between December 2010 and March 2011 remained within a range of 12°C - 15 °C (Figure 2-24b). Discharge followed a typical daily trend, with troughs and peaks occurring at approximately 07:00 and 14:00, respectively. During these daily fluctuations, the discharge was recorded to rise from 1 m³/s to 4 m³/s. Using the WSC's winter discharge measurements taken on 3rd January (120 m³/s), 1st February (104 m³/s) and 8th March (103 m³/s) 2011, the GBWTP is calculated to contribute approximately 1-4% of the discharge in NSR during winter conditions. The river temperature recorded along the right bank of the NSR at Station 22.51 km (Figure 2-24c) clearly captures the effect of the effluent with river temperatures remaining between 3 °C and 10 °C throughout the season.

Figure 2-24c shows the river temperature measured along the left and right banks of the river at Station 28.02 km. The river temperature as measured along the right bank, varying between 0 °C and 2 °C, is significantly higher than that measured along the left bank where the river temperature remained constantly at 0 °C following freeze-up. The GBWTP outfall is on the right bank of the NSR and the elevated river temperature recorded along the right bank at Station 28.02 km indicates the that the effluent from the plant is not mixed across the width of the channel at this location.

A similar observation is made when comparing river temperature data collected at the SWIPS platform, 45 m from the right bank, and the Campbell monitoring station, 15 m from the right bank, at Station 28.55 km. The river temperature captured by the Campbell monitoring station typically ranged between 0 °C and 5 °C while those captured at the SWIPS station ranged only between 0 °C and 1 °C. Three factors are likely contributing to this difference in water temperature: (i) the effluent plume from GBWTP is concentrated along the right bank at this location, (ii) there is an outfall from the Clover Bar Energy Centre a short distance upstream of the Campbell monitoring station (Ghobrial et al., 2010; Maxwell, 2012), and (iii) the greater depth at which the SWIPS was deployed may have provided more insulation against overlying air. The contrast in water temperatures between the two instruments is reflected in the images captured by the SLR camera which, during the development of the open lead, shows the ice first melting along the right bank. The open lead then spreads out laterally towards the center

of the channel. The river temperature at the SWIPS platform appears to be more dependent upon fluctuations in the air temperature (Figure 2-25c) than in the discharge and temperature of effluent from GBWTP (Figure 2-25b). Owing to the often partial or thin ice cover present at Station 28.55 km, there is less insulation between the river and the air. This results in increased heat loss from the river and therefore, the river temperature trend largely mimics that of the air. The effect of warm effluent from the outfalls is not as obvious at Stations 28.84 km (Figure 2-26c) and Station 35.70 km (Figure 2-27c) where river temperatures fluctuated between 0 °C and 2 °C.

The first station at which the GBWTP open lead was observed is Station 28.02 km, as shown in Figure 2-24d. A stable ice cover is observed to form once the surface pan concentration reaches 100%. Within 6 days, the ice cover was observed to deteriorate as the open lead began to develop, quickly expanding to occupy approximately 60% of the channel width. The width of the open lead at this location varied during the winter and fluctuations in the width are clearly associated with changes in air temperature, with the ice cover growing during colder periods and shrinking during warmer periods.

Development of the ice cover is similar at Stations 28.55 km (Figure 2-25d) and 28.84 km (Figure 2-26d). A stable ice cover initially forms after surface pan concentration reached approximately 95%. The combination of the warm water effluents from the GBWTP and the Clover Bar Energy Center, is sufficient to prevent the ice cover from covering 100% the width of the channel. Within a few days, the ice cover deteriorates, and the open lead expands to occupy a greater portion of the channel. At Station 28.55 km, the open lead is typically estimated to occupy approximately 20% of the channel while at Station 28.84 km, the open lead is estimated to occupy approximately 40% of the channel. Figure 2-28 shows an aerial photograph, taken by Ghobrial (2012) on 3rd January 2010, of the area around Station 28.55 km. It confirms that the variance in the width of the open lead between these locations is reasonable. The width of the open lead at these two stations remained relatively constant throughout the season. Mid-season ice pan events were observed at both stations.

The open lead was observed to advance and retreat several times at Station 35.70 km, as shown in Figure 2-27. The downstream propagation of the open lead to and beyond

Station 35.70 km, is strongly linked to fluctuations in the air temperature. Rises in the air temperature in early and late January and in early and mid-February lead to the appearance of open water at Station 35.70 km, albeit with some lag time. Based on the observations at this station and at Station 28.02 km, it appears that the warm water effluent enables the formation of the open lead and the air temperature controls its width and extent.
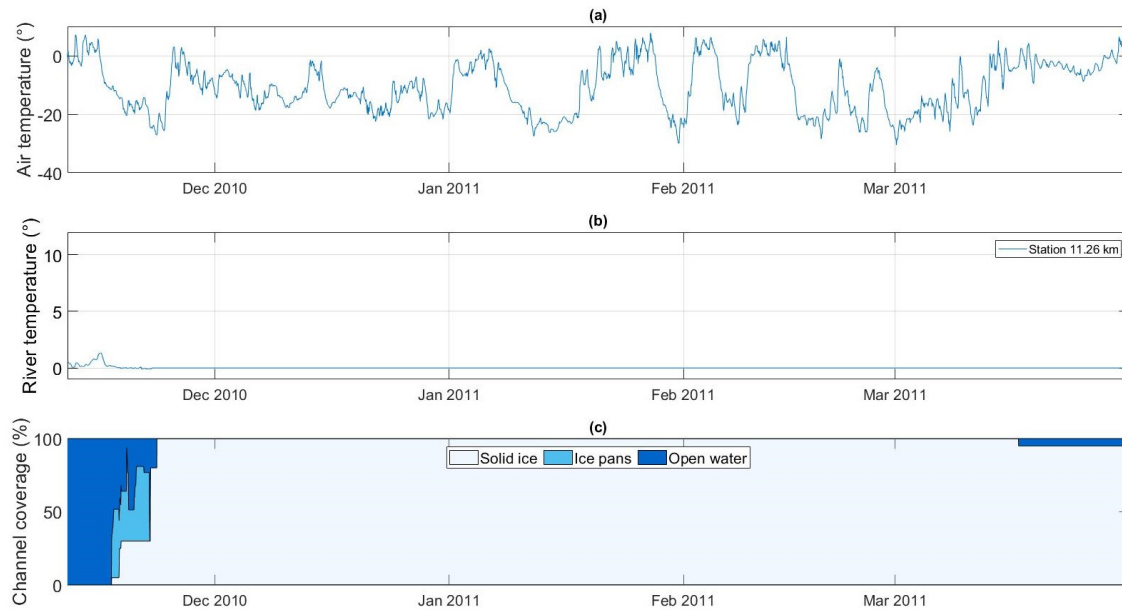
Figure 2-20. a) Air temperature, EAS Weather Station; b) River temperature at Station 11.26 km and; c) Percentage of channel as solid ice, ice pans and open water as measured at Station 00.00 km.
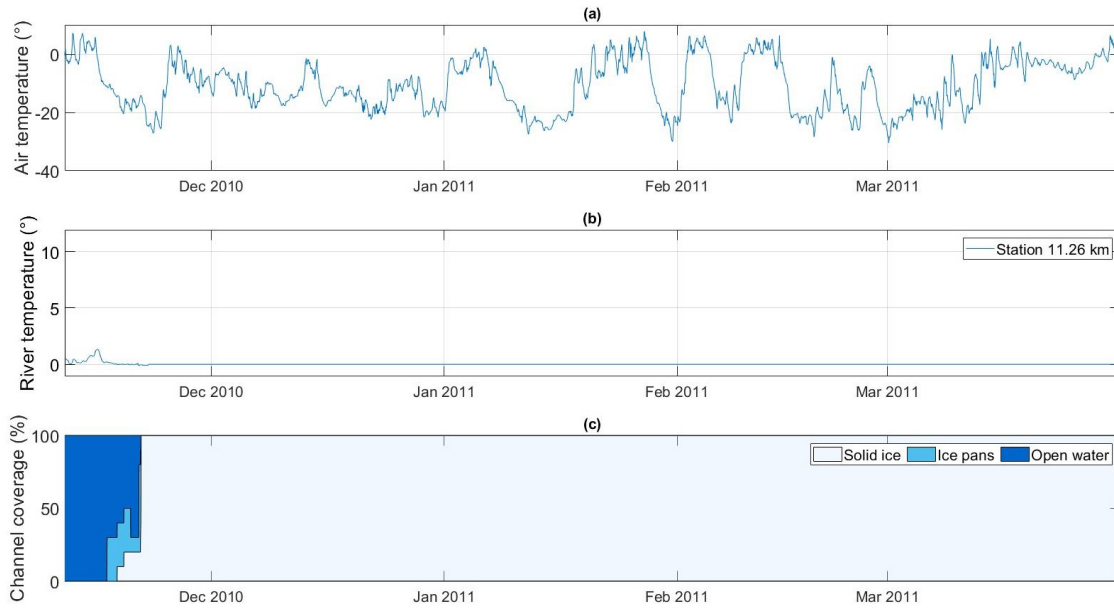
Figure 2-21. a) Air temperature, EAS Weather Station; b) River temperature at Station 11.26 km and; c) Percentage of channel as solid ice, ice pans and open water as measured by the EAS camera at Station 11.26 km.
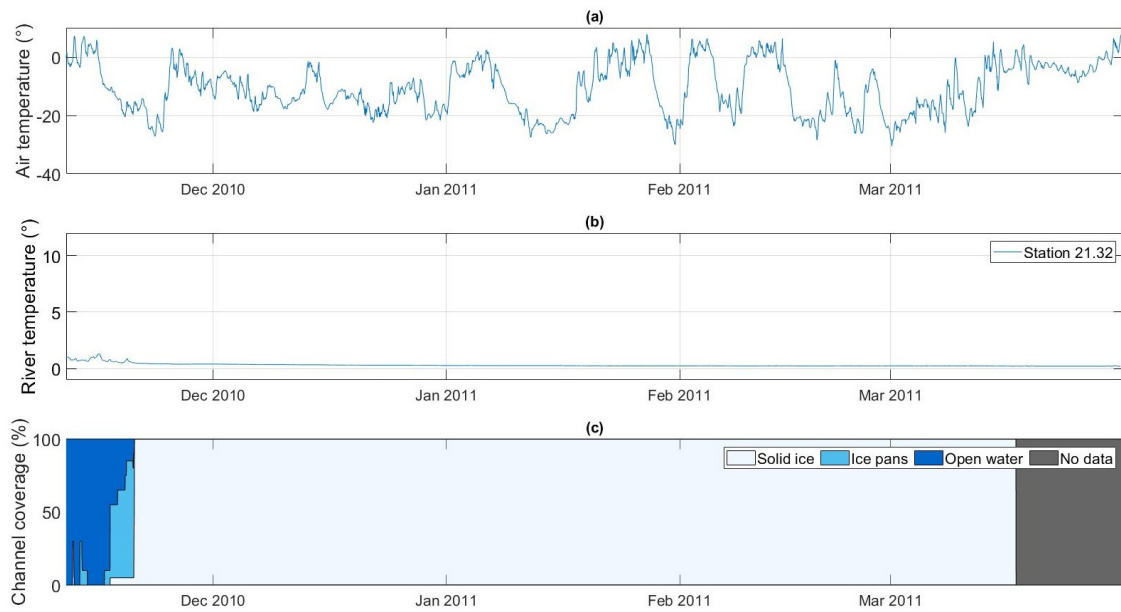
Figure 2-22. a) Air temperature, EAS Weather Station; b) River temperature at Station 21.32 km and; c) Percentage of channel as solid ice, ice pans and open water as measured by the game camera at Station 21.56 km.

Station 22.51 km - 10:00 AM 9th December 2010.

GBWTP outfall & upstream extent of open lead

Station 28.02 km - 09:00 AM 12th December 2010.

Station 28.55 km - 09:00 AM, 22nd February 2011.

Station 28.84 km - 09:00 AM 6th February 2011.

Station 35.68 km – 16:00 PM 6th January 2011.

Figure 2-23. Sample images of the GBWTP open lead during winter 2010-11 at Stations 22.51 km – 35.68 km. Flow direction is given by the blue arrows. Photo credit: Joshua Maxwell.
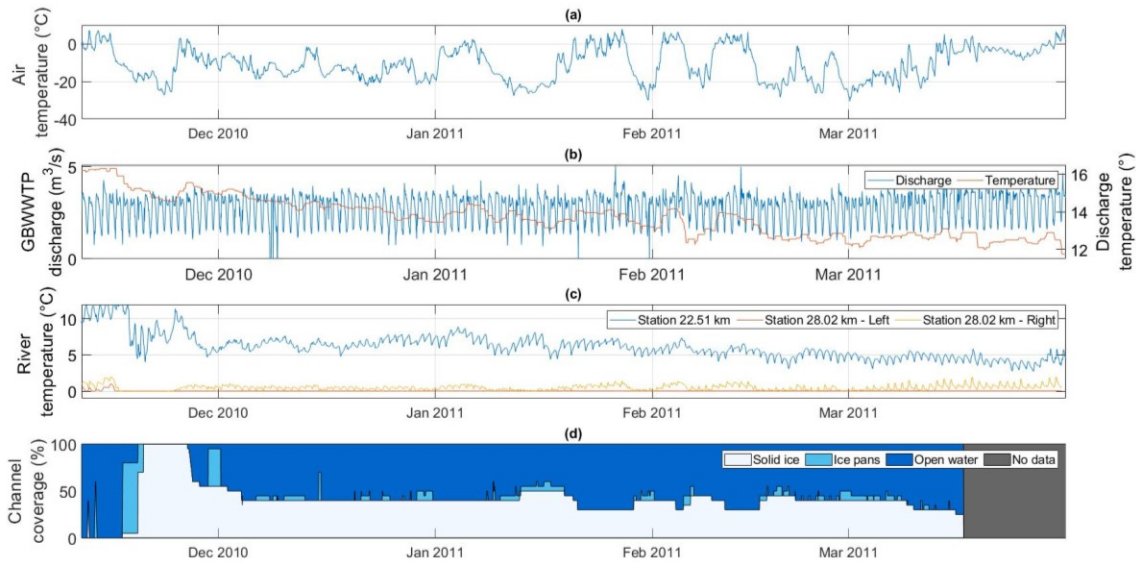
Figure 2-24. a) Air temperature, EAS Weather Station; b) GBWTP effluent temperature and discharge, Station 22.09 km; c) River temperatures at Stations 22.51 km, 28.02 km (left) and 28.02 km (right) and; d) Percentage of channel as solid ice, ice pans, and open water as measured by the game camera at Station 28.02 km.
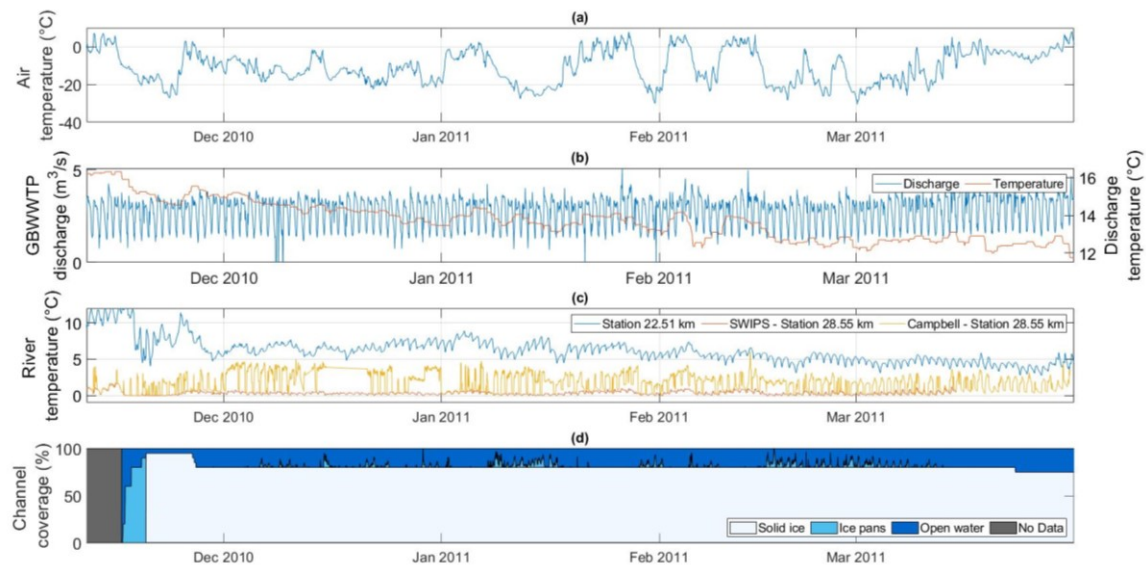
Figure 2-25. a) Air temperature, EAS Weather Station; b) GBWTP effluent temperature and discharge; c) River temperatures at Stations 22.51 km and 28.55 km; d) Percentage of channel as solid ice, ice pans and open water as measured by the SLR Camera and SWIPS at Station 28.55 km.
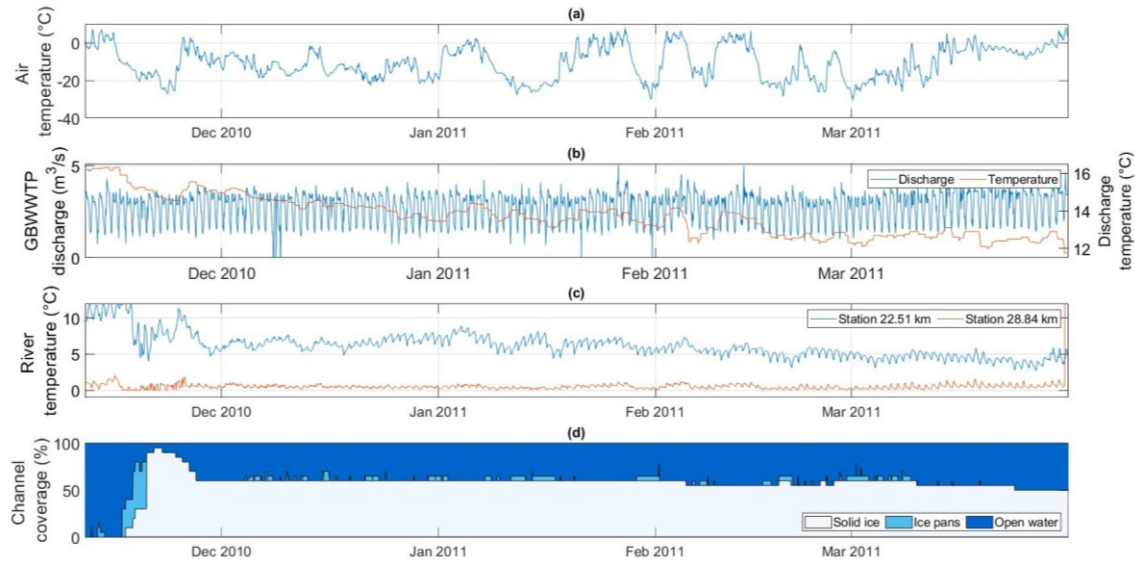
Figure 2-26. a) Air temperature, EAS Weather Station; b) GBWTP effluent temperature and discharge; c) River temperatures at Stations 22.51 km and 28.84 km and; d) Percentage of channel as solid ice, ice pans and open water as measured by the game camera at Station 28.84 km.
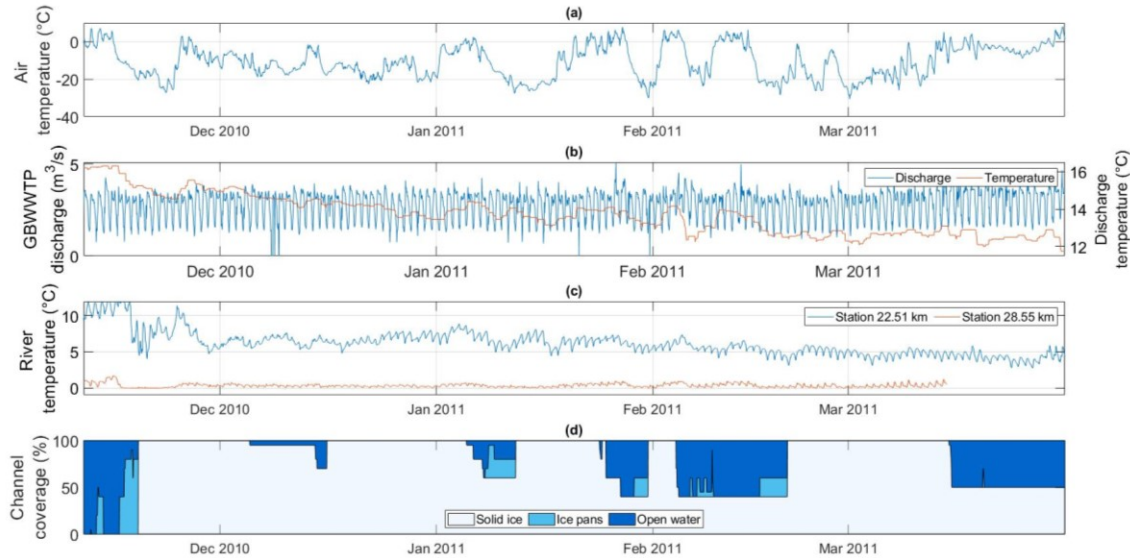
Figure 2-27. a) Air temperature, EAS Weather Station; b) GBWTP effluent temperature and discharge, Station 22.09 km; c) River temperature at Stations 22.51 km and 28.55 km and; d) Percentage of channel as solid ice, ice pans and open water as measured at Station 35.68 km.

Figure 2-28 Aerial photograph of the SWIPS site, Station 28.55 km, on 3rd January 2010.

2.4.8. Supercooling

The ability to evaluate the suspended frazil concentration based on a calibrated coefficient and river temperature could be valuable given the documented problems with frazil slush blocking water intakes (Daly 1991; Richard and Morse 2008; Kempema and Ettema 2015). This problem is known to occur in the North Saskatchewan River. Here, a correlation between supercooling intensity and the production of frazil ice is explored using SWIPS measured suspended concentrations and water temperature data. Supercooling intensity can be considered as a function of both the magnitude of supercooling and its duration. Given that supercooling events tend not to occur over monthly or even daily time-scales, an adaptation of the DDF method was introduced on a minute-scale to provide cumulative degree-minutes of supercooling (DMS). Starting at the beginning of a supercooling event, the DMS are calculated until the water

temperature returns to above-zero. The following equation was used to relate the intensity of supercooling to peak frazil production:

$$C_{pk} = \beta_1\sqrt{DMS} \hspace{6cm} \text{[2-2]}$$

where, C_{pk} represents the peak frazil concentration (%), β_1 is an empirically derived coefficient and DMS represents the cumulative degree-minutes of supercooling. This relationship was applied to the data collected by the SWIPS during the winters of 2009-10 and 2010-11 fitted β_1 of 0.0013 $°C^{-1/2}\cdot min^{-1/2}$ and 0.0074 $°C^{1/2}\cdot min^{-1/2}$, respectively. The results for 2009-10 and 2010-11 are shown in Figure 2-29 and Figure 2-30, respectively. Tsang (1984 and 1986) measured suspended frazil concentrations of between 0% and 0.25% on the Beauharnois Canal and between 0% and 0.03% on the St. Lawrence River, Quebec. The majority of supercooling events observed on the NSR in 2009-10 were lower-intensity events resulting in low peak suspended frazil concentrations of between 0.0016% and 0.01%. Even fewer high intensity events were observed during the winter of 2010-11, with all of the events recorded having a DMS of 64 °C·min or less. Despite this, approximately half of the events resulted in measured suspended frazil concentrations of between 0.02% and 0.06%.

There were some significant differences in the datasets from each of these two winters. The lowest temperature recorded at the SWIPS platform was -0.088 °C in 2009-10 compared with -0.050 °C in 2010-11. The average duration of supercooling in 2009, 10.05 hours, was also longer than the average of 6.49 hours observed in 2010. There is some uncertainty in the water temperature data given that the accuracy and precision of the instrumentation is 0.1ºC and 0.01ºC, respectively. Maxwell (2012) also noted that '*none of the temperature sensors used in the field deployment could accurately measure super-cooled water. Both SWIPS units registered super-cooled values but exhibited a considerable amount of scatter…. However, super cooling presence can still be detected on a binary (true or false)*'. Although these factors could be partly responsible for the higher magnitude supercooling events which were observed in 2009-10, they do not explain why higher peak concentrations of suspended frazil were observed in 2010-11. More data is required to further explore and to verify the relationship presented in equation [2-2].
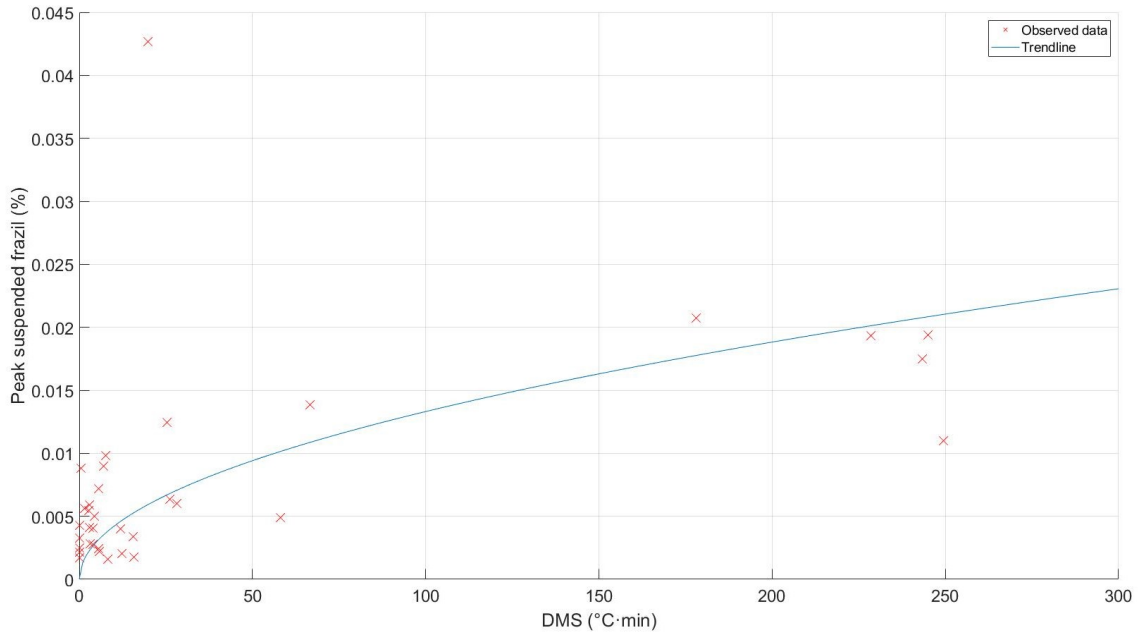
Figure 2-29. Relationship between cumulative degree-minutes of supercooling and peak suspended frazil concentration in 2009-10.
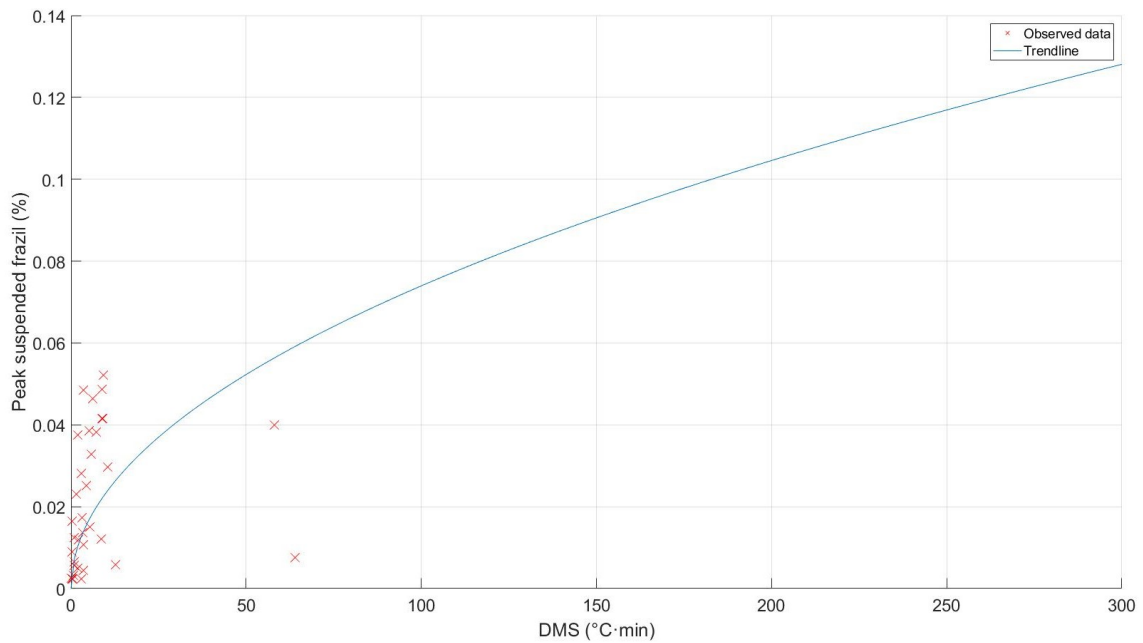
Figure 2-30. Relationship between cumulative degree-minutes of supercooling and peak suspended frazil concentration in 2010-11.

2.4.9. Degree days of thawing (break-up)

Break-up on the NSR typically occurs in late-March to mid-April and is predominantly thermal. Mechanical processes, such as break-up ice jams have been observed such as during break-up 2020. In a process similar to that used in calculating DDF during freeze-up, the degree-days of thawing (DDT) have been calculated using images and the air temperatures measured from the EAS Weather Station. DDT calculations began with the first five consecutive days of above-zero air temperatures and any occasional sub-zero air temperatures were subtracted in the calculations. As shown in Figure 2-31, the DDT for break up on the NSR between 2010 and 2020 varied between 4 °C·Days in 2013 and 74 °C·Days in 2019. All other DDT values varied between 24 °C·Days and 44 °C·Days. It is interesting to note that an exceptionally high DDF value of 208 °C·Days was observed during freeze-up in 2018 and an extraordinarily high DDT value was observed during break-up 2019. The other seasons show no obvious trend with corresponding high or low pairs of DDF and DDT.

Figure 2-31 shows a trend of decreasing DDT values in years which break-up was later. When break-up occurs later, the ice cover is typically exposed to more solar radiation (both in the number of days and the hours of daylight in those days) which contributes significantly to melting of the ice cover (Hicks, 2016). The relatively small range of DDT values is surprising given that the DDT method does not consider the effect of solar radiation or other key factors such as warm water inflows, the formation of open leads and dynamic break-up processes. Many scientists and engineers adapt the DDT method to better account for solar radiation by using a base of -5 °C rather than a base of 0 °C. This method was applied to the NSR but was found to yield a wider range of DDT values.
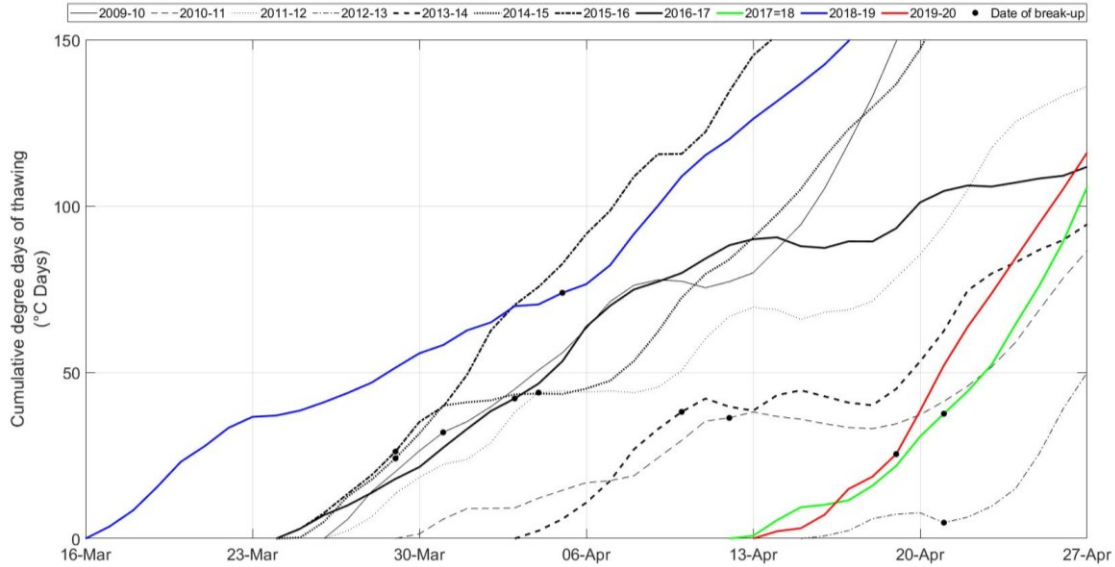
Figure 2-31. Cumulative degree days of thawing for break-up.

2.4.10. Linear heat transfer model

A linear heat transfer model was applied to the NSR using the last ice thickness measurement of each season, and solar radiation and air temperature data from the EAS Weather Station. It is assumed that either there is no significant difference in the thickness of the ice cover between Stations 6.87 km and 11.26 km, or that break-up at these two stations occurs near-simultaneously. The net heat flux between ice and the air, ϕ_{ia}, is calculated using equation [2-3] and the change in ice thickness, Δt_j is subsequently calculated using equation [2-4]:

$$\phi_{ia} = h_{ia}(T_a - T_i) + \phi_s(1 - \alpha) \tag{2-3}$$

$$\Delta t_j = \frac{\Delta t \phi_{ia}}{\rho_i L_m} \tag{2-4}$$

Where h_{ia} is a linear heat transfer coefficient, T_a is the air temperature, T_i is the temperature of the ice, ϕ_s is the sum of the shortwave radiation, α is the albedo, Δt is the time-step, ρ_i is the ice density (920 kg/m^3) and L_m is the latent heat of fusion of ice (333.4 kJ/kg). In this case, both h_{ia} and α are calibration parameters; consistent parameter values are applied in the model for each year.

A key assumption of the linear heat transfer model is that the temperature of the ice is equal to 0 °C. In all years except 2009-10, the last ice thickness measurement was taken prior to the average daily air temperature rising above 0 °C. As such, the calibrated Stefan equation (Section 2.4.6) was used to project the ice thickness measurements until the time when the average daily air temperature rose above 0 °C.

Figure 2-32 compares the results of the linear heat transfer model with the observed dates of break-up in 2010-2015. A linear heat transfer coefficient of 12 $W/m^2°C$ was selected for use in this study. This value is within the reasonable range of 8-20 $W/m^2°C$ published by Hicks (2016). An albedo value of 0.5, which is typical for melting snow (Hicks, 2016), was applied. This is a good medium considering that under real conditions, the albedo should be expected to decrease from a value of 0.9-0.8 when melting of the ice cover begins, down to a value of 0.1-0.3 imminently prior to break-up. As can be seen in Figure 2-32, the linear heat transfer model performs well in predicting break-up in 2012, 2013 and 2015 but is 13 early in predicting break-up in 2010, 9 days and 4 days late in predicting break-up in 2011 and 2014, respectively. The average error in predicting break-up was 5.2 days.

In a second linear heat transfer model, the albedo for each individual year was calibrated separately to match the linear heat transfer model's predicted date of break-up to the observed break-up date. For all seasons it was possible to match the observed break-up date using the linear heat transfer model. The linear heat transfer coefficient, h_{ia}, was once again kept at a constant value of 12 $W/m^2°C$. Matching the linear heat transfer model's break-up to the observed break-up date required a range of albedo values between 0.325 to 0.775. One of the key factors which should be expected to influence the albedo value is the depth and freshness of the snowpack. Figure 2-33 shows a strong relationship between the cumulative snowfall between freeze-up and break-up and the optimized albedo for that particular season. this relationship yields an R^2 value of 0.55. An interesting trend is observed with a lower albedo used in seasons in which there was greater cumulative snowfall. Intuitively, the reverse relation would be expected given the higher albedo values associated with fresh snow and old snow (Hicks, 2016). However, one possible explanation for this relationship might be that greater cumulative snowfall

causes the development of thicker snow ice, which has an albedo lower than fresh snow, typically in the range of 0.3-0.55 (Hicks, 2016).
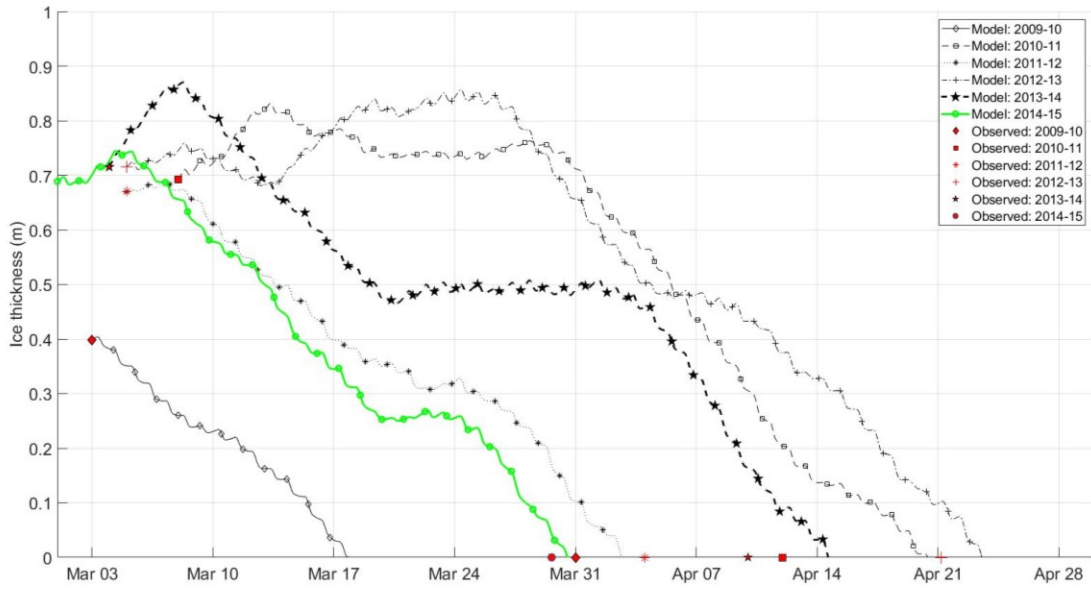
Figure 2-32. Ice decay on the North Saskatchewan River as modeled by the linear heat transfer model.
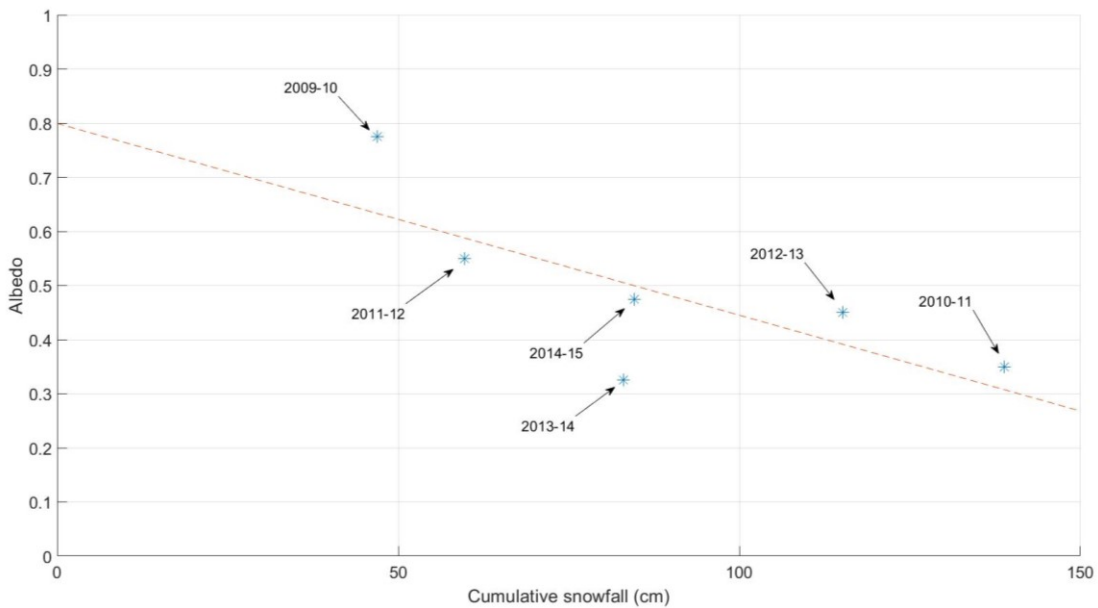
Figure 2-33.Scatter plot, including linear regression, showing the relationship between the cumulative snowfall between freeze-up and break-up with the optimized albedo used in the linear heat transfer model.

2.5. Conclusions

This chapter presents a summary of the meteorological, hydrometric and river ice data available for a reach of the NSR in Edmonton. The data analyses conducted in this study show that the ice regime in the NSR is highly complex. Between 2009-2019, the DDF for the formation of a stable ice cover ranged between 52 °C·Days and 208 °C·Days. Several locations within the study reach have been identified as causing ice congestion and are probable bridging locations. Between 2009-2019 the ice front progression rates were found to vary between 0.96 km/day and 8.6 km/day. Stage-up was also variable in both magnitude and duration during this time period. Relationships between the air temperature and the initial depth prior to stage-up and the magnitude of stage-up have been identified. However, these relationships do not completely capture or explain the type of stage-up experienced each year. There is evidence of several river ice phenomena including mechanical thickening and juxtaposed ice covers. The cumulative degree-days of air temperature method and the proposed cumulative degree-minutes of water supercooling relationship appear to capture the general trend of ice thickness and frazil concentrations, respectively. Many contributing factors have been left out of these empirical methods and this can be seen from the wide range of DDF at the day of first ice pan and complete ice cover, as well as the scatter of the ice thickness and peak frazil concentration data when plotted against DDF or DMS. A range of DDT values of between 4 °C·Days and 74 °C·Days were identified for break-up to occur. Finally, the linear heat transfer model has proven capable of giving an indication as to the timing of break-up, but additional data, such as the albedo, is required for more accurate results (to the same day). All of these analyses have provided a general characterization of the thermal ice regime of the NSR but are not sufficient to completely explain the observed variation and phenomena.

3.0 Modeling study of the North Saskatchewan River[1]

[1] *A modified and shorter version of this chapter was published in the International Association for Hydro-Environment Engineering and Research's 25th Symposium on Ice (Howley et al., 2020).*

3.1. River1D Model description

River1D is a public-domain model that was initially developed as a hydrodynamic model which solves the Saint Venant equations using the Characteristic Dissipative Galerkin method (Hicks and Steffler, 1992). The model has since been adapted on several occasions to incorporate several river ice processes and is now considered to be a physically-based, 1D, comprehensive river ice process model. The ice jam modules are contained in a stand-alone component which has not been utilized in this study. The River1D suite is capable of simulating river ice processes from freeze-up through to break-up.

The transformation of River1D from a hydrodynamic model to an ice process model began when Andrishak and Hicks (2005) enhanced the rectangular channel approximation model to include thermal ice processes using control volume principles in an Eulerian frame of reference. This development allowed simulation of water temperature, production of suspended frazil, formation of surface ice and solid ice, ice front location and thermal ice growth and melt (Andrishak and Hicks, 2005; Andrishak and Hicks, 2008; Hicks et al. 2009). The heat transfer between the water and air was simplified from a full energy budget, which requires significant amounts of data, to a linear heat transfer approach requiring only air temperature and solar radiation data (Andrishak & Hicks, 2008). Separately, She and Hicks (2005) adapted the model to include the steady ice jam profile equation and the ice resistance effects on ice jam release waves. Dynamic ice jam formation was incorporated into the model by She et al. (2009). Further developments were made in simplifying the full energy budget method to a simplified linear heat transfer equation (She et al. 2012) and enhancing the model capability to include simulation of dynamic wave propagation in multi-channel networks (Blackburn et al. 2015).

Andrishak and Hicks (2005) and She and Hicks (2005) acknowledged the potential limitations in using rectangular channel approximations and acknowledged that improvements in simulated results could be achieved using natural channel geometry. Blackburn and She (2019) reformulated the River1D model to accommodate natural channel geometry. During development of this version of the model, it was enhanced to include supercooling, frazil accretion, re-entrainment, anchor ice formation and release, border ice formation, under-cover transport of frazil and ice cover formation (Blackburn and She, 2019). The ice transport equations are solved using the Streamline Upwind Petrov-Galerkin finite element method (Blackburn & She, 2019). It is this natural channel geometry version of the model, with the additional capability of including multiple user-defined bridging locations, which is used in this study of the NSR.

River1D allows for meteorological data from multiple weather stations to be used by way of atmospheric zones. The user may determine which reaches of a model domain are to be included in each atmospheric zone. To accommodate confluences or difluences, multiple upstream (and/or downstream) boundary conditions can be included in the model with unique inflow hydrographs and ice inputs for each boundary condition.

The model has been calibrated and validated using a comprehensive dataset from the Susitna River, Alaska (Blackburn and She, 2019). Ye and She (2019) also used the specified ice conditions component of the model to test six mechanical break-up criteria using data from the Athabasca and Peace Rivers, Alberta. Although the effects of urban influences on river ice processes have not yet been modeled, the current version of River1D presents an opportunity to test this affect. Additionally, the opportunity to further validate the natural channel geometry version of River1D is one of the reasons for its choice as the model used in this study.

3.1.1. River1D Governing Equations

Following Blackburn and She (2019), the governing equations of River1D are outlined in this section. With consideration given to the presence of an ice cover and anchor ice, the mass and momentum equations are:

$$\frac{\partial A}{\partial t} + \frac{\partial Q_w}{\partial x} = \frac{\rho_i \partial A_i}{\rho_w \partial t} + (1 - p_a) \frac{\partial A_{an}}{\partial t}$$ [3-1]

$$\frac{\partial Q_w}{\partial t} + \frac{\partial (\beta Q_w U_w)}{\partial x} + g A_w \frac{\partial H}{\partial x} + g A_w S_f = 0$$ [3-2]

Where A is the cross-sectional area to the water surface; t is time; Q_w is the discharge of water under and through the ice; x is the streamwise path of the river; ρ_i is the density of ice, A_i is the cross-sectional area of the surface ice including border ice and the under-cover moving frazil layer; ρ_w is the density of water; p_a is the porosity of anchor ice, A_{an} is the cross-sectional area of anchor ice; β is a momentum flux correction coefficient; U_w is the average velocity of water flowing under and through the ice; g is acceleration due to gravity; A_w is the cross-sectional area of water under and through the ice; H is the water surface elevation (relative to a datum); S_f is the friction slope.

Manning's equation [3-3] is used to evaluate the friction slope and a composite roughness approach, using the Sabaneev equation [3-4] (Uzuner, 1975), is employed when a stationary ice cover is present.

$$Q = \frac{1}{n} A R^{\frac{2}{3}} \sqrt{S}$$ [3-3]

$$\frac{n_c}{n_2} = \left[\frac{1 + \phi \left(\frac{n_1}{n_2}\right)^{\frac{3}{2}}}{1 + \phi} \right]^{\frac{2}{3}}$$ [3-4]

where Q is discharge; n is Manning's roughness coefficient; R is the hydraulic radius; S is the channel slope; n_c is the composite roughness (bed and under ice cover); n_1 is the roughness of the underside of an ice cover; n_2 is the bed roughness; and ϕ is the ratio of the ice affected wetted perimeter, P_i to the bed affected wetted perimeter, P_b.

Water temperature.

A conservation of thermal energy equation, giving consideration to the water-ice mixture, is used to simulate the water temperature according to Shen (2010, cited in Blackburn and She, 2019):

$$\frac{\partial(A_w e_{wi})}{\partial x} + \frac{\partial(Q_w e_{wi})}{\partial x} = \frac{B_o(1-C_i)}{\rho_w}\emptyset_{wa} - \frac{(B_oC_i + f_bB_{ws})}{\rho_w}\emptyset_{ia} \tag{3-5}$$

$$-\frac{(B_oC_i + P_bC_{an} + f_bB_{ws})}{\rho_w}\emptyset_{wi} + B_o\frac{\rho_i}{\rho_w}L_i\eta C_f + P_bC_{an}\frac{\rho_i}{\rho_w}L_i\gamma C_f$$

$$-B_oC_i\frac{\rho_i}{\rho_w}L_i\beta_{re}\left(t_{si} + t_{fs}(1-p_f)\right) - B_oC_i\frac{\rho_i}{\rho_w}L_i\beta_{re}(t_{ui(1-p_f)})$$

where e_{wi} is the thermal energy per unit mass of ice-water mixture; B_o is the width of the water surface clear of border ice; C_i is the surface ice concentration (%); ϕ_{wa} is the net rate of heat exchange, per unit of surface area, between water and air; f_b is the fraction of the channel covered by border ice, B_{ws} is the total width of the channel at the water surface (excluding any overbank flow); ϕ_{ia} is the net rate of heat exchange per unit surface area between ice and the air; C_{an} is the fraction of bed covered by anchor ice; ϕ_{wi} is the net rate of heat exchange, per unit surface area, between water and ice; L_i is the latent heat of ice; η is the rate of frazil rise; C_f is the volumetric concentration of suspended frazil ice; γ is the rate of frazil ice accretion to the bed; β_{re} is the rate of surface ice re-entrainment that occurs when the ice velocity, U_i, exceeds the ice velocity threshold for re-entrainment U_{i_re}; t_{si} is the thickness of the solid ice layer; t_{fs} is the thickness of the frazil slush layer; p_f is the porosity of the frazil slush and; t_{ui} is the thickness of the under-cover moving frazil layer. Table 5 describes each term included in the conservation of thermal energy equation [3-5] and when they are active.

Table 5. Terms of the conservation of thermal energy equation.

Term	Represents	Considered when
1	Net heat exchange between water and air	Always
2	Net heat exchange between water and air through the ice cover	$T_w > 0$ °C and $T_a < 0$ °C.
3	Net heat exchange between water and ice	Always
4	Frazil rise	$T_w < 0$ °C
5	Frazil accretion to bed	$T_w < 0$ °C
6	Re-entrainment of surface ice to suspended frazil layer	$U_i > U_{i\_re}$ and $U_i > 0$
7	Re-entrainment of under-cover moving frazil to suspended frazil layer	$U_w > U_{i\_re}$ and $U_i = 0$

River1D uses a linear heat transfer approach (Andrishak and Hicks, 2008) for the heat exchange between water and air:

$$\emptyset_{wa} = -\emptyset_s + h_{wa}(T_w - T_a) - j_{wa}T_a + k_{wa} \qquad [3\text{-}6]$$

Where Φ_s is the net incoming solar radiation, h_{wa} and j_{wa} are linear heat transfer coefficients; k_{wa} is a linear heat transfer constant; and T_w is the water temperature.

Suspended frazil

In calculating suspended frazil, the model gives consideration to both the thermal growth and decay of frazil along with mass (frazil) transfer between the surface frazil, under-cover moving frazil and anchor ice layers:

$$\frac{\partial(A_w C_f)}{\partial t} + \frac{\partial(Q_w C_f)}{\partial x} = \frac{\emptyset_{fw}}{\rho_i L_i} - B_o \eta C_f - P_b C_{an} \gamma C_f \qquad [3\text{-}7]$$

$$+ B_o C_i \beta_{re} \left(t_{si} + t_{fs}(1 - p_f) \right) + B_o C_i \beta_{re}(t_{ui}(1 - p_f))$$

where ϕ_{fw} is the net rate of heat exchange, per unit surface area, between suspended frazil particles and water. It is calculated according to equation [3-8]:

$$\phi_{fw} = -\frac{2N_u^f K_w}{d_e r_o}\left(C_f + C_{fo}\right)A_w T_w \qquad \text{[3-8]}$$

where N_u^f is the Nusselt number of a suspended frazil particle; K_w is the thermal conductivity of water; d_e is the typical frazil particle thickness; r_o is the typical frazil particle radius; and C_{fo} is the frazil seeding concentration. Table 6 describes each of the terms in the suspended frazil production and transport equation and, where relevant, notes the conditions under which each of the terms are active.

Table 6. Terms of the suspended frazil production and transport equation.

Term	Represents	Considered when
1	Growth and decay.	Always
2	Rise of suspended frazil to the surface frazil layer.	Always
3	Accretion of suspended frazil to the river bed.	Always
4	Re-entrainment of surface ice to the suspended frazil layer.	$U_i > U_{i\_re}$ and $U_i > 0$
5	Re-entrainment of under-cover moving frazil to the suspended frazil layer.	$U_i > U_{i\_re}$ and $U_i = 0$

Border ice

River1D gives consideration is given to both static border ice, meaning border ice that develops from thermal growth, and dynamic border ice, meaning border ice that develops or grows through the attachment of ice pans. Static border ice growth is assumed to occur if all of the following three criteria, developed by Matousek (1984, cited in Blackburn and She, 2019) are met:

- $T_w < 0\ °C$
- $T_a < 0\ °C$

- $U_{wl} / U_{cr} < 0.167$

where U_{wl} is the local water velocity adjacent to the border ice and U_{cr} is a user-specified maximum water velocity for frazil ice accretion. Border ice accretion due to static growth is assumed to follow the DDF approach (Blackburn and She, 2019).

Dynamic border ice growth is assumed to occur if both of the following criteria are met:

- $0.167 < U_{wl}/U_{cr} < 1$
- $C_i > 0.1$

If these criteria are not met, the first term in equation [3-9] is not considered by River1D in calculating the lateral accretion of border ice. Dynamic border ice growth is assumed to follow an empirical model developed by Michel et al. (1982, cited in Blackburn and She, 2019).

Considering accretion caused by both static and dynamic growth, border ice is calculated using equation [3-9]:

$$\frac{dB_b}{dt} = aC_i^b \left(\frac{U_{wl}}{U_{cr}}\right)^d \frac{\phi_{wa}}{\rho_i L_i} + e \frac{\emptyset_{DDF}}{\rho_i L_i} \qquad [3\text{-}9]$$

where B_b is the border ice width from a given bank; a, b and e are coefficients; U_{wl} is the local open water velocity adjacent to the border ice; U_{cr} is the maximum water velocity for border ice accretion; e is a border ice equation coefficient; and Φ_{DDF} is the rate of heat loss based on the degree-days of freezing.

Border ice thickness is considered to follow the wedge-shaped theory presented by Clark (2013) and thus the rate of border ice thickness growth and decay is calculated using equation [3-10]:

$$\frac{dt_b}{dt} = \frac{-h_{wa}T_a - \phi_s}{\rho_i L_i \left(1 + \frac{h_{wa}t_b}{K_i}\right)} - \frac{\phi_{wi}}{\rho_i L_i} \qquad [3\text{-}10]$$

where t_b is the border ice thickness and K_i is the thermal conductivity of ice.

<u>Anchor ice</u>

River1D is capable of simulating anchor ice and although this variable was simulated, there was no data available to validate the results. Anchor ice accumulations change according to the rate of frazil accretion and the rate of thermal growth or decay, and is calculated according to Shen (2010, cited in Blackburn and She, 2019):

$$\frac{dt_{an}}{dt} = \frac{\gamma C_f}{(1 - p_a)} - \frac{\phi_{wi}}{\rho_i (1 - p_a) L_i} \qquad [3\text{-}11]$$

The net rate of heat exchange between the water and ice, ϕ_{wi}, is calculated according to Ashton (1973):

$$\phi_{wi} = \frac{\alpha_{wi} U_w^{0.8}}{D_{ui}^{0.2}} T_w \qquad [3\text{-}12]$$

where α_{wi} is the coefficient for turbulent heat exchange between water and ice and D_{ui} is the undercover flow depth. Table 7 provides a description of each of the terms included in the anchor ice equation [3-11] and notes, where relevant, under which condition those terms are taken into consideration.

Table 7. Terms of the anchor ice equation.

Term	Represents	Considered when
1	Growth of anchor ice due to frazil accretion	$T_w < 0$ °C
2	Thermal growth and decay	Always

In addition to anchor ice growth and decay, consideration is also given to anchor ice release in River1D. Anchor ice releases if either of the following two conditions are met:

- $T_w > 0$ °C

- $t_{an} > \frac{\pi}{3\sqrt{3}} \frac{d_s (\rho_s - \rho_w)}{(1 - p_a)(\rho_w - \rho_i)}$

where t_{an} is the anchor ice thickness; d_s is the average diameter of the bed material; and ρ_s is the average density of the bed material.

<u>Surface ice</u>

A two-layer approach is utilized with solid ice and frazil slush layers. The surface ice concentration along the channel is given by:

$$\frac{\partial(B_o C_i)}{\partial t} + \frac{\partial(U_i B_o C_i)}{\partial x} = \frac{B_o(1-C_i)\eta C_f}{t'_f(1-p_f)} + \frac{B_o(1-C_i)\emptyset_{wa}}{t'_{si}\rho_i L_i}$$

$$+ \frac{(1-C_i)S_{ui}}{(1-p_f)t_{ui}} - B_o \beta_{re} C_i$$

[3-13]

where t'_{si} is the initial thickness of ice which has newly formed between ice pans once they have stopped moving; t'_f is the thickness of new frazil pans; and S_{ui} is a source term representing the exchange between the under-cover moving (A_{ui}) and stationary (A_{fs}) frazil layers. Table 8 provides a description of each of the terms in the surface ice concentration equation and notes when each of the terms is considered.

Table 8. Terms of the surface ice concentration equation.

Term	Represents	Considered when
1st	Frazil rise	Always
2nd	Freezing between stationary ice	$U_i = 0$ and $T_a < 0$
3rd	Transfer from under cover moving frazil layer	Always
4th	Re-entrainment of surface ice	$U_i > U_{i\_re}$

Mass conservation equations [3-14] and [3-15] are used for the frazil slush and solid ice layers, respectively. For the frazil slush layer:

$$\frac{\partial A_{fs}}{\partial t} + \frac{\partial U_i A_{fs}}{dx} = \frac{B_o \eta C_f}{(1-p_f)} - \frac{B_o C_i \emptyset_{ia}}{\rho_w p_f L_i} - \frac{B_o C_i \emptyset_{wi}}{\rho_i(1-p_f)L_i}$$

$$-B_o C_i \beta_{re} t_{fs} + \frac{S_{ui}}{(1-p_f)}$$

[3-14]

Table 9 presents a description of each of the terms in the frazil slush mass conservation equation and notes under which conditions each of the terms is given consideration.

Table 9. Terms of the frazil slush mass conservation equation.

Term	Represents	Considered when
1st	Frazil rise	$U_i > 0$
2nd	Pore water freezing	$A_{fs} > 0$ and $T_a < T_w \leq 0 \ °C$
3rd	Decay at the water-ice interface	$A_{fs} > 0$ and $T_w < 0 \ °C$
4th	Re-entrainment of surface ice	$U_i > U_{i\_re}$ and $U_i > 0$
5th	Transfer from under-cover moving layer	Always

For the solid ice layer:

$$\frac{\partial A_{si}}{dt} + \frac{\partial U_i A_{si}}{\partial x} = f_1 \frac{B_o C_i \emptyset_{ia}}{\rho_i L_i} - \frac{B_o C_i \emptyset_{wi}}{\rho_i L_i} + \frac{B_o (1 - C_i) \emptyset_{wa}}{\rho_i L_i} - B_o C_i \beta_{re} t_{si} \qquad [3\text{-}15]$$

where f_1 is a conditional constant and depends on whether melting of solid ice, freezing of the water column, freezing of pore water or any other process is taking place. Details are provided in Blackburn and She (2019). Table 10 presents a description of each of the terms in the solid ice mass conservation equation and notes under which conditions each of the terms is given consideration.

Table 10. Terms of the solid ice mass conservation equation.

Term	Represents	Considered when
1st	Growth and decay	$U_i > 0$
2nd	Growth and decay at water and ice interface	$A_{fs} = 0$
3rd	Freezing between ice pans	$U_i = 0$ and $T_a > 0$
4th	Re-entrainment of surface ice	$U_i > U_{i\_re}$ and $U_i > 0$

Ice cover formation at multiple locations is enabled in the model but requires the user to specify the time and location of each bridging event. The Froude number at the cross-section immediately upstream of the ice cover is used to determine whether ice cover propagation will occur through juxtapositioning, hydraulic thickening or whether mechanical thickening will occur. The Froude number is calculated according to:

$$F_r = \frac{U_w}{\sqrt{gD}} \qquad\qquad \text{[3-16]}$$

where D is the hydraulic depth.

The ice front progresses in a juxtaposed manner if the Froude Number at the location of the ice front is less than a user-defined maximum (maximum Froude number for juxtapositioning). When this mode of progression is active, the expected thickness of the ice accumulation is set equal to the thickness of the incoming ice pans. If the Froude number exceeds the maximum Froude number for juxtapositioning but is less than a separate user specified maximum Froude number for ice front progression, the ice front progresses upstream in a hydraulic thickening or mechanical thickening mode. In this scenario, the narrow and equilibrium ice jam theories are used to calculate the expected ice thickness of the ice accumulation.

The ice front location(s) is used to determine the ice velocity in the model. Ice in a reach in which an ice front has not passed is considered to have a velocity equal to the water velocity. Ice in a reach through which the ice front has passed is considered to be stationary. The velocity of the undercover moving layer is considered separately and continues to move at the velocity of the water despite the presence of a stable ice cover.

The ice front location is tracked according to Uzuner and Kennedy (1976, cited in Blackburn and She, 2019):

$$X_i^{t+\Delta t} = X_i^t - \frac{C_i(t_{si} + (1-p_f)t_{fs})U_i\Delta t}{t_{le}(1-p_j) - C_i(t_{si} + (1-p_f)t_{fs})} \qquad\qquad \text{[3-17]}$$

where t is the model time corresponding to the ice front location; t_{le} is the expected thickness of the ice accumulation following formation of the ice cover (m); and p_i is the expected porosity of the ice accumulation following formation of the ice cover.

Under-cover transport

Equation [3-18] describes how the under-cover transport of frazil is considered in the model:

$$\frac{\partial A_{wi}}{\partial t} + \frac{\partial U_{wi} A_{wi}}{\partial x} = \frac{B_o \eta C_f}{(1 - p_f)} - B_o C_i \beta_{re} t_{ui} - \frac{S_{ui}}{(1 - p_f)} \tag{3-18}$$

where U_{ui} is the velocity of the under-cover moving frazil layer. Table 11 presents a description of each of the terms in the under-cover transport equation and notes under which conditions each of the terms is given consideration.

Table 11. Terms of the under-cover transport equation.

Term	Represents	Considered when
1st	Frazil rise	$U_i = 0$
2nd	Re-entrainment of under-cover moving frazil	$U_{ui} > U_{i\_re}$ and $U_i = 0$
3rd	Transfer to the frazil slush layer	Always

3.2. Model setup and configuration

The river geometry for the study site was originally collected in-house by Alberta Environmental Protection in 1991 (IDG 1995). It was later converted to HEC-RAS format by NHC (2007). A total of 48 surveyed cross-sections were available within the study reach with an average spacing of 621 m. An additional 562 interpolated cross-sections were added to provide an average and maximum cross-section spacing of 48 m and 50 m, respectively. The model domain was extended approximately 10 km downstream to Station 39.35 km, so that a fixed water level could be used as a downstream boundary. A sensitivity analysis showed that the backwater effects caused by the downstream boundary is minimal within the study reach. The bed profile of the study reach is provided in Figure 3-1.

For each simulation, the initial conditions were established using a steady state simulation in River1D. All simulations were conducted with a time-step of 18 seconds. Simulation results were output from the model at an interval of 30 minutes.

The model includes one lateral inflow which is the effluent from GBWTP at Station 22.09 km. Hourly data, which included the effluent discharge and the temperature, were provided by EPCOR Utilities Inc. who operate GBWTP. The lateral inflow from all tributaries was assumed to be negligible during winter conditions. The most notable of these tributaries is Whitemud Creek which joins the North Saskatchewan at Station 3.90 km. No data is available for inflows from other urban outfalls within the study reach.
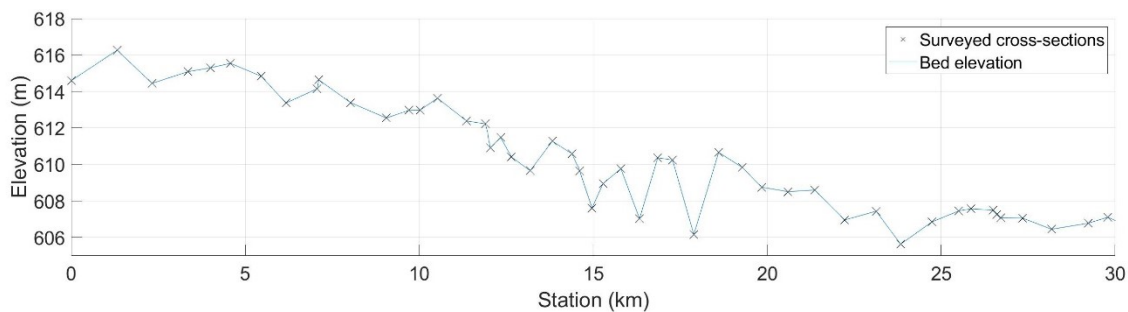
Figure 3-1. Bed profile of the study reach.

3.2.1. Upstream boundary conditions

Discharge data were not available at the upstream boundary but were available at the WSC gauge (Station 14.48 km) until 31st October in 2009 and 4th November in 2010. Daly (2013) notes that ice pans moving at or near the flow velocity have minimal effect on the flow conditions and that significant shear stresses are required to decrease the velocity of pans. As such, an open water rating curve was used to extend the discharge data, using water surface elevation data from the same WSC Gauge, until the time the surface ice concentration was observed to approach 90%.

During the 2010-11 ice season, the WSC collected direct winter discharge measurements at Hawrelak Park footbridge, Station 6.87 km, on three occasions: (i) 3rd January 2011; (ii) 1st February 2011; and (iii) 8th March 2011. Similarly, the WSC collected winter discharge measurements at the same location on three occasions during the 2009-10 ice season: (i) 7th January 2010; (ii) 3rd February 2010; and (iii) 3rd March 2010. In each ice

season, winter discharge between these points and open water conditions was estimated using linear interpolation. Subsequently, a hydropeaking pattern was artificially created, maintaining a similar magnitude to what had been observed prior to the freeze-up period.

Table 12 summarizes the average and standard deviation of the water release from the Brazeau and Big Horn reservoirs. The average release from the Big Horn Dam is almost identical between the two years and although the standard deviation is also similar, the higher value of 26.5 m^3/s suggests a hydro-peaking pattern of a slightly higher magnitude in 2010-11. The difference in statistics for the Brazeau Reservoir between the two years is significantly greater, with both a higher average release and a higher standard deviation observed in 2010-11. Owing to these differences, a hydro-peaking pattern with a greater magnitude was deemed appropriate while generating the estimated winter discharge for the 2010-11 season. Hydropeaking magnitudes of approximately $\pm$ 25 m^3/s and $\pm$ 15 m^3/s were used for the 2010-11 and 2009-10 simulations, respectively. The timing of peak and low flows was determined using water surface elevation data from the WSC gauge.

The estimated winter discharge was shifted by wave travel time (equation [3-19]), 3.86 km/hr, to the upstream boundary.

$$c = \sqrt{gD} \qquad\qquad\qquad [3\text{-}19]$$

Finally, the magnitude of the boundary condition discharge was adjusted to account for attenuation within the study reach. Peak flows were increased by 1.5% while low flows were decreased by 4%. These percentages were selected by analyzing the discharge error during open water conditions at Station 14.48 km during early calibration simulation. A plot of the discharge used as the boundary conditions are included in Figure 3-2(a) and Figure 3-3(a).

Water temperature was recorded by RTDs on a one-minute interval at the University of Alberta's chilled water systems intake, Station 10.53 km. Spikes in the dataset, caused by warm and pressurized backwater flushes, were removed. There is additional uncertainty in this data as the RTDs are inaccessible and are rarely calibrated. The raw RTD data showed the water temperature to be below 0 °C for most of the winter season. Given that

this is unlikely to be the case at the upstream boundary it was assumed that the water temperature remained at 0 °C from the time that the ice front was observed passing by the upstream boundary until the water temperature recordings exceeded 0 °C in the spring. It is assumed that there is no diffusion or temperature change between the upstream boundary of the model and Station 10.53 km. As such, this water temperature was also shifted by wave travel time to the upstream boundary for use as a boundary condition. The water temperature boundary condition used in the 2010-11 and 2009-10 simulations is provided in Figure 3-2(b) and Figure 3-3(b), respectively. The 2009-10 simulation was limited in duration owing to uncertainty in the water temperature condition at the upstream boundary. The water temperature recorded at the University of Alberta's chilled water systems intake, from which the boundary condition is based, was affected by ice during the middle of April, with temperatures recorded as low as -1.4 °C and an average temperature of -0.34 °C between 4th and 15th April 2010.

For the 2010-11 simulation, hourly images captured by a game camera positioned at the upstream boundary were visually analyzed to generate an estimate of the surface ice concentration. MATLAB image processing was used to binarize a sample of images, calculate the surface ice concentration and then to validate the visually estimated surface ice concentrations. Sample images are included in Appendix A and the time-series of the boundary condition used in the 2010-11 simulation is provided in Figure 3-2(c). A camera was not deployed at the upstream boundary during the 2009-10 winter season. As such, images from the EAS camera at Station 11.26 km were used to estimate the surface ice concentration. The surface ice concentration was then moved to the upstream boundary via wave travel time. The surface ice concentration boundary condition used in this simulation are shown in Figure 3-3(c),

The incoming suspended frazil flux was not measured and was assumed to be zero. Incoming pan thickness data were not available at the upstream boundary. Estimates of the ice pan thickness were made using equation [3-20] which was established based upon a weak relationship between the surface ice concentration and pan drafts, as measured by the SWIPS instrumentation at Station 28.55 km, and shown in Figure 3-4.

$$t_f = (0.0015 \times C_i) + 0.1209 \qquad\qquad [3\text{-}20]$$

The estimated incoming pan thicknesses used in the upstream boundary conditions are shown in Figure 3-2(d) and Figure 3-3(d).

Table 12 Release statistics for the Brazeau and the Big Horn reservoirs.

Year	Big Horn Reservoir		Brazeau Reservoir	
	Average	Standard deviation	Average	Standard deviation
	(m³/s)	(m³/s)	(m³/s)	(m³/s)
2009-10	70.9	21.3	28.6	24.1
2010-11	71.0	26.5	44.0	36.5
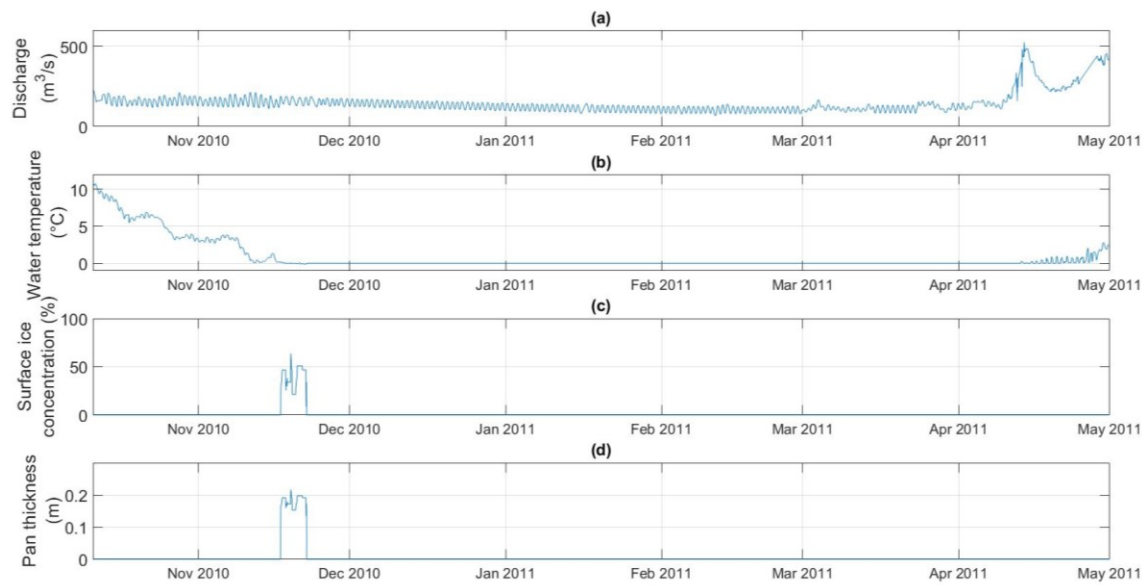
Figure 3-2. 2010-11 Upstream boundary conditions: (a) discharge, (b) Water temperature, (c) Surface ice concentration as a percentage of the channel and, (d) ice pan thickness (m).
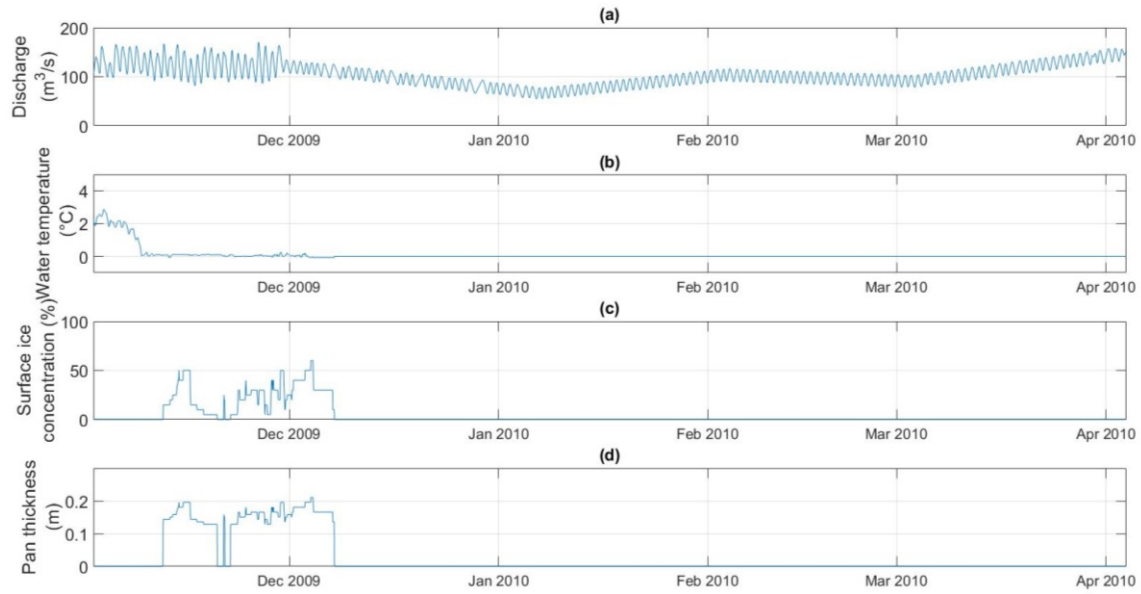
Figure 3-3. 2009-10 Upstream boundary conditions: (a) discharge, (b) Water temperature, (c) Surface ice concentration as a percentage of the channel and, (d) ice pan thickness (m).
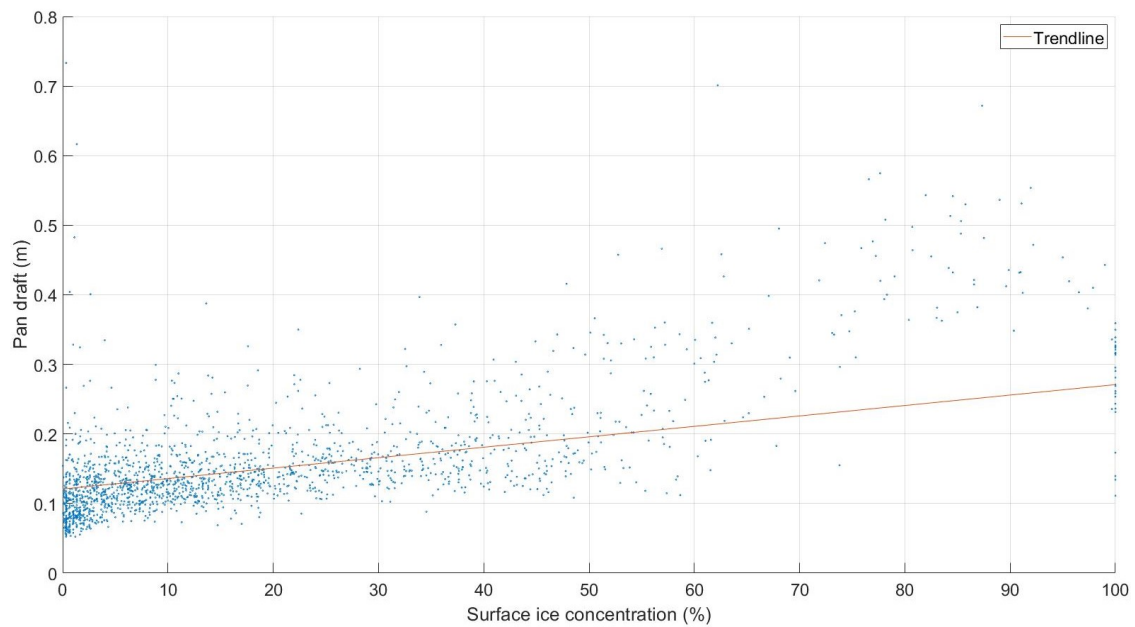
Figure 3-4. Relationship between the surface ice concentration and the pan draft as measured by the SWIPS instrumentation.

3.2.2. *Lateral inflow: GWBTP discharge and effluent temperature, 2010-11*

Figure 3-5 shows the effluent temperature and discharge data used as the GBWTP lateral inflow in the 2010-11 simulations. There is a trend of decreasing effluent temperature from October until April 2011. The mean effluent temperature for the 2010-11 winter season was 14.0 °C. The discharge pattern follows a daily trend with daily minimum discharges occurring between 07:00 and 09:00 each morning and peak discharge occurring through in the evening and early night. A mean discharge of 2.9 m³/s was recorded between 11ᵗʰ October 2010 and 1ˢᵗ May 2011.

Figure 3-6 presents the effluent temperature and discharge from GBWTP during the 2009-10 winter season. The discharge and effluent temperature from GBWTP during the 2009-10 season is comparable to that of 2010-11. Between 2ⁿᵈ November 2009 and 5ᵗʰ April 2010, the mean discharge was 2.7 m³/s and the mean effluent temperature was 13.8 °C. During the same period in 2010-11, the mean discharge was 2.8 m³/s and the mean effluent temperature was 13.8 °C. The daily discharge pattern was also similar during the two seasons.
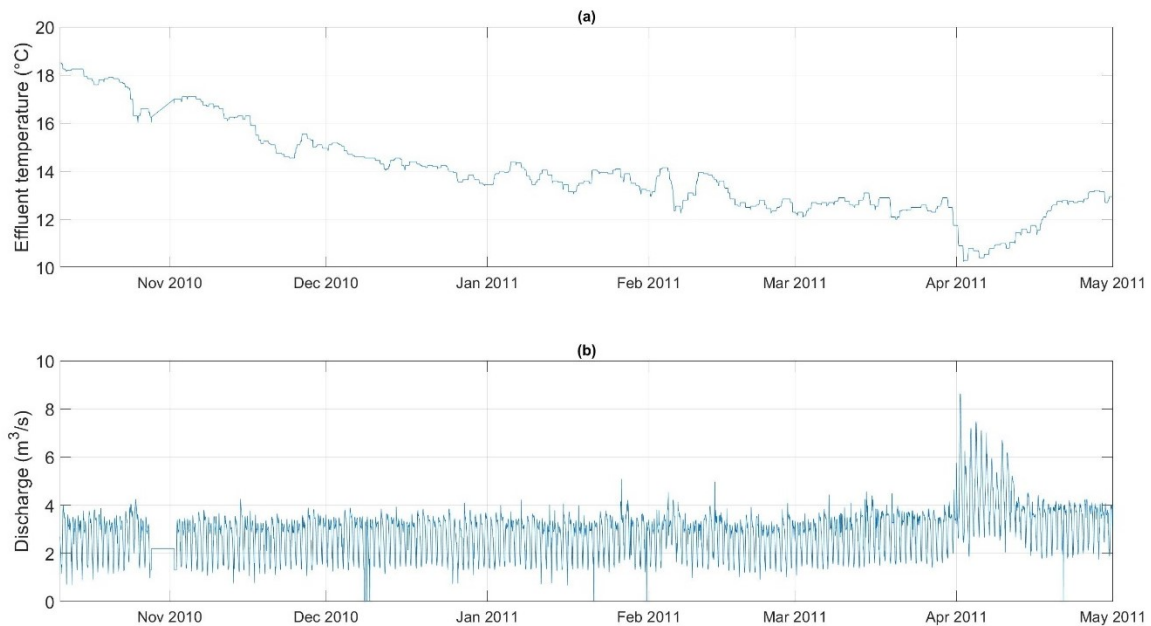
Figure 3-5. 2010-11 GBWTP (a) effluent temperature, and (b) outflow discharge.
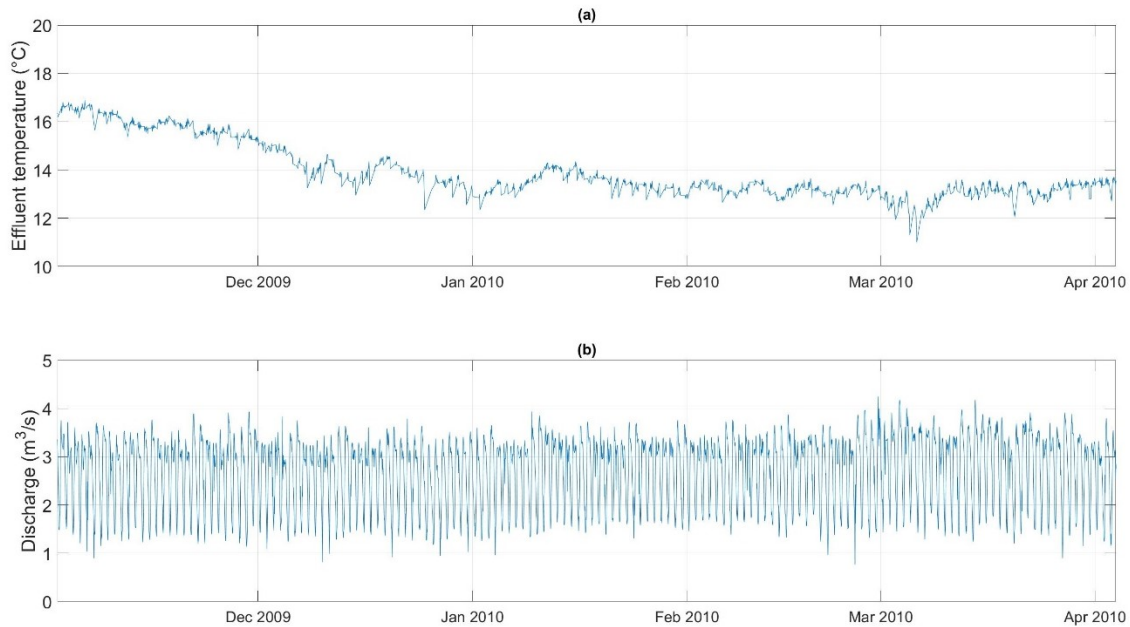
Figure 3-6. 2009-10 GBWTP (a) effluent temperature, and (b) outflow discharge.

3.2.3. *Meteorological data: air temperature and solar radiation*

Air temperature data was collected at two locations during the 2010-11 winter season. The University of Alberta's Weather Station, adjacent to Station 11.26 km, collected air temperature data on an hourly interval and a Campbell monitoring station deployed on the right bank of the river at Station 28.55 km collected air temperature data on a 5-minute interval. It was assumed that the air temperature collected by the Campbell monitoring station, which was situated in the river valley, would provide a more accurate representation of the conditions at river level. A simple sensitivity analysis showed greater agreement between the simulated and observed water temperatures when data from the Campbell monitoring station was used rather than when the University of Alberta's air temperature data was used. The Campbell monitoring station was removed from the study site on 31st March 2011. For the period between 31st March and 30th April 2011 air temperatures from the EAS Weather Station were used. The average air temperature during the simulation period was -6.0 °C.

Solar radiation data was only available from the University of Alberta's Weather Station. An albedo value of 0.15 was applied to the raw solar radiation data. Owing to the depth of the river valley and growth of coniferous trees along the riverbanks, shading effects

along the NSR are significant. This is especially true during the winter months when the sun's declination angle is greater. These shading effects are exacerbated in sections of the river that flow laterally from west to east. To accommodate this in the simulations, the model was divided into two atmospheric zones based upon channel orientation. A shading factor of 0.18 was applied to the solar radiation data in the shaded atmospheric zone. The average solar radiation for zone1 and zone2 was 68.4 W/m^2 and 56.3 W/m^2, respectively.

Air temperatures from the Campbell monitoring station, which was again deployed at Station 28.55 km, were used in the 2009-10 simulation. EAS Weather Station air temperatures were used from the time the Campbell monitoring Station was removed on 13th January 2010 until the end of the simulation on 5th April 2010. The average air temperature during the simulation was -5.4 °C and the average solar radiation in atmospheric zones 1 and 2 were 28.7 W/m^2 and 23.6 W/m^2, respectively. For comparison, during the same period, the air temperature in 2010-11 was -9.2 °C while the solar radiation in atmospheric zones 1 and 2 were 52.1 W/m^2 and 42.9 W/m^2, respectively.
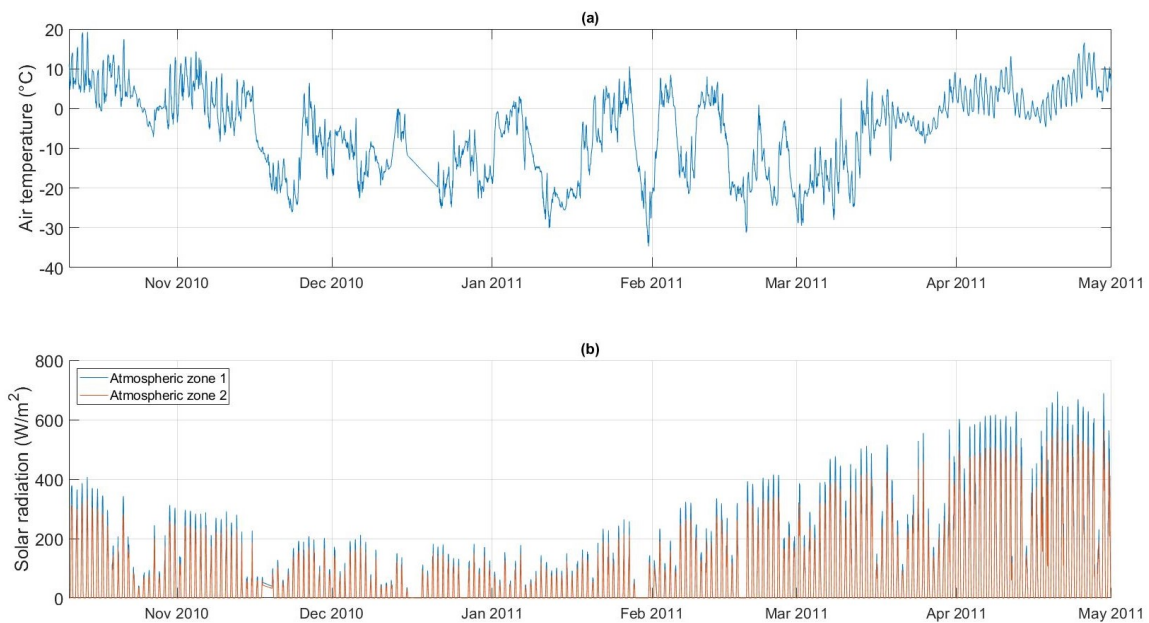
Figure 3-7. Meteorological conditions used in the 2010-11 simulations: (a) air temperature and (b) solar radiation.
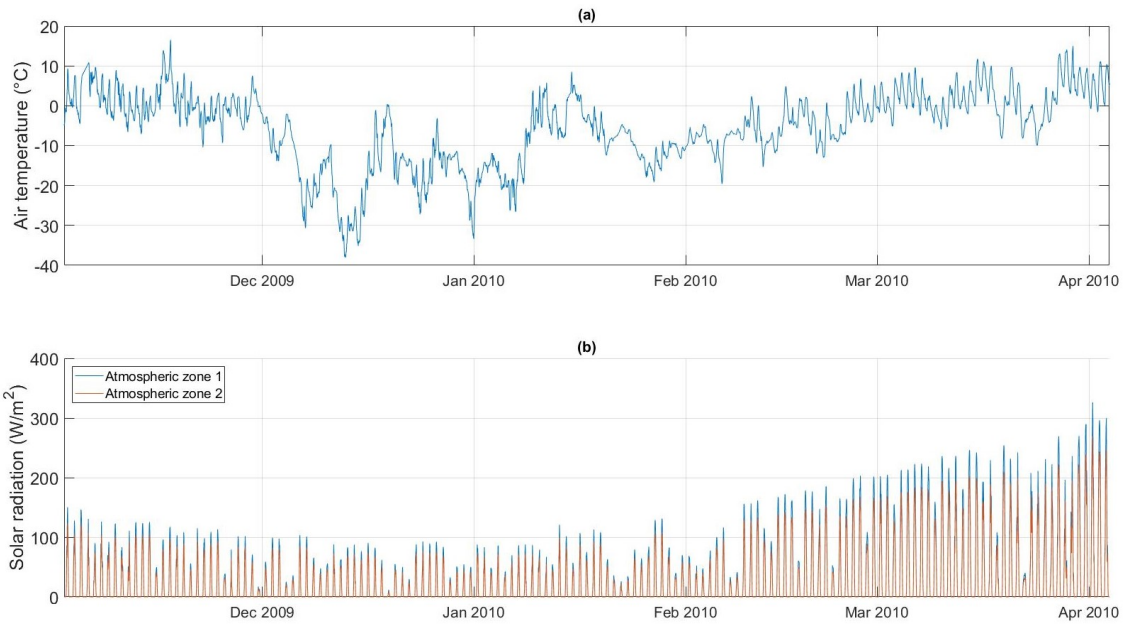
Figure 3-8. Meteorological conditions used in the 2009-10 simulations: (a) air temperature and (b) solar radiation.

3.2.4.   Parameter values

Table 13 provides a complete list of the parameter values used in model simulations. Parameter values were calibrated for the NSR so that simulated results best matched observed data. The value used in this study for new frazil pan thickness is lower than values previously used in the literature but is justified by the average pan draft of 0.14 m measured by the SWIPS instrumentation. Finally, the value for h_{ia} was increased slightly from 12 W/m²/°C as used in the Linear Heat Transfer model, Section 2.4.10, to 14 W/m²/°C as this provided a slightly improved performance in simulating the timing of break-up.

Table 13. Adopted parameter values for River1D simulations.

Parameter name	Adopted value	Values in literature
Albedo, α	0.15	0.05 – 0.15 (Hicks 2016)
Linear heat transfer coefficient, h_{wa} (W/m²/°C)	14	8 – 20 (Andres 1988)
Linear heat transfer coefficient, h_{ia}	12	10 – 20 (Ashton 2011)

(W/m^2/°C)		
Rate of frazil rise, η (m/s)	0.001	0.0001 – 0.001 (Timalsina et at 2013)
Porosity of frazil slush, p_f	0.6	0.43 – 0.85 (Hicks 2016)
New frazil pan thickness, t'_f (m)	0.14	0.3 (She et al. 2012)
Maximum fraction of channel covered by border ice	0.75	0.7 (Blackburn & She 2019)
Maximum velocity for dynamic border ice growth, U_{cr} (m/s)	0.8	0.4 – 1.2 (Lal and Shen 1991)
Max Froude number for ice front progression	0.13	0.08 - 0.13 (Ashton 1986)
Porosity between ice floes at the ice front	0.6	0.6 (Jasek et al. 2011)
[γ]Density of ice, ρ_i (kg/m^3)	917	917 (Lal and Shen 1991; Comfort and Abelnour 2013)
[γ]Frazil seeding concentration, C_{fo} (%)	0.00001	
[γ]Typical frazil particle thickness, d_e (m)	0.0003	0.0003 (Wang et al. 1995) 0.00013 (Malenchak 2011)
[γ]Typical frazil particle radius, r_o (m)	0.001	0.00012 - 0.00146 (McFarlane, 2014) 0.0005 - 0.0015 (Andrishak and Hicks, 2005) 0.001 (Wang et al., 1995)
[γ]Nusselt number for typical suspended particle, $\boldsymbol{N_u^f}$	4.0	4.0 (Wang et al., 1995; Malenchak, 2011)
[γ]Coefficient of turbulent heat exchange	1187	1187 (Ashton, 1973; Andrishak and Hicks, 2008)
[γ]Rate of surface ice re-entrainment, β_{re} (1/s)	0.00001	0.00001 (Wang et al., 1995; Malenchak, 2011)
[γ]Re-entrainment velocity threshold, U_{i_re} (m/s)	1.06	1.06
[γ]Solid ice initial thickness, t'_{si} (m)	0.001	0.001 (Lal and Shen, 1991)
[γ]Frazil particle shape factor	1.0	1.00 ± 0.03 (Beltaos, 2013)
[γ]Average diameter of frazil granules in	0.01	0.01 (Shen and Wang, 1995)

coverload, (m)		
$^\gamma$Critical flow strength for undercover transport	0.041	0.041 (Shen and Wang, 1995)
$^\gamma$Porosity of anchor ice, p_a	0.4	0.4 (Malenchak, 2011) 0.47 (Jasek, 2016)
$^\gamma$Frazil accretion rate, γ (m/s)	0.00001	0.01 – 0.00001 (Malenchak, 2011; Timalsina et al., 2013)
$^\gamma$Fraction of bed covered by anchor ice, C_{an}	0.25	-
$^\gamma$Bed material average diameter, d_s (m)	0.05	-
$^\gamma$Density of bed material, ρ_s (kg/m^3)	2650	-
$^\gamma$Border ice equation coefficient a	14.1	14.1 (Michel et al., 1982)
$^\gamma$Border ice equation coefficient b	1.08	1.08 (Michel et al., 1982)
$^\gamma$Border ice equation coefficient c	-0.93	-0.93 (Michel et al., 1982)
$^\gamma$Border ice equation coefficient e	9.75	
Maximum fraction of channel covered by border ice, f_b	0.75	0.7 (Blackburn and She, 2019)
Maximum velocity for dynamic border ice growth, U_{cr} (m/s)	0.8	0.4 (Lal and Shen, 1991; Malenchak, 2011) 1.2 (Michel et al., 1982)
$^\gamma$Maximum Froude number for juxtaposition	0.06	0.04 (Wang et al., 1995) 0.06 (Lal and Shen, 1991)
Porosity of newly formed ice cover, p_i	0.4	0.6 (Blackburn and She, 2019) 0.6 (Jasek et al., 2011)
$^\gamma$Ice to ice friction coefficient	1.28	1.28 (Pariset and Hausser, 1961; Pariset et al., 1966; Lal and Shen, 1991)
$^\gamma$Ice cohesion	700	700 (Calkins, 1984)
$^\gamma$Ice cover to open water solar radiation ratio	0.85	-

$^\gamma$Parameter value adopted from Blackburn and She (2019).

3.3. Model calibration (2010-11)

3.3.1. Open water calibration

The model was first calibrated for open-water conditions by adjusting the Manning's roughness values of the channel bed for four regions within the model reach. The calibrated roughness values range from 0.030 - 0.034. This is a slight increase on the values used by NHC (2007) and IDG (1995) in their respective Flood Risk Mapping Studies. Open water simulation performance was assessed quantitatively using water level data from Stations 14.48 km, 21.32 km, 22.51 km and 28.84 km. During the open water simulation period of 13th October to 4th November 2010, the simulated water level remained within 0.06 m of the observed. This calibration tolerance was deemed acceptable given uncertainty relating to the datum of the depth recording equipment, two-dimensional flow effects and potential errors in measuring water levels.
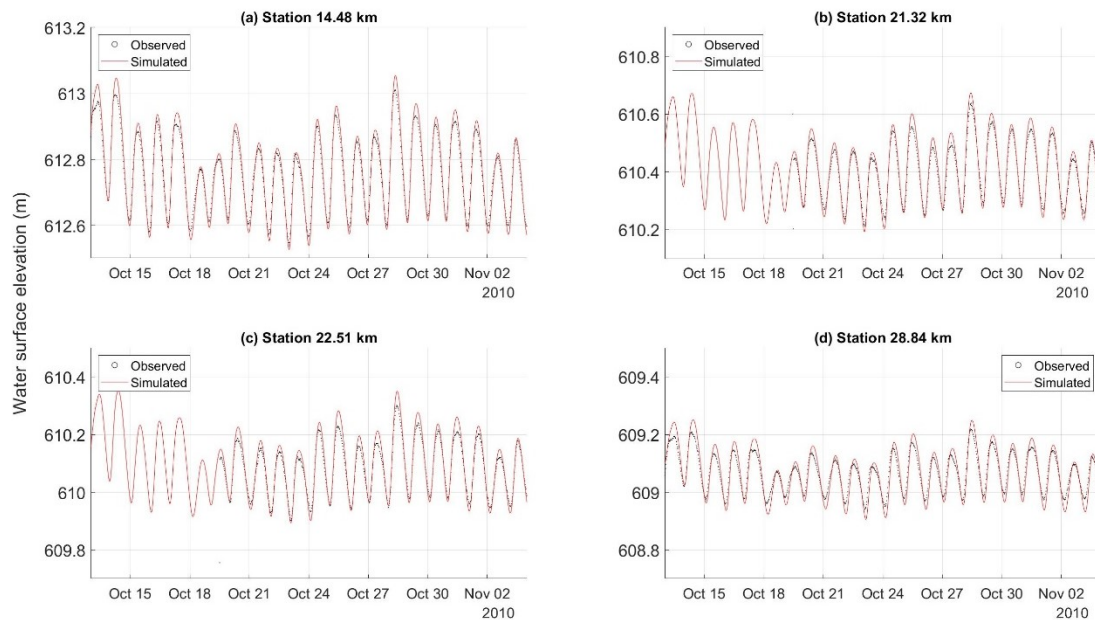
Figure 3-9. Observed and simulated water surface elevations between 13th October 2010 and 4th November 2010 at (a) Station 14.48 km, (b) Station 21.32 km, (c) Station 22.51 km, and (d) Station 28.84 km.

3.3.2. Water temperature

Calibration of the heat transfer coefficient, h_{wa}, was essential in achieving strong agreement between the observed and simulated water temperatures. Several values were

selected from the range of reasonable values, 8 – 20 W/m^2/°C, published in the literature (Andres 1988). With a value of 14 W/m^2/°C, the model was able to accurately capture the timing of the zero-degree isotherm. The additional terms, j_{wa} and k_{wa}, included in the linear heat transfer model, equation [3-6], were set to zero as they did not improve model performance.

Figure 3-10 presents the simulated water temperatures at Stations 10.53 km, 21.32 km, 22.51 km, 28.02 km, 29.55 km and 28.84 km. These simulated water temperatures are compared with the observed water temperatures as captured by an RTD in the University's chilled water systems intake at Station 10.53 km, Mini-Divers at Stations 21.32 km, 22.51 km, 28.02 km and 28.84 km and the SWIPS at Station 28.55 km.

During freeze-up, the model performed exceptionally well at Stations 10.55 km, 28.02 km, 28.55 km and 28.84 km, with R^2 values greater than 0.94 and RMSEs of between 0.15 °C - 0.45 °C. At these locations, the model closely replicated the cooling trend of the observed data and also accurately captured the point of the zero-degree isotherm, at which water temperatures dropped to 0 °C. The strong performance at Station 10.53 km is to be expected given that the observed data was shifted by wave travel time to form the upstream boundary condition (see Section 3.2.1).

The observed cooling trend at Station 21.32 km was also well replicated by the model until 16th November as shown in Figure 3-10b. At this time, the simulated water temperature dropped to 0 °C while the observed data stabilized between 0.4 °C and 0.6 °C. The observed water temperature was not recorded as having dropped as low as 0 °C during the entire deployment period. The author is not aware of any outfalls or other urban features which contribute warm water upstream of this location. According to the manufacturer specifications, the Mini-Diver which recorded the water temperature at this location, has a temperature accuracy of ± 0.1 °C. However, Maxwell (2012) noted that the Mini-Divers did not perform within the manufacturer specifications and as such there is some uncertainty in the water temperature data collected by the Mini-Diver's.

At station 22.51 km, Figure 3-10c, the observed water temperature was collected by a Mini-Diver located towards the right bank of the river and within the effluent plume of

GBWTP. Figure 3-13, an aerial image showing the surface ice conditions around Station 23.46 km on 24th January 2010, clearly shows that upstream of Station 23.46 km, the effluent plume and open lead are confined to a narrow portion of the river along the right bank. In this area the water temperature is clearly two dimensional and as such, River1D should not be expected to perform well at this location.

There is evidence that the warm effluent discharged from GBWTP remained somewhat confined to the right bank for at least 6 km downstream. Two Mini-Divers were deployed at Station 28.02 km, with one Mini-Diver located adjacent to the banks on either side of the river. Figure 3-10d shows the observed and simulated water temperatures at Station 28.02 km for the entire season. During the mid-winter period, defined as the period between freeze-up and break-up, the mean and maximum water temperatures observed near the left bank were 0.03 °C and 0.04 °C, respectively. Following freeze-up, the observed water temperature along the left bank remained consistently at ~0.03 °C. For the same period, the mean and maximum water temperatures observed near the right bank, within the effluent plume of GBWTP, were 0.42 °C and 1.38 °C, respectively. Except when the simulated water temperature was 0 °C, the simulated water temperature fit between the water temperatures observed by the Mini-Divers on either side of the river. This pattern is clearly visible in Figure 3-11 which shows the simulated and observed water temperatures at this station for a short duration in January 2011.

During the mid-season period the water temperatures simulated by the model were consistent at 0 °C for stations upstream of GBWTP, where a stable ice cover remained in place. This is apparent in the plots showing the water temperatures at Stations 10.52 km and 21.32 km (Figure 3-10a and b). Downstream of GBWTP, at Stations 22.51 km, 28.02 km, 28.55 km, and 28.84 km (Figure 3-10c, d, e and f), the simulated water temperatures remained within a range of 0 - 1 °C. However, fluctuations in the water temperature were also simulated. These fluctuations followed the trends in the effluent temperature and discharge.

When compared to the observed data at Stations 28.02 km, 28.55 km and 28.84 km, the model performed well in capturing the warming and cooling trends during the mid-winter period, but generally underestimated the water temperatures. This underestimation is

caused by the limitation of using a one-dimensional (1D) model in a reach where the water temperature is two-dimensional (2D). An example of the model capturing the trend of the observed water temperature at Station 28.02 km is provided in Figure 3-11. The simulated water temperature rises with the water temperature data collected along the right bank between 19th January and 28th January, but the simulated water temperature is generally in the region of 0.40 °C to 0.75 °C lower than the observed.

It is not possible to assess the performance of the model in simulating water temperatures during break-up. There is a large degree of uncertainty in the observed water temperature at Station 10.53 km during break-up given that warm water backflushes, designed to clear suspended frazil ice from the water intake, have been removed from the data. The Mini-Divers and SWIPS instrumentation were removed from the river prior to the end of March 2011 and as such, there is no data to which the simulated results can be compared. Break-up did not occur until 9th – 11th April 2011. It is interesting to note that a pattern of increasing simulated water temperatures are apparent during the day from 5th April 2011, as shown in Figure 3-10.

Figure 3-12 shows the simulated water temperatures at Stations 0.00 km, 6.87 km, 10.53 km, 21.32 km, 22.51 km, and 28.55 km. There is little variation in the water temperatures throughout the study reach, with the exception of the aforementioned mid-season fluctuations in water temperatures downstream of GBWTP.
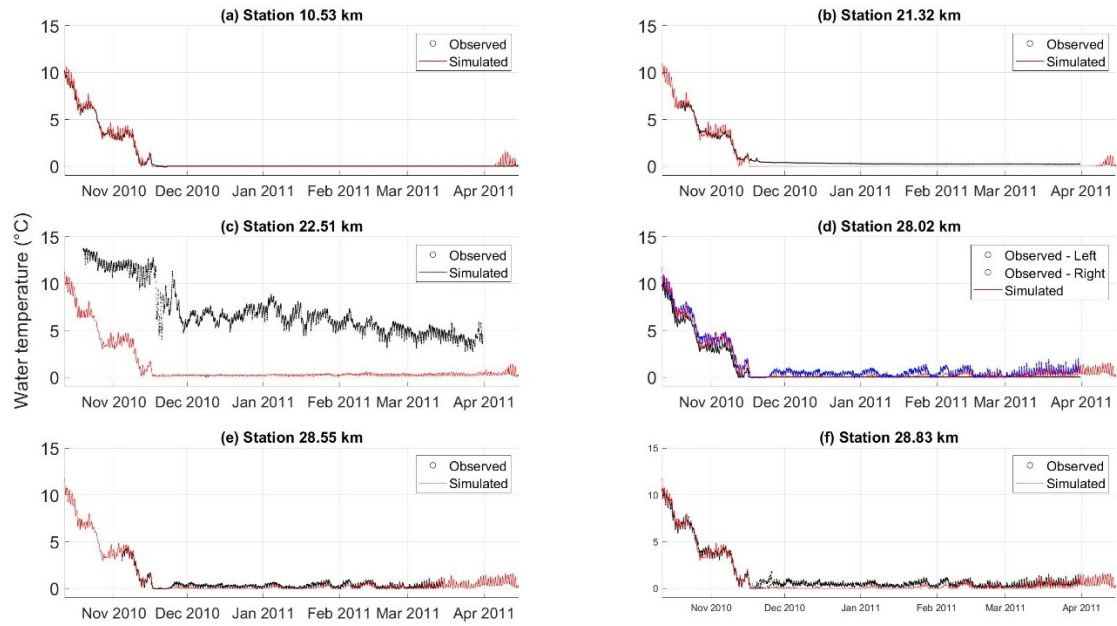
Figure 3-10. Observed and simulated water temperatures for the 2010-11 season at Stations a) 10.53 km, b) 21.32 km, c) 22.51 km, d) 28.02 km, e) 28.55 km, and f) 28.84 km.
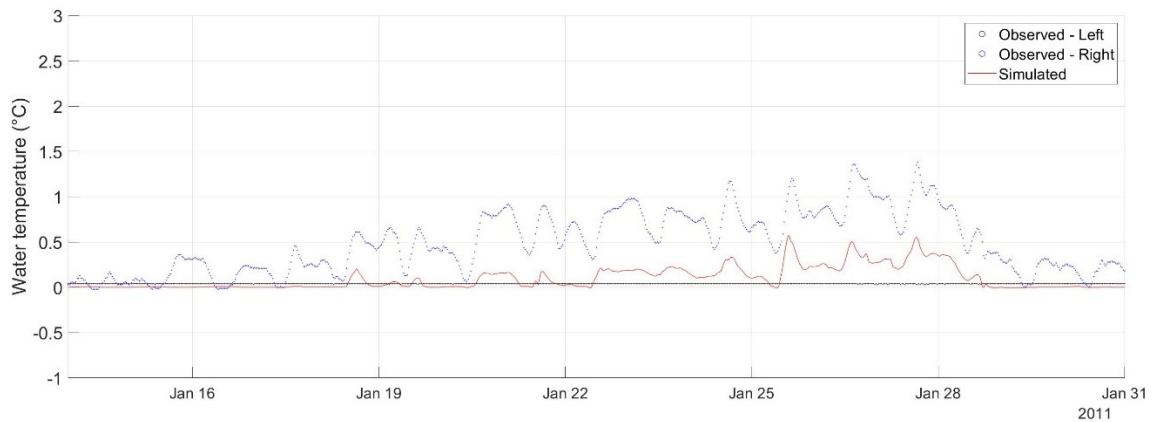
Figure 3-11. Simulated and observed water temperatures at Station 28.02 km between 14th January and 31st January 2011.
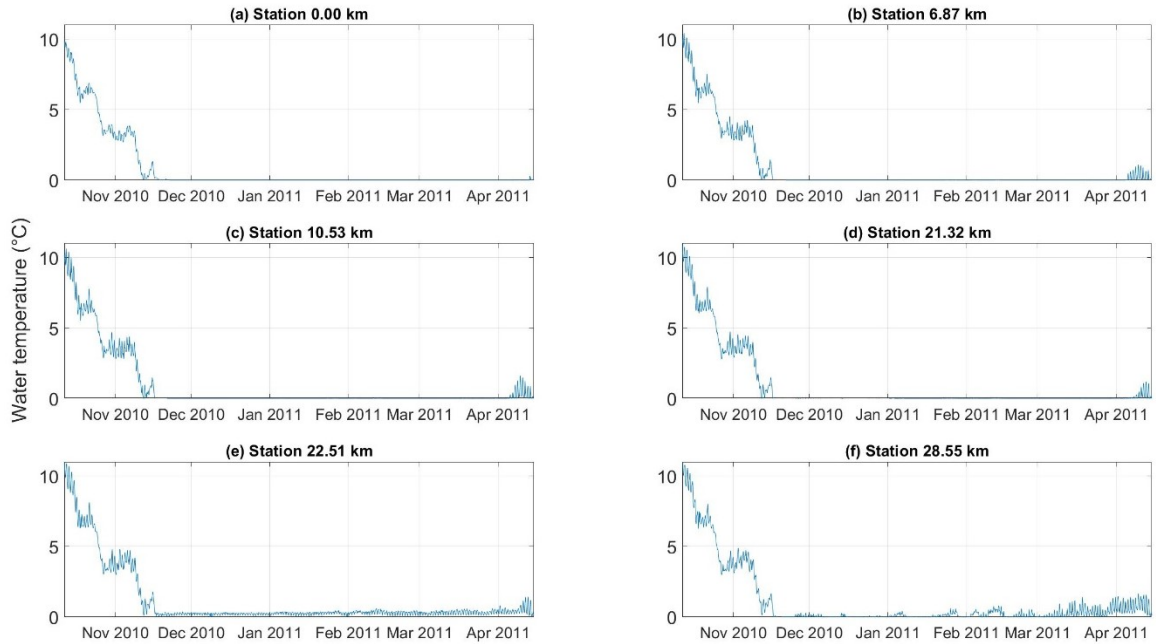
Figure 3-12. Simulated water temperatures at Stations (a) 0.00 km, (b) Station 6.87 km, (c) Station 10.53 km, (d) Station 21.32 km, (e) Station 22.51 km and (f) Station 28.55 km.

Figure 3-13. Aerial image showing the surface ice conditions in the area of Station 23.46 km on 24th January 2010. Photo credit: Tadros Ghobrial & Joshua Maxwell.

3.3.3. Ice front propagation

It was identified that accurately simulating the ice front progression would be necessary for the model to perform well in simulating both stage-up and the surface ice concentration. A strong performance in simulating the ice front progression was achieved by setting the maximum Froude number for ice front progression to 0.13. This is at the upper limit of the range of values, 0.08 – 0.13, published in the literature (Ashton 1986). Several other parameters were identified as having a smaller effect on the rate of ice front progression. Among these parameters were the frazil slush porosity, which was set to 0.6, and the maximum velocity for border ice growth, which was set to 0.8 m/s. The sensitivity of the simulated ice front progression to several model parameters is discussed in further detail in Section 3.5.1.

In addition to the model parameters, the ice front propagation was sensitive to the timing and location of the user-defined bridging events. The timing and exact location of bridging events were not recorded in 2010. However, approximate bridging locations were identified from the aerial photographs taken during a flight over the study reach on 3rd December 2009 (Maxwell et al. 2011; Ghobrial et al. 2013). It is known that bridging typically occurs at the same locations each year (Beltaos 1995). The aerial images indicated that up to 7 bridging locations may exist within the modeling study reach (Table 3), with several of these bridging locations are in close proximity to one another. To avoid adding unnecessary complexity, only three bridging locations were included in the model. The first bridging location is at the model's downstream boundary, Station 39.35 km, enabling the ice front to progress into the study reach. A second bridging location was included at Station 18.37 km, where significant border ice growth and constriction of the channel is known to occur as shown in Figure 2-5e. A third bridging location was included at Station 14.01 km, between the two suspected bridging locations at Station 15.24 km and 13.48 km where ice pan congestion occurs around two bends in the river as shown in Figure 2-5g and Figure 2-5h. These locations were selected to best represent the bridging locations throughout the study site. The omission of additional nearby bridging locations was assumed not to significantly affect the simulated ice front progression.

The timing of bridging events was estimated based on the ice front progression as observed by game cameras installed at the upstream boundary and at Stations 11.26, 13.04, 21.56, 28.02, 28.55 and 28.84 km. The bridging events used in the 2010-11 simulation are given in Table 14.

Figure 3-14 shows the simulated ice front propagation, along with the points at which the front was observed by the river-side cameras. The simulated front passed within 11.5 hours of the observed ice front at each of the observed data points. Model performance at Stations 28.55 km and 13.04 km was exceptionally strong with the simulated ice front passing within 30 minutes of the observed. On average, the discrepancy between the simulated and observed ice fronts was 4.5 hours.

The average simulated progression through the study reach was 12.20 km/day. This is comparable to the observed front progression rate of 11.57 km/day through the same reach. Included in Table 15 are the observed and simulated front progression rates for pre-defined regions of the study reach (see Section 2.4.5). It is notable that the simulated ice front progression rate is more consistent than the observed when comparing the different regions. The simulated ice front propagated faster than the observed through regions C and E but was slower through regions B and D. Regions A and F cannot be compared as these regions are not entirely contained within the modeling study reach.

It would be reasonable to expect some improvement in the timing of the simulated front propagation through the reach if the precise bridging locations and times had been recorded and more robust data were available for the upstream boundary condition. In the model, bridging at Station 14.01 km was delayed until 2.5 hours after the user defined bridging time. This is because the Froude number at this location exceeded the parameter value for the maximum Froude number for ice front progression until the downstream ice front approached.

Figure 3-15 shows the location of the three simulated ice fronts over the entire winter season. Much of the monitoring equipment, including all cameras except those at Stations 11.26 km and 13.04 km were removed prior to break-up in April 2011. As such, there are fewer data points with which to assess the model's performance in simulating the ice

front retreat. The simulated ice front retreat at Stations 11.26 km and 13.04 km were 6.0 days and 4.6 days late, respectively. The model performed well when compared to the Linear Heat Transfer Model, discussed in Section 2.4.10, which predicted break-up 9 days late at Station 11.26 km.

In the model, Stations 11.26 km and 13.04 km are both within the reach affected by ice front 3 (noted in Figure 3-15) which was initiated by bridging at Station 14.01 km. This ice front extended to the upstream boundary where the decay of the ice cover was halted for a period of approximately 7.5 days beginning on 6th April 2011, as shown in Figure 3-16(a). This delay in ice decay is attributed to uncertainty in the water temperature used as the upstream boundary condition which was fixed at 0 °C until the morning of 13th April 2011. In River1D, each of the ice fronts must retreat from the upstream end of the front location and thus the retreat of Ice front 3 did not occur until the simulated ice cover at the upstream boundary had completely melted. This was not simulated until 15th April 2011. Once the ice thickness at the upstream boundary had reduced to zero the retreat of the simulated ice front to the bridging location at Station 14.01 km happened in under 30 minutes.

Investigating the simulated ice thickness and the time at which the simulated ice thickness had completely melted offers an alternative method for assessing the model's performance in simulating break-up. Figure 3-16b and c show time-series plots of the ice thickness during early April at Stations 11.26 km and 13.04 km. At Station 11.26 km, the simulated ice thickness dropped to 0 m at 19:30 on 9th April 2011, only 4.5 hours after the time of observed break-up. The simulated ice thickness at Station 13.04 km dropped to 0 m at 11:00 on 11th April 2011, approximately 11 hours after break-up was observed at this station. This indicates that the model is capable of simulating break-up with a high degree of accuracy but also highlights areas for improvement in the upstream boundary condition and in simulating ice front retreat.

The remaining two ice fronts, which were instigated by bridging at Stations 18.41 km and the model's downstream boundary, were more gradual in their retreat. Ice front 1 (shown in Figure 3-15) retreated at a rate of 3.02 km/day while ice front 2 retreated at a rate of 1.44 km/day.

Once the ice front progression had been simulated with a reasonable degree of accuracy, little calibration of the other parameters was required to achieve good agreement between simulated and observed values for the remaining variables.

Table 14. Location and timing of estimated bridging events, 2010-11.

Bridging location (km)	Time of bridging
39.35	18-Nov-2010 22:30
18.37	20-Nov-2010 17:00
14.01	20-Nov-2010 23:00

Figure 3-14. Simulated ice front propagation, freeze-up 2010-11.

Table 15. Observed and simulated ice front progression rates through defined regions A-F during freeze-up 2010-11.

Region [†]	Station (km)	Observed ice front progression rate (km/day)	Simulated ice front progression rate (km/day)
A	N/A	8.2	(outside model study reach)
B	0 - 11.26	14.2	10.60
C	11.26 – 14.48	3.9	11.89
D	14.48 – 21.32	30.7[‡]	12.59
E	21.32 – 28.55	11.6	23.97
F	N/A	11.8	(outside model study reach)

[†] Regions are shown in Figure 2-2.

[‡] Affected by bridging.
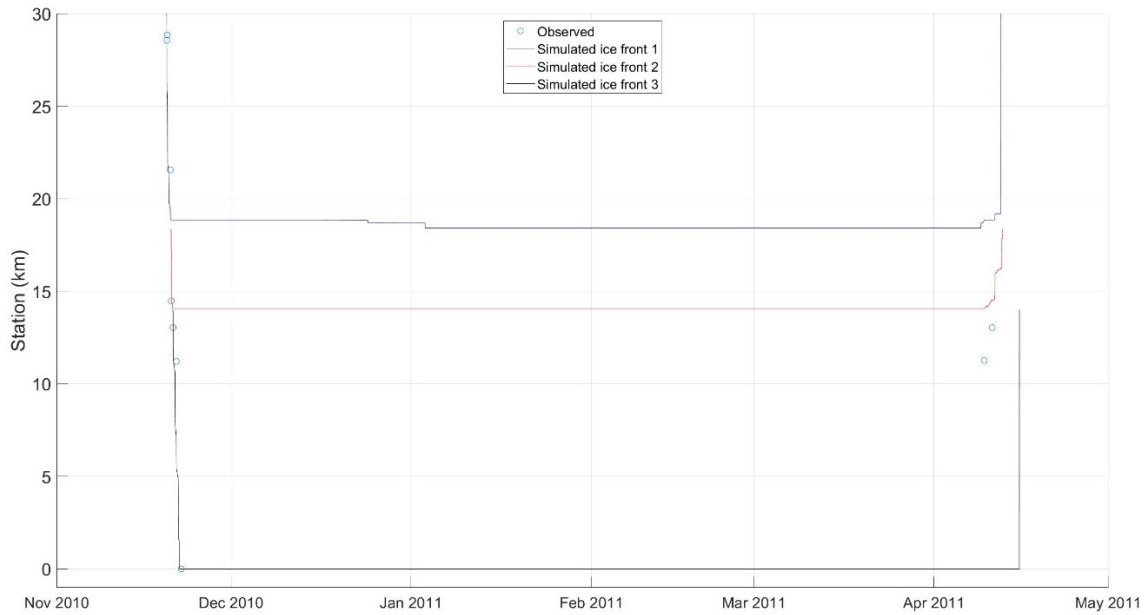
Figure 3-15. Simulated ice front locations for the entire season, 2010-11.
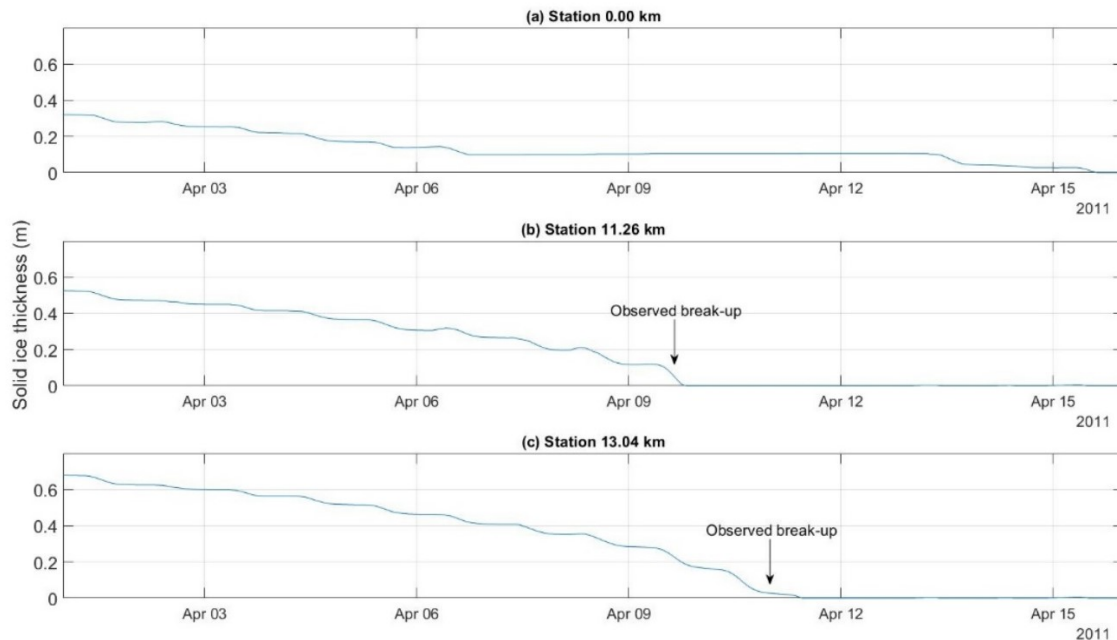
Figure 3-16. Simulated ice thicknesses during break-up at (a) Station 00.00 km, (b) Station 11.26 km, and (c) Station 13.04 km.

3.3.4. Border ice

The simulated border ice fractions are compared with the observed border ice fractions which were visually estimated from images captured at Stations 11.26 km, 13.04 km, 21.46 km, 28.02 km, 28.55 km and 28.84 km. The results are displayed in Figure 3-17. The timing of border ice growth in the model was very accurate. Except at Station 28.02 km, where the simulated border ice growth occurred approximately 18 hours later than the observed, the growth of border ice in the model occurred at the same time as the observed. There was a tendency for the model to underestimate the fraction of the channel occupied by border ice, especially at Stations 13.04 km, 21.46 km, 26.88 km and 28.84 km.

Following freeze-up, simulated border ice fractions remained stable, as should be expected, until break-up. It is notable that the model simulated a local variation in the timing of border ice retreat between Stations 28.02 km, 28.55 km and 28.84 km. The border ice fraction at the former two stations reduced to zero in the middle of February while the border ice fraction at Station 28.84 km remained at a value of approximately 0.07 until reducing to zero in mid-March.

Figure 3-18 is a time-series plot of the simulated border ice thickness at Stations 11.26 km, 13.04 km, 21.46 km, 28.02 km, 28.55 km and 28.84 km. The model utilizes the wedge-shaped border ice concept is utilized in the model and as such the border ice thickness shown in Figure 3-18 is for the thickest section of the border ice at each station. The growth rate for border ice, from the onset of growth to the global peak, was consistent at each of these stations at 0.9 – 1 cm/day. Peak thickness at stations downstream of GBWTP was significantly less than upstream and occurred 64 days after the beginning of growth while peak thickness at stations upstream of GBWTP occurred after 116 days of growth. Similarly, border ice decay began much sooner at stations downstream of GBWTP than those upstream. This resulted in slightly lower decay rates of 2.5 cm/day at stations downstream of GBWTP as compared to an average of 2.9 cm/day at stations upstream of GBWTP. There was a second growth of border ice growth at Station 28.84 km beginning on 15th February 2011. This border ice remained in place until 17th March 2011.
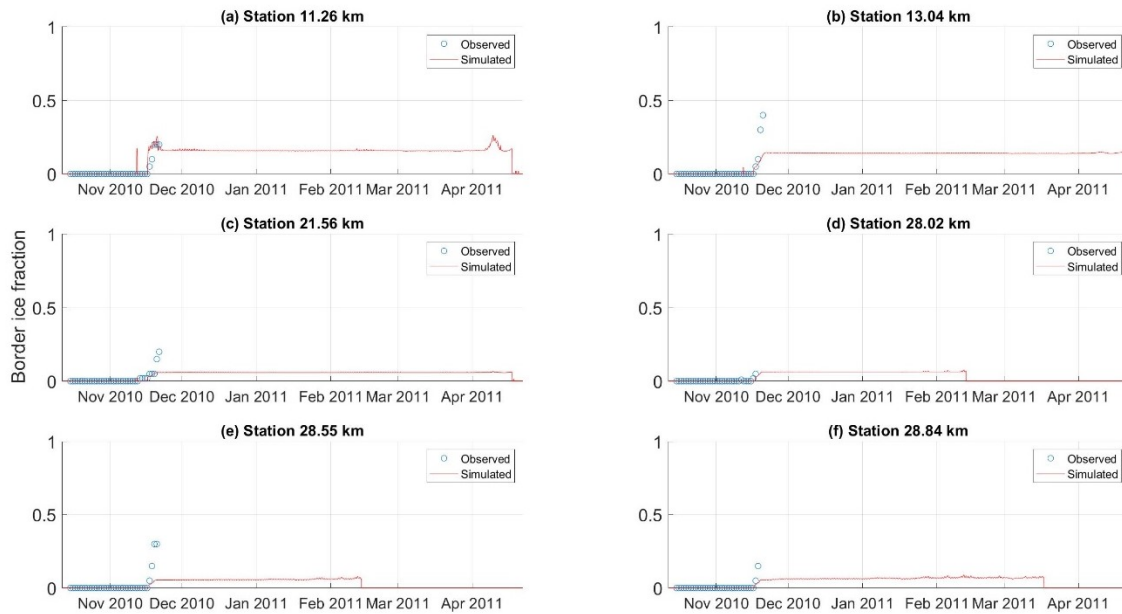
Figure 3-17. Simulated and observed border ice fractions at (a) Station 11.26 km, (b) Station 13.04 km, (c) Station 21.56 km, (d) Station 28.02 km, (e) Station 28.55 km, and (f) Station 28.84 km.
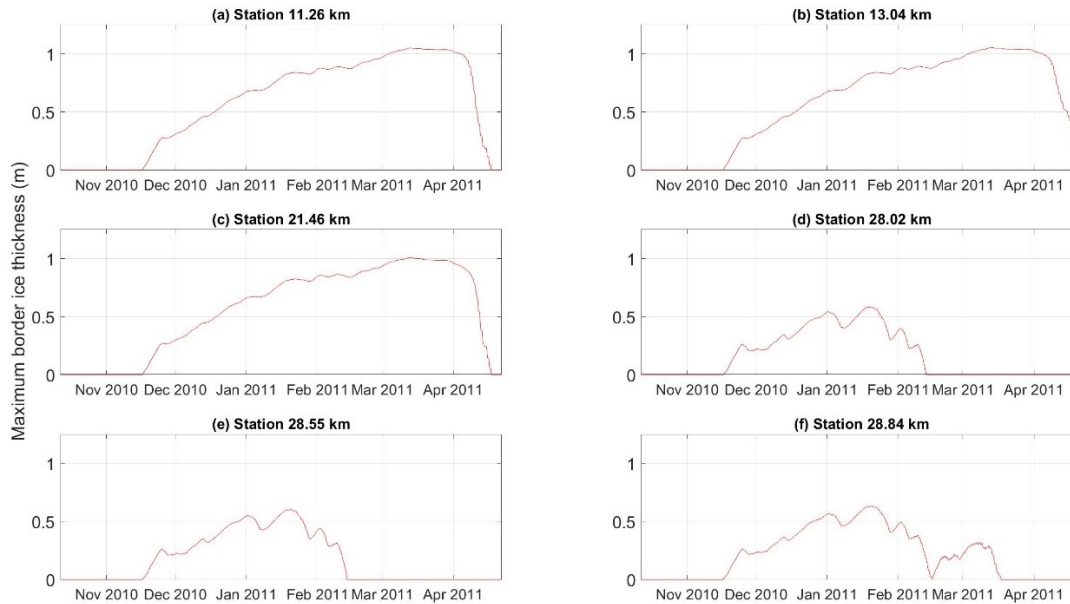
Figure 3-18. Simulated maximum border ice thickness at (a) Station 11.26 km, (b) Station 13.04 km, (c) Station 21.56 km, (d) Station 28.02 km, (e) Station 28.55 km, and (f) Station 28.84 km.

3.3.5. *Suspended frazil concentration*

Figure 3-19a shows the simulated suspended ice concentration at Station 14.48 km. Suspended ice was simulated at this location prior to freeze-up and to a lesser extent, following break-up. The simulated suspended concentration ranged between 0.001% and 0.061% and is close to the range of suspended ice concentration values obtained by the SWIPS at Station 28.55km and also close to the range of 0.005% to 0.033% obtained by the SWIPS deployed by Jasek et al. (2011) on the Peace River. At Station 14.48 km, surface ice concentration reached 100% at 20:00 on 20th November 2010 yet the model results show suspended ice concentration until 17:00 on 21st November 2010. It seems unlikely, due to the insulating effects of a surface ice cover, that the suspended frazil simulated by the model was produced by heat loss at this location. Surface conditions remained open upstream of Station 14.48 km, with the ice front propagating to the upstream boundary on 22nd November 2010. Thus, it is likely that the simulated suspended frazil at Station 14.48 km between 20:00 on 20th November and the 22nd November was produced upstream and then carried downstream in the flow.

Simulated concentrations of suspended frazil ice were compared with the observed results collected by the SWIPS instrumentation at Station 28.55 km, as shown in Figure 3-19b. During the freeze-up period, the simulated suspended frazil concentrations are of the correct order of magnitude when compared to the observed. Suspended ice concentrations measured by SWIPS instrumentation have previously been compared to modeled results during a study of the Peace River by Jasek et al. (2011). In that study, CRISSP1D overestimated suspended frazil concentrations by approximately 1 order of magnitude. As such, it is encouraging to see River1D's strong performance in simulating suspended frazil concentrations of the correct order of magnitude. The timing of the increases in suspended ice concentration is also very good; the first simulated peak on 17th November 2010, begins to rise within an hour of the observed rise in suspended frazil concentration.

Following freeze-up, the model returned a suspended frazil concentration of 0% for most of the simulation. However, small, isolated spikes of less than 0.01% suspended frazil concentration were simulated, for example on 1st December 2010 and 7th January 2011. Except for two events in January 2011 which occurred under air temperatures of -11.06 °C and -8.51 °C, each of the post freeze-up spikes in suspended frazil concentrations occurred while the air temperature was -12 °C or less. Additionally, the spikes almost always occurred with open water conditions simulated in the section of river between 23.74 km and 27.53 km. The mid-winter spikes in simulated suspended frazil concentration did not always coincide with spikes in the observed suspended frazil concentration, likely because the model did not fully capture the formation of the GBWTP open lead.

The model was re-run for the period between 10th and 24th November 2010 with the simulation results output at a 1-minute interval. This was undertaken to investigate whether an improved resolution would alter the simulation results. The difference in the model output was minimal, with no additional frazil events identified. Additionally, the magnitude of the frazil events was largely unchanged and where differences in the model results did exist, these differences were in the region of 0.001 % and considered to be negligible.
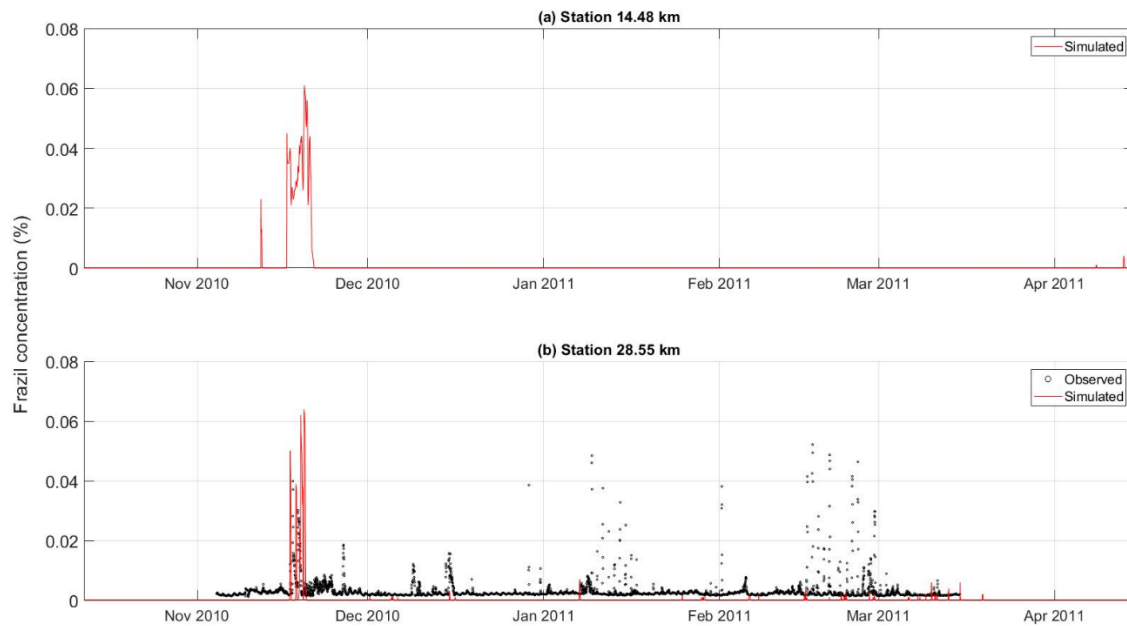
Figure 3-19. Suspended frazil ice concentrations at (a) Station 14.48 km and (b) Station 28.55 km, 2010-11.

3.3.6. Surface ice concentration

Figure 3-20 compares the simulated surface ice concentrations to the surface ice concentrations estimated from the riverside cameras and calculated from the SWIPS. During freeze-up, the simulated surface ice concentrations follow the general trend of increasing surface ice concentration. In particular, the model performed well in capturing the timing of rapid increase in surface pan concentration.

The simulated surface ice concentrations for stations upstream of GBWTP, shown in Figure 3-20a, b, c and d, remained at or near 100% following freeze-up. Small fluctuations in the surface ice concentration, typically between 100% and 98%, were simulated at these stations during the mid-winter period. An example from Station 11.26 km between 2nd and 5th February 2011, where the surface ice concentration fluctuated daily within the range of 98-100%, is shown in Figure 3-21. Owing to the hydro-peaking pattern, a similar pattern of increasing and decreasing water surface widths is also visible in the simulated data. On 4th February 2011, the water surface width increased by 1.7 % and this was matched with a reduction in surface ice concentration to 98.3 %. However,

given that the hydro-peaking pattern is present throughout the simulation, alone it is not sufficient to explain the change in surface ice concentration. Between 09:00 on 2nd February and 10:30 on 5th February 2011, the air temperature was positive, ranging between 0 to 8.5 °C. These high mid-season air temperatures are sufficient to prevent freezing of the water made available by the increase in surface width. Similar patterns are obvious elsewhere in the data, including again at Station 11.26 km between 11th and 15th November 2011, where the surface ice concentration fluctuated to a greater degree, between 90% and 100%. This phenomenon in the simulated data is only observed when the air temperatures are mild.

Downstream of Station 11.26 km, an outfall at the University of Alberta is known to cause a small open lead to form. This open lead is visible in the observed data at Station 11.26 km (Figure 3-20b). No discharge or water temperature data is available for this outfall and as such it has not been included in the model. Other than downstream of GBWTP, the surface ice concentration throughout the remainder of the study reach, both simulated and observed, remained at, or very close to 100%.

The simulated and observed surface ice concentrations for Stations 28.55 km and 28.84 km are shown in Figure 3-20 (e) and Figure 3-20 (f). Both of these stations are situated downstream of GBWTP. At Station 28.55 km the simulated surface ice concentrations can be compared with the SWIPS measurements of the surface ice concentration in the open lead. With the exception of one event on 5th February 2011, each of the spikes in the surface ice concentration measured by the SWIPS occurred when the simulated ice cover was between 90% and 100 %.

In general, the simulated mid-winter surface ice concentrations downstream of GBWTP are characterized by larger and more consistent fluctuations in the surface ice concentration and/or periods of complete open water conditions (0% surface ice concentration). Observations of the open lead have shown it to fluctuate in size and length but at times extends at least 13.5 km downstream and occupies more than 60% of the channel width. Being a one-dimensional model, River1D averages the water temperature across the channel width whereas in reality the warm effluent from GBWTP is largely concentrated along the right bank of the river. As such, the increased melting of

the ice which occurs adjacent to the right bank is not replicated. Simulation results for two additional stations which are also situated downstream of GBWTP, Station 23.74 km and 27.53 km, are provided in Figure 3-22. The effect of GBWTP in the model results was most apparent between these two stations.
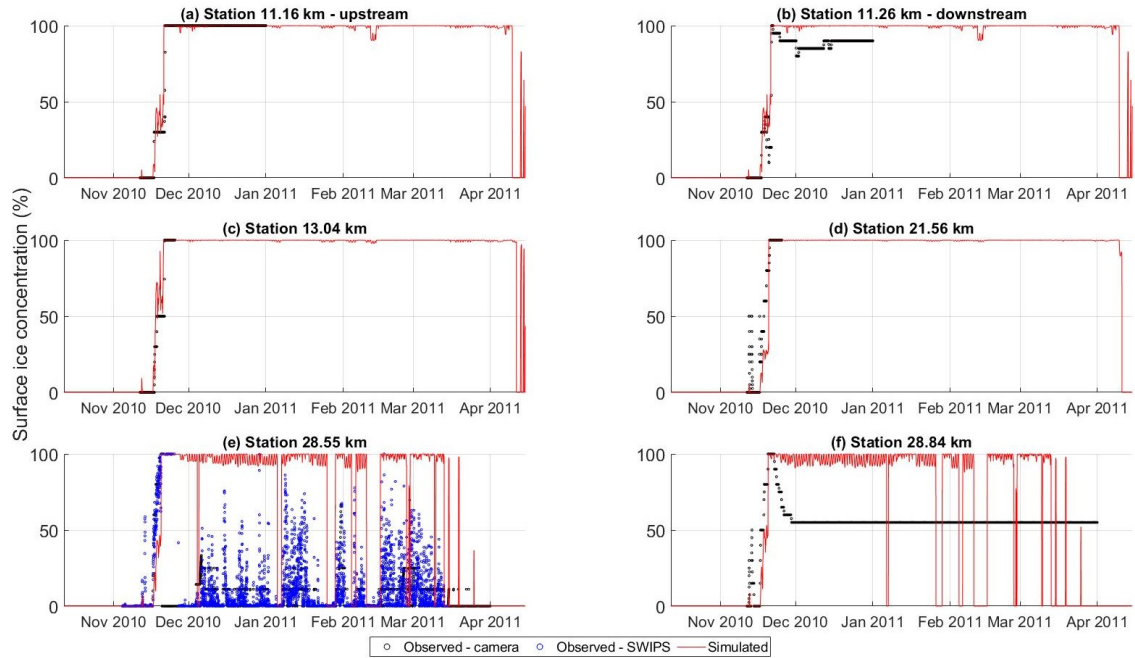
Figure 3-20. Surface ice concentrations at (a) upstream facing camera, Station 11.26 km, (b) downstream facing camera, Station 11.26 km, (c) Station 13.04 km, (d) Station 21.56 km, (e) Station 28.55 km, (f) Station 28.84 km.
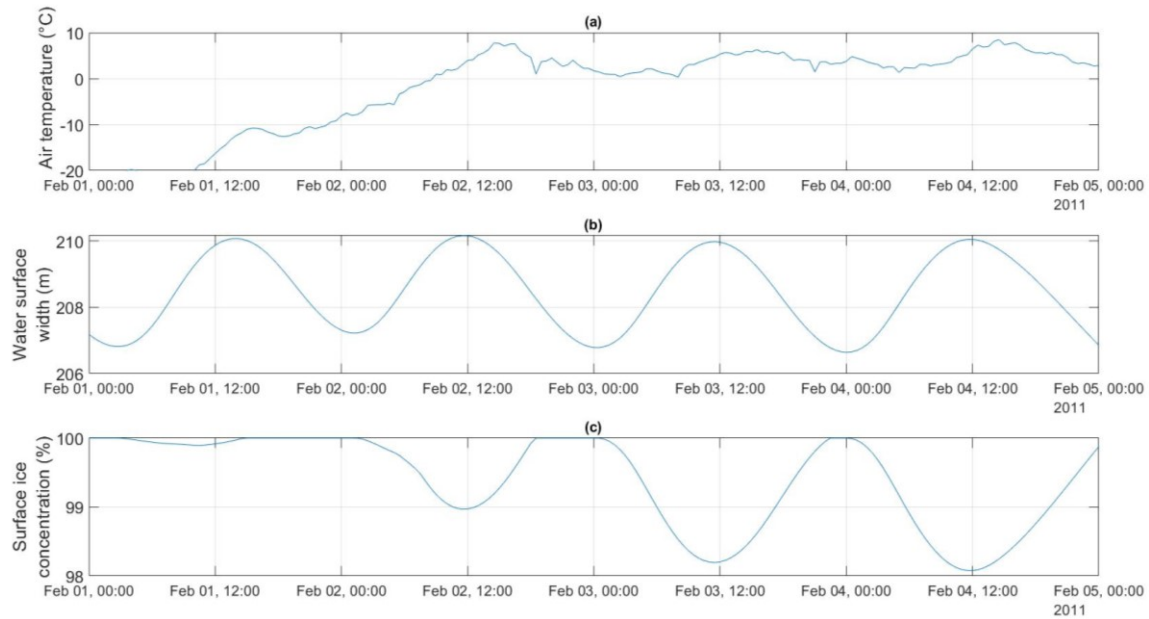
Figure 3-21. Variables at Station 11.26 km including (a) air temperature, (b) surface water width, and (c) surface ice concentration.
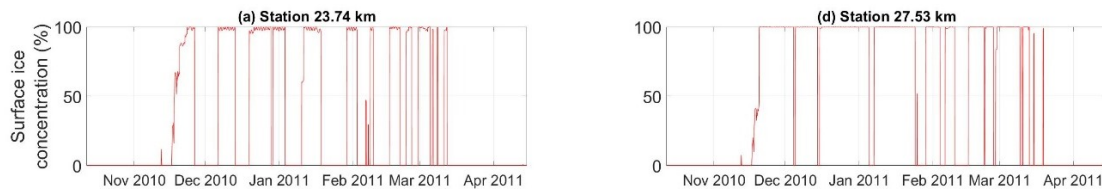
Figure 3-22. Simulated surface ice concentration at (a) Station 23.74 km and (b) 27.53 km.

3.3.7. Ice thickness

Figure 3-23 shows the simulated frazil slush and solid ice thicknesses at Stations 0.00 km, 6.87 km, 21.99 km, and 22.13 km. Except for Station 22.13 km which is immediately downstream, each of these stations is situated upstream of GBWTP. The pattern in simulated ice thicknesses at stations upstream of GBWTP is similar with large and sudden spike in frazil slush thicknesses coinciding with the passing of the ice front. Following freeze-up, the model simulated zero frazil slush thickness at Stations 0.00 km, 6.87 km, and 21.99 km but a gradual growth in the simulated solid ice thickness did occur. At station 6.87 km, shown in Figure 3-23b, the simulation results are compared with the three ice thickness measurements obtained by the Water Survey of Canada.

When comparing the simulation results to these measurements, the model overestimated the solid ice thickness by 7 cm on 3rd January and underestimated the solid ice thickness by 4 cm and 9 cm on 1st February and 8th March, respectively.

Stations 21.99 km and 22.13 km are situated immediately upstream and downstream of GBWTP, respectively and there is a stark contrast in the simulation results between these two stations. Simulation results at Station 21.99 km follow the same pattern as other stations situated upstream of GBWTP. Except for a short period of time at the beginning of December, the model simulated zero solid ice at Station 22.13 km. The maximum simulated solid ice thickness at this station was 0.035 m on 19th November 2010. A significant frazil slush accumulation was simulated at this location, lasting from freeze-up on 20th November 2010, until 7th February 2011. In River1D, frazil slush is confined to the width between the border ice. This is one reason for the particularly thick slush accumulation at this location.

The slush accumulation simulated at Station 22.13 km extended less than 2 km downstream. Frazil slush simulated at Station 24.03 km (Figure 3-24a) was limited to a short duration during freeze-up, between 16th November and 22nd November 2010. A thin layer of solid ice, fluctuating between 0 m and 0.035 m, was simulated following freeze-up. At this location, the average simulated solid ice thickness through the entire simulation period was 0.002 m. Simulation results at Station 27.34 km (Figure 3-24b) were similar to those at 24.03 km except that the solid ice thickness during the mid-winter period were greater, with the thickness fluctuating between 0 m and 0.135 m. The frequency of periods where no solid ice was simulated solid ice thickness was simulated was less and the duration of these periods was also shorter. An average solid ice thickness of 0.0175 m was simulated at this location throughout the entire simulation period.

At Station 28.55 km Figure 3-24c, the simulated results can be compared with the draft measurements obtained by the SWIPS. The magnitude of the simulated ice thicknesses at Station 28.55 km are comparable to those at Station 27.34 km. There is good agreement in the timing of increased and decreased ice thicknesses, with both observed and simulated ice thicknesses climbing sharply on 16th November and decreasing between 24th and 26th November 2010. Following this period, the model did simulate the growth

and reduction of solid ice, but it was always significantly lower than the draft measurements obtained by the SWIPS.

At several locations, including Stations 21.99 km, 22.13 km, Station 24.03 km, Station 27.34 km, and Station 28.55 km, the model simulated spikes in the frazil slush thickness following retreat of the ice front. For example, the ice front retreated downstream of Station 24.03 km at 12:00 on 12th April 2011 and several spikes in the frazil slush thickness were simulated beginning at 04:00 13th April 2011. These spikes coincided with spikes in the suspended frazil concentration at some locations, including at Station 14.48 km as shown in Figure 3-19. Additionally, the spikes in suspended frazil and frazil slush occurred at night and when the air temperature was between 0 °C and -5 °C.

The WSC measured ice thicknesses at Station 6.87 km and the timing of break-up at Station 11.26 km, as observed by the EAS camera, were used in the linear heat transfer model (Section 2.4.10). For the purposes of the linear heat transfer model, it was assumed that either there is no significant difference in the thickness of the ice cover between Stations 6.87 km and 11.26 km, or that break-up at these two stations occurs near-simultaneously. Figure 3-25 compares the simulated solid ice thickness at Stations 6.87 km and 11.26 km. The simulation results show the ice thickness to be between 12cm - 15 cm thicker at Station 11.26 km. Field measurements would be required to validate the difference in ice thickness between these two stations. Additionally, the solid ice simulated by the model melted completely at Station 6.87 km approximately 3 days before at Station 11.26 km. As such, the model indicates that the assumptions made in the linear heat transfer model may not be valid and this error in the assumptions goes some way to explaining the poor performance of the linear heat transfer model.
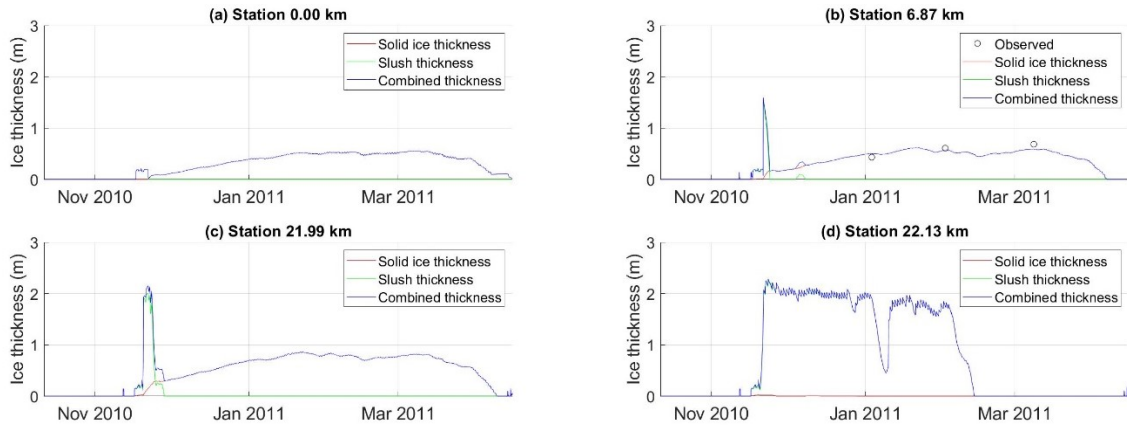
Figure 3-23. Observed and simulated ice thicknesses at (a) Station 0.00 km, (b) Station 6.87 km, (c) Station 21.99 km, and (d) Station 22.13 km.
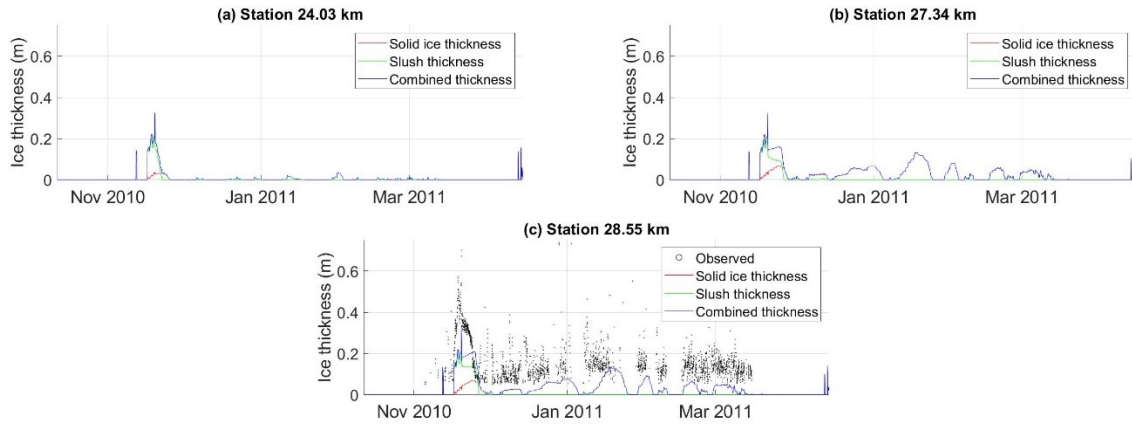
Figure 3-24. Observed and simulated ice thicknesses at (a) Station 24.03 km, (b) Station 27.34 km, and (c) Station 28.55 km, 2010-11.
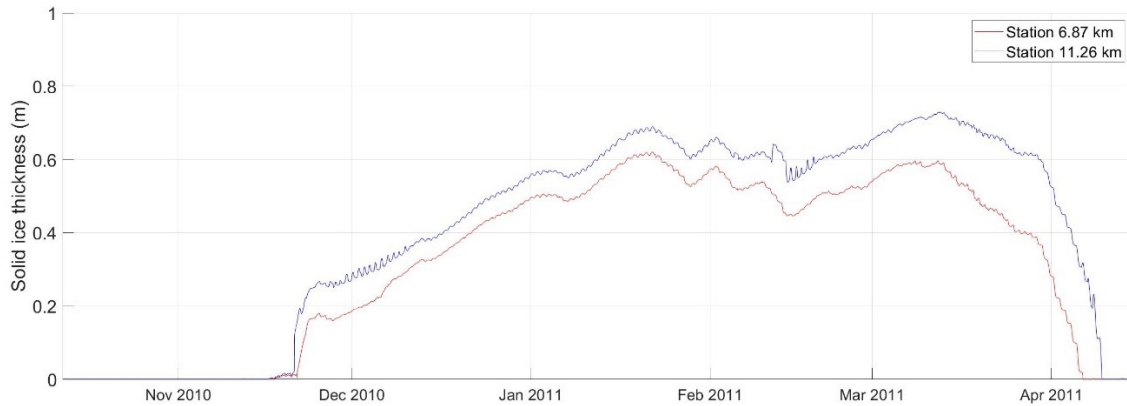
Figure 3-25. Simulated solid ice thickness at Stations 6.87 km and 11.26 km, 2010-11.

3.3.8. *Water surface elevation*

Figure 3-26 presents the simulated and observed water surface elevations. The simulated data are compared with data from the WSC Gauge at Station 14.48 km, Mini-Divers at Stations 21.32 km, 22.51 km, 28.02 km, and 28.84 km and the SWIPS at Station 28.55 km. The timing of stage-up is well captured at all locations and the model also performed well in simulating the magnitude of stage-up at stations upstream of GBWTP. At Station 14.80 km, the model results show stage-up to have begun 5 hours earlier than the observed stage-up. The increase in simulated water surface elevations to peak stage-up took 76 hours while the time taken for the observed water surface elevation to reach its peak during stage-up was 209.5 hours. The water surface elevations were very similar, 613.38 m and 613.88 m for the simulated and observed water surface elevations, respectively.

Simulated stage-up at Station 21.32 km began at 08:00 on 19th November and ended 22.5 hours later at 06:30 on 21st November 2010. Observed stage-up at Station 21.32 km was significantly slower, spreading over 244 hours between 09:30 on 19th November and 13:30 on 29th November 2010. The peak water surface elevations were again very similar, with a peak simulated water surface elevation of 611.27 m and a peak observed water surface elevation of 611.23 m. It is noticeable that the drop of approximately 0.5 m in observed water surface elevations at Stations 14.48 km and 21.32 km, immediately prior to stage-up, was not replicated in the model. An additional upstream bridging

event(s), unaccounted in the model or boundary condition, could be responsible for this drop in water levels.

Downstream of GBWTP, the model's performance in the timing of stage-up remained strong with stage-up beginning approximately 2.5 hours early at Stations 22.51 km, 28.02 km, 28.55 km and 28.84 km. At these stations, the model also performed well in simulating the length of time between the beginning of stage-up and the peak water surface elevation. At Station 22.51 km, 19 hours elapsed between the onset of stage-up and the peak simulated water surface elevation while 21 hours elapsed between the observed onset of stage-up and the peak observed water surface elevation. Similarly, at Stations 28.02 km, 28.55 km and 28.84 km, the difference in duration between the length of simulated and observed stage-up was minimal, approximately 1.5 hours.

The magnitude of stage-up was well captured at Station 22.51 km with 0.01 m between the simulated peak water surface elevation of 610.59 m and the observed peak of 610.60 m. The model did not capture the drop in water surface elevations immediately following stage-up which is apparent in the observed data at Station 22.51 km. The magnitude of stage-up at Station 28.02 km, 28.55 km and 28.84 km was underestimated in the model by 0.28 m, 0.18 m and 0.23 m, respectively.

Following freeze-up, the model overestimated water surface elevations upstream of GBWTP and underestimated water surface elevations downstream of GBWTP. The model calculates ice roughness values based on the ice thickness, according to Nezhikhovskiy (1964), and does not account for smoothing. Several smaller outfalls which may contribute to the thinning of the ice cover in the central part of the city have not been included in the model. The decrease in water surface elevations downstream of the plant is caused by a reduction in the simulated solid ice thicknesses and increased hydraulic efficiency. On 29th November 2010, the average simulated solid ice thickness throughout the study reach was 0.16 m while the simulated solid ice thickness downstream of GBWTP was only 0.01 m, with several cross sections showing no solid ice. It is possible that the post-freeze-up performance of the model downstream of GBWTP could be improved if consideration of the roughness of border ice was given consideration and this is identified as a potential area for improvement in River1D.

Figure 3-27 through to Figure 3-32 show the simulated discharge, solid ice thickness, ice roughness and water surface elevations for Stations 14.48 km, 21.32 km, 22.51 km, 28.02 km, 28.55 km and 28.84 km. There is a clear difference in solid ice thicknesses and ice roughness values between stations situated upstream of GBWTP and those situated downstream of GBWTP. Through the duration of the simulation the average simulated ice roughness at Stations 14.48 km and 21.32 km was 0.0380 and 0.0384, respectively. At both of these locations the maximum ice roughness calculated by the model was approximately 0.064. The ice roughness in the model did not increase above zero throughout the simulation at Station 22.513 km. Moving further downstream of GBWTP, the average ice roughness increased from 0.0004 at Station 28.02 km to 0.0006 at Station 28.55 km and then to 0.0008 at Station 28.84 km. Shortly after freeze-up in 1981, Gerard and Andres (1982) calculated the roughness height of the underside of the ice cover along the NSR at Stations 5.84 km, 6.86 km, 9.84 km, 15.01 km, and 17.28 km. The ice roughness values reported by Gerard and Andres (1982) varied between 0.035 and 0.045. In comparison, the ice roughness values calculated by the model for stations upstream of GBWTP appear to be high and are in the range of roughness values expected for breakup ice jams as reported by Beltaos (2001). The values downstream of GBWTP are significantly lower than published values of ice roughness. The effect of the roughness of a partial ice cover on the flow is not captured by the model.

The Mini-Divers and the SWIPS instrumentation were removed from the river prior to break-up in the spring of 2011. Additionally, there is some uncertainty in the water surface elevation data from the Water Survey of Canadas gauge. The peak water surface elevation observed at this station was 616.16 m at 11:00 on 13th April 2011 while the station was not ice affected. At this time, the reported discharge was 524.4 m^3/s. However, a discharge of 520.6 m^3/s during open water conditions on 4th July 2011 returned a water surface elevation of 614.18 m. This value is closer to the peak water surface elevation of 614.65 m simulated by the model at 13:00 on 14th April 2011. Owing to these reasons, it is difficult to assess the performance of the model in simulating water surface elevations during break-up.
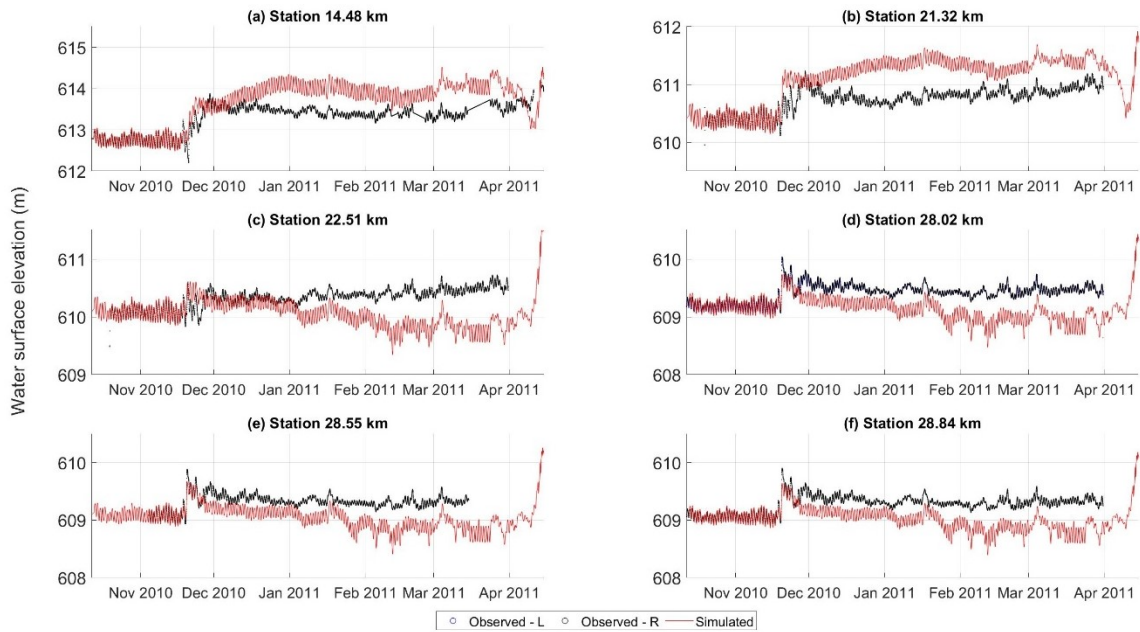
Figure 3-26. Observed and simulated water surface elevations at (a) Station 14.48 km, (b) Station 21.32 km, (c) Station 22.51 km, (d) Station 28.02 km, (e) Station 28.55, and Station 28.84 km.
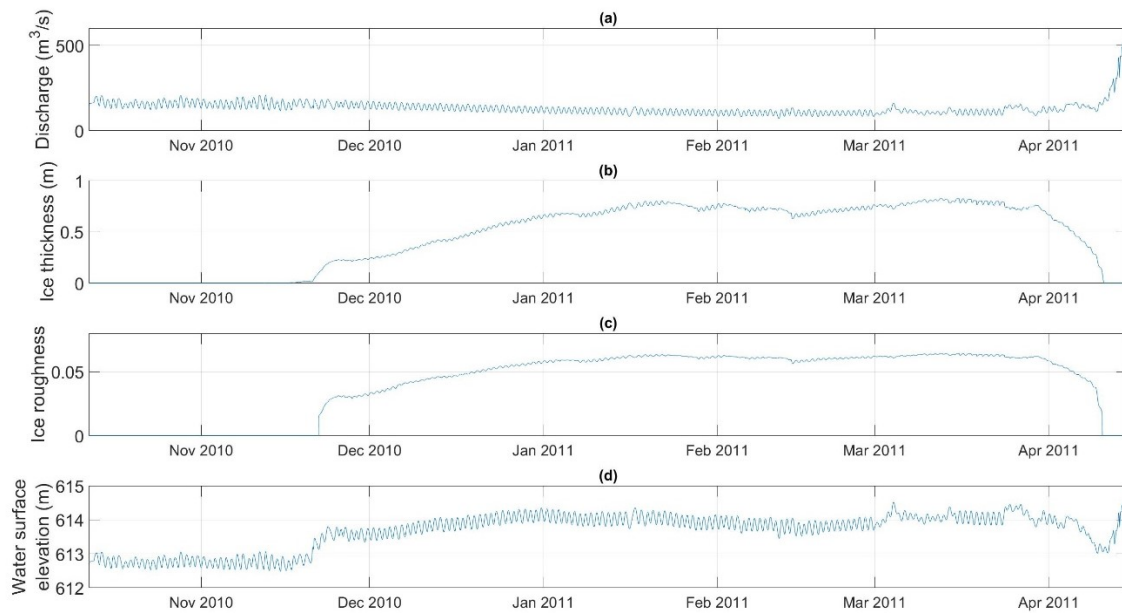
Figure 3-27. Showing simulated results for (a) discharge, (b) solid ice thickness, (c) ice roughness, and (d) water surface elevation at Station 14.48 km.
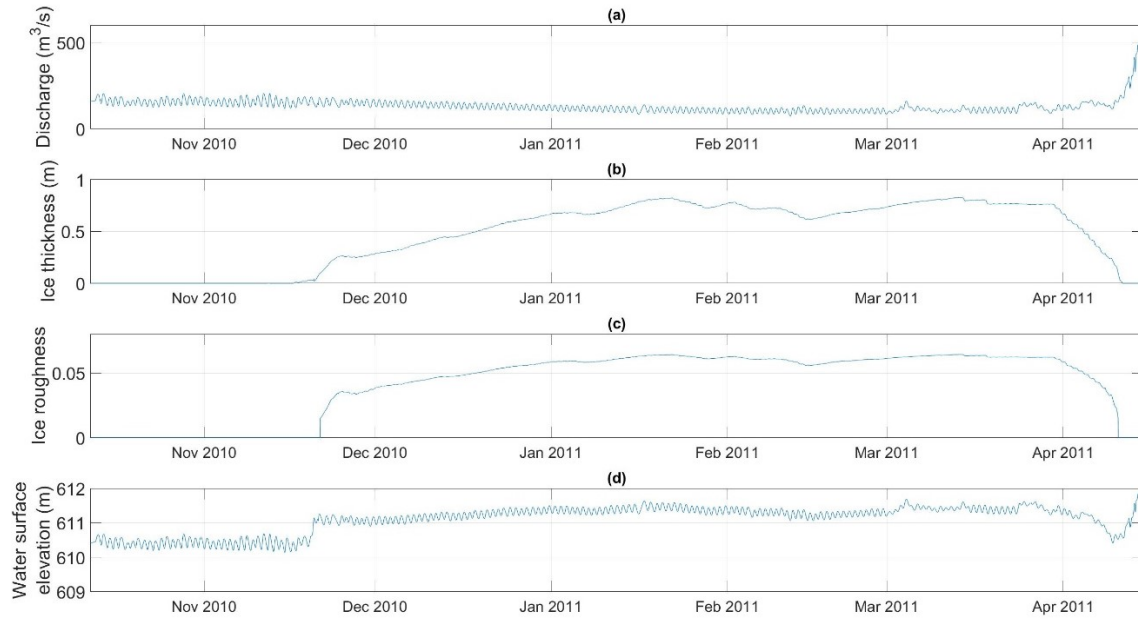
Figure 3-28. Showing simulated results for (a) discharge, (b) solid ice thickness, (c) ice roughness, and (d) water surface elevation at Station 21.32 km.
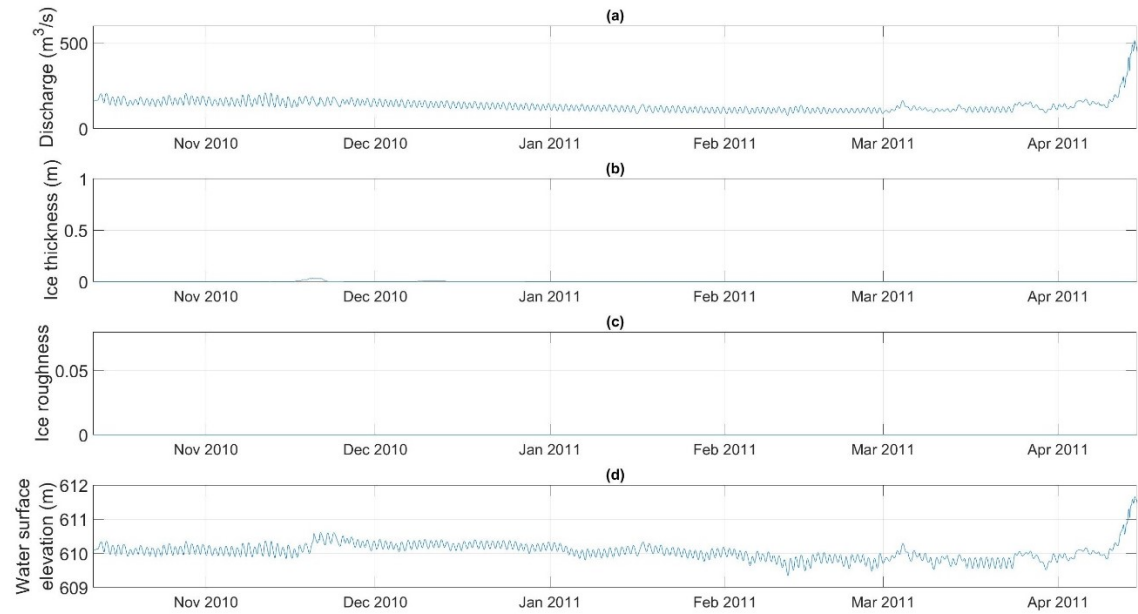
Figure 3-29. Showing simulated results for (a) discharge, (b) solid ice thickness, (c) ice roughness, and (d) water surface elevation at Station 22.51 km.
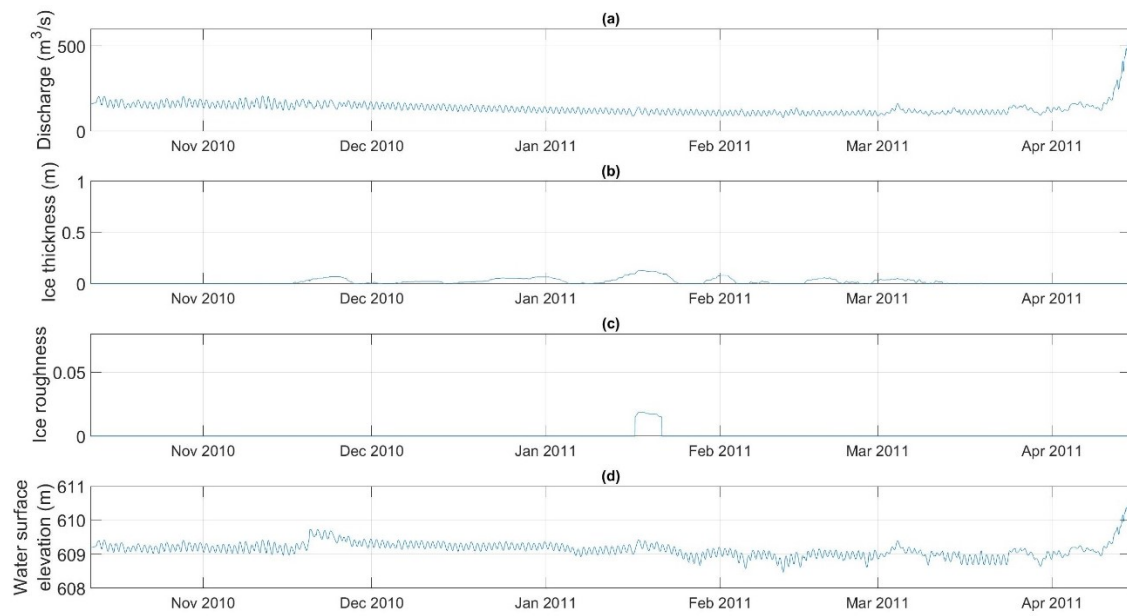
Figure 3-30. Showing simulated results for (a) discharge, (b) solid ice thickness, (c) ice roughness, and (d) water surface elevation at Station 28.02 km.
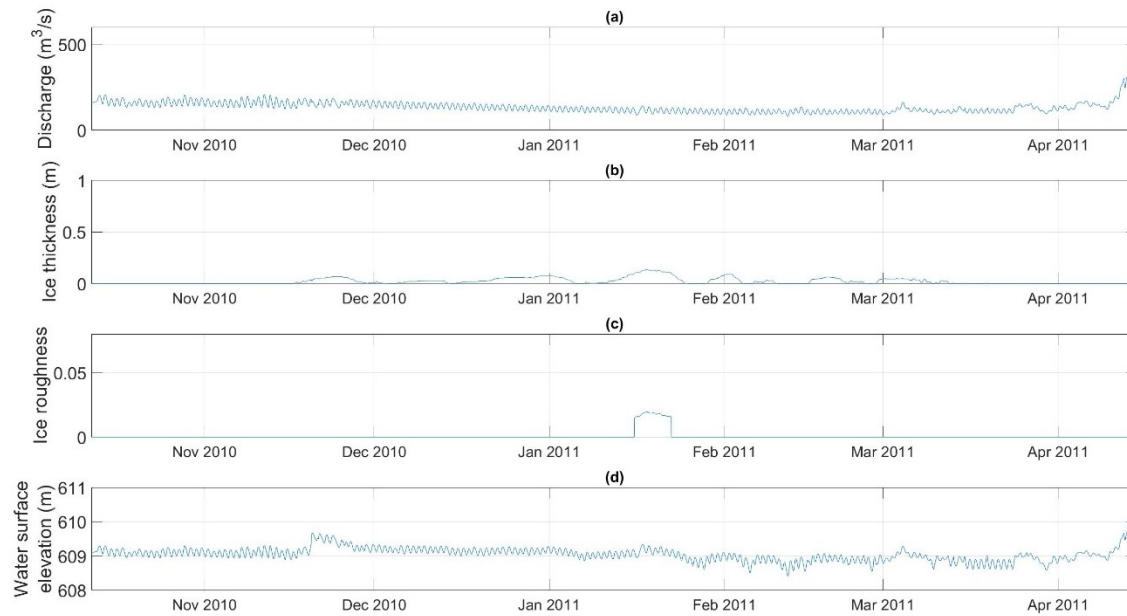
Figure 3-31. Showing simulated results for (a) discharge, (b) solid ice thickness, (c) ice roughness, and (e) water surface elevation at Station 28.55 km.
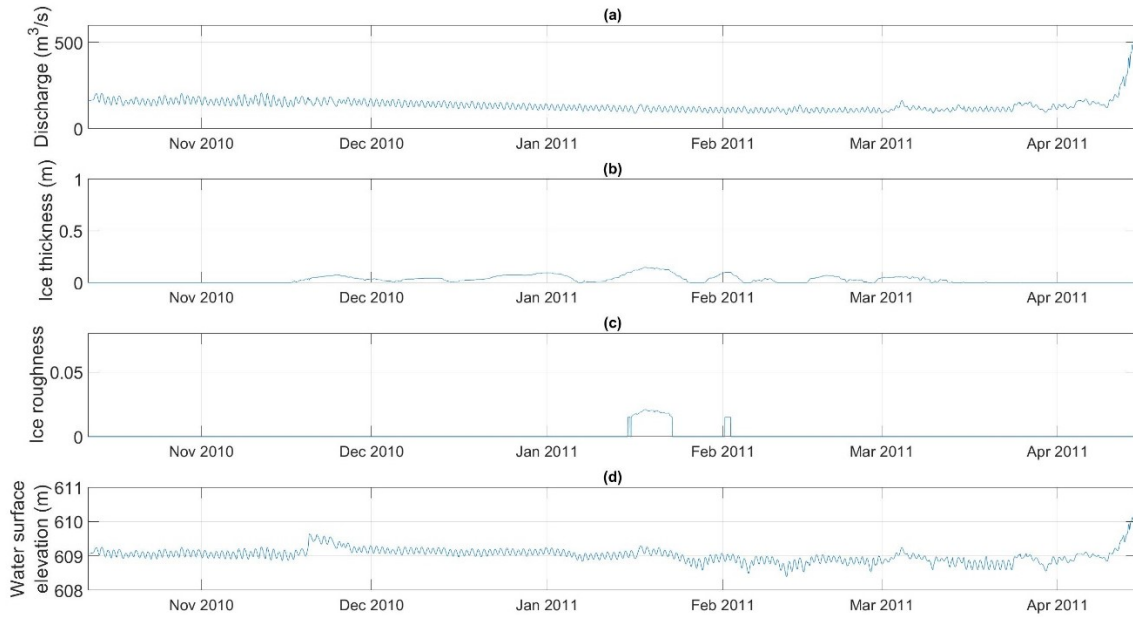
Figure 3-32. Showing simulated results for (a) discharge, (b) solid ice thickness, (c) average border ice thickness, (d) ice roughness, and (e) water surface elevation at Station 28.84 km.

3.4. Model validation (2009-10)

3.4.1. *Open water validation*

Water surface elevation data from the WSC Gauge at Station 14.48 km and from the SWIPS instrumentation at station 28.55 km are available for assessing the model performance during open water conditions. Between 3rd November and 13th November 2009, the simulated water surface elevation at Station 14.48 km remained within 0.06 m of the observed. Agreement between the simulated and observed water surface elevations at Station 28.55 km was less impressive, with the simulated water surface elevations varying up to 0.1 m away from the observed. Nonetheless, this validation tolerance was deemed acceptable given uncertainty relating to the datum of the depth recording equipment, two-dimensional flow effects and potential errors in measuring water levels.
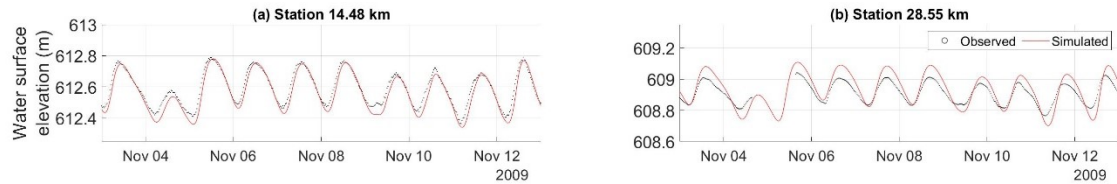
Figure 3-33. Observed and simulated water surface elevations between 3rd November 2009 and 13th November 2009 at (a) Station 14.48 km, and (b) Station 28.55 km.

3.4.2. Water temperature

Figure 3-34 shows the simulated water temperatures at Stations 10.53 km, 21.32 km, 22.51 km, 28.02 km, 29.55 km and 28.84 km. These simulated water temperatures are compared with the water temperatures recorded by the RTD in the University's chilled water systems intake at Station 10.53 km and the SWIPS instrumentation at Station 28.55 km.

The model accurately captured the cooling trend and the point of zero-degree isotherm at Station 10.53 km, with an R^2 value of 0.97 and an RMSE of 0.15 °C during freeze-up. As with the calibration simulation, a strong performance at this location is to be expected given that the observed data from this location was used to estimate the water temperature condition at the upstream boundary. The maximum supercooling simulated by the model at Station 10.53 km was -0.035 °C at 03:30 on 13th November and 00:00 on 19th November 2009. Simulated water temperatures between 16th November and 20th November were overestimated by the model, as shown in Figure 3-35. The simulated water temperature closely follows the trend in air temperatures which were exceptionally high during this period, with a maximum temperature of 16.5 °C.

The simulated and observed water temperatures at Station 28.55 km are shown in Figure 3-34e. The model was again successful in capturing the cooling trend prior to freeze-up with an R^2 value of 0.937 and a RMSE of 0.24 °C. However, the point of zero-degree isotherm was not accurately simulated at this location. The observed water temperature first dropped below 0 °C at 07:00 12th November 2009 while the simulated water temperature first dropped below 0 °C at 09:30 on 22nd November 2009. Figure 3-36 shows the air temperature, the surface ice concentration at the upstream boundary, and the surface ice concentration, combined frazil slush and solid ice thickness, and the

simulated water temperature at Station 28.55 km between 9th and 24th November 2009. The model overestimated water temperatures until the end of November. It is notable that the surface ice concentration at Station 28.55 km closely mimics the surface ice concentration at the upstream boundary and is significantly lower than the observed surface ice concentration from 16th November onwards. The simulated ice thickness drops to zero on 16th November. This lack of an insulating ice layer combined with the elevated air temperatures likely contributes to the overestimation of water temperatures at this location.

The maximum simulated supercooling at Station 28.55 km was -0.036 °C at 05:00 on 3rd December 2009. At this time, the water temperature recorded by the SWIPS was significantly lower, -0.074 °C. The maximum supercooling recorded by the SWIPS, -0.0868 °C occurred at 08:30 on 28th November. This occurred during the period where the model overestimated water temperatures, as discussed above.

Following freeze-up and upstream of GBWTP (Figure 3-34a and b) the simulated water temperature remained consistently at 0 °C. Downstream of GBWTP (Figure 3-34c, d, e and f) the mid-season water temperatures fluctuated between approximately 0 °C and 0.8 °C. At Station 22.51 km, these water temperature fluctuations persisted throughout the entire mid-season period. However, further downstream at Station 28.02 km, 28.55 km and 28.84 km there was an extended period between 6th December 2009 and 7th January 2010 where the simulated water temperature remained close to 0 °C. These cooler water temperatures occurred while the simulated surface ice concentration at this location was high. Other than fluctuations at stations downstream of GBWTP, the simulated water temperature throughout the study reach is relatively consistent.
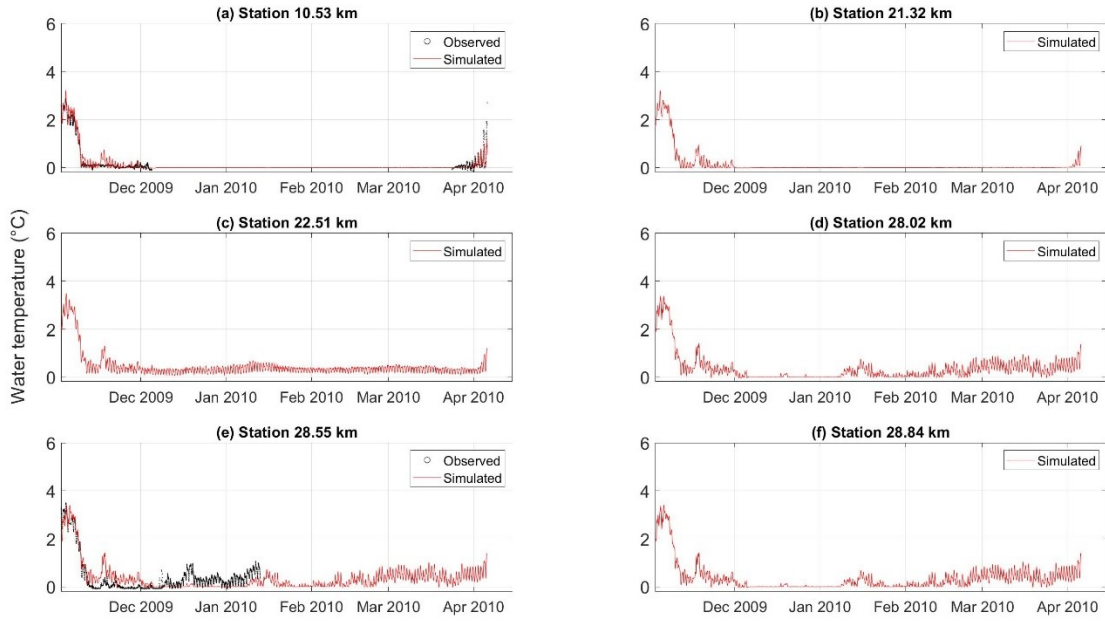
Figure 3-34. 2009-10 observed and simulated water temperatures at (a) Stations 10.53 km, (b) Station 21.32 km, (c) Station 22.51 km, (d) Station 28.02 km, (e) Station 28.55 km, and (f) Station 28.84 km.
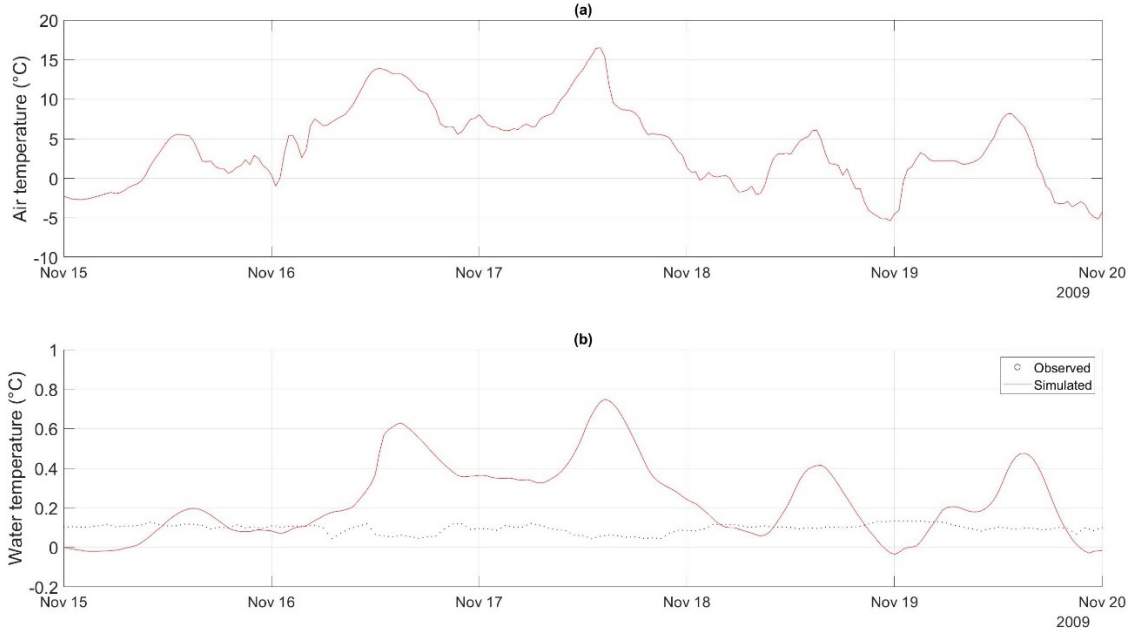
Figure 3-35. (a) observed air temperature and (b) observed and simulated air temperature at Station 10.53 km, 2009-10.
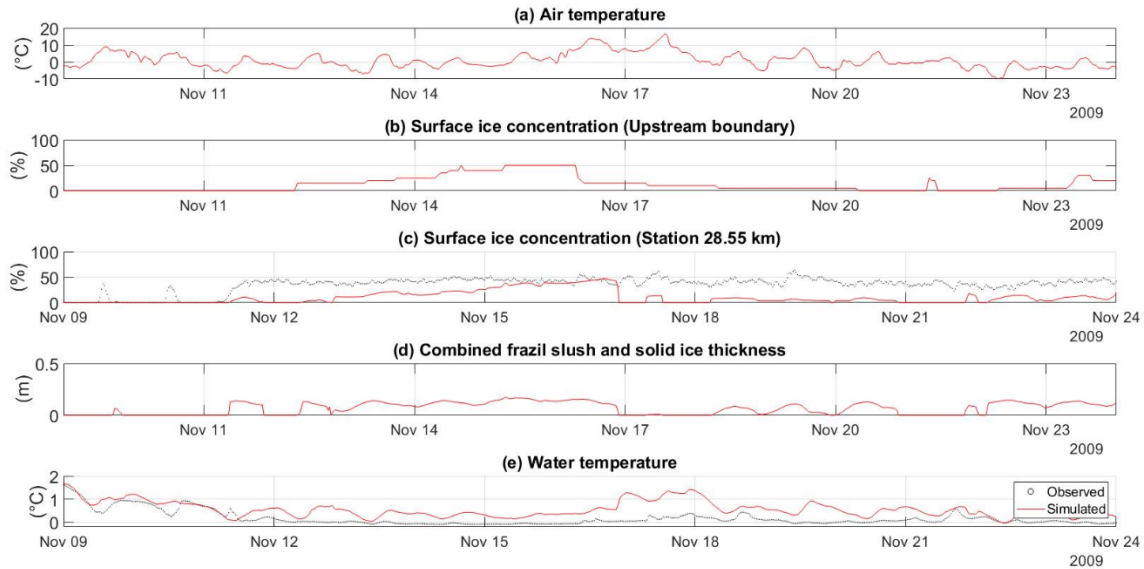
Figure 3-36. 2009-10 time-series showing (a) Air temperature, (b) surface ice concentration at upstream boundary, (c) simulated surface ice concentration at Station 28.55 km, (d) simulated combined frazil slush and solid ice thickness at Station 28.55 km, (e) observed and simulated water temperatures at Station 28.55 km.

3.4.3. Ice front propagation

Two of the bridging locations, Stations 39.35 km and 14.01 km, used in the validation simulation were identical to those used in the calibration simulation. The flow condition at Station 18.37 km prevented the activation of the second ice front and so the bridging event was moved approximately 140 m downstream to Station 18.51 km where, as a result of the channel geometry, the Froude Number was lower. Aerial images captured by Ghobrial et al. (2013) showed that bridging had not occurred on 3rd December 2009, but the ice concentration, which was over 80-90% in many areas, suggested that bridging would imminently occur should the supply of ice pans into the study reach continue. The ice front was recorded passing by cameras at Station 11.26 km and 28.55 km at 15:00 on 5th December and 00:00 on 6th December 2009, respectively. This provided a relatively small window in which bridging could have occurred. The user defined bridging times and locations which were applied in the validation run are provided in Table 16.

The simulated ice front is included in Figure 3-37. As with the calibration run, the model performed well in simulating the ice front propagation. At Station 28.55 km, the

simulated ice front arrived approximately 1.5 hours early and at Station 11.26 km, approximately 9 hours late. Owing to the Froude number exceeding the maximum Froude number for ice front progression, bridging in the model was delayed at Stations 18.51 km and 14.01 km by 18 and 15 hours, respectively. This caused the delay in the arrival of the simulated ice front at Station 11.26 km but did not affect the ice front in the downstream end of the model. In some instances, such as the bridging location at Station 14.01 km the arrival of a downstream ice front is necessary to change the flow conditions and activate additional ice fronts in the model. The average simulated progression through the study reach was 12.5 km/day which is very similar to the average simulated progression rate of 12.2 km/day simulated in 2010-11.

There is a gap in the simulated ice front between Stations 18.65 km and 18.51 km. The progress of Ice Front 1 slowed significantly between 07:30 on 6th December and 02:30 on 7th December. This happened due to the bridging event at Station 18.51 km which initiated Ice Front 2 at 16:30 on 5th December and cut off the surface ice supply downstream. Ice front 1 did not progress further upstream than 18.62 km. The resultant discontinuous ice cover has been observed in the study reach. Figure 3-38 shows the surface ice conditions upstream and downstream of Station 15.06 km on 21st November 2020. There is a clear section of open water between a downstream ice front and an upstream bridging location. These sections of open water do not remain open for the duration of winter but typically freeze-over in the days or weeks following the passing of the ice front. A similar process occurs in the model. Analysis of the simulated surface ice conditions and ice thickness at Station 18.56 km, between the two simulated ice fronts, shows the channel to be ice covered at this location.

The simulated rates of ice front progression are provided in Table 17. The rate of ice front progression through region B, 10.31 km/day, is very similar to the rate of 10.60 km/day simulated during the 2010-11 season. In region C, the rate of ice front progression during the validation simulation, 6.55 km/day, was slower than the rate of 11.89 km/day simulated in the calibration run. The rate of progression through region D is not available since the timing of the bridging events caused the simulated ice front to first appear in the upstream area of the region. The rate of ice front progression through

116

Region E was exceptionally fast, 34.71 km/day. Although this is significantly higher than the rate of front progression through the same region in the 2010-11 simulation, during both calibration and validation simulations the ice front progressed quickest through this region. The difference in the simulated rate of ice front propagation between the two simulations is likely a combination of the ice supply (the surface ice concentration defined in the upstream boundary condition) and the Froude number which is largely controlled by the discharge. The average discharge in the period between the arrival of the simulated ice front at Station 28.84 km and the upstream boundary, was 113.5 m^3/s and 151.6 m^3/s in 2009-10 and 2010-11, respectively.

Figure 3-39 shows the location of the three ice fronts over the entire winter season. The camera at Station 28.55 km was removed prior to break-up in Spring 2010. As such, the only location at which the timing of the simulated ice front retreat may be assessed is Station 11.26 km. The simulated ice front retreat was 5.1 days later than break-up as observed by the camera a Station 11.26 km. Ice front retreat in River1D must begin at the upstream extent of the ice front. In the case of Ice front 3 in the validation simulation, the upstream extent of ice front 3 is the model's upstream boundary.

Figure 3-40 shows the air temperature, water temperature and the ice thickness at the upstream boundary, Station 0.00 km. At this location, the ice cover began melting on 14th February 2010 and continued to melt until 30th March 2010 when ice melting stalled. The simulated ice remained 4.3 cm thick until melting resumed at 11:00 on 4th April 2010. The driving force behind the resumption of melting appears to be an increase in water temperature, with the water temperature rising above 0 °C for the first time since freeze-up at the same time the ice melting resumed, 11:00 on 4th April 2010. As such, it seems reasonable to conclude that the delayed retreat in Ice front 3 is caused by uncertainty in the upstream boundary's water temperature condition.

Figure 3-41 shows the ice thickness at Stations 11.26 km and 13.04 km and the melting pattern between 24th March and 7th April 2010. The ice thickness at Station 11.26 km reduced to zero at 00:30 on 4th April 2010, approximately 4.5 days later than break-up was recorded by the camera at this location. The simulated ice thickness at the time of observed break-up was greater than 20 cm at this location.

Although there is no observed data with which to compare break-up at Station 13.04 km, it is interesting to note that the ice thickness melted to 0 cm at 20:00 on 5th April 2010, 43.5 hours later than at Station 11.26 km. This is comparable to the 38.5 hours that elapsed between complete melting of the ice cover at Stations 11.26 km and 13.04 km during the calibration simulation of 2010-11.

The model again performed well when compared to the linear heat transfer model (Section 2.4.10) which predicted break-up 13 days early. Additionally, when considering the performance of River1D and the linear heat transfer model during both years of simulation, it is notable that River1D was more consistent, simulating break-up several days late in both years. In comparison, the linear heat transfer model was less consistent, predicting break-up 9 days late in 2011 and 13 days early in 2010.

Table 16. Location and timing of estimated bridging events, 2009-10.

Bridging location (km)	Time of bridging
39.35	04-Dec-2009 12:30
18.51	04-Dec-2009 22:30
14.01	05-Dec-2009 05:30
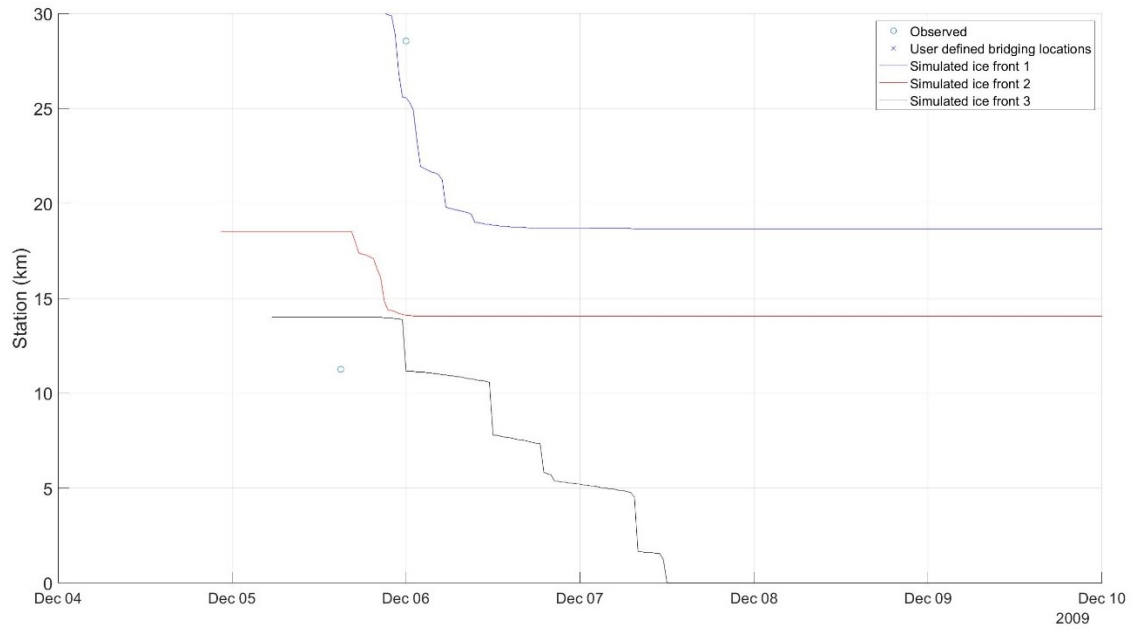
Figure 3-37. Simulated ice front propagation, freeze-up 2009-10.
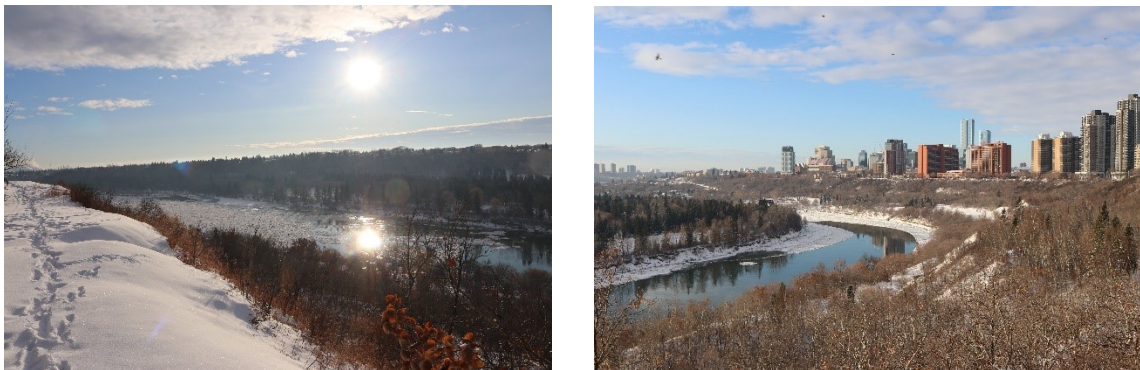
Figure 3-38. Surface ice conditions downstream (left) and upstream (right) of Station 15.06 km on 21st November 2020.

Table 17. Observed and simulated ice front progression rates through defined regions A-F during freeze-up 2010-11.

Region [†]	Station (km)	Observed ice front progression rate (km/day)	Simulated ice front progression rate (km/day)
A	N/A	8.2	(outside model study reach)
B	0 - 11.26	14.2	10.31
C	11.26 – 14.48	3.9	6.55
D	14.48 – 21.32	30.7[‡]	N/A
E	21.32 – 28.55	11.6	34.71
F	N/A	11.8	(outside model study reach)

[†] Regions are shown in Figure 2-2.

[‡] Affected by bridging
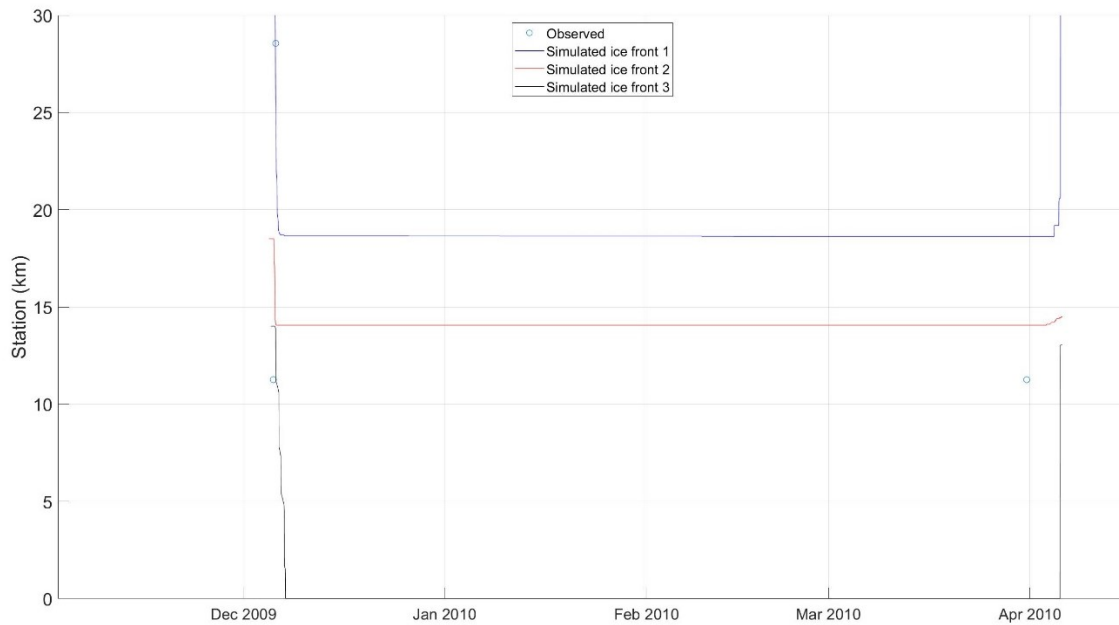
Figure 3-39. Simulated ice front locations for the entire season, 2009-10.
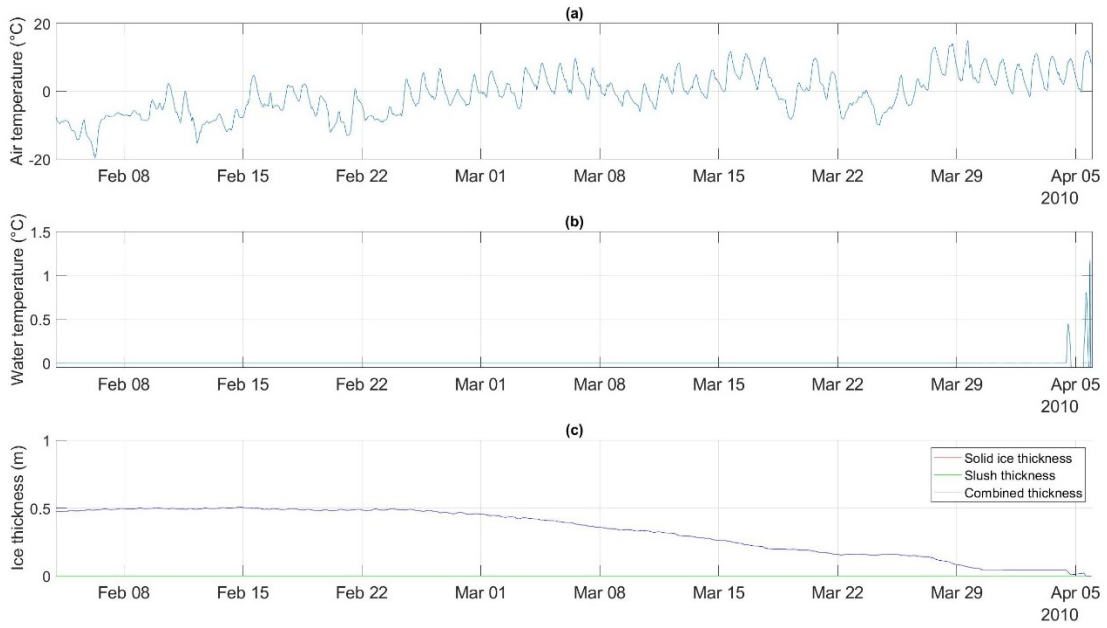
Figure 3-40. (a) Air temperature, (b) water temperature and (c) ice thickness at the upstream boundary, Station 0.00 km, 4th February to 6th April 2010.
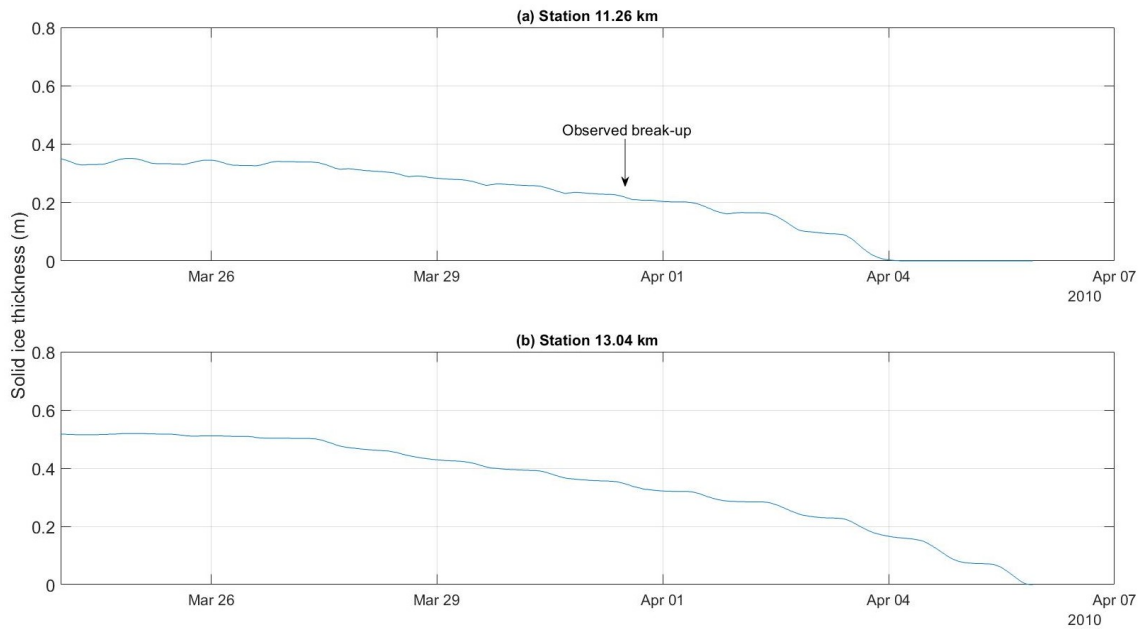
Figure 3-41. Simulated ice thicknesses during break-up at (a) Station 11.26 km and (b) Station 13.04 km, 2009-10.

3.4.4. Border ice

Figure 3-42 shows the simulated border ice fractions at Stations 11.26 km, 13.04 km, 21.56 km, 28.02 km, 28.55 km, and 28.84 km. At Station 11.26 km, the simulated border ice fraction is compared with the observed border ice fraction which was visually estimated from images from the EAS camera. In the model, stable border ice, the border ice which remained in place for the duration of the mid-winter period, began growing on 1st December 2009. Prior to this, several instances of border ice growth and retreat were simulated. Although this pattern was not present in the observed data, there was one instance of border ice growth and retreat between 15th November and 17th November 2009. Stable border ice in the observed data began growing on 21st November 2009, 11 days earlier than was simulated by the model. Despite this discrepancy, both the observed and simulated border ice fractions stabilized at similar values at this station. The model simulated a stable border ice fraction of 0.14 while the stable border ice fraction estimated from the images was 0.15.

At each of the stations shown in Figure 3-42 the magnitude of the stable border ice fraction was very similar between the calibration and validation simulations, as shown in Table 18. The biggest difference between the simulated stable border ice fractions was 0.02, equivalent to 2% of the channel width, at Station 11.26 km. This suggests that the border ice fractions are similar each year. However, further data collection would be required to verify this.

The simulated maximum border ice thicknesses at Stations 11.26 km, 13.04 km, 21.56 km, 28.02 km, 28.55 km, and 28.84 km are shown in Figure 3-43. The rate of border ice growth between the onset of growth and the simulated global peak is different for stations upstream and downstream of GBWTP. At stations downstream of GBWTP (Stations 28.02 km, 28.55 km, and 28.84 km) an average growth rate of approximately 1.85 cm/day was simulated. Peak border ice thickness at these stations was simulated after only approximately 37 days of ice growth. During the same period, the average growth rate at Stations upstream of GBWTP was comparable at approximately 2.0 cm/day. However, it took approximately 85 days of simulated border ice growth for the maximum

thickness to develop at stations upstream of GBWTP and through the 85 days an average border ice growth rate of 1.1 cm/day was simulated.

Peak ice thicknesses of 89 – 90 cm were simulated at Stations 11.26 km, 13.04 km and 21.56 km and 69 – 70 cm at Stations 28.02 km, 28.55 km, and 28.84 km. During the calibration simulation of 2010-11, thicker border ice of approximately 1.01 m, was simulated upstream of GBWTP and a thinner ice cover of between 59 cm and 64 cm was simulated at the stations downstream of GBWTP.
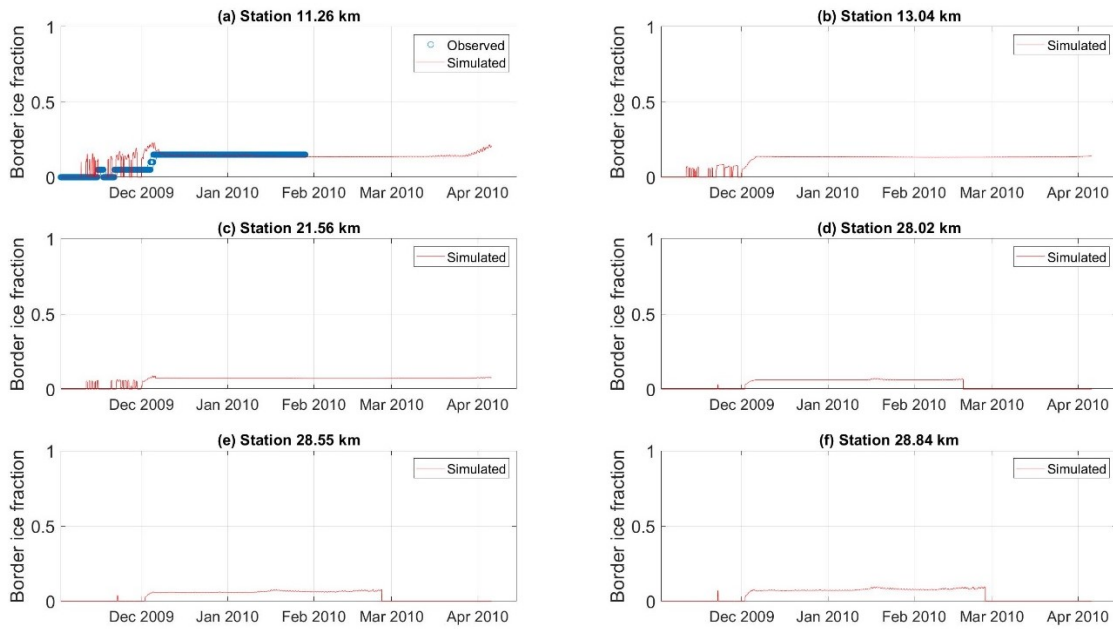
Figure 3-42. 2009-10 observed and simulated border ice fractions at (a) Station 11.26 km, (b) Station 13.04 km, (c) Station 21.56 km, (d) Station 28.02 km, (e) Station 28.55 km, and (f) Station 28.84 km.

Table 18. Stable border ice fractions for both calibration and validation simulations.

Station (km)	Stable border ice fraction, 2009-10	Stable border ice fraction, 2010-11
11.26	0.14	0.16
13.04	0.14	0.14
21.56	0.07	0.06
28.02	0.06	0.06
28.55	0.06	0.06
28.84	0.07	0.07
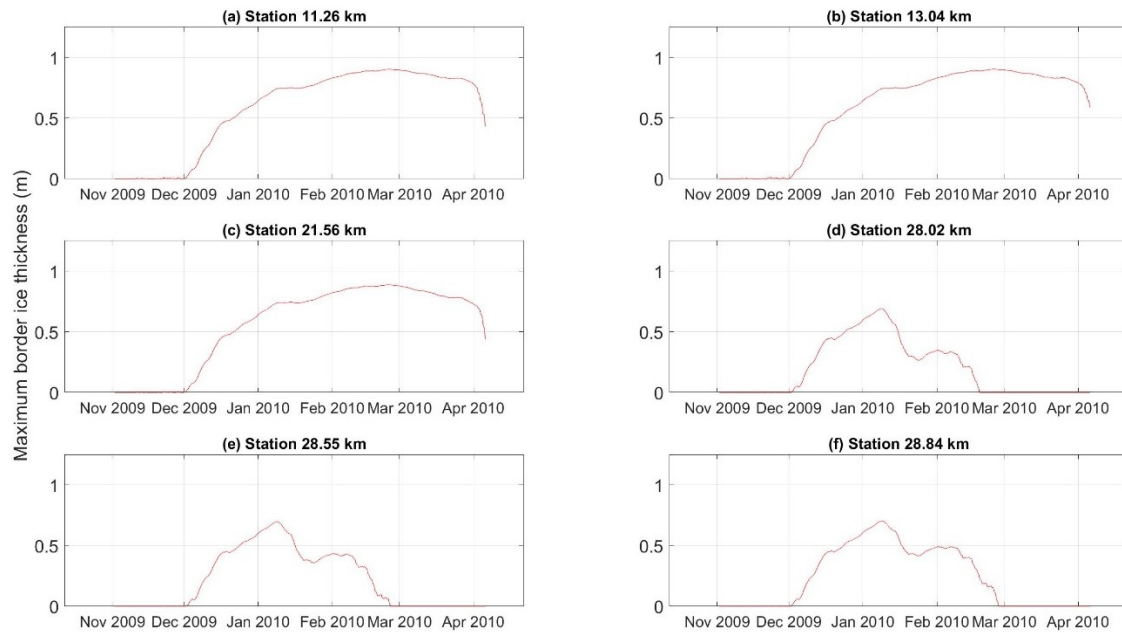
Figure 3-43. 2009-10 simulated maximum border ice thickness at (a) Station 11.26 km, (b) Station 13.04 km, (c) Station 21.56 km, (d) Station 28.02 km, (e) Station 28.55 km, and (f) Station 28.84 km.

3.4.5. Suspended frazil concentration

Figure 3-44a shows the simulated suspended frazil concentration at Station 14.48 km during the 2009-10 ice season. Several frazil events were simulated during the freeze-up period with suspended frazil concentrations ranging up to 0.031%. This value of peak

suspended frazil concentration is significantly less than the peak value of 0.061% simulated during the 2010-11 season. All but one of the simulated frazil events lasted less than a day. There was an extended frazil event simulated by the model beginning 22:30 on 30th November and ending at 15:00 on 6th December 2009. Following this frazil event, no more suspended frazil ice was simulated by the model at this location until 5th April 2010. The ice front passed through Station 14.48 km at 21:30 on 5th December 2009 and it is not surprising that the frazil events stopped shortly after this time.

At Station 28.55 km the simulated suspended frazil concentrations are compared to the data collected by the SWIPS instrumentation, as shown in Figure 3-44b. The simulated suspended frazil concentrations are again of the correct order of magnitude and the peak value of 0.050 % is comparable to the peak value of 0.061 % simulated during the 2010-11 season. Several frazil events which were recorded by the SWIPS instrumentation between the 13th November and 1st December 2009 were not replicated by the model. The first of these occurred on 14th November 2009. At this time, the model overestimated water temperature as discussed in Section 3.4.2. The overestimation of water temperatures meant that supercooling did not occur in the model and this explains the lack of simulated frazil events.

Three major frazil events were simulated by the model during freeze-up. The first of these occurred between 06:00 and 12:30 on 2nd December 2009 and a peak frazil concentration of 0.048 % was simulated. The SWIPS also recorded a frazil event on this day between 04:30 and 11:00. The peak frazil concentration recorded by the SWIPS was 0.019%. The second simulated frazil event occurred on 3rd December with the model returning a peak concentration of 0.05%. No frazil events were recorded by the SWIPS at this time. Finally, the third simulated frazil event started at 08:00 on 5th December, peaked at 10:30 and ended by 16:30 on the same day. This event returned a peak simulated frazil concentration of 0.034%. A smaller frazil event was recorded by the SWIPS between 05:30 and 22:30 on this day.

Following freeze-up, several smaller frazil events were simulated during the mid-winter period with suspended ice concentrations ranging from 0.001% to 0.016%. These events

were of a lower magnitude and a shorter duration than the events simulated during freeze-up. In the model, each of these events coincided with supercooling at this location.
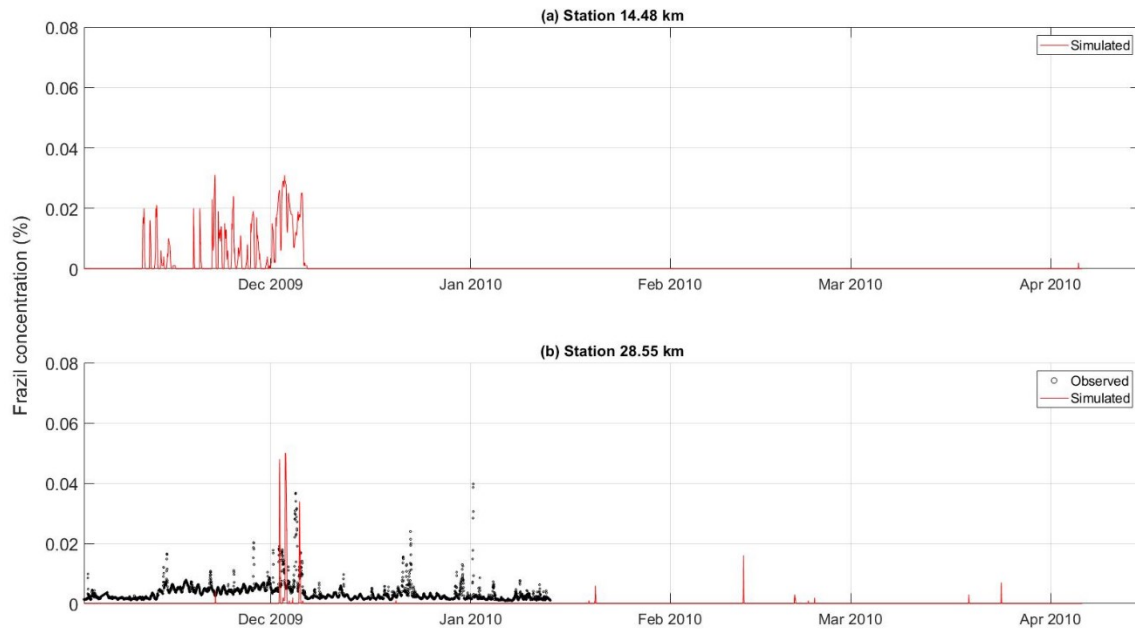
Figure 3-44. 2009-10 suspended surface ice concentrations at (a) Station 14.48 km and (b) Station 28.55 km.

3.4.6. *Surface ice concentration*

The simulated surface ice concentrations at Stations 11.26 km, 13.04 km, 21.56 km, 28.55 km and 28.84 km are shown in Figure 3-45. At Station 11.26 km, the simulated surface ice concentrations are compared with surface ice concentrations visually estimated from images captured by the EAS camera. At this location, there is good agreement in the timing of rapid surface ice increase. The observed surface ice concentration increased to 100% at 09:00 on 5th December while the simulated surface ice concentration rose to 100% at 00:30 on 6th December 2009. This agreement is to be expected given the strong performance of the model in simulating the ice front propagation (see Section 3.4.3). In addition to this, the model also performed well in simulating the timing and magnitude of increases and decreases in surface ice concentration prior to freeze-up. The simulated surface ice concentration fluctuated between 92% and 100 % for periods of both December and January. These fluctuations

were caused by an increase in the water surface width which in turn was caused by increasing discharge and hydro-peaking.

The pattern of simulated surface ice concentrations during freeze-up was similar at all stations. Although the pattern of increases and decreases was similar, the magnitude of the surface ice concentration varied between stations. For example, higher surface ice concentrations were simulated at Station 13.04 km and lower concentrations were simulated at Station 21.56 km. These variations in surface ice concentration are not a function of the local channel geometry or border ice fractions. However, the upstream channel geometry should be expected to play a role in changing surface ice concentrations by congesting or dispersing ice pans as they move downstream.

Compared to the calibration simulation of 2010-11, the increase in surface ice concentration from 0 % to 100% was a much more gradual process in 2009-10. For example, at Station 11.26 km, the process took just 4.4 days during freeze-up in 2010-11 and a much longer duration of 23.9 days during 2009-10.

The surface ice concentrations as calculated from the SWIPS measurements are compared to the simulated surface ice concentrations at Station 28.55 km, as shown in Figure 3-45e. Prior to the arrival of the ice front on 5th December 2009, the model underestimated surface ice concentrations. Additionally, a spike in the observed surface ice concentrations on 3rd December 2009 was not simulated at all. Following freeze-up, the simulated surface ice concentrations fluctuated between 93% and 100 % and several instances of 0 % surface ice cover were simulated during the mid-winter period. The model largely simulated open water conditions at this location from mid-February onwards. Only three periods of surface ice cover were simulated between mid-February and break-up, with each period lasting approximately 2 days. This pattern is a little different to that simulated during 2010-11 where the surface ice concentration remained high, with shorter periods of open water conditions, until the end of March 2011.

The simulated surface ice concentrations at Stations 23.74 km and 27.53 km are shown in Figure 3-46. At Station 23.74 km, the surface ice concentration drops to 0% on 9th January 2010 and remains at 0% for the entire season. This is different to the surface ice

concentration simulated at this location during the winter of 2010-11 where periods of open water and complete ice cover were simulated throughout the winter season. The simulated surface ice concentrations at Station 27.53 km in both simulations are similar between freeze-up and mid-February. Following this time, the 2009-10 model simulated longer periods of open water conditions and fewer spikes in surface ice concentration. One factor contributing to a more pronounced open lead in 2009-10 compared to 2010-11 is the air temperature. The average air temperature during the 2009-10 simulation was -5.4 °C, while during the same period in 2010-11 an average air temperature of -9.2 °C was recorded.
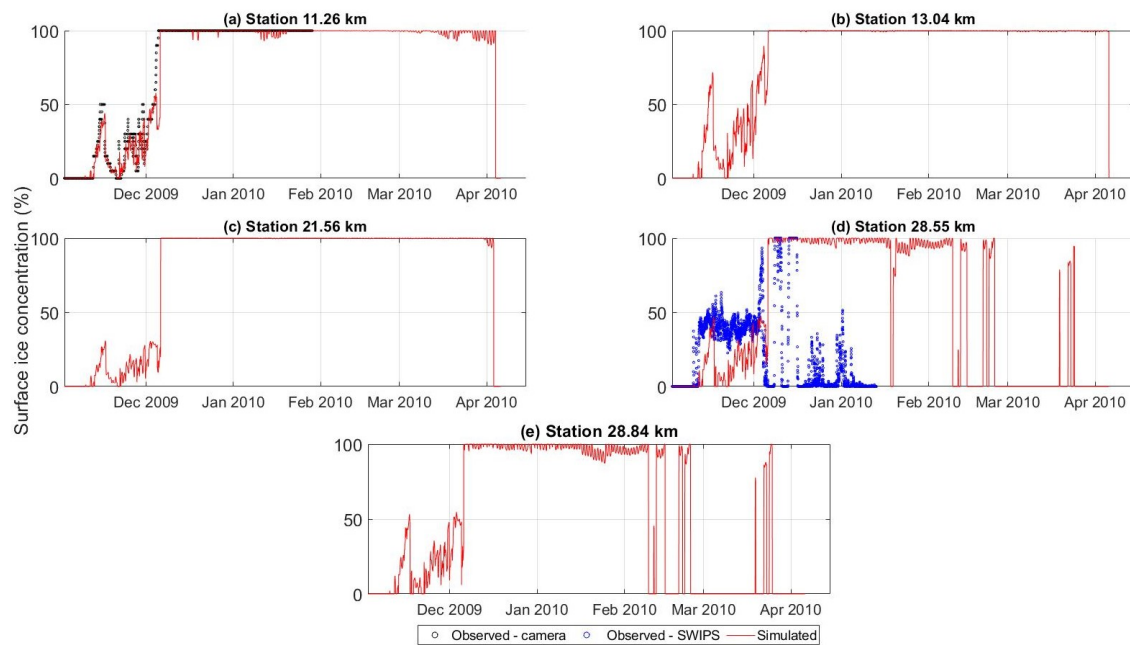
Figure 3-45. Surface ice concentrations at (a) Station 11.26 km, (b) Station 13.04 km, (c) Station 21.56 km, (d) Station 28.55 km, (e) Station 28.84 km, 2009-10.
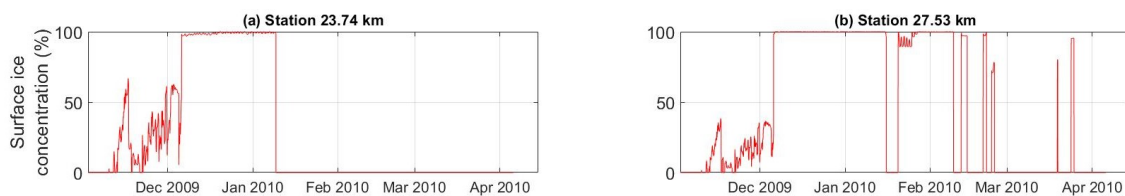
Figure 3-46. Simulated surface ice concentration at (a) Station 23.74 km and (b) 27.53 km, 2009-10.

3.4.7. *Ice thickness*

Figure 3-46 presents the simulated frazil slush, solid ice and combined ice thicknesses at Stations 0.00 km, 6.87 km and 21.99 km, and 22.13 km. At the three stations upstream of GBWTP, the pattern of solid ice growth and decay over the duration of the simulation is similar. However, the thickness of the frazil slush simulated by the model during freeze-up varied by location. At Station 0.00 km, the results were similar to those produced by the 2010-11 model, with a period of frazil slush simulated prior to the passing of the ice front followed by the growth of solid ice. No frazil slush was simulated at Station 0.00 km once the ice front had passed.

At Station 6.87 km, the simulated ice thickness is compared with the WSC measured ice thicknesses. In the model, the ice thickness was overestimated by 23 cm on 7th January 2010, 19 cm on 3rd February 2010, and 15 cm on 3rd March 2010. A peak solid ice thickness of 66 cm was simulated on 14th February 2010. This is comparable to the peak solid ice thickness of 66 cm which was simulated by the 2010-11 model. A very sudden increase in the frazil slush thickness, from 18 cm to 25 cm, was simulated as the ice front passed during the evening of 6th December 2009. This increase was minor when compared to the increase in simulated frazil thickness of approximately 1.5 m as the ice front passed through this location in the 2010-11 model.

The model generated similar patterns in ice thickness at Stations 21.99 km and 22.13 km. At Station 21.99 km, immediately upstream of GBWTP, the spike in frazil slush of 1.57 m at the time of freeze-up was slightly lower than the 2.01 m simulated during 2010-11. The frazil slush simulated at Station 22.13 km was also less thick when compared to the 2010-11 model. As shown in Figure 3-46d, the frazil slush reduced significantly between December 2009 and late January 2010. A mid-winter minimum of 0.13 m was simulated on 28th January 2010. Following this minimum, the frazil slush thickness increased and a sharp increase of approximately 0.5 m was simulated on 9th February 2010. This increase in frazil slush does not appear to be driven by atmospheric conditions, with mild air temperatures and average solar radiation input to the model at this time.

The simulated ice thicknesses at Stations 24.03 km, 27.34 km, and 28.55 km are shown in Figure 3-48. The simulated ice thicknesses at all three stations are similar during freeze-

up, with a spike in the thickness of frazil slush occurring on 5th December 2009. At Station 24.03 km, frazil slush was present between 11th November and 17th December. This period was followed by zero ice thickness for the duration of the simulation. The periodic increases in solid ice which were simulated in the 2010-11 model were not simulated in the 2009-10 model.

At Station 27.34 km the model simulated the growth of solid ice from the time following the passing of the ice front until the beginning of December. The solid ice peaked at a thickness of 0.21 m between 6th and 8th January 2010. Following this peak, the simulated solid ice decayed quickly, reducing to zero within a week. Between mid-January and the end of the simulation the model simulated several periods of minor solid ice growth, but the ice thickness did not exceed 0.02 m and did not remain in place for more than 5 days.

Figure 3-48c shows the simulated solid, frazil slush and combined thicknesses, along with the pan draft measurements captured by the SWIPS which was located in the open lead at Station 28.55 km. The model performed well in simulating the timing of increases in the frazil slush thickness prior to and during freeze-up. The magnitude of the frazil slush at this time was underestimated by approximately 15 cm in the model. The growth of solid ice following freeze-up followed a similar trend to that at Station 27.34 km, with the solid ice thickness increasing between 6th December 2009 and 9th January 2010 and then reducing to zero on 17th January 2010. Several mid-season increases in the solid ice thickness were simulated by the model. However, these increases in solid ice thickness were smaller and lasted for a shorter duration than the mid-winter increases in solid ice thickness simulated in the 2010-11 model.
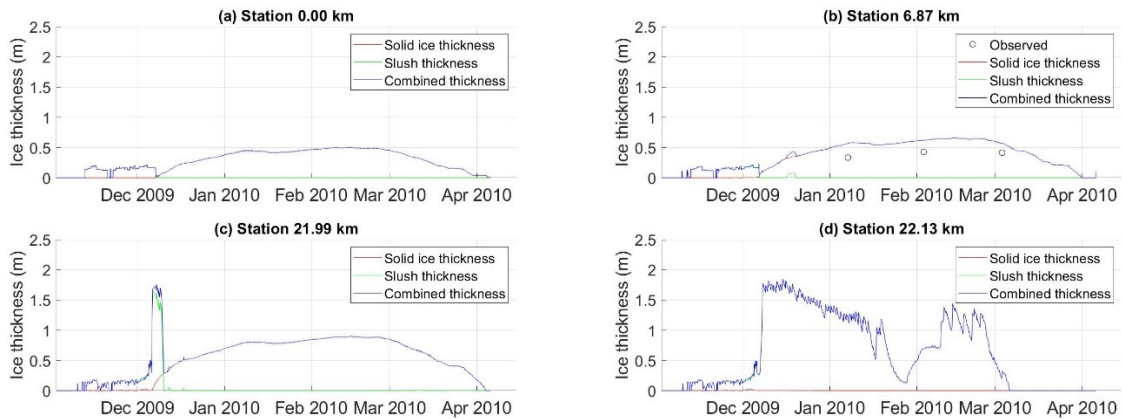
Figure 3-47. Observed and simulated ice thicknesses at (a) Station 0.00 km, (b) Station 6.87 km, (c) Station 21.99 km, and (d) Station 22.13 km, 2009-10.
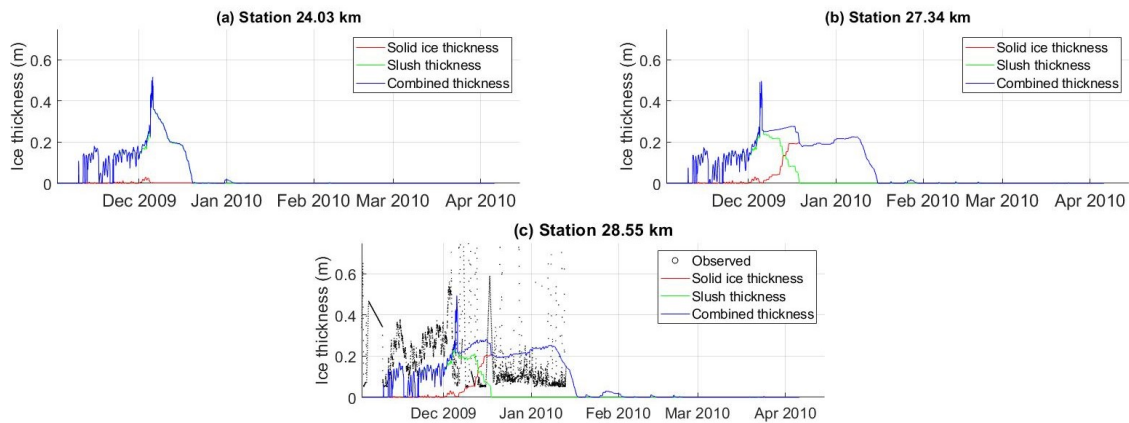
Figure 3-48. Observed and simulated ice thicknesses at (a) Station 24.03 km, (b) Station 27.34 km, and (c) Station 28.55 km, 2009-10.

3.4.8. *Water surface elevation*

The simulated water surface elevations are included in Figure 3-49. There is a similar trend at Stations 14.48 km and 21.32 km, both of which are situated upstream of GBWTP. A second trend is also evident at Stations 22.51 km, 28.02 km, 28.55 km and 28.84 km, which are all situated downstream of GBWTP. At Station 14.48 km, shown in Figure 3-49a, the simulation results can be compared with data from the WSC Gauge. Stage-up, as simulated by the model, began at 23:00 on 4th December and a water surface elevation of 613.1 m was simulated at 16:00 on 6th December. This was followed by a more gradual increase in water surface elevations to approximately 613.5 m on 18th

December 2009. Observed stage-up at this location was a two-part process beginning at 14:30 on 8th December with the water surface elevation then rising to 613.2 m at 17:30 on 11th December 2009. The water surface elevation was reasonably consistent between 11th December and 18th December. The second phase of stage-up started at 21:00 on 18th December 2009. A peak water surface elevation of 613.6 m was recorded at 15:30 on 21st December 2009. The difference in timing of simulated and observed stage-up-up at this location is indicative that the model did not perform well in simulating the timing of the ice front at this location. This could have been caused by additional bridging events which have not been accounted for in the model or due to uncertainty in the timing of bridging as applied in the model. The difference in water surface elevations immediately following observed stage-up was approximately 0.1 m.

Following stage-up at Station 14.48 km, the simulated water surface elevation rose until reaching a peak of approximately 614.2 m in early February and declining thereafter. At this time, the model overestimated water surface elevations by almost 1 m. Figure 3-50 shows the simulated discharge, ice thickness, ice roughness and surface water elevation at Station 14.48 km. Uncertainty in the discharge defined in the upstream boundary condition is likely a contributing factor to this overestimation. The mid-winter trend in water surface elevations tracks the changes in discharge while decline in water surface elevations during late March and early April are caused by smoothing and decay of the ice cover. The calculated ice roughness values are similar to those calculated to the model in the calibration simulation. At Station 14.48 km, average and peak ice roughness values of 0.042 and 0.065 were calculated by the model. As mentioned in Section 3.3.8, the ice roughness values are high relative to those published in the literature and are a likely cause of the overestimation of mid-winter water surface elevations.

Similar stage-up and trends in the water surface elevation were simulated at Stations 22.51 km, 28.02 km, 28.55 km and 28.84 km, all of which are downstream of GBWTP. At Station 28.55 km, the simulated water surface elevation is compared with the water surface elevation estimated from the SWIPS data. In the model, stage-up started from a water surface elevation of 608.7 m at 02:30 on 5th December 2009 and peaked at 609.3 m at 11:00 on 6th December 2009. Relative to those stations upstream of GBWTP, observed

stage-up occurred over a much shorter period of time. The observed stage-up started 3 hours earlier than simulated, at 23:30 on 4th December 2009. The water surface elevation estimated by the SWIPS rose to a peak of 609.4 m at 07:30 on 6th December 2009. The model performed well in simulating both the timing and the magnitude of stage-up at this location.

Following stage-up, the model also performed well in simulating the general trend in simulated water surface elevations. Simulated water surface elevations were underestimated between 10th and 14th December 2009 and overestimated between 16th and 20th December 2009 and again between 4th and 11th January 2010. The SWIPS were removed from the river and as such there is no data with which to compare the model results at this location beyond 13th January 2010.

Figure 3-51 shows the shows the simulated discharge, ice thickness, ice roughness and surface water elevation at Station 28.55 km. Except for a period between 13th December 2009 and 15th January 2010, the simulated ice thickness was insignificant and as such the ice roughness was deemed negligible by the model. The drop in water surface elevation through mid-January was caused by the decay and smoothing of the ice cover. Throughout the remainder of the simulation the water surface elevation was controlled by the discharge at this location.
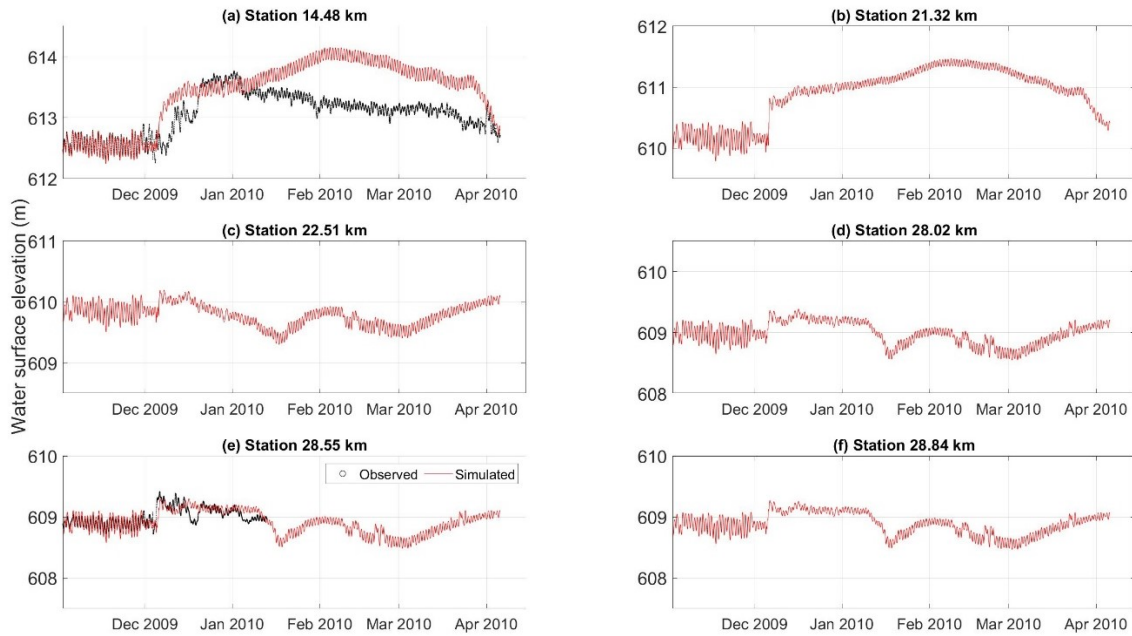
Figure 3-49. Observed and simulated water surface elevations at (a) Station 14.48 km, (b) Station 21.32 km, (c) Station 22.51 km, (d) Station 28.02 km, (e) Station 28.55, and Station 28.84 km, 2009-10.
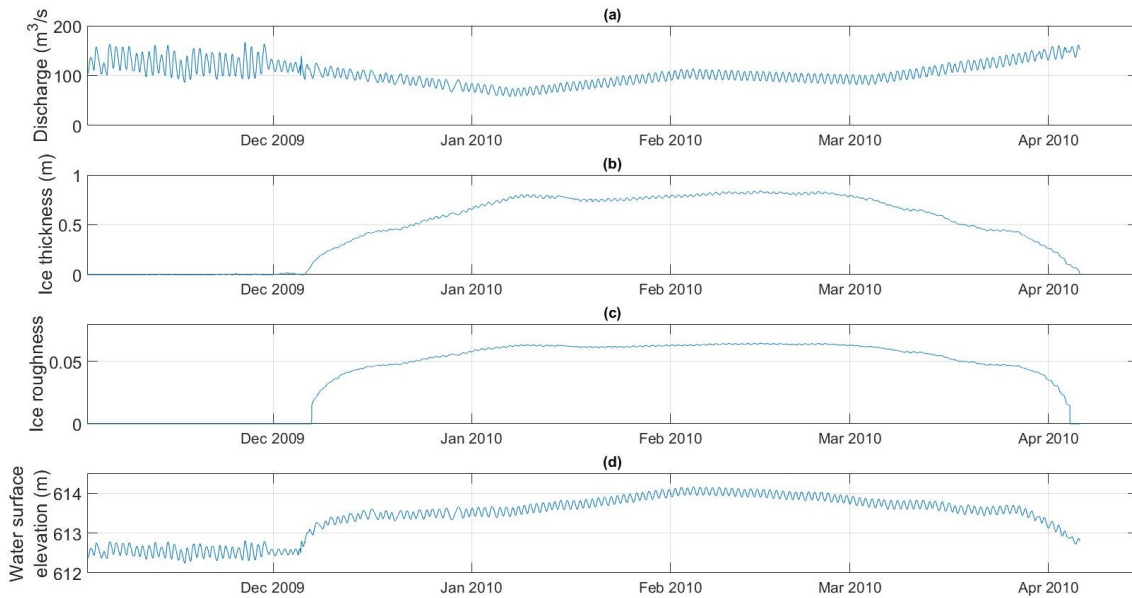
Figure 3-50 2009-10 simulated results for (a) discharge, (b) solid ice thickness, (c) ice roughness, and (d) water surface elevation at Station 14.48 km.
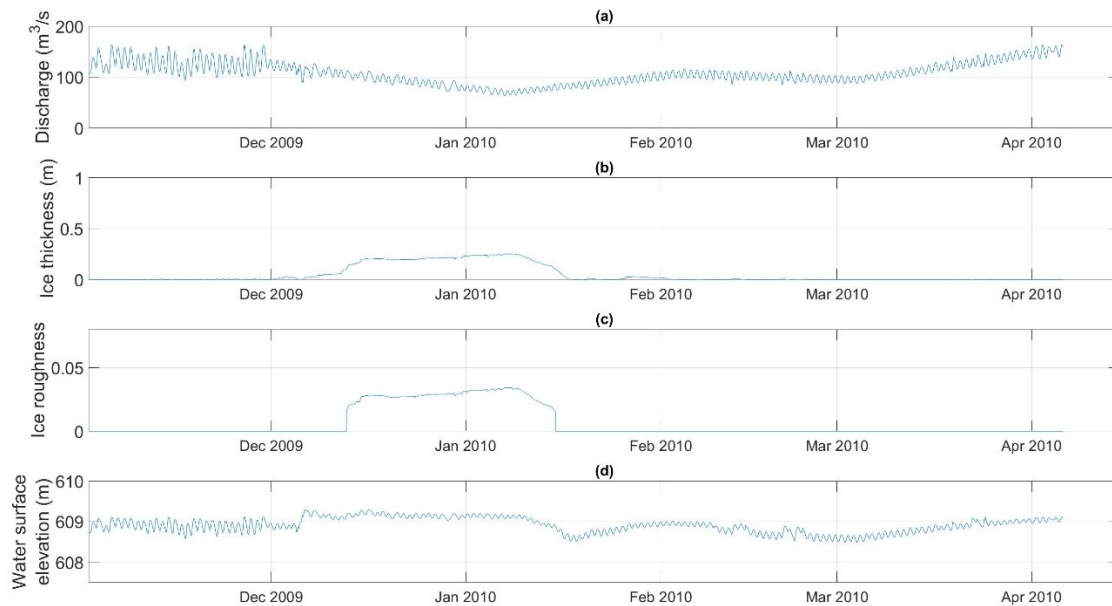
Figure 3-51. 2009-10 simulated results for (a) discharge, (b) solid ice thickness, (c) ice roughness, and (d) water surface elevation at Station 28.55 km.

3.5. Sensitivity analyses

Each of the following sensitivity analyses were conducted using the calibration model results (2010-11) as a baseline.

3.5.1. Ice front progression sensitivity analysis

Single variable sensitivity analysis was conducted to assess the effect of several variables and parameters on the ice front propagation. The simulated ice front progression as shown in Figure 3-14 is considered a baseline for the sensitivity analysis and all results from additional simulations are compared to it. A range of reasonable parameter values, extracted from those found in the literature and listed in Table 13, were selected for the sensitivity analysis. A summary of the simulations and their results is provided in Table 19. Plots showing the simulated results of the sensitivity analysis are presented in Figure 3-52 - Figure 3-61. The effect on the ice front propagation shown in Table 19 is in relation to the other values used for each parameter and is not for comparison between different parameters.

The ice front propagation was by far most sensitive to the maximum Froude number for ice front propagation. The value used in the baseline, 0.13, is at the upper limit of values

found in the literature and both values used in the sensitivity analysis, 0.105 and 0.08, returned a slower ice front propagation as shown in Figure 3-52. In the baseline simulation, the ice front arrived at the upstream boundary, Station 0.00 km, at 03:30 on 22nd November 2010. When the maximum Froude number for ice front propagation was set to the lowest value of 0.08 the ice front did not arrive at the upstream boundary until after 2nd December 2010. However, once the ice front was delayed beyond 22nd November, the delay was further exacerbated as the surface ice concentration at the upstream boundary reduced to zero at 11:00 on 22nd November. At the time that the ice supply was cut off, the ice front was 14 hours and 23.5 hours behind the baseline with the maximum Froude number for ice front propagation was set to 0.105 and 0.08, respectively.

Figure 3-53 shows the sensitivity of the ice front propagation to changes in the frazil slush porosity. Three values were used in this sensitivity analysis: 0.4, 0.6 (baseline) and 0.67. Reducing the frazil slush porosity from the baseline to the minimum value of 0.4 resulted in the arrival of the ice front at the upstream boundary 12.5 hours earlier. The ice front which was initiated at the model's downstream boundary arrived at the upstream bridging locations in advance of the bridging time and as such only a single ice front was simulated. The baseline value for the frazil slush porosity, 0.6, is close to the highest published value of 0.67 found in the literature. Nonetheless, an increase in frazil slush porosity from 0.6 to 0.67 resulted in the simulated ice front arriving at the upstream boundary 5 hours later than the baseline simulation.

The ice front progression was not overly sensitive to the maximum velocity for dynamic border ice growth. Values of 1.2 m/s, 0.8 m/s (baseline), and 0.4 m/s were used in this sensitivity analysis. Each of the three ice fronts arrived at the upstream boundary within 5 hours of each other as shown in Figure 3-54. When the maximum velocity for border ice growth was set to 0.4 m/s and 1.2 m/s, the ice front's arrival at the upstream boundary was delayed by 5 and 2 hours, respectively. Between the study's downstream boundary (Station 28.84 km) and Station 11.00 km, the ice front progression was quickest with the maximum velocity for dynamic border ice progression set to 0.4 m/s.

The sensitivity of the ice front progression to the thickness of newly formed ice pans is shown in Figure 3-55. Increasing the thickness of newly formed ice pans from the baseline value of 0.14 m to 0.20 m caused no change in ice front propagation. Decreasing the thickness of newly formed ice pans to 0.10 m caused little change in the ice front progression except between Station 11.00 km and the upstream boundary, where it was slower. This ice front arrived at the upstream boundary 3.3 days later than in the baseline. However, the front arrived at Station 0.33 km only 8.5 hours later than the baseline simulation and the additional delay between Stations 0.33 km and the upstream boundary is attributed to a lack of ice supply.

This sensitivity analysis also included running simulations for the maximum Froude number for ice front progression via juxtapositioning (Figure 3-56), the rate of frazil rise (Figure 3-57) and the porosity between pans at the ice front (Figure 3-58). However, the ice front propagation was largely insensitive to these parameters.

In addition to testing the sensitivity of the ice front propagation to parameter values, the effect of adjusting the upstream boundary conditions for water temperature, incoming pan thickness and the surface ice concentration was also tested. The ice front propagation was insensitive to the water temperature condition at the upstream boundary with negligible change in the front propagation when the water temperature was adjusted by $\pm$ 15% (Figure 3-59).

The incoming pan thicknesses were varied by $\pm$ 20% compared to the baseline, and the resulting ice front propagations are presented in Figure 3-60. Increasing the incoming pan thicknesses by 20%, relative to the baseline, caused a faster ice front propagation between the downstream boundary and Station 5.36 km. This ice front slowed between Station 5.36 km and the upstream boundary and arrived at the upstream boundary at the same time as the baseline simulation. Reducing the incoming pan thicknesses by 20% caused the ice front progression to slow throughout the study reach and the arrival of the ice front at the upstream boundary was delayed by 4.5 hours.

Finally, the sensitivity of the ice front progression to the surface ice concentration condition at the upstream boundary was tested by running simulations with $\pm$ 20% from

the baseline simulation. The results are shown in Figure 3-61. Increasing the surface ice concentration by 20% caused the ice front progression to speed up, especially downstream of Station 5.36 km. The ice front slowed upstream of Station 5.36 km and arrived at the upstream boundary 0.5 hours earlier than the baseline simulation. Reducing the surface ice concentration by 20% caused the ice front propagation to slow down throughout the entire study reach. In this simulation, the ice front arrived at the upstream boundary condition 5 hours later than the baseline.

Table 19. Ice front propagation sensitivity analysis results.

Parameter/ variable	Values tested	Effect on ice front propagation	Arrival of ice front at Station 0 km relative to baseline (hours)
Maximum Froude number for ice front progression	0.13	Baseline	N/A
	0.105	Slower	108.5*
	0.08	Slowest	>240*
Maximum Froude number for ice front progression via juxtapositioning	0.06	Baseline	N/A
	0.04	Faster	-0.5
	0.13	Slower	0.5
Rate of frazil rise (m/s)	0.00100	Baseline	N/A
	0.01350	Slowest	2
	0.00004	Slower	1
Frazil slush porosity	0.6	Baseline	N/A
	067	Slower	5
	0.4	Faster	-12.5
Maximum velocity for border ice growth (m/s)	0.8	Baseline	N/A
	0.4	Slowest	5
	1.2	Slower	2
New pan thickness (m)	0.14	Baseline	N/A
	0.10	Slower	79*
	0.20	Same	0
Porosity between pans at the ice front	0.60	Baseline	N/A
	0.67	Same	0
	0.40	Faster	-0.5
Boundary condition: water temperature	Baseline	Baseline	N/A
	+ 15 %	Same	0
	- 15 %	Same	0
Boundary condition: incoming pan thickness	Baseline	Baseline	N/A
	+ 20 %	Slower	4.5
	- 20 %	Faster	0
Boundary condition: surface ice concentration	Baseline	Baseline	
	+ 20 %	Faster	-0.5
	- 20 %	Slower	5

*Delay of ice front propagation to Station 0 km exacerbated by lack of ice supply.
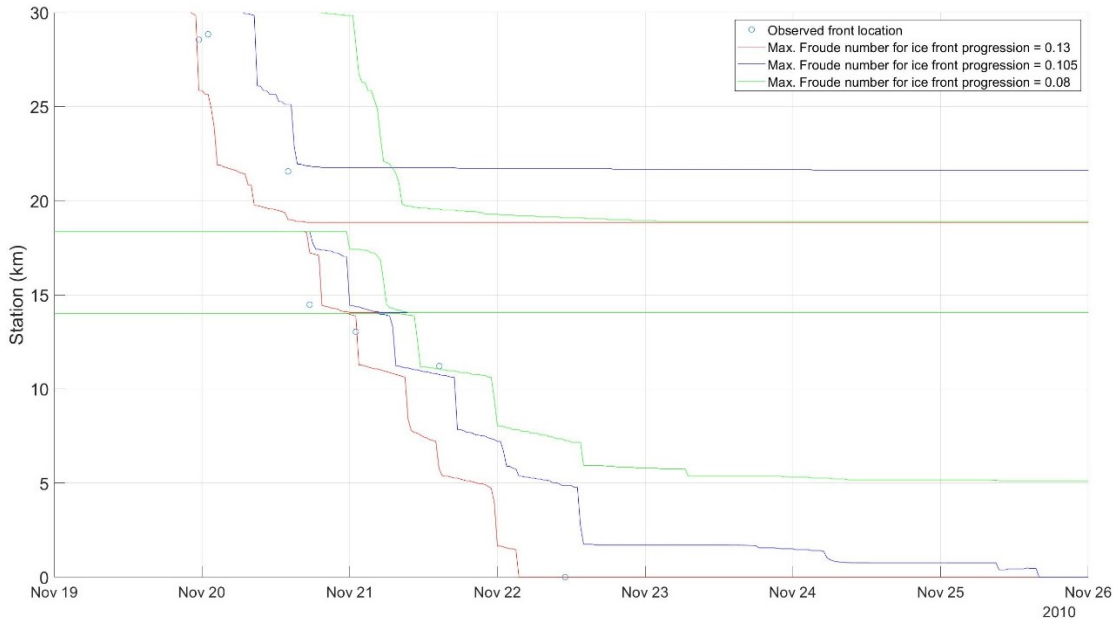
Figure 3-52. Ice front propagation sensitivity analysis: maximum Froude number for ice front progression.
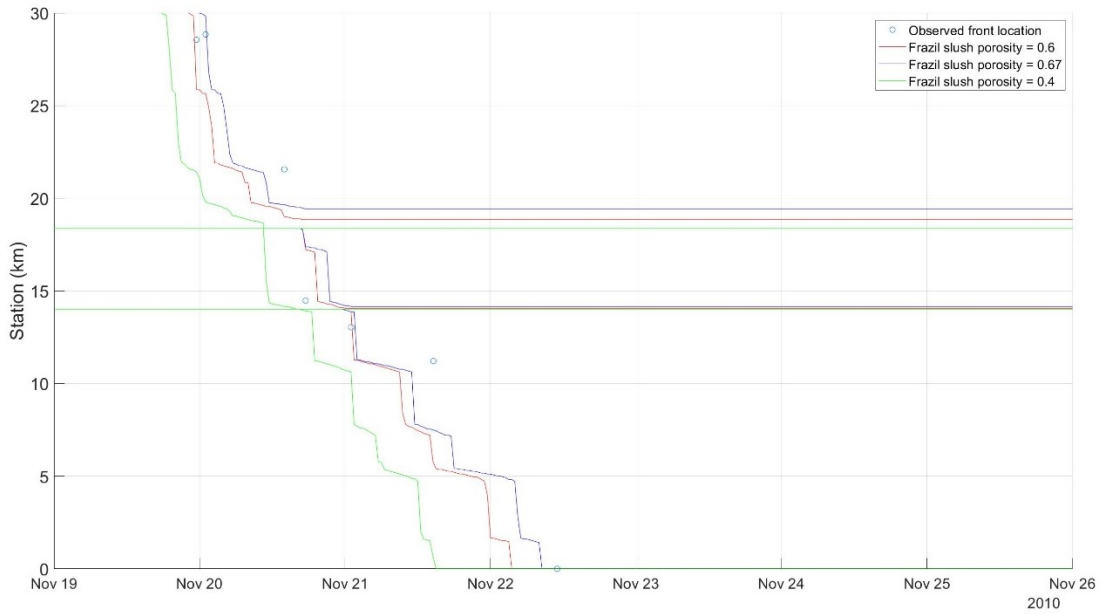
Figure 3-53. Ice front propagation sensitivity analysis: frazil slush porosity
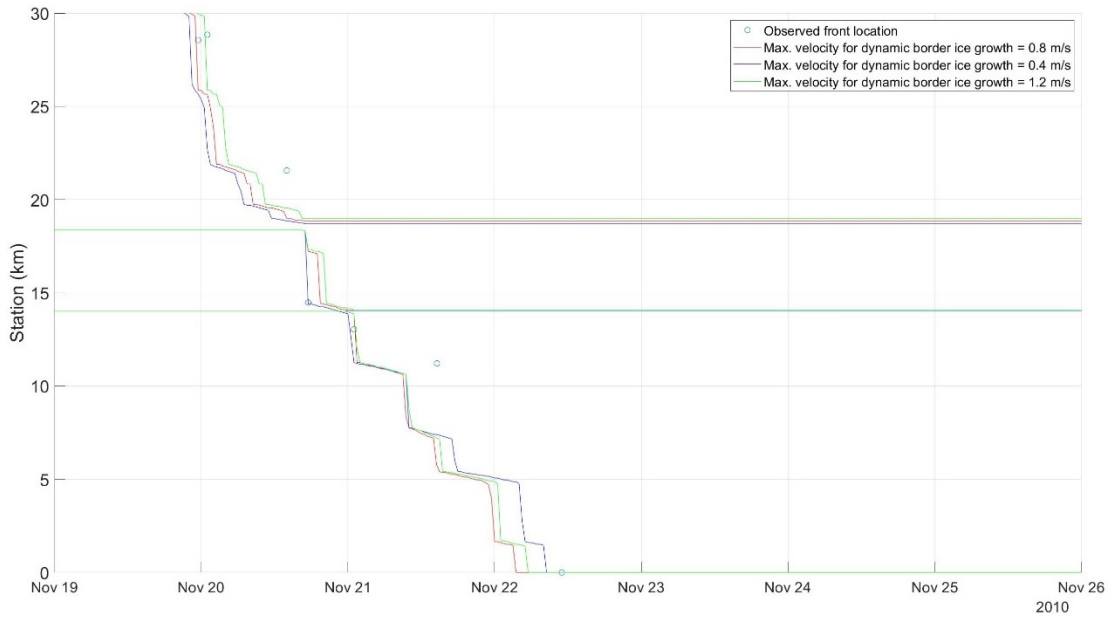
Figure 3-54. Ice front propagation sensitivity analysis: maximum velocity for dynamic border ice growth.

Figure 3-55. Ice front propagation sensitivity analysis: thickness of newly formed ice pans.
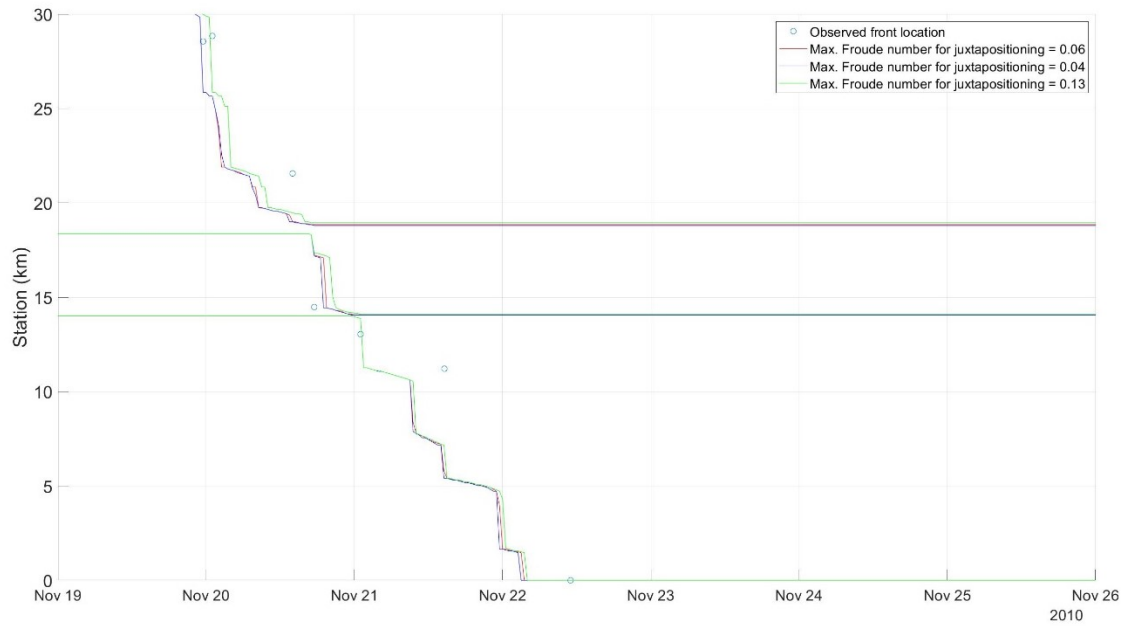
Figure 3-56. Ice front propagation sensitivity analysis: maximum Froude number for ice front progression via juxtapositioning.

Figure 3-57. Ice front propagation sensitivity analysis: rate of frazil rise.
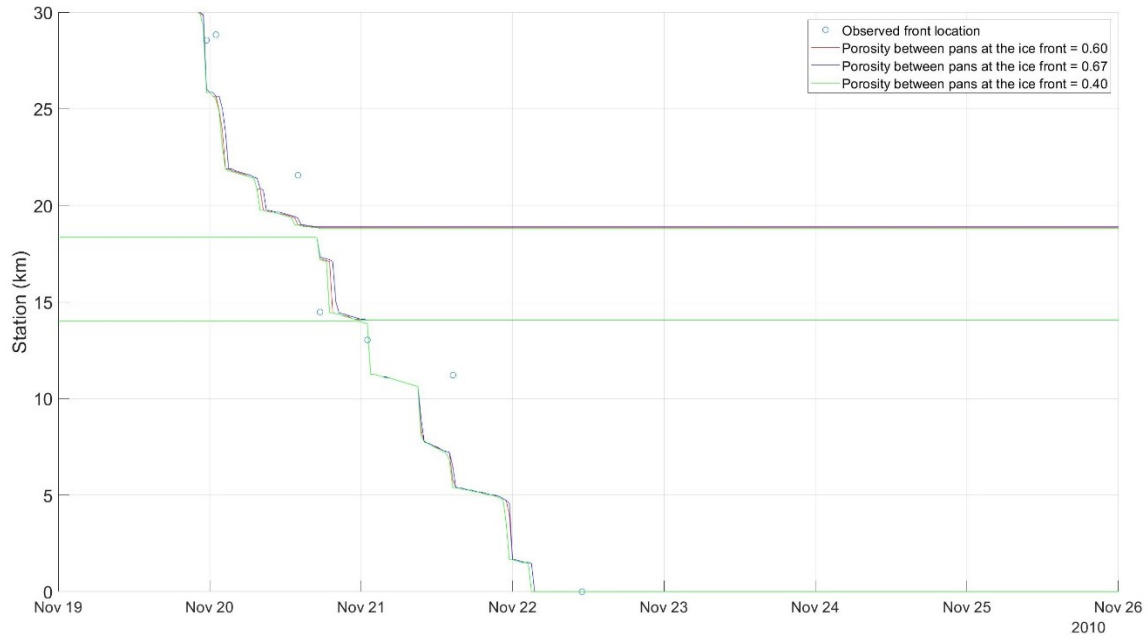
Figure 3-58. Ice front propagation sensitivity analysis: porosity between pans at the ice front.

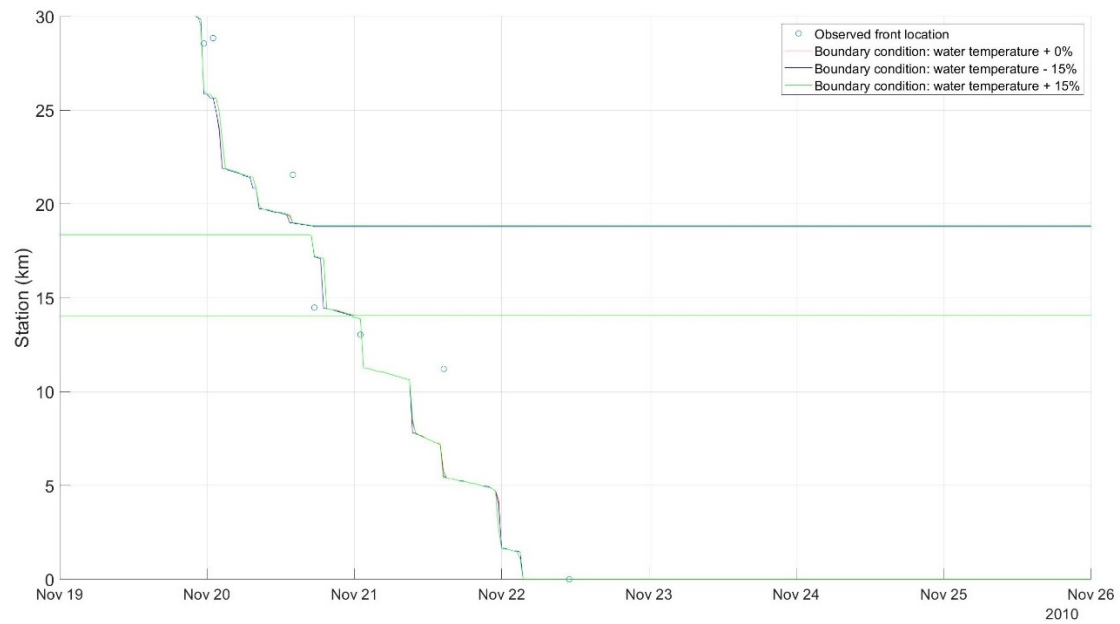Figure 3-59. Ice front propagation sensitivity analysis: water temperature condition at the upstream boundary.
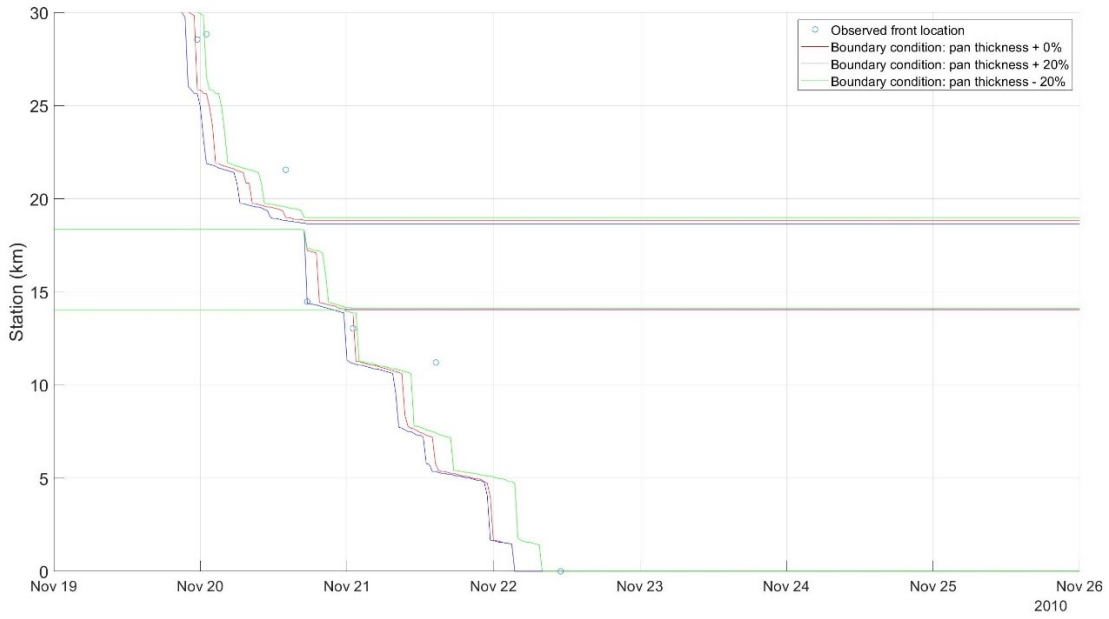
Figure 3-60. Ice front propagation sensitivity analysis: incoming pan thickness condition at the upstream boundary.
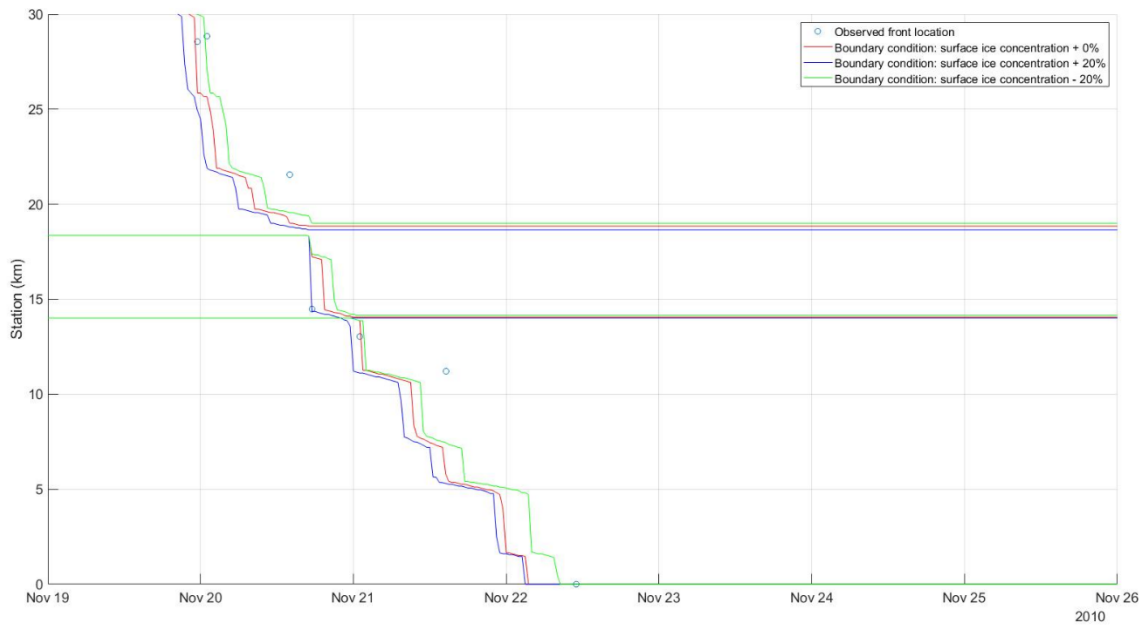
Figure 3-61. Ice front propagation sensitivity analysis: surface ice concentration condition at the upstream boundary.

3.5.2. GBWTP sensitivity analysis

A simple sensitivity analysis was performed to investigate the influence of GBWTP on the surface ice concentration. Figure 3-62 shows the surface ice concentrations at Station 11.26 km, 13.04 km, 23.74 km and 27.53 km both with the GBWTP inflow present in the model and without the GBWTP inflow. The simulated surface ice concentration at both Station 11.26 km and Station 13.04 km are unaffected by the presence of GBWTP and this is to be expected given these stations are approximately 11 km and 9 km, respectively, upstream of GBWTP. There is a significant difference in the simulated results at Stations 23.74 km and 27.53 km when the GBWTP inflow was removed from the model. Instead of the pattern of periodic open water conditions as was experienced with the GBWTP inflow present, a stable and ice cover formed and remained in place until break-up in April 2011.

The sensitivity of the ice thickness to the inclusion or exclusion of GBWTP from the model was also tested. Figure 3-63 compares the combined frazil slush and solid ice thicknesses between simulations with and without the GBWTP outflow included in the model. At Station 6.87 km, Figure 3-63a, there is no difference between the two simulations. Figure 3-63b shows the simulated ice thicknesses at Station 21.99 km, immediately upstream of GBWTP. The timing of the increase in ice thickness beginning on 16th November is very similar between the two simulations. The maximum ice thicknesses simulated at the time of freeze-up, between 16th November and 23rd November, was also similar with a maximum ice thickness of 2.15 m with GBWTP included and a maximum ice thickness of 2.32 m with GBWTP excluded from the model. At this location, there was a significant difference in the two simulations following freeze-up. When GBWTP was included, the simulated ice thickness dropped to 0.3 m by 28th November. In contrast, when GBWTP was excluded from the model, the simulated ice thickness remained elevated, between 1.43 m and 1.81 m, until 5th January 2011. Although both simulations returned a similar trend in ice thicknesses from 5th January onwards, the simulated ice was approximately 0.1 m thicker in the simulation which excluded GBWTP.

The effects of the effluent from GBWTP on the ice thickness are more obvious at Station 23.04 km (Figure 3-63c). When GBWTP is excluded from the model, the spike in ice thickness begins on 16th November rather than on 11th December. Additionally, the thickness of the ice, which is predominantly slush ice at this time, is much greater, approximately 3.3 m rather than 1.9 m. The time at which the slush ice reduces at this station is similar between the two simulations, with a drop in ice thickness through January. Figure 3-64 shows the simulated solid ice thickness at Station 23.04 km with and without GBWTP included in the model. The model simulated solid ice growth through the mid-winter period, with a solid ice cover approximately 1 m thick apparent until beginning to melt in March. This was not present in the simulation when GBWTP was omitted from the model.

At Station 28.55 km (Figure 3-63c), the model simulated growth and reduction of solid ice in a similar pattern to that observed upstream of GBWTP. It should be noted that, relative to Station 21.99 km and 23.04 km, there was minimal frazil slush simulated at this location during either simulation. This sensitivity analysis confirms that although the model is not completely capturing the openings that appeared after the passing of the ice front, the outflow is influencing the simulated slush and solid ice thicknesses.
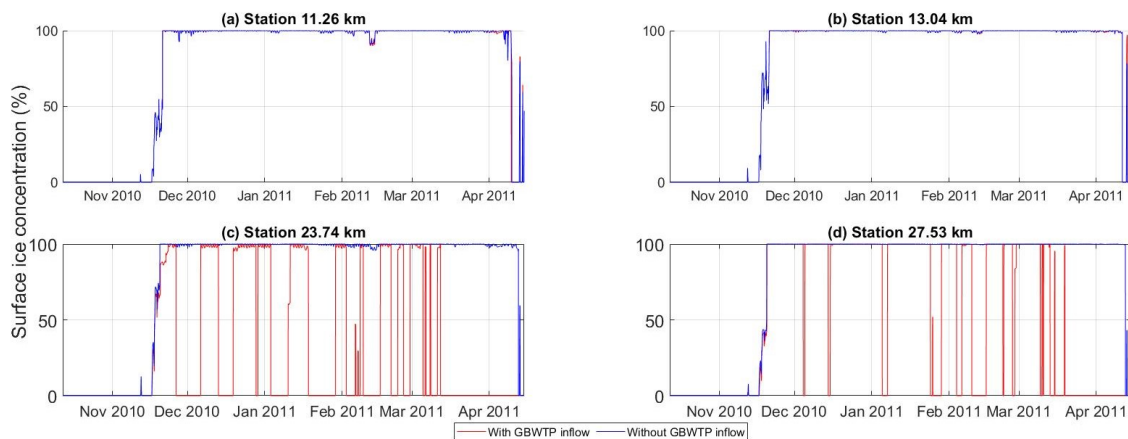
Figure 3-62. Sensitivity analysis showing the surface ice concentrations at (a) Station 11.26 km, (b) Station 13.04 km, (c) Station 23.74 km, and (d) Station 27.53 km with (red) and without (blue) the lateral inflow from GBWTP.
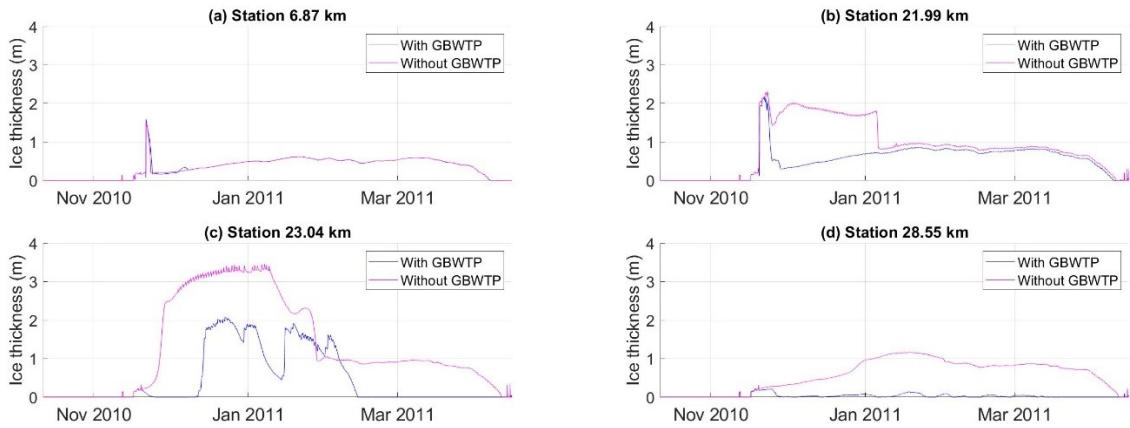
Figure 3-63. Sensitivity analysis showing the combined frazil slush and solid ice thicknesses at (a) Station 6.87 km, (b) Station 21.99 km, (c) Station 23.04 km, and (d) Station 28.55 km with (blue) and without (magenta) the lateral inflow from GBWTP.
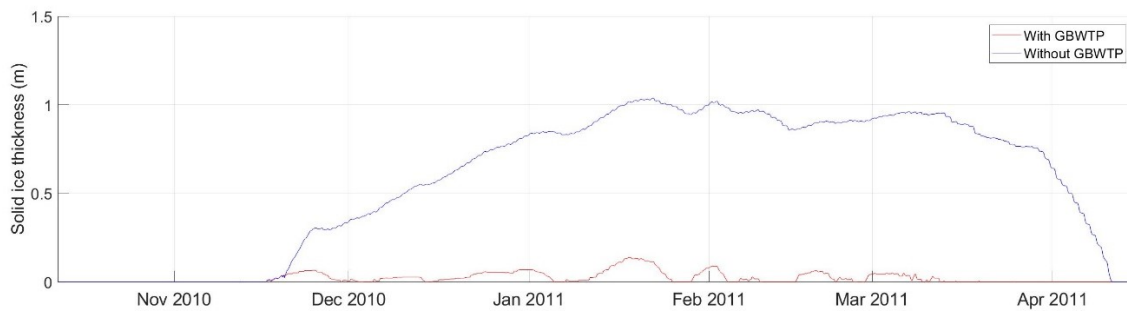
Figure 3-64. Sensitivity analysis showing the solid ice thickness at Station 23.04 km with and without GBWTP included in the model.

3.5.3. Ice roughness sensitivity analysis

A sensitivity analysis was conducted to investigate the effect of the ice roughness on the simulated water surface elevations. For the purposes of this sensitivity analysis, the model simulation presented in Section 3.3, in which the ice roughness was calculated based upon the solid ice thickness following Nezhikhovskiy (1964), is referred to as the baseline simulation. At Stations 14.48 km and 21.32 km, the maximum ice roughness calculated by the baseline model was 0.064. These values are within the range of values, 0.04 – 0.1, identified by Beltaos (2001) as the roughness of a break-up ice jam. The ice roughness values calculated by the model are also significantly higher than those

suggested by Carey (1966) for rippled ice covers such as those which are affected by warm water discharge from urban outfalls.

Two additional simulations, using user-specified ice roughness values of 0.045 and 0.03 were performed. The results of these simulations are compared with the baseline simulation during freeze-up in Figure 3-65. During freeze-up, the user-defined ice roughness values are higher than the baseline and as such, there is a pattern of higher magnitude stage-up with the user-defined ice roughness values. The higher roughness values also caused an earlier stage-up, indicative of a faster front progression. This is likely due to the ice roughness causing a more significant backwater effect and generating more favorable flow conditions for front propagation. The highest magnitude stage-up was simulated with the user-defined ice roughness of 0.045 and the lowest magnitude stage-up was simulated in the baseline model. At Station 14.48 km, the peak water surface elevation was approximately 0.4 m higher with a user-defined ice roughness value of 0.045 when compared with the baseline simulation. In addition to this, stage-up began approximately 29 hours earlier. The differences in the timing and magnitude of stage-up is less noticeable at Stations 28.02 km, 28.55 km and 28.84 km where the ice effects are reduced by the GBWTP outflow.

Figure 3-66 shows the water surface elevations of the three simulations for the entire simulation period. As the simulations progressed into the mid-winter period, the simulated ice thicknesses at stations upstream of GBWTP increased and the ice roughness values in the baseline model also increased. By 19th December 2010, the ice roughness of the baseline simulation had surpassed both of the user-defined ice roughness values and as such the baseline model simulated higher water surface elevations. At the stations downstream of GBWTP, Stations 22.51 km, 28.02 km, 28.55 km and 28.84 km, the pattern is less clear. During period when no ice cover was present in the models, the water surface elevations simulated by the models was equal – for example between 10th – 16th February 2011 at Station 22.51 km. When ice was present in the model, the highest water surface elevation was simulated by the model with the user-defined ice roughness of 0,045, followed by the model with the user-defined ice roughness of 0.03 and the lowest water surface elevations were simulated by the baseline model.
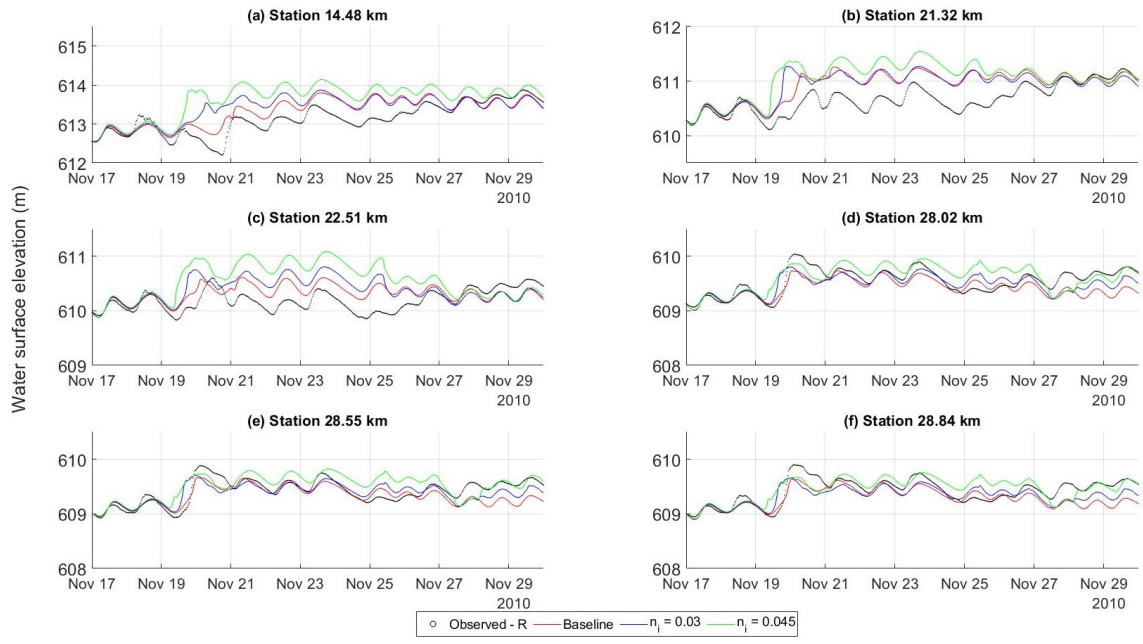
Figure 3-65. Sensitivity analysis showing water surface elevations during freeze-up at Stations (a) 14.48 km, (b) 21.32 km, (c) 22.51 km, (d) 28.02 km, (e) 28.55 km, and (f) 28.84 km under different ice roughness conditions.
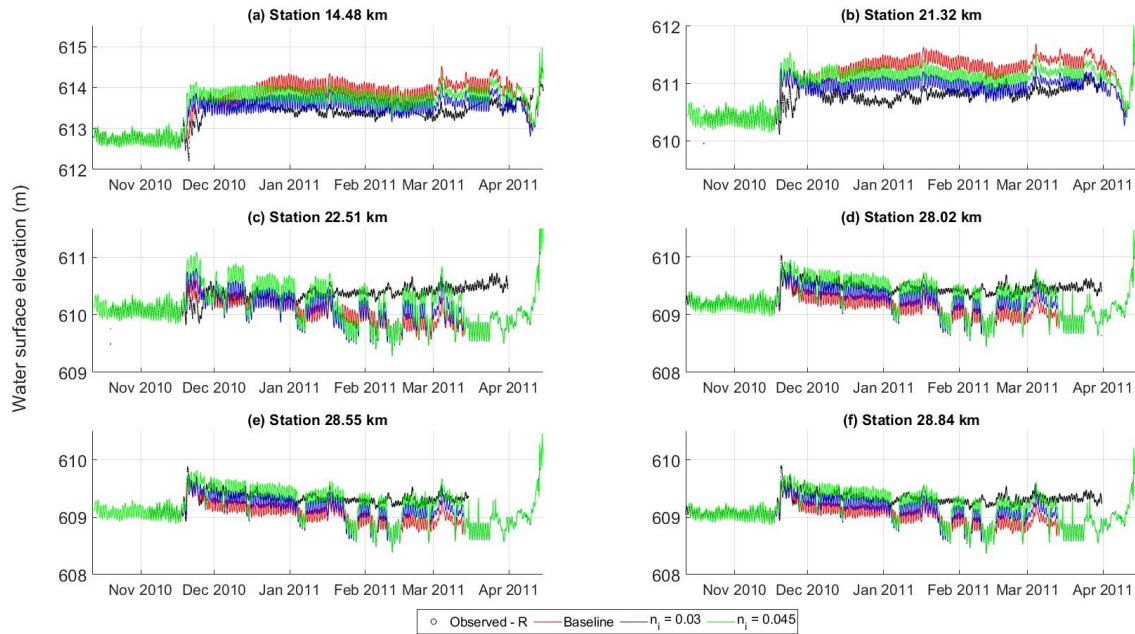
Figure 3-66. Sensitivity analysis showing water surface elevations at Stations (a) 14.48 km, (b) 21.32 km, (c) 22.51 km, (d) 28.02 km, (e) 28.55 km, and (f) 28.84 km under different ice roughness conditions.

3.5.4. Conclusions

A hydraulic model of the NSR through Edmonton, capable of simulating river ice processes through the entire winter season, has been developed. The model has been successfully calibrated and validated using a comprehensive data set from the 2010-11 and 2009-10 winter seasons. Strong agreement between the observed and simulated data was achieved for an unprecedented number of ice variables was achieved. The particularly strong simulation results for the water temperatures and suspended frazil concentrations are encouraging and suggest that the model could be used to help address the problem of blockages of water intakes within the study reach. Although the model did not perfectly replicate the open lead, the effect of the warm water discharge was apparent in the simulated surface ice concentrations, and the solid and frazil slush thicknesses.

Sensitivity analysis has identified the ice front progression to be most sensitive to the maximum Froude number for ice front propagation and the frazil slush porosity. The ice front was also sensitive to the surface ice concentration and the incoming pan thicknesses

as defined in the upstream boundary condition. This emphasizes the importance of robust boundary conditions.

4.0 Summary and conclusions[1]

Modified sections of this chapter have been published in in the Committee on River Ice Processes and the Environment's 20th Workshop on River Ice (Howley et al., 2019) and the International Association for Hydro-Environment Engineering and Research's 25th Symposium on Ice (Howley et al., 2020).

4.1. River ice regime of the North Saskatchewan River through Edmonton

In addition to providing a brief review of previous works conducted along the NSR through Edmonton, this thesis presents a summary of the meteorological, hydrometric and river ice data available for the study reach. The data analyses conducted in this study show that the ice regime in the NSR is highly complex with evidence of several interesting processes such as bridging, ice front progression in both juxtaposed and mechanical thickening modes, consolidation events and ice jams, thermal ice growth and the development of open leads having been observed within the study reach.

The DDF for the formation of a complete or stable ice cover ranged between 52 °C·Days and 208 °C·Days. Lower DDF values were identified for freeze-up events which occurred later in the season.

Stage-up is highly variable with rises of between 0.8 m and 1.9 m having been recorded between 2009 and 2019. There is evidence that several complex processes, including mechanical thickening, freeze-up jams, and consolidation and mobilization events have occurred within the study reach. A weak correlation showing higher magnitude stage-up with higher pre-stage-up depths has been identified. A second relationship, linking the warmer average daily air temperature on the day of freeze-up with higher stage-up depth, was also identified.

Between 2009-2019, the ice front progression rate was found to vary between 0.96 – 8.6 km/day. Further analysis of the progression rate through the entire study reach in 2010 revealed different progression rates, between 3.9 km/day and 14.2 km/day, through different sections of the river. Slower ice front progression rates were identified in steeper sections of the river and faster ice front progression was observed in more gradual sections of the river.

A novel approach for relating the degree minutes of supercooling, or the intensity of supercooling, to the peak suspended frazil concentration has been proposed. The approach utilizes an empirical coefficient, β_1, which must be calibrated. Using suspended frazil concentrations derived from the SWIPS data, β_1 coefficients of 0.0013 °C $^{1/2}$·min$^{-1/2}$ and 0.0074 °C $^{1/2}$·min$^{-1/2}$ were calibrated for 2010-11 and 2009-10, respectively.

The Stefan equation was found to be a reasonable predictor of the ice thickness at Station 6.87 km when an α_1 value of 0.019 m°C$^{-1/2}$Day$^{-1/2}$ is used, albeit with some outlying results. Between 2010-2020 the DDT for break-up ranged between 4 °C·Days and 74 °C·Days. An interesting trend of decreasing DDT values in years in which break-up occurred later was identified. A linear heat transfer model was calibrated to predict break-up. A linear heat transfer coefficient of 12 W/m^2°C and an albedo value of 0.5 were applied and in each of the years between 2009-2014 the linear heat transfer model was able to predict break-up to within 13 days of the observed break-up.

These empirical methods appear to capture the characteristics of the NSRs river ice regime. However, many contributing factors have been neglected. This can be seen from the wide range of DDF and DDT values, the scatter of the ice thickness and peak frazil concentration data when plotted against DDF or DMS and the error in predicting break-up using the linear heat transfer model.

4.2. Modeling of an urban river with River1D

A hydraulic model of the NSR, capable of simulating the river ice processes of the study reach, has been successfully developed, calibrated and validated. The model performed well in simulating several variables and strong agreement between the observed and simulated data was achieved for an unprecedented number of river ice variables.

The model performed exceptionally well in simulating water temperatures, capturing both the cooling trend during freeze-up and the timing of the zero-degree isotherm in 2010-11. Although the simulated water temperatures in 2009-10 were also encouraging, the model did not perform as well at Station 28.55 km and this has emphasized the importance of robust upstream boundary conditions. The ice front propagation was

successfully simulated in both calibration and validation models, with the ice front passing within 11.5 hours and 9 hours of the observed data in 2010 and 2009, respectively.

Closely linked to the ice front progression is the timing of stage-up, which matched well with the observed data in both 2010 and 2009. Agreement between the magnitude of simulated and observed stage-up was also impressive, with similar peak water surface elevation values following stage-up. However, the duration of stage up did differ in the model when compared to the observed data. Stage-up in the model was more abrupt, in 2010 occurring 133.5 hours quicker in the model when compared to the observed. Upstream of GBWTP, the model overestimated the mid-winter water surface elevations in both calibration and validation simulations.

The model was able to capture the timing of rapid increase in surface ice concentration in both calibration and validation simulations. Although the model struggled to replicate the open lead downstream of GBWTP, fluctuations in the surface ice concentration were simulated along with several periodic reductions in the surface ice concentration down to 0%.

The particularly strong simulation results for suspended frazil concentration in 2010-11 are encouraging. The simulated suspended concentrations ranged between 0.001% and 0.061% and are of the same order of magnitude as measured concentrations of suspended frazil published in the literature.

The model was successful in simulating ice thicknesses at Station 6.87 km to within 9 cm of the WSC measured ice thicknesses of 2010-11. In the validation model, the simulated ice thicknesses deviated up to 23 cm from the WSC measured ice thicknesses. Despite this, the model did capture the trend of ice growth during both calibration and validation simulations. Although the model's performance in simulating the retreat of the ice front was less successful, the timing of the reduction of ice thickness to zero was identified as a reasonable surrogate indicator for simulated break-up. On each occasion, the simulated ice thickness reduced to zero within 4.5 days of observed break-up.

Single variate sensitivity analysis was conducted, and the simulated ice front progression was found to be most sensitive to the maximum Froude number for ice front progression, frazil slush porosity, and the pan thickness and surface ice concentration defined in the upstream boundary condition.

The surface ice concentration upstream of GBWTP was unaffected by the presence or absence of the GBWTP outflow. However, predictably, the periodic open water conditions that were simulated when the GBWTP outflow was included in the model was replaced by a stable ice cover when the GBWTP outflow was excluded from the model. The ice thickness downstream of GBWTP was also very sensitive to the presence or absence of the GBWTP outflow.

4.3. Recommendations for future research

The modeling efforts summarized in this thesis are a strong foundation on which additional work may be accomplished. The model may be applied in a predictive manner, especially given the strong performance in simulating the ice front propagation and the suspended frazil concentrations. Aerial images of the study reach have identified 7 areas where surface ice congestion has occurred. Further data collection programs could be implemented to verify whether these locations develop into bridging locations and to confirm whether the bridging locations remain the same from year to year. Additionally, the development and integration of bridging criteria into the model would remove the requirement for user-defined bridging locations and enhance the predictive capability of the model.

The 2019-20 ice season saw the formation of freeze-up and break-up ice jams. This phenomenon, which to the author's knowledge has not previously been documented within the study reach, could be indicative of a changing regime and future research could use the River1D model of the NSR to investigate what other changes might be expected under changing conditions and/or climate.

A novel method linking the peak suspended frazil concentration with the magnitude of supercooling has been proposed. However, more data, particularly from higher intensity and higher concentration frazil events, are required to verify the proposed DMS method.

The model's strong performance in simulating the suspended frazil concentrations indicates that the model could be used to help address the issue of blockages of water intakes by frazil ice. Acquisition of data relating to the timing and magnitude of such blockages would be required for such an exercise.

It may be possible to optimize the model for break-up prediction. This could be of benefit to the operators of Edmonton's two drinking water plants, who are concerned with the rapid increase in water turbidity associated with river ice break-up. Furthermore, consideration could be given to adjusting the way that River1D handles the ice front retreat and to integrating dynamic break-up processes into the model.

One of the bigger challenges with this research has been the uncertainty in the model boundary conditions. It is recommended that future works include the implementation of a field data collection program designed specifically for a modeling project. The collection of data at the model boundary is key to improving confidence in model results. Alternatively, it may be possible to extend the model upstream to remove the reliance on the boundary condition and instead allow the ice variables which are included in the upstream boundary condition to instead be produced by the model. Finally, the use of a 2D model is recommended for further investigations of the GBWTP open lead.

References

Alfredsen, K., 2015. Modelling ice effects on head loss at hydropower intakes. 18th Workshop on the Hydraulics of Ice Covered Rivers. Quebec City, Quebec, Canada, Committee on River Ice Processes and the Environment.

Andres, D. 1988. Observation and prediction of the 1986 breakup on the Athabasce River upstream of Fort McMurray, Alberta. Alberta Research Council Report No. SWE-88/03.

Andres, D. 1999. The Effects of Freezing on the Stability of a Juxtaposed Ice Cover. The 10th Workshop on the Hydraulics of Ice Covered Rivers, Winnipeg, Manitoba, Canada, Committee on Rver Ice Processes and the Environment.

Andres, D. and Van Der Vinne, G. 2001. Calibration of Ice Growth Models for Bare and Snow Covered Conditions: A Summary of Experimental Data from a Small Prairie Pond. The 11th Workshop on the Hydraulics of Ice Covered Rivers, Ottawa, Ontario, Canada, Committee on River Ice Processes and the Environment.

Andres, D. Van Der Vinne, G., Johnson, B. and Fonstad, G. 2003. Ice Consolidation on the Peace River: Release Patterns and Downstream Surge Characteristics. 12th Workshop on the Hydraulics of Ice Covered Rivers, Edmonton, Alberta, Canada, June 19-20, 2003, Committee on River Ice Processes and the Environment.

Andrishak, R. and Hicks, F. 2005. Impact of Climate Change on the Winter Regime of the Peace River in Alberta. Prepared for: Climate Change Research Users Group, Alberta Environment.

Andrishak, R., Hicks, F., 2008. Simulating the effects of climate change on the regime of the Peace River. Canadian Journal of Civil Engineering 35, 461–472.

Ashton, G.D. 1973. Heat transfer to ricer ice covers. Proceedings of the 30th Eastern Snow Conference, Amherst, Massachusas, 8-9 February 1973. Eastern Snow Conference, Monmouth, Maine, pp.125-135.

Ashton, G. D., 1979. River Ice: The presence of ice on rivers changes their behavior, interferes with their use, and causes severe economic disruption. American Scientist. Vol. 67, No. 1, pp38-45.

Ashton, G.D. (Ed.), 1986. River and Lake Ice Engineering. Water Resources Publications, Littleton, Colorado.

Ashton, G. D. 2011. River and lake ice thickening, thinning, and snow ice formation. Cold Regions Science and Technology 68 pp3-19.

Beltaos, S. (Ed), 1995. River Ice Jams. Water Resources Publications, Littleton, Colorado.

Beltaos, S. 2001. Hydraulic roughness of breakup ice jams. ASCE Journal of Hydraulic Engineering, 127(8) pp650-656.

Beltaos, S. 2013. Chapter 7 - Freezeup Jamming and Formation of Ice Cover, in River Ice Formation, (S, Beltaos, ed.), Committee on River Ice Processes and the Environment, Edmonton, Alberta, 181-255.

Beltaos, S. and Tang, P. 2013. Applying HEC-RAS to simulate river ice jams: snags and practical hints. 17th Workshop on River Ice, Edmonton, Alberta, Canada, July 12-24, 2013, Committee on River Ice Processes and the Environment.

Beltaos, S. and Wong, J. 1986. Downstream transition of river ice jams. ASCE Journal of Hydraulic Engineering, 112 (2), pp91-110.

Beltaos, S., Burrell, B., Miller, L. and Sullivan, D. 2003. Hydraulic Interaction Between Ice And Bridges. 12th Workshop on the Hydraulics of Ice Covered Rivers, Edmonton, Alberta, Canada, June 19-20, Committee on River Ice Processes and the Environment.

Bijeljanin, M. and Clark, S. P. 2011. Application of Numerical Modelling Towards Prediction of River Ice Formation on the Upper Nelson River. 16th Workshop on

River Ice, Winnipeg, Manitoba, September 18-22, 2011, Committee on River Ice Processes and the Environment.

Blackburn, J. and She, Y., 2019. A comprehensive public-domain river ice process model and its application to a complex natural river. Cold Regions Science and Technology. 163, 44-58.

Blackburn, J., She, Y., Hicks, F. and Nafziger, J. 2015. Ice Effects on Flow Distribution in the Mackenzie Delta. 18th Workshop on the Hydraulics of Ice Covered Rivers, Quebec City, Quebec, Canada, August 18-20, 2015, Committee on River Ice Processes and the Environment.

Brayall, M. and Hicks, F. E. 2012. Applicabilty of 2-D modeling for forecasting ice jam flood levels in the Hay River Delta, Canada.Canadian Journal of Civil Engineering, 39.

Brown, R. S., Power, G., Beltaos, S., and Beddow, T.A. 2000. Effects of hanging ice dams on winter movements and swimming activity of fish. Journal of Fish Biology. 57, 1150-1159.

Carson, R.W. and Groeneveld, J.L. 1997. Evolution of the ICESIM Model. The 9th Workshop on River Ice, Fredericton, New Brunswick, Canada. Committee on River Ice Processes and the Environment.

Calkins, D.J. 1984. Instream Ice Calibration of Computer Model. Alaska Power Authority

Carey, K.L. 1966. Observed configuration and computed roughness of the underside of river ice, St Croix River, Wisconsin. Geological Survey Research, U.S. Geological Survey Professional Paper 550-B, B192-B198

Chen, Y., and She. Y. 2019. Temporal and Spatial Variations of River Ice Breakup Timing across Canada. 20th Workshop on the Hydraulics of Ice Covered Rivers. Ottawa, Ontario, Canada, Committee on River Ice Processes and the Environment.

Chen, F., Shen, H.T. and Jayasundara, N.C. 2006. A one-dimensional comprehensive river ice model. 18th International Symposium on Ice, Sapporo, Japan, 28th August – 1st September 2006. International Association of Hydro-Envionment Engineering and Research.

Choles, J. 1997. Analysis of the Post-regulation Freeze-up Regime on the North Saskatchewan River. Masters of Science Thesis in Water Resources Engineering. Department of Civil and Environmental Engineering, University of Alberta.

Clark, S. 2013. Chapter 3 - Border and Skim Ice, in River Ice Formation, (S. Beltaos, ed.). Committee on River Ice Processes and the Environment, Edmonton, Alberta, 77-106.

Comfort, G. and Abelnour, R. 2013. Ice Thickness Prediction: A Comparison of Various Practical Approaches. 17th Workshop on River Ice, Edmonton, Alberta Canada, July 21-24, 2013, Committee on River Ice Processes and the Environment.

Daly, S. 1991. Frazil Ice Blockage of Intake Trash Racks. Cold Regions Technicl Digest, USA Cold Regions Research and Engineering Laboratory, Hanover, New Hampshire. 91(1).

Daly, S. 2013. Chapter 4 - Frazil Ice, in River Ice Formation, (S. Beltaos, ed.), Committee on River Ice Processes and the Environment, Edmonton, Alberta, 107-134.

Daly, S. and Ettema, R. 2006. Frazil Ice Blockage of Water Intakes in the Great Lakes. Journal of Hydraulic Engineering 132(8): 814-824.

Daly, S. and Vuyovich, C. 2003. Modeling river ice with HEC-RAS. 12th Workshop on the Hydraulics of Ice Covered Rivers, Edmonton, Alberta, Canada, June 19-20, 2003. River Ice Processes and the Environment, Committee on River Ice Processes and the Environment.

Environment Canada. 2013. RIVICE Model – User's Manual. Available online: http://giws.usask.ca/rivice/Manual/RIVICE_Manual_2013-01-11.pdf

Environment Canada. 2018. Real-Time Hydrometric Data Graph for North Saskatchewan River at Edmonton (05DF001) [AB] https://wateroffice.ec.gc.ca/report/real_time_e.html?stn=05DF001

EPCOR. 2020. Gold Bar Process & Operations https://www.epcor.com/about/who-we-are/where-we-operate/edmonton/Pages/gb-wastewater-treatment-plant.aspx

Flato, G. and Gerard, R. 1986. Calculation of ice jam thickness profiles. 4th Workshop on River Ice, Montreal, Quebec, Canada, Committee on River Ice Processes and the Environment

Gebre, S., Timalsina, N., and Alfredsen, K. 2014. Some Aspects of Ice-Hydropower Interaction in a Changing Climate. Energies, 7, 1641-1655.

Gerard, R. and Andres, D. 1982 Hydraulic roughness of freeze-up ice accumulations: North Saskatchewan River through Edmonton. 2nd Workshop on the Hydraulics of Ice Covered Rivers, Edmonton, Alberta, Canada, Committee on River Ice Processes and the Environment.

Ghobrial, T. R. 2012. Charaterization of Suspended Frazil and Surface Ice in Rivers Using Sonars. PhD Thesis, University of Alberta, Edmonton, Canada.

Ghobrial, T.R., Loewen, M., Hicks, F. and Maxwell, J. 2010. Monitoring Frazil Ice Evolution during Freeze-up using the Shallow Water Ice Profiling Sonar. 20th International Symposium on Ice, Lahti, Finland, June 14 – 18, 2010. International Association of Hydro-Envionment Engineering and Research.

Ghobrial, T.R., Loewen, M.R., and Hicks, F. 2013. Continuous monitoring of river ice during freeze-up using upward looking sonar. Cold Regions Science and Technology, 86: 69–85.

Girling, W. C., and Groeneveld, J. 1999. Anchor Ice Formation below Limestone Generating Station. 10th Workshop on the Hydraulics of Ice Covered Rivers, Winnipeg, Manitoba, Canada, Committee on River ice Processes and the Environment.

Hains, D., and Zabilansky, L. 2005. The Effects of River Ice on Scour and Sediment Transport. 13th Workshop on the Hydrauilics of Ice Covered Rivers, Hanover, New Hampshire, United States, Committee on River Ice Processes and the Environment.

Hicks, F. 1997. An analysis of historical freeze-up on the North Saskatchewan River below the Bighorn Dam. Prepared for TransAlta Utilities Corporation. 39 pp.

Hicks, F. 2016. An Introduction to River Ice Engineering for Civil Engineers and Geoscientists. CreateSpace Independent Publishing Platform. 159 pp.

Hicks, F. and Steffler, P. 1992. A characteristic dissipative galerkin scheme for open channel flow. ASCE Journal of Hydraulic Engineering, 118.

Hicks, F. Andrishak, R. and She, Y. 2009. Modeling Ice Cover Consolidation during Freeze-up on the Peace River, AB. 15th Workshop on River Ice, St John's, Newfoundland and Labrador, Canada, June 15-17, 2009, Committee on River Ice Processes and the Environment.

Howley, R., Ghobrial, T., and She, Y. 2019. Thermal regime in the North Saskatchewan River in Edmonton. 20th Workshop on the Hydraulics of Ice Covered Rivers, Ottawa, Ontario, Canada, Committee on River Ice Processes and the Environment.

Howley, R. She, Y. and Ghobrial, T. 2020. A Modeling Study of Complex River Ice Processes in an Urban River. 25th International Symposium on Ice, Trondheim, Norway, 23-25 November 2020. International Association of Hydro-Environment Engineering and Research.

IDG. 1995. North Saskatchewan River at Edmonton Flood Risk Mapping Study (Phase II – Upper Reach). Submitted to Alberta Environmental Protection.

Jasek, M. 2016. Investigations of anchor ice formation and release waves. Proceedings of the 23rd International Symposium on Ice, Ann Arbor, Michigan. International Association for Hydro-Environment Engineering and Research.

Jasek, M. 2019. An Emerging Picture of Peace River Break-up Types that Influence Ice Jam Flooding of the Peace-Athabasca Delta Part 2: Insights from the comparison of the 2014 and 2018 Break-ups. 20th Workshop on the Hydraulics of Ice Covered Rivers, Ottawa, Ontario, Canada, Committee on River Ice Processes and the Environment.

Jasek, M. and Lavelley, J. 2003. Safety during River Ice Data Collection. 12th Workshop on the Hydraulics of Ice Covered Rivers, Edmonton, Alberta, Canada, June 19-20, 2003, Committee on River Ice Processes and the Environment.

Jasek, M. and Pryse-Phillips, A. 2015. Influence of the proposed Site C hydroelectric project on the ice regime of the Peace River. Canadian Journal of Civil Engineering. 42. pp645-655.

Jasek, M., Ashton, G., Shen, H.T., and Chen, F. 2005. Numerical Modeling of Storage Release during Dynamic River Ice Break-up. 13th Workshop on the Hydraulics of Ice Covered Rivers, Hanover, New Hampshire, USA, September 15-16, 2005. Committee on River Ice Processes and the Environment.

Jasek, M., Ghobrial, T., Loewen, M., Hicks, F., 2011. Comparison of CRISSP modeled and SWIPS measured ice concentrations on the Peace River. Proc. 16th Workshop on River Ice, Winnipeg, Manitoba, September 18-22, Committee on River Ice Processes and the Environment.

Jasek, M. Gauthier, Y., Poulin, J. and Bernier, M. 2013. Monitoring Freeze-up on the Peace River at the Vermillion Rapids using RADARSAT-2 SAR data. 17th Workshop on River Ice, Edmonton, Alberta, Canada, July21-24, 2013, Committee on River Ice Processes and the Environment.

Jasek, M., Shen, H.T., Pan, J. and Paslawski, K. 2015. Anchor Ice Waves and their Impact on Winter Ice Cover Stability. 18th Workshop on the Hydraulics of Ice Covered Rivers, Quebec City, Quebec, Canada, August 18-20. Committee on River Ice Processes and the Environment.

Johnson, R.P., and Kostras, T.V. 1980. Physical hydraulic model study of ice-covered river. Proceedings of the ASCE Specialty Conference: Computer and Physical Modeling in Hydraulic Engineering, Chicago, Illinois, USA.

Judge, D. G., Lavender, S. T., Carson, R. W., and Ismail, S. 1997. Headpond Ice Jams - Where Will They Occur? The 9th Workshop on River Ice, Frederickson, New Brunswick, Canada, Committee on River Ice Processes and the Environment.

Kalke, H. and Loewen, M. 2017. Predicting Surface Ice Concentration using Machine Learning. 19th Workshop on the Hydraulics of Ice Covered Rivers, Whitehorse, Yukon, Canada, July 9-12, 2017, Committee on River Ice Processes and the Environment.

Kalke, H., McFarlane, V., Ghobrial, T. R., and Loewen, M. R. 2019. Field Measurements of Supercooling in the North Saskatchewan River. 20th Worlshop on the Hydraulics of Ice Covered Rivers, Ottawa, Ontario, Canada, Committee on River Ice Processes and the Environment.

Kempema, E, W. and Ettema, R. 2015. Frazil or Anchor Ice Blockage of Submerged Water Intakes? 18th Workshop on the Hydraulics of Ice Covered Rivers, Quebec City, QC, Canada, August 18-20, 2015, Committee on River Ice Processes and the Environment.

Kempema, E., Osada, K., Remlinger, B. and Ettema, R. 2019. Anchor-Ice-Related Flooding along Flat Creek, Jackson, Wyoming: Inshights from a Stream in Mountainous Terrain. 20th Workshop on the Hydraulics of Ice-Covered Rivers, Ottawa, Ontario, Canada, Committee on River Ice Processes and the Environment.

Lal, A.M., Shen, H.T., 1991. A mathematical model for river ice processes. Journal of Hydraulic Engineering. **117** (7), 851-867.

Lindenschmidt, K. 2017. RIVICE - A Non-Proprietary, Open-Source, One-Dimensional River-Ice Model. Water 9 314

Lindenschmidt, K., Baulch, H., and Cavaliere, E. 2018. River and Lake Ice Processes - Impacts of Freshwater Ice on Aquatic Ecosystems in a Changing Globe. Water 10, 1586.

Liu, N., Kells, J. and Lindenschmidt, K.E. 2015. Mapping River Ice Cover Breakup Induced by Hydropeaking Operations. 18th Workshop on the Hydraulics of Ice Covered Rivers, Quebec City, Quebec, Canada, August 18-20, 2015, Committee on River Ice Processes and the Environment.

Malenchak, J. 2011. Numerical Modelling of Ricer Ice Processes on the Lower Nelson River. PhD Thesis. University of Manitoba, Winnipeg, Canada.

Matousek, V. 1984. Types of Ice Run and Conditions for their Formation. Proceedings of the 7th International Symposium on Ice, Hamburg, Germany. International Association of Hydro-Environment Engineering and Research.

Matousek, V. 1988. Hypothesis of Dynamic Ice Bridge Formation. Ice Symposium 1988. International Association of Hydro-Envionment Engineering and Research.

Maxwell, J. 2012. Characterization of the Winter Regime of an Urban River. MSc Thesis, University of Alberta, Edmonton, Canada.

Maxwell, J., Hicks, F. and Loewen, M. 2011. Study of Freeze-up Ice Characteristics on the North Saskatchewan River. 16th Workshop on River Ice, Winnipeg, Manitoba, Canada, September 18-22, 2011, Committee on River Ice Processes and the Environment.

McFarlane, V. 2014. Laboratory Studies of Suspended Frazil Ice Particles. MSc Thesis. University of Alberta, Edmonton, Canada.

McFarlane, V., Loewen, M. and Hicks, F. 2017. Measurements of the size distribution of frazil ice particles in three Alberta Rivers. Cold Regions Science and Technology, 142: 100-117.

Michel.B. 1971. Winter regime of rivers and lakes. US Army Cold Regons Research and Engineering Laboratory, Hanover, New Hampshire.

Michel, B., Marcotte, N., Fonesca, N. and Rivard, G. 1982. Formation of border ice in the Ste.Anne River. Proceedings of the 2nd Workshop on the Hydraulics of Ice Covered Rivers, Edmonton, Alberta, Canada, Committee on River Ice Processes and the Environment.

Nafziger, J. Morley, J. Hicks, F., Linnansarri, T., Fraser, A., Pennell, C. and Cunjak, R. 2011. Freeze-up, breakup, and winter ice observations on four small regulated and unregulated streams in Newfoundland, Canada. 16th Workshop on River Ice, Winnipeg, Manitoba, Canada, September 18-22, 2011, Committee on River Ice Processes and the Environment.

Nezhikhosky, R.A., 1964. Coefficient of roughness of bottom surface of slush ice cover. Soviet Hydrology, Selected Papers. **2**, 127-150.

NHC., 2007. North Saskatchewan River Flood Risk Mapping Study; Devon to Fort Saskatchewan (Excluding Edmonton). Submitted to Alberta Environment.

Nguyen, C., Dow, K., Malenchak, J., Morris, M. and Westmacott, J. Observations of Anchor Ice Formation and Release at Clark Lake/ Split Lake. 19th Workshop on the Hydraulics of Ice Covered Rivers, Whitehorse, Yukon, Canada, July 9-12, 2017, Committee on River Ice Processes and the Environment.

Osterkamp, T. E. 1978. Frazil ice formationL A Review. ASCE Journal of the Hydraulics Dicision, 104.

Pariset, E., Hausser, R. 1961. Formation and evolution of ice covers on rivers. Transactions of the Engineering Institute of Canada. 5(1)

Pariset, E., Hausser, R., Gagnon, A. 1966. Formation of ice covers and ice jams in rivers. ASCE Journal of Hydraulics Division. 92 (HY6), 1–24.

Prowse, T. D. 2001a. River Ice Ecology. I: Hydrologic, Geomorphic and Water-Quality Aspects. Journal of Cold Regions Engineering 15(1) 1-16.

Prowse, T. D. 2001b. River Ice Ecology. II: Biological Aspects. Journal of Cold Regions Engineering 15(1) 17-33.

Prowse, T.D., Bonsal, B. R., Duguay, C. R. and Lacroix, M. P. 2007. River-ice break-up/freeze-up: a review of climatic drivers, historical trends and future predictions. Annals of Glaciology 46.

Richard, M. and Morse, B. 2008. Multiple frazil ice blockages at a water intake in the St. Lawrence River. Cold Regions Science and Technology 53 pp131-149.

Rokaya, P. Morales-Marin, L. and Lindenschmidt, K.E. 2017. A physically-based modelling framework for operations forecasting of river ice breakup. Advances in Water Resources 139.

Rokaya, P. Wheater, H. and Lindenschmidt, K. 2019. Promoting Sustainable Ice-Jam Flood Management along the Peace River and Peace-Athabasca Delta. Journal of Water Resources Planning and Management, 145 (1).

Rousseau, Sauve, Warren, Inc., and Hydro-Quebec, 1983. Simulation des conditions de glace en riviere – documentation de programme. Montreal, Quebec, Canada.

She, Y. and Hicks, F. 2005. Incorporating Ice Effects in Ice Jam Release Surge Models. 13th Workshop on the Hydraulics of Ice Covered Rivers, Hanover, New Hampshire, USA, September 15-16, 2005, Committee on River Ice Processes and the Environment.

She, Y., Hicks, F., Steffler, P. and Healy, D. 2009. Constitutive model for internal resistance of moving ice accumulations and Eulerian implementation for river ice jam formation. Cold Regions Science and Technology 55.

She, Y., Hicks, F. and Andrishak, R. 2012. The role of hydro-peaking in freeze-up consolidation events on regulated rivers. Cold Regions Science and Technology 73.

Shen, H. T. 2010. Mathematical modeling of river ice processes. Cold Regions Science and Technology 62 2-13

Shen, H.T. and Wang, D.S. 1995. Under cover transport and accumulation of frazil granules. ASCE Journal of Hydraulic Engineering. 121 (2) pp107-118.

Steffler, P. and Blackburn, J. 2002. River2D Two-Dimensional Depth Averaged Model of Ruver Hydrodynamics and Fish Habitat. Introduction to Depth Averaged Modeling and User's Manual.

TALAS. 1995. RIVICE Model Documentation: Volume II - Technical Appendices, Report submitted to the River Ice Model Project Steering Committee, November 1995.

Tatinclaux, J. and Lee, C. 1978. Initiation of ice jams - a laboratory study. Canadian Journal of Civil Engineering 5 202-212.

Theriault, I., Saucet, J.P. and Taha, W. 2010. Validation of the Mike-Ice model simulating river flows in presence of ice and forecast of changes to the ice regime of the Romaine river due to hydroelectric project. 20th International Symposium on Ice, Lahti, Finland. International Association of Hydro-Environment Engineering and Reearch.

Timalsina, N.P., Charmasson, J. and Alfredsen, K. T. 2013. Simulation of the ice regime in a Norwegian regulated river. Cold Regions Science and Technology 94 pp61-73.

Timalsina, N.P., Gebre, S.B. and Alfredsen, 2013. Climate change impact on the river ice regime in a Norwegian regulated river. 17th Workshop on River Ice, Edmonton, Alberta, Canada, July21-24, 2013, Committee on River Ice Processes and the Environment.

Total E&P Canada Ltd. 2007. Environmental Baseline Study: Hydrology. Calgary, Alberta, Canada. 36 pages.

Tsang, G. 1984. Concentration of frazil in flowing water as measured in laboratory and in the field. Proceedings of the 7th International Association of Hydro-Environment Engineering and Research Ice Symposium. 3.

Tsang, G. 1986. Preliminary report on field study at Lachine Rapids of cooling of river and formation of frazil and anchor ice. 4th Workshop on River Ice, Montreal, Quebec, Canada, Committee on River Ice Processes and the Environment.

Turcotte, B., Burrell, B.C. and Beltaos, S. 2019. The Impact of Climate Change on Breakup Ice Jams in Canada: State of knowledge and research approaches. 20th Workshop on the Hydraulics of Ice Covered Rivers, Ottawa, Ontario, Canada, Committee on River Ice Processes and the Environment.

Turcotte, B., Nafziger, J., Clark, S., Beltaos, S., Jasek, M., Alfredsen, K., Lind, L. and Stander, E. 2017. Monitoring river ice processes: Sharing experience to improve successful research programs. 19th Workshop on the Hydraulics of Ice Covered Rivers, Whtiehorse, Yukon, Canada. Committee on River Ice Processes and the Environment.

Tuthill, A.M., Wuebben, J.L. and Gagnon, J.J. ICETHK User's Manual. CRREL Special Report 98-11. US Army Corps of Engineers, September, 1998.

Urroz, G. and Ettema, R. 1994. Small-scale experiments on ice-jam initiation in a curved channel. Canadian Journal of Civil Engineering 21 719-727.

Uzuner, M.S. 1975. The composite roughness of ice covered streams. Journal of Hydraulic Research, 13.

Uzuner, M.S. and Kennedy, J. F. 1976. Theoretical model of river ice jams. ASCE Journal of the Hydraulics Division, 102.

Wang, J. and Chen, P. 2011. Progress in Studies on Ice Accumulation in River Bends. Journal of Hydrodynamics 23 (6) 737-744.

Wang, D.S., Shen, H.T. and Crissman, R.D. 1995. Simulation and analysis of upper Niagara River ice-jam conditions. Journal of Cold Regions Engineering 9 (3) pp119-134.

Warren, S., Puestow, T., Richard, M., Khan, A.A., Khayer, M. and Lindenschmidt, K. 2017. Near Real-time Ice-Related Flood Hazard Assessment of the Exploits River in Newfoundland, Canada. 19th Workshop on the Hydraulics of Ice Covered Rivers, Whitehorse, Yukon, Canada, July 9-12, 2017, Committee on River Ice Processes and the Environment.

Wazney, L., Clark, S, P. and Wall, A. 2017. Freeze-up Jam Observations on the Dauphin River. 19th Workshop on the Hydraulics of Ice Covered Rivers, Whitehorse, Yukon, Canada, July 9-12, 2017, Committee on River Ice Processes and the Environment.

Whitfield, P. and McNaughton, B. 1986. Dissolved-oxygen depressions under ice cover in two Yukon rivers. Water Resources Research.

Ye, Y. and She, Y. 2019. Evaluating Criteria for Mechanical Breakup Initiation Using Field Data. 20th Workshop on the Hydraulics of Ice Covered Rivers, Ottawa, Ontario, Canada, Committee on River Ice Processes and the Environment.

Zhang, F. and Lindenschmidt, K., 2017. River ice Hydraulic Modeling of the Slave River Delta. 19th Workshop on the Hydraulics of Ice Covered Rivers, Whitehorse, Yukon, Canada, July 9-12, 2017, Committee on River Ice Processes and the Environment.

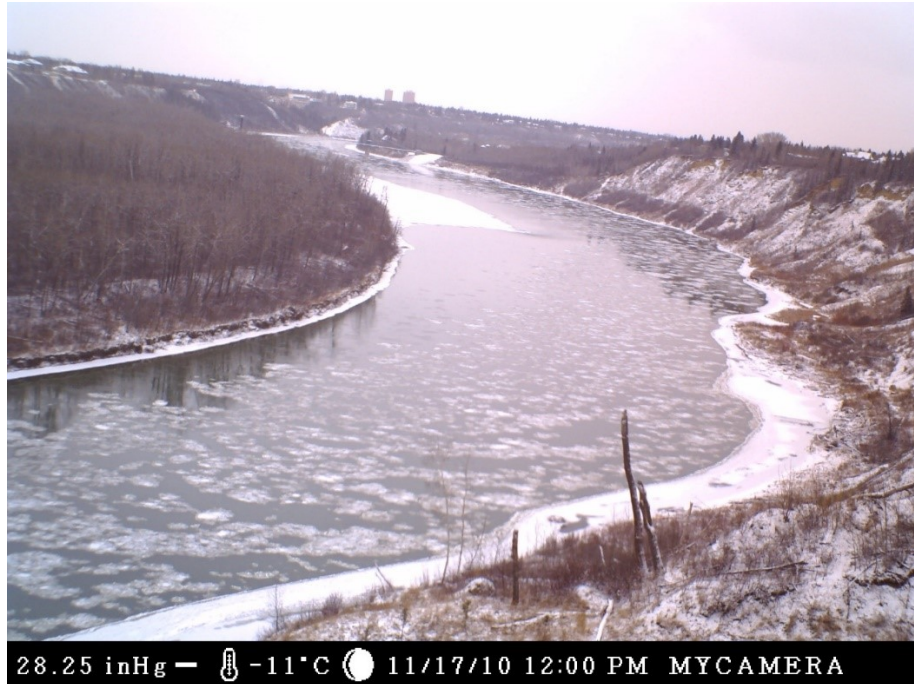# Appendix A – Example images showing surface ice concentration at the upstream boundary, 2010-11.

28.25 inHg — -11°C 11/17/10 12:00 PM MYCAMERA

Figure A-1. Surface ice concentration at Station 0.00 km, 17th November 2010 12:00.

27.98 inHg — -15°C 11/18/10 12:00 PM MYCAMERA

Figure A-2. Surface ice concentration at Station 0.00 km, 18th November 2010 12:00.

Figure A-3. Surface ice concentration at Station 0.00 km, 19th November 2010 12:00.

Appendix B – Ice thickness plots.
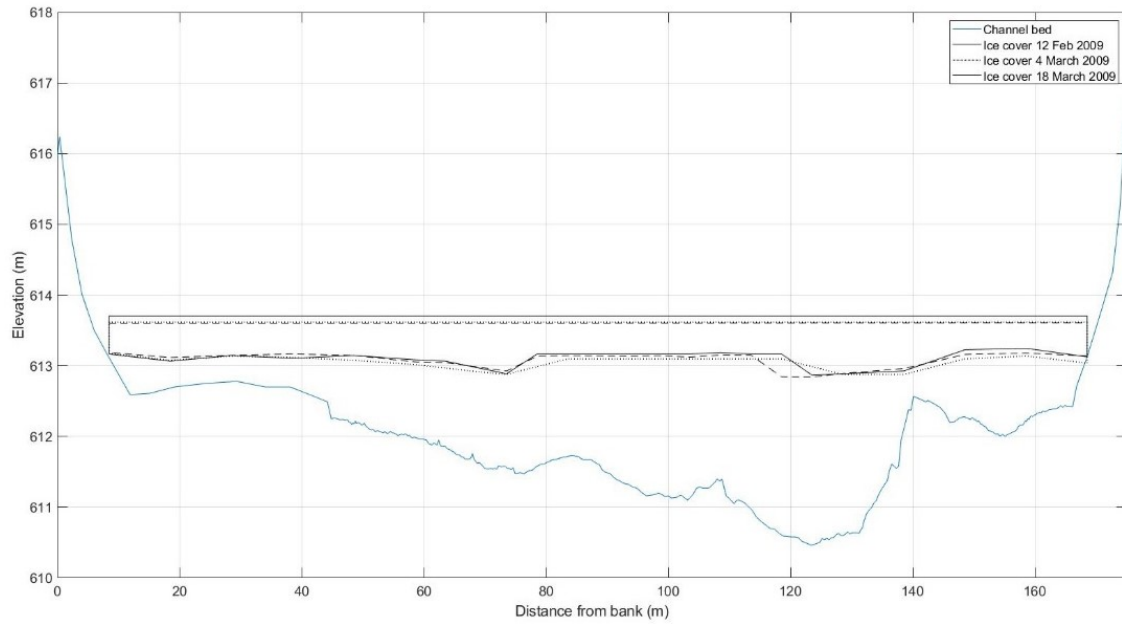
Figure B-1. Ice thickness profiles: 2009.
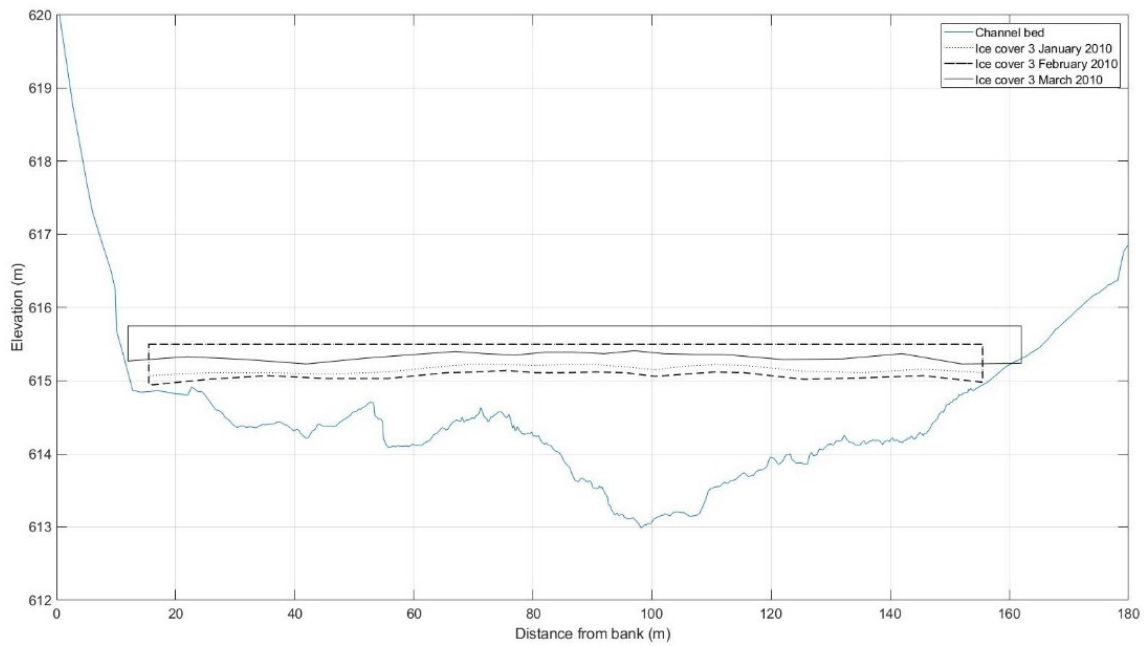
Figure B-2. Ice thickness profiles: 2010.
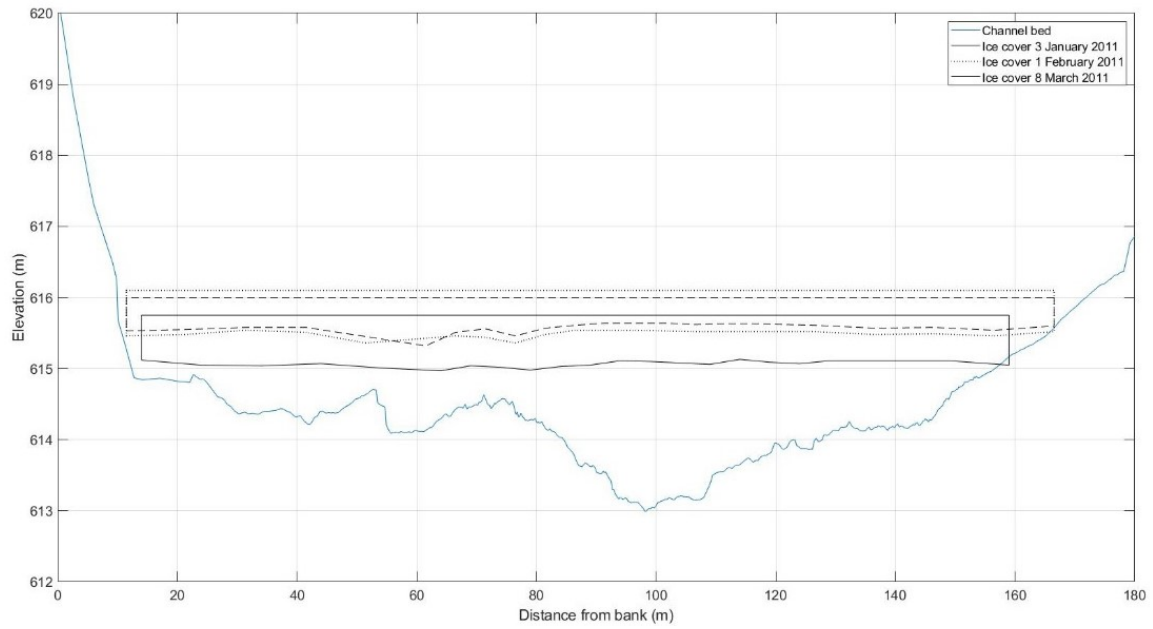
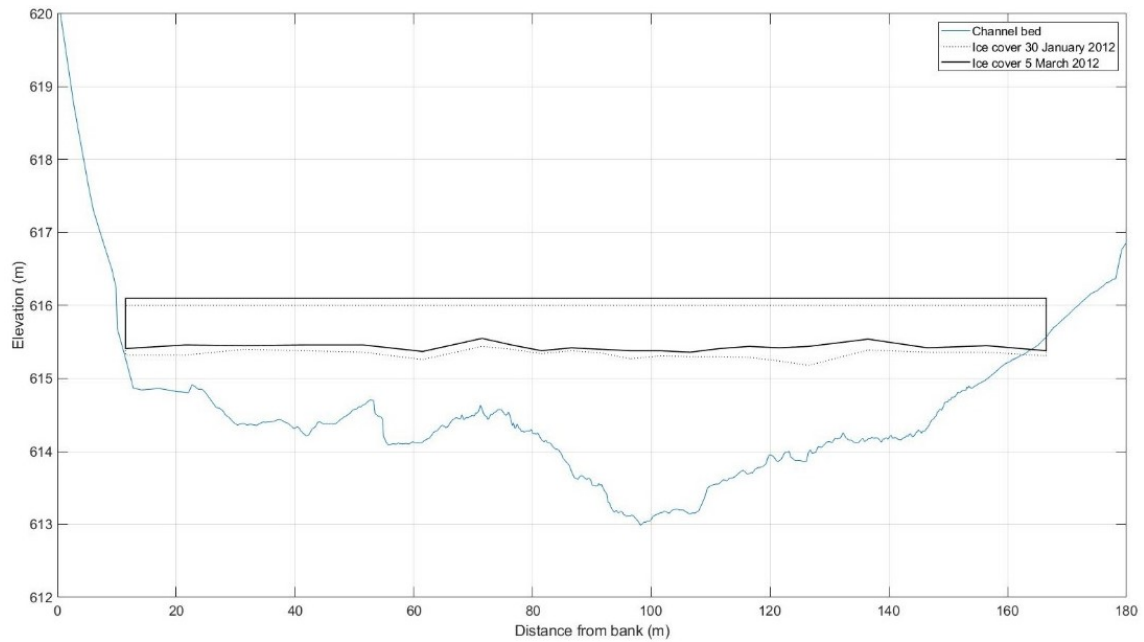Figure B-3. Ice thickness profiles: 2011.
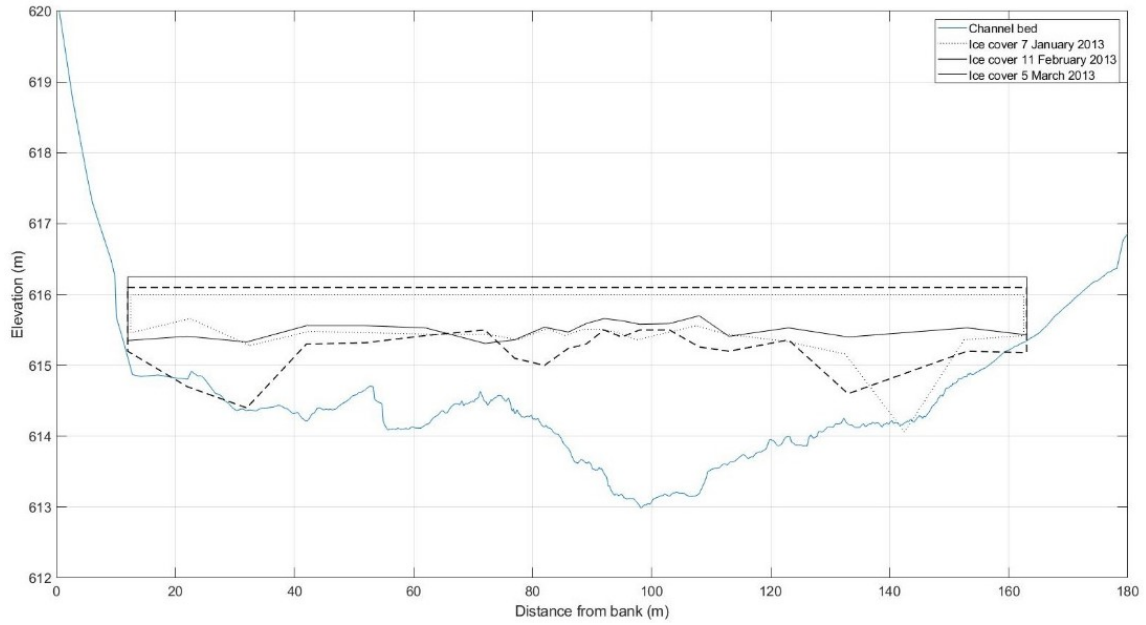

Figure B-4. Ice thickness profiles: 2012.
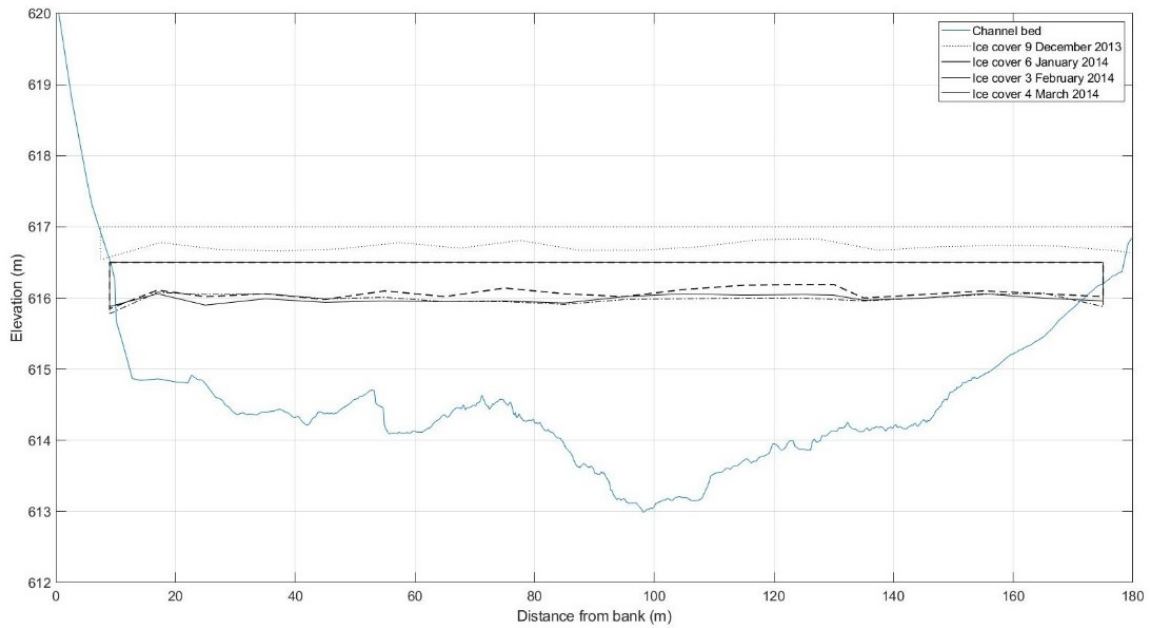
Figure B-5. Ice thickness profiles: 2013.
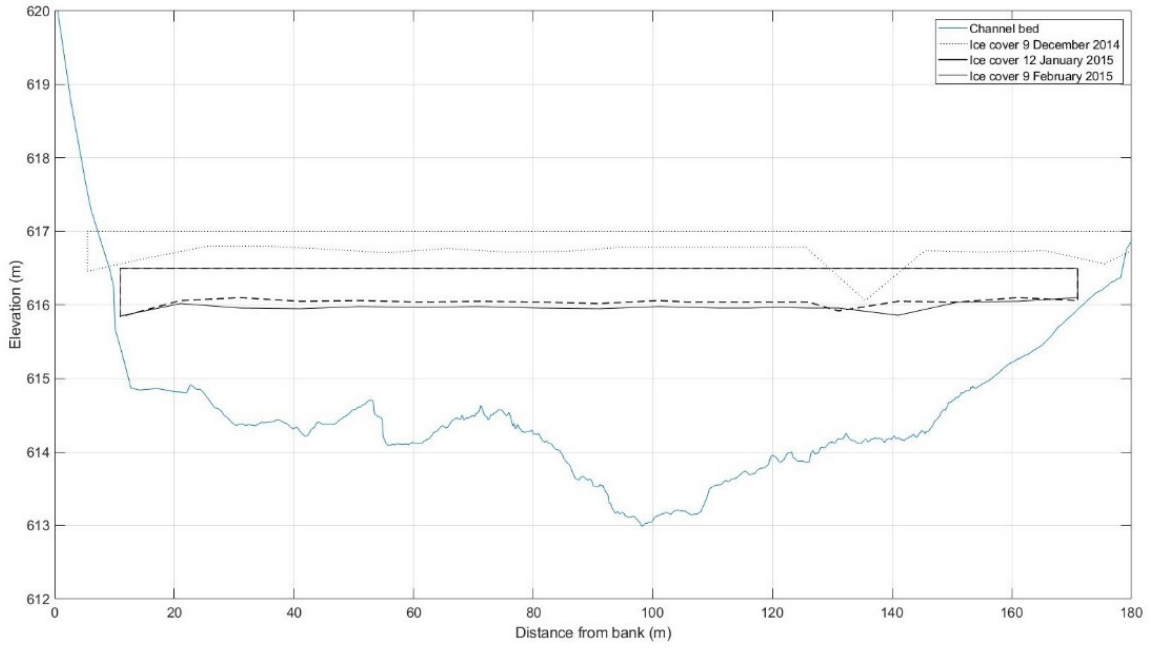

Figure B-6. Ice thickness profiles: 2013-14.

Figure B-7. Ice thickness profiles: 2014-15.